

**IMPROVING COUPLING EFFICIENCY BY USING
ADIABATIC TRANSITION IN PHOTONIC
CRYSTAL WAVEGUIDES**

**A Thesis Submitted to
the Graduate School of Engineering and Sciences of
İzmir Institute of Technology
in Partial Fulfillment of the Requirements for the Degree of**

MASTER OF SCIENCE

in Physics

**by
Zebih ÇETİN**

**July 2012
İZMİR**

We approve the thesis of **Zebih ÇETİN**

Examining Committee Members:

Prof. Dr. Orhan ÖZTÜRK
Department of Physics, İzmir Institute of Technology

Prof. Dr. M. Salih DİNLEYİCİ
Department of Electrical and Electronics Engineering, İzmir Institute of Technology

Assoc. Prof. Dr. H. Sami SÖZÜER
Department of Physics, İzmir Institute of Technology

13 July 2012

Assoc. Prof. Dr. H. Sami SÖZÜER
Supervisor, Department of Physics
İzmir Institute of Technology

Prof. Dr. Nejat BULUT
Head of the Department of
Physics

Prof. Dr. R. Tuğrul SENGER
Dean of the Graduate School of
Engineering and Sciences

ACKNOWLEDGMENTS

I would like to thank my supervisor, Assoc. Prof. Dr. H. Sami SÖZÜER, who has supported me throughout my thesis with his patience and knowledge. I attribute the level of my Masters degree to his encouragement and effort and without him this thesis would not have been completed or written.

I also want to thank my friends at department of physics at İzmir Institute of Technology for their friendship. Especially i would like to thank my friends Adem Enes Erol, Neslihan Eti and H. Duygu Şengün for their great support.

Finally, I thank my family for supporting me throughout all my studies at University.

ABSTRACT

IMPROVING COUPLING EFFICIENCY BY USING ADIABATIC TRANSITION IN PHOTONIC CRYSTAL WAVEGUIDES

Photonic crystal waveguides (PhCWGs), designed by removing one or more slabs from a perfectly periodic structures, are possibly future optoelectronic circuit elements that promising a good ability to confine light in a direction and allowing it to propagate in other direction. One of the problem in their application is the coupling from a PhCWG to a completely different structure. This difficulty arrives from sudden change in structure's geometry. In this thesis, to over come this difficulty we used a transition region between two photonic crystal structures that have completely different geometrical parameters. According to our simulation results we find that by using transition region, coupling can be achieved almost without any loss.

ÖZET

FOTONİK KRİSTAL DALGA KILAVUZLARINDA ADYABATİK GEÇİŞ KULLANARAK BAĞLANTI ETKİNLİĞİNİN ARTIRILMASI

Kusursuz bir periyodik yapıdan bir veya daha fazla plaka kaldırılarak tasarlanmış Fotonik Kristal dalga Kılavuzları (FKDK), ışığın belli yönlerde ilerlemesine engel olup diğer yönlerde klavuzlanmasına olanak sağlayan özelliği sayesinde optoelektronik devre elemanları olarak kullanılabilmeleri yönünde gelecek vaat eden bir uygulama olarak ortaya çıkmıştır. Bu uygulamalar sırasında karşılaşılan problemlerden biri, bir fotonik kristal (FK) yapıdan başka bir yapıya geçişte yaşanan kayıplardır. Bu problem, bir FK yapıdan diğer yapıya geçişlerin ani bir şekilde olmasından kaynaklanmaktadır. Bu tezde farklı yapılar arasındaki geçişler sırasında yaşanan bu kayıpları azaltmak için geçişlerin daha yavaş olduğu bir geçiş geometrisi kullandık. Yaptığımız simülasyon sonuçlarına göre bu geçişler hemen hemen hiçbir kayıp olmadan gerçekleşmektedir.

TABLE OF CONTENTS

| | |
|---|------|
| LIST OF FIGURES | viii |
| LIST OF TABLES | xxii |
| CHAPTER 1. INTRODUCTION | 1 |
| CHAPTER 2. THEORY OF PHOTONIC CRYSTALS AND WAVEGUIDES | 5 |
| 2.1. Ordinary Slab Waveguide | 5 |
| 2.1.1. Transverse Electric (TE) Modes | 12 |
| 2.1.1.1. Even Transverse Electric (TE) Modes | 13 |
| 2.1.1.2. Odd Transverse Electric (TE) Modes | 20 |
| 2.1.2. Transverse Magnetic (TM) Modes | 31 |
| 2.1.2.1. Even Transverse Magnetic (TM) Modes | 32 |
| 2.1.2.2. Odd Transverse Magnetic (TM) Modes | 39 |
| 2.2. Photonic Crystal Theory | 49 |
| 2.2.1. 1D Photonic Crystals | 52 |
| 2.2.2. 2D Photonic Crystals | 55 |
| 2.3. Photonic Crystal Waveguides | 58 |
| 2.3.1. 1D Photonic Crystal Waveguides | 58 |
| 2.3.2. 2D Photonic Crystal waveguides | 58 |
| 2.4. Adiabatic Coupling | 60 |
| 2.5. Finite Difference Time Domain Method | 65 |
| CHAPTER 3. IMPROVING COUPLING EFFICIENCY | 68 |
| 3.1. Coupling Process | 68 |
| 3.1.1. Coupling from Thin to Thick Waveguides | 69 |
| 3.1.2. Coupling from Thick to Thin Waveguides | 74 |
| 3.2. Calculation of Coupling Coefficients | 93 |
| 3.2.1. Continuous source | 98 |
| 3.2.2. Gaussian source | 100 |

| | |
|--|-----|
| CHAPTER 4. COUPLING SINGLE-SLAB WAVEGUIDES | 103 |
| 4.1. Single Slab to Single Slab Waveguide | 103 |
| 4.2. Two Stage Coupling of Single Slab Waveguide | 113 |
| CHAPTER 5. COUPLING SINGLE-SLAB TO 1D PHOTONIC CRYSTAL WAVEGUIDES | 119 |
| 5.1. Tapering Only Defect Line | 119 |
| 5.2. Single slab to Multi Slab Coupling-A different Approach | 126 |
| 5.3. Taper Fail | 132 |
| CHAPTER 6. COUPLING MULTI-SLAB TO MULTI-SLAB WAVEGUIDE | 137 |
| 6.1. Coupling Between Two Different Waveguide | 137 |
| 6.2. Multi to Multi slab WG-Same lattice constant | 143 |
| CHAPTER 7. COUPLING SINGLE-SLAB TO 2D LINE DEFECT PHOTONIC CRYSTAL WAVEGUIDES | 149 |
| 7.1. One-Stage Coupling | 149 |
| 7.2. Two-Stage Coupling | 156 |
| CHAPTER 8. CONCLUSION | 161 |
| REFERENCES | 163 |

LIST OF FIGURES

| <u>Figure</u> | <u>Page</u> |
|---|-------------|
| Figure 2.1. Two media with dielectric constants ϵ_d and ϵ . The blue dashed lines represent wave fronts. The red dashed arrows represent the propagation vectors. Dark gray region represents a dielectric material with thickness $2R_d$ and with higher dielectric constant, ϵ_d . Light gray represents the background dielectric material with a lower dielectric constant, ϵ_b | 6 |
| Figure 2.2. Graph of $\tan(\tilde{\gamma}_d)$ and $\tilde{\gamma}_b/\tilde{\gamma}_d$ for even TE modes. | 15 |
| Figure 2.3. $\tilde{\omega} = \omega R/2\pi c$ versus $\tilde{\beta} = \beta R/2\pi$ plotted for even TE modes for a slab waveguide of thickness $2R_d$. The slab waveguide and the background has dielectric constant of $\epsilon_d = 13$ and $\epsilon_b = 1$ respectively. | 16 |
| Figure 2.4. Graph of the functions $\tan(\tilde{\gamma}_d)$ and $(-1/\tilde{\gamma}_b)\tilde{\gamma}_d$ for even TE modes. | 22 |
| Figure 2.5. $\tilde{\omega} = \omega R_d/2\pi c$ versus $\tilde{\beta} = \beta R_d/2\pi$ plotted for odd TE modes of a slab waveguide with thickness of $2R_d$. The slab waveguide and the background materials have dielectric constant of ϵ_d and ϵ_b respectively. | 23 |
| Figure 2.6. $\tilde{\omega}$ versus $\tilde{\beta}$ plotted for even TE (Blue lines) and odd TE modes (Red lines) of a slab waveguide with thickness $2R_d$ | 24 |
| Figure 2.7. First two even TE mode profiles, TE_0 and TE_2 , and First two odd TE mode profiles, TE_1 and TE_3 . The propagation constant is $\tilde{\beta} = 0.6$. The dielectric constant of slab is $\epsilon_d = 13$ and the dielectric constant of background is $\epsilon_b = 1$. The thickness of slab is $2R_d$ | 26 |
| Figure 2.8. Energy density profiles for first two even TE modes, TE_0 and TE_2 , and first two odd TE modes, TE_1 and TE_3 . The propagation constant is $\tilde{\beta} = 0.6$. The dielectric constant of slab is $\epsilon_d = 13$ and the dielectric constant of background is $\epsilon_b = 1$. The thickness of slab is $2R_d$ | 27 |
| Figure 2.9. Poynting vector for both even and odd TE modes. The dielectric constant of slab is ϵ_d and the dielectric constant of background is ϵ_b . The thickness of slab is $2R_d$. The propagation constant is $\tilde{\beta} = 0.6$ | 30 |
| Figure 2.10. Graph of $\tan(\tilde{\gamma}_d)$ and $(\epsilon_d\tilde{\gamma}_b/\epsilon_b)\frac{1}{\tilde{\gamma}_d}$ for a chosen $(\epsilon_d\tilde{\gamma}_b/\epsilon_b)$ and their intersection. | 34 |
| Figure 2.11. $\tilde{\omega}$ versus $\tilde{\beta}$ plotted for even TM modes of a slab waveguide with thickness $2R_d$ | 35 |
| Figure 2.12. Graph of $\tan(\tilde{\gamma}_d)$ and $(-\epsilon_b/(\epsilon_d\tilde{\gamma}_b))\tilde{\gamma}_d$ functions for a chosen $-\epsilon_b/(\epsilon_d\tilde{\gamma}_b)$ value and their intersections. | 40 |

| | |
|--|----|
| Figure 2.13. $\tilde{\beta}$ versus $\tilde{\omega}$ graph of odd TM modes of a single slab waveguide with dielectric constant $\epsilon_d = 13$ and thickness $2R_d$. The dielectric constant of the background is $\epsilon_b = 1$ | 41 |
| Figure 2.14. Graph of $\tilde{\beta}$ versus $\tilde{\omega}$ plotted for both even TM (Blue lines), and odd TM (Red lines) modes for single slab waveguide with thickness $2R_d$ and dielectric constant of slab and background are $\epsilon_d = 13$ and $\epsilon_b = 1$ respectively. | 42 |
| Figure 2.15. First two even TM mode profiles (TM ₀ and TM ₂) and energy densities of each modes of slab waveguide. The dielectric constant of slab is ϵ_d and the dielectric constant of background is ϵ_b . The thickness of slab is $2R_d$. The propagation constant is | 44 |
| Figure 2.16. Electromagnetic energy density distribution of even TM modes, ($u_{em,0}$ and $u_{em,2}$), and odd TM modes, ($u_{em,1}$ and $u_{em,2}$), along z -coordinate. The dielectric constant of slab is $\epsilon_d = 13$ and the dielectric constant of background is $\epsilon_b = 1$. The thickness of slab is $2R_d$ | 45 |
| Figure 2.17. Poynting vector profile along z -direction for even, (TM ₀ and TM ₂), and odd, (TM ₁ and TM ₃) TM modes of slab waveguide. The dielectric constant of slab is ϵ_d and the dielectric constant of background is ϵ_b . The thickness of slab is $2R_d$ | 48 |
| Figure 2.18. A graphical representation of adiabatic transition of the Hamiltonian from H_i to H_f . The graph on the left hand represents adiabatic transition of a particle. The graph on the right-hand side represents the adiabatic transition of a electromagnetic mode coupling from an initial state to a final state. | 61 |
| Figure 3.1. The single-slab waveguide on the left-hand side has thickness of $d_{in} = 2$ with $\epsilon_a = 13$, the single-slab waveguide on the right-hand side has thickness of $d_{out} = 12$ with $\epsilon_a = 13$. Background has dielectric constant of $\epsilon_b = 2.25$. Two slabs are butt joined. | 69 |
| Figure 3.2. Single-slab waveguide band structure for transverse electric (TE) mode. Red dashed lines represent the first three guided modes of single-slab of thickness $d_{in} = 2$ and dielectric constant of $\epsilon_a = 13$, black solid lines represent the band structure of waveguide that has thickness of $d_{out} = 12$ and dielectric constant $\epsilon_a = 13$. The background for both waveguide has dielectric constant of $\epsilon_b = 2.25$ | 70 |

| | |
|---|----|
| Figure 3.3. The single-slab waveguide on the left-hand side has thickness of $d_{in} = 2$ with $\epsilon_a = 13$, the single-slab waveguide on the right-hand side has thickness of $d_{out} = 12$ with $\epsilon_a = 13$. Background has dielectric constant of $\epsilon_b = 2.25$. FDTD simulation of z - component of electric field E_z of TE mode profile along waveguide without taper region. | 72 |
| Figure 3.4. The slab on the left-hand side has thickness of $d_{in} = 2$ with dielectric constant of $\epsilon_a = 13$, the slab waveguide on the right-hand side has thickness of $d_{out} = 12$ with dielectric constant of $\epsilon_a = 13$. Background has dielectric constant of $\epsilon_b = 2.25$. FDTD simulation of z -component of electric field E_z of TE mode profile along waveguide with taper region introduced. | 73 |
| Figure 3.5. Dielectric structure of butt joined single-slab waveguide, input part thickness $d_{in} = 12$ with $\epsilon_a = 13$, output part thickness is $d_{out} = 2$ with $\epsilon_a = 13$. Background has dielectric constant of $\epsilon_b = 2.25$ | 74 |
| Figure 3.6. Band structure of single slab waveguide calculated for TE modes. Black lines represent band structure of single-slab with thickness $d_{out} = 2$ and dielectric constant of $\epsilon_a = 13$. Red line is the guided mode of single-slab waveguide with thickness $d_{in} = 12$ and dielectric constant of $\epsilon_a = 13$. The background of both waveguide has the same dielectric constant of $\epsilon_b = 2.25$ | 76 |
| Figure 3.7. Dielectric structure, input part thickness $d_{in} = 12$ with $\epsilon_a = 13$, output part thickness $d_{out} = 2$ with $\epsilon_a = 13$. Background has dielectric constant of $\epsilon_b = 2.25$. FDTD simulation of TE mode, operating mode is even with frequency $\tilde{\omega} = 0.3565$ and wave vector $\tilde{k} = 1.264$, and there is no taper region introduced. | 77 |
| Figure 3.8. Band structure of single slab waveguide calculated for TE modes. Black lines represent band structure of single slab with thickness $d_{out} = 2$ and dielectric constant of $\epsilon_a = 13$. Red line is the guided modes of single slab waveguide with thickness $d_{in} = 12$ and dielectric constant of $\epsilon_a = 13$. The background of both waveguide has dielectric constant of $\epsilon_b = 2.25$. The green lines are the first guided modes of single-slab with intermediate thickness of $d_{out} = 10, 8, 6, 5.8, \dots 2.2$ | 79 |

| | |
|---|----|
| Figure 3.9. Dielectric profile of structure, the waveguide on the left hand side has thickness of $d_{in} = 12$ and the waveguide on right hand side has thickness of $d_{out} = 2$ with taper region introduced. FDTD simulation of TE mode, operating mode is odd, and in this simulation we introduce taper region. | 80 |
| Figure 3.10. Band structure of single slab waveguide with thickness of $d_{out} = 2$, which has dielectric constant of $\epsilon_a = 13$ (black lines). The first two guided modes of input waveguide which has thickness $d_{in} = 12$ and dielectric constant $\epsilon_a = 13$ (red dashed lines). Both waveguides are immersed in the same region with dielectric constant $\epsilon_b = 2.25$. The green lines represent the second guided modes of waveguides with intermediate thickness $d_{out} = 10, 8, 6, 5.8, \dots 2.2$ | 82 |
| Figure 3.11. Dielectric profile of waveguide structure without taper region introduced. FDTD simulation of z -component of electric field (E_z) of TE mode taken for four different output slab thickness, $d_{out} = 8, d_{out} = 6, d_{out} = 4$, and $d_{out} = 2$, while keeping the input slab thickness constant $d_{in} = 12$. The operating mode has odd symmetry with frequency $\tilde{\omega} = 0.3565$ and wave vector $\tilde{k} = 1.200$ | 84 |
| Figure 3.12. Dielectric profile of structure with taper region introduced. FDTD simulation of z -component of electric field for TE mode. Mode profiles are taken for four different output slab thickness, $d_{out} = 8, d_{out} = 6, d_{out} = 4$, and $d_{out} = 2$ while the input slab thickness is kept constant, $d_{in} = 12$ | 86 |
| Figure 3.13. Band structure of single-slab waveguide with thickness of $d_{out} = 2$ and dielectric constant of $\epsilon_a = 13$, (black lines). First three guided mode of single-slab waveguide with thickness of $d_{in} = 12$ with dielectric constant of $\epsilon_a = 13$. Both waveguides are immersed in a background with dielectric constant $\epsilon_b = 2.25$. The green lines are the third guided modes of single-slab with core width $d_{out} = 10, 8, 6, 5.8, \dots 2.2$ | 88 |
| Figure 3.14. Dielectric profile of waveguide structure without taper region introduced. FDTD simulation of z -component of electric field (E_z) of TE mode. The operating mode has even symmetry with frequency $\tilde{\omega} = 0.3565$ and wave vector $\tilde{k} = 1.088$. The mode profiles are taken for four different output slab thickness, $d_{out} = 8, d_{out} = 6, d_{out} = 4$, and $d_{out} = 2$. Input part thickness is kept constant, $d_{in} = 12$ | 90 |

| | |
|---|-----|
| Figure 3.15. Dielectric profile of the waveguide structure with taper region introduced. FDTD simulation of z -component of electric field (E_z) of TE mode, the operating mode is even. The mode profiles are taken for four different output thickness, ($d_{out} = 8$, $d_{out} = 6$, $d_{out} = 4$, and $d_{out} = 2$) while input slab thickness kept constant, $d_{in} = 12$ | 92 |
| Figure 3.16. Transverse electric mode distribution viewed along $x - axes$ taken at $y = 0$, and there is no taper region, incoming mode couple to three even modes as seen. Drop in amplitude of EM wave is due to back reflection and radiation to background at the interface. | 98 |
| Figure 3.17. TE mode profile viewed along $x - axes$ taken at $y = 0$, we introduce taper region in this structure, taper region force incoming mode to couple first single mode of output part. | 99 |
| Figure 3.18. z -component of electric field distribution along the center of waveguide structure in the x -direction. Two waveguide are butt joined to each other. The incoming mode couple to three even mode as seen from figure. Drop in amplitude of TE mode is due to back reflection and radiation to background at the interface. | 101 |
| Figure 3.19. Electric field distribution along waveguide in the x -direction at the center of waveguide taken at four different time step ($t = 25$, $t = 30$, $t = 35$, and $t = 40$). Two single-slab waveguides are joined by a taper region | 102 |
| Figure 4.1. Dielectric profile of waveguide structure without taper region introduced. The input waveguide has thickness of $d_{in} = 12$ and the output waveguide has thickness of $d_{out} = 2$. Both waveguide have the same dielectric constant of $\epsilon_a = 13$. The waveguide structure is immersed in a background with dielectric constant of $\epsilon_b = 2.25$ | 103 |
| Figure 4.2. Band structures of single-slab waveguides of thickness $d_{out} = 2$ and dielectric $\epsilon_a = 13$ (black solid lines). First guided mode of single-slab waveguide of thickness $d_{in} = 12$ with dielectric $\epsilon_a = 13$ (red dashed lines). The background has dielectric constant of $\epsilon_b = 2.25$ | 104 |

- Figure 4.3. Dielectric profile of waveguide structure without taper region introduced. The input waveguide has thickness of $d_{in} = 12$ and the output waveguide has thickness of $d_{out} = 2$. Both waveguide have the same dielectric constant of $\epsilon_a = 13$. The waveguide structure is immersed in a background with dielectric constant of $\epsilon_b = 2.25$. FDTD simulation of z -component of electric field (E_z) profile for TE mode is shown. 106
- Figure 4.4. Dielectric profile of waveguide structure with taper region introduced. The input and output single slab waveguides thickness are $d_{in} = 12$ and $d_{out} = 2$. The dielectric constant are same for both slab which is $\epsilon_a = 13$. The whole structure is immersed in a background with dielectric constant $\epsilon_b = 2.25$. FDTD simulation of z - component of electric field shown for four different time step. The operating mode is generated by using a Gaussian mode source with frequency and wave vector $\tilde{\omega} = 0.2840$, $\tilde{k} = 1$ respectively. 107
- Figure 4.5. Transmission values versus taper length found by FDTD simulation. Butt-coupling case ($L = 0a$) and adiabatic coupling case ($L > 0a$) are shown for five different input waveguide thickness ($d_{in} = 4, 6, 8, 10, 12$) while keeping the output waveguide thickness constant ($d_{out} = 2$). 108
- Figure 4.6. Dielectric profile of waveguide structure consisting of two butt joined single-slab. Input slab has thickness of $d_{in} = 2$ with dielectric constant of $\epsilon_a = 13$. Output slab has thickness of $d_{out} = 12$ with dielectric constant of $\epsilon_a = 13$. The background medium has dielectric constant of $\epsilon_b = 2.25$ 109
- Figure 4.7. Band structure of single-slab waveguide. Black lines represents single-slab waveguide with thickness of $d_{out} = 12$ with dielectric constant $\epsilon_a = 13$ immersed in a background with dielectric constant $\epsilon_b = 2.25$. The two red dashed lines represent first two guided modes of single-slab waveguide with thickness $d_{in} = 2$ and dielectric constant $\epsilon_a = 13$. The background has $\epsilon_b = 2.25$. The intersection of blue dashed lines indicates our operating mode with frequency $\tilde{\omega} = 0.3565$ and wave vector $\tilde{k} = 1$ 110

- Figure 4.8. Dielectric profile of waveguide structure consisting of two butt joined single-slab. Input slab has thickness of $d_{in} = 2$ with dielectric constant of $\epsilon_a = 13$. Output slab has thickness of $d_{out} = 12$ with dielectric constant of $\epsilon_a = 13$. FDTD simulation of electric field distribution of waveguide structure that is made by butt joined single-slabs. 111
- Figure 4.9. Dielectric profile of waveguide consist of input region with thickness of $d_{in} = 2$, trapezoidal taper region and output region with thickness of $d_{out} = 12$. All waveguide region have same dielectric constant of $\epsilon_a = 13$. The waveguide structure immersed in a background with dielectric constant of $\epsilon_b = 2.25$. Electric field profile of TE mode taken at four different time along waveguide that is adiabatically connected with a transition region. 112
- Figure 4.10. The waveguide structure consisting of three single-slab waveguides that are butt joined. The input region thickness is $d_{in} = 8$ with dielectric constant $\epsilon_a = 13$. The intermediate region thickness is $d_{int} = 2$ with dielectric constant $\epsilon = 13$. The output region thickness is $d_{out} = 8$ with dielectric constant $\epsilon_a = 13$. The whole structure is immersed in a background material with dielectric constant of $\epsilon_b = 2.25$ 113
- Figure 4.11. Band structure of single-slab waveguide with thickness $d_{int} = 2$ with dielectric constant of $\epsilon = 13$ immersed in a medium with dielectric constant of $\epsilon = 2.25$, black lines. Dashed red lines represents guided modes of single slab waveguide with thickness $d_{in} = 8$ with dielectric constant of $\epsilon = 13$ immersed in a medium with dielectric constant of $\epsilon = 2.25$ 114
- Figure 4.12. Dielectric structure of waveguide without taper region introduced. The waveguide consist of input region, intermediate region, and the output region. FDTD simulation of electric field component, (E_z) , of TE mode profile shown for four different time step. The operating frequency and wave vector are $\tilde{\omega} = 0.1027$ and $\tilde{k} = 0.3$ respectively. 116
- Figure 4.13. Dielectric profile of waveguide structure consisting of an input part, transition region, intermediate region and an output part. FDTD simulation of electric field component (E_z) for TE mode profile for four different time step for frequency $\tilde{\omega} = 0.1027$ and wave vector $\tilde{k} = 0.3$.. 117

| | |
|--|-----|
| Figure 4.14. Transmission values versus taper length found by using FDTD simulation. Transmission value for butt-coupling ($L = 0a$) and adiabatic coupling ($L > 0a$) is shown. | 118 |
| Figure 5.1. Dielectric profile of a waveguide that is made by a single slab waveguide with thickness of $d_{in} = 8$ and dielectric constant of $\epsilon_a = 13$, and a multi-slab waveguide with slab thickness of $d_{clad} = 1$ and dielectric constant $\epsilon_a = 13$ and defect line thickness of $d_{out,def} = 2$ with dielectric constant $\epsilon_d = 13$. The whole waveguide is immersed in air, $\epsilon_b = 1$ | 120 |
| Figure 5.2. Band structure calculated for TE mode of multi-slab waveguide (Black lines). The waveguide is made by slabs of thickness $d_{clad} = 1$ with dielectric constant $\epsilon_a = 13$. The defect line has thickness of $d_{out,def} = 2$ with same dielectric constant with cladding slabs. Red dashed line is first guided mode of input part (single slab waveguide) which has thickness of $d_{in} = 8$ with dielectric constant $\epsilon_a = 13$. The background is air, ($\epsilon_b = 1$). | 121 |
| Figure 5.3. Dielectric profile of a single slab waveguide and a multi-slab waveguide. Mode profile of electric field (E_z) found by FDTD simulation. The field profiles are taken at four different time, in this structure there is no taper region introduced. | 123 |
| Figure 5.4. FDTD simulation of structure, consist of a single-slab waveguide, a taper region, and multi-slab waveguide. The single-slab waveguide on left called input part we introduce a taper region which gradually change from $d_{in} = 8$ to $d_{out,def} = 2$ | 124 |
| Figure 5.5. Transmission versus taper length. The output thickness are kept constant while we increase the single slab waveguide thickness from $d_{in} = 4$ to $d_{in} = 10$ | 125 |
| Figure 5.6. Dielectric profile of structure consist of a single-slab waveguide of thickness $d_{in} = 10$ with dielectric constant $\epsilon_a = 13$ (input) and multi-slab waveguide consist of cladding slabs of thickness $d_{clad} = 1$ with dielectric constant $\epsilon_a = 13$ and defect line thickness of $d_{out,def} = 2$ with dielectric constant $\epsilon_a = 13$. The background has dielectric constant of $\epsilon_b = 1$ (output). | 126 |

| | |
|--|-----|
| Figure 5.7. Band Structure calculated for TE mode of multi-slab waveguide with cladding and defect line thickness of $d_{clad} = 1$, $d_{out,def} = 2$ respectively. The dielectric constants are $\epsilon_a = 13$ and $\epsilon_d = 13$, black lines. The red dashed line is the first guided mode of input part (single slab waveguide) which has thickness of $d_{in} = 10$ and dielectric constant $\epsilon_a = 13$ | 127 |
| Figure 5.8. Dielectric profile of structure consist of a single-slab waveguide of thickness $d_{in} = 10$ with dielectric constant $\epsilon_a = 13$ (input) and multi-slab waveguide consist of slabs of thickness $d_{clad} = 1$ with dielectric constant $\epsilon_a = 13$. The defect line of multi-slab waveguide has thickness of $d_{out,def} = 2$ with dielectric constant $\epsilon_a = 13$ The background has dielectric constant of $\epsilon_b = 1$ (output). | 128 |
| Figure 5.9. FDTD simulation of z -component of electric field of TE mode, in this structure there we introduced taper region with 50 unit cell long. Dielectric structure, which consist of a single- slab waveguide (input), a taper region and multi-slab waveguide (output). | 130 |
| Figure 5.10. Transmission values versus taper length calculated with FDTD method. Butt coupling and adiabatic coupling situations are shown, $L = 0a$ and $L = 50a$ | 131 |
| Figure 5.11. Band Structure calculated for TE mode of multi-slab waveguide, cladding thickness is $d_{clad} = 3$, cladding dielectric constant is $\epsilon_a = 13$, defect line thickness is $d_{def} = 2$, defect line dielectric constant is $\epsilon_d = 13$. The background dielectric constant is $\epsilon_b = 2.5$. Red line is first guided mode of input part (single slab waveguide) which has thickness of $d_{in} = 8$ and dielectric constant is $\epsilon_a = 13$ immersed in a background with dielectric constant $\epsilon_b = 2.5$. The intersection of blue lines indicate the operating mode. | 132 |
| Figure 5.12. Dielectric structure, which consist of a single-slab waveguide (input), multi-slab waveguide (output). Electric field distribution, E_z , of TE mode found by FDTD simulation. In this structure there is no taper region. | 134 |
| Figure 5.13. FDTD simulation of TE mode, z -component of electric field, E_z , in this structure we introduced taper region which gradually changing their thickness. Dielectric structure, which consist of a single-slab waveguide (input), a taper region and multi-slab waveguide (output). | 135 |

- Figure 5.14. Transmission values versus taper length of a waveguide structure that is its guided mode is above continuum region. Taper length changed from $L = 0a$ (without transition region) to $L = 100a$ (with transition region). 136
- Figure 6.1. The waveguide on the left-hand side has lattice constant a_1 with cladding and defect line thickness of $d_{in,clad} = 2$, $d_{in,def} = 6$ respectively. The waveguide on the right-hand side has lattice constant $a_2 = 0.5a_1$ with cladding and defect line thickness of $d_{out,clad} = 1$, $d_{out,def} = 2$ respectively. Both waveguides are immersed in air background, $\epsilon_b = 1$ 138
- Figure 6.2. Black lines represent the band structure calculated for TE mode of multi-slab waveguide (the output waveguide) made by slabs of thickness $d_{out,clad} = 1$ with dielectric constant $\epsilon_a = 13$. The defect line has thickness of $d_{out,def} = 2$ with same dielectric constant of cladding, $\epsilon_d = 13$. The background is air, ($\epsilon_b = 1$). The red line represents the first guided mode of multi-slab waveguide (the input waveguide) which has geometric parameters, $d_{in,clad} = 2$, $d_{in,def} = 6$, and the dielectric constants of cladding and defect line are, $\epsilon_a = \epsilon_d = 13$. The background is air, $\epsilon_b = 1$ 138
- Figure 6.3. Dielectric structure of two multi-slab waveguide. The waveguide on the left-hand side has lattice constant a with cladding and defect line thickness of $d_{in,clad} = 2$, $d_{in,def} = 6$ respectively. The waveguide on the right-hand side has lattice constant $0.5a$ with cladding and defect line thickness of $d_{out,clad} = 1$, $d_{out,def} = 2$ respectively. Both waveguides are immersed in air background, $\epsilon_b = 1$. Both waveguide cladding and defect line have the same dielectric constant of $\epsilon_a = \epsilon_d = 13$. FDTD simulation of z -component of electric field (E_z) for TE mode with frequency $\tilde{\omega} = 0.1351$ and wave vector $\tilde{k} = 0.4$ 140

- Figure 6.4. Dielectric profile of the waveguide structure with taper region introduced. The waveguide on the left-hand side is made by slabs of thickness $d_{in,clad} = 2$ with dielectric constant $\epsilon_a = 13$ and the defect line of thickness $d_{in,def} = 6$ with dielectric constant $\epsilon_d = 13$. The waveguide on the right-hand side is made by slabs of thickness $d_{out,clad} = 1$ with $\epsilon_b = 13$ and the defect line is made by a slab of thickness $d_{out,def} = 2$ with $\epsilon_a = 13$. The background is air, ($\epsilon_b = 1$). FDTD simulation of z -component of electric field for TE mode with frequency $\tilde{\omega} = 0.1351$ and wave vector $\tilde{k} = 0.4$. In this structure we introduced taper region of $L = 50a$ long. 141
- Figure 6.5. Transmission value change versus taper length of two waveguides with different lattice constant and different cladding and core slab thickness. $L = 0a$ represents the direct coupling case where $L > 0$ represents the adiabatic coupling case. 142
- Figure 6.6. Dielectric structure of waveguide. The waveguide on the left-hand side (input part) is made by slabs of thickness $d_{in,clad} = 2$ and the defect line thickness is $d_{in,def} = 6$ with $\epsilon_a = 13$. The waveguide on the right-hand side (output part) is made by slabs of thickness $d_{out,clad} = 1$ and the defect line thickness is $d_{out,def} = 1.4$ with $\epsilon_a = 13$. The background is air, ($\epsilon_b = 1$). 143
- Figure 6.7. Band Structure calculated for TE mode of multi-slab waveguide, Black lines are modes of waveguide with slabs and defect line thickness $d_{out,clad} = 1$, $d_{out,def} = 1.4$ respectively. Red dashed line is first guided mode of waveguide with slabs and defect line thickness $d_{out,clad} = 2$, $d_{out,def} = 6$ respectively. Intersection of the blue line represent our operating mode with frequency and wave vector $\tilde{\omega} = 0.1630$, $\tilde{k} = 0.5$ 144
- Figure 6.8. Dielectric structure of waveguide without taper region introduced. The waveguide on the left-hand side (input part) is made by slabs of thickness $d_{in,clad} = 2$ with ϵ_a and the defect line thickness is $d_{in,def} = 6$ with $\epsilon_d = 13$. The waveguide on the right-hand side (output part) is made by slabs of thickness $d_{out,clad} = 1$ with $\epsilon_a = 13$ and the defect line thickness is $d_{out,def} = 1.4$ with $\epsilon_d = 13$. The background is air, ($\epsilon_b = 1$). FDTD simulation of electric field that is in the z -direction is shown for the waveguide without taper region. 146

- Figure 6.9. Dielectric structure of waveguide with taper region of length $L = 100a$ introduced. FDTD simulation of z -component of electric field in the case of taper region introduced. The waveguide on the left-hand side made by slabs of thickness $d_{in,clad} = 2$, the line defect has thickness of $d_{in,def} = 6$ and the waveguide on the right-hand side is made by slabs of thickness $d_{out,clad} = 1$, the defect line thickness is $d_{out,def} = 1.4$. All slabs have same dielectric constant $\epsilon_a = \epsilon_d = 13$. The background is air, ($\epsilon_b = 1$) 147
- Figure 6.10. Transmission values versus taper length calculate using FDTD method. The red curve shows the transmission value calculated using 30 resolution per period and the blue curve shows the transmission value calculated using 60 resolution per period. The butt-coupling case ($L = 0a$) and adiabatic coupling case ($L > 0a$) is shown. 148
- Figure 7.1. Dielectric structure of butt joined waveguide which is made of a single slab waveguide of thickness $d_{in} = 12$ and 2-D line defect PhCWG made of cylindrical rods of radius $R = 1$ and defect line with thickness $d_{out,def} = 2$. All waveguide parts have same dielectric constant of $\epsilon_a = 13$. The background has dielectric constant $\epsilon_b = 2.25$ 150
- Figure 7.2. Band structure of a 2-D line defect PhCWG calculated for TE modes. The photonic crystal is made by cylindrical rods arranged in a square lattice. The defect line has thickness $d_{out,def} = 2$ with dielectric constant $\epsilon_d = 13$ and the cylindrical rods have radius $R = 1$ with same dielectric constant of defect line. The background has dielectric constant of $\epsilon_b = 2.25$. The red line is the operating mode of single-slab with thickness $d_{in} = 12$ with dielectric constant $\epsilon_a = 13$ immersed in a background with dielectric constant of $\epsilon_b = 2.25$. The intersection of blue dashed lines is the operating frequency and wave vector, $\tilde{\omega} = 0.1219$ and $\tilde{k} = 0.4$ respectively. 151
- Figure 7.3. Dielectric structure of butt joined waveguide and z -component of electric field profile of TE mode along structure which is made of a single-slab waveguide of thickness $d_{in} = 12$ and 2D line defect PhCWG made of cylindrical rods of radius $R = 1$ and defect line with thickness $d_{out,def} = 2$. All waveguide parts have same dielectric constant of $\epsilon_a = 13$. The background has dielectric constant $\epsilon_b = 2.25$ 153

| | |
|--|-----|
| Figure 7.4. The dielectric structure of single-slab WG and 2-D line defect PhCWG joined by a taper region. We introduced cylindrical transition region for the background of single-slab WG. Trapezoidal transition geometry is used between single-slab WG and the defect line of 2-D line defect PhCWG. Electric field distribution, (E_z), found by FDTD simulation. Snapshot of field taken for four different time step. | 154 |
| Figure 7.5. Transmission values for TE-polarized electric field, E_z , for the structure of single slab and 2-D line defect PhCWG calculated using FDTD simulation, one stage coupling. Transmission values versus taper length calculated for every $5a$ starting from $L = 0a$, (butt coupling) to $L = 50a$ is shown. | 155 |
| Figure 7.6. Waveguide structure consist of three region, the waveguide on left called input part has thickness of $d_{in} = 12$, intermediate part is 2-D line defect PhCWG has defect line of thickness $d_{int,def} = 2$ and cylindrical rods of radius $R = 1$, and the output part has same thickness with input part. All three part has same dielectric constant $\epsilon_a = 13$. The background has dielectric constant of $\epsilon_b = 2.25$ | 156 |
| Figure 7.7. FDTD simulation of structure, which consist of three waveguides, the waveguide on left called input part has thickness of $d_{in} = 12$, intermediate part is 2-D line defect PhCWG has defect line of thickness $d_{int,def} = 2$ and cylindrical rods of radius $R = 1$, and the output part has same thickness with input part, $d_{out} = 12$. All three part has same dielectric constant $\epsilon_a = 13$. The background has dielectric constant of $\epsilon_b = 2.25$ | 158 |
| Figure 7.8. Dielectric profile of waveguide with taper region length of $L = 100a$ where a is lattice constant. The structure is constructed with a single-slab waveguide which is called input region, a taper region is introduced between input waveguide and 2-D line defect PhCWG. Between 2-D line defect PhCWG and output region we introduce another taper region. The z -component of electric field (E_z) distribution for TE mode found by FDTD simulation. | 159 |

Figure 7.9. Transmission values for TE mode for the structure of single-slab waveguide and 2-D line defect PhCWG calculated using FDTD simulation. In this simulation, the operating mode first coupled form single slab waveguide to 2-D line defect PhCWG and then coupled back to single slab waveguide, two stage-coupling. Transmission values versus taper length calculated for every $5a$ starting from $L = 0a$, (butt coupling) to $L = 100a$, (adiabatic coupling) is shown. 160

LIST OF TABLES

| <u>Table</u> | | <u>Page</u> |
|--------------|---|-------------|
| Table 2.1. | Confinement factors for even and odd TE modes for $\tilde{\beta} = 0.6$ | 29 |
| Table 2.2. | Confinement factors for even and odd TM modes for $\tilde{\beta} = 0.6$ | 47 |
| Table 3.1. | Coupling coefficient of TE mode, in one structure there is no taper region, and in the second structure we introduce taper region in which geometry of waveguide gradually changes and finally reach the output parts dimensions. | 100 |

CHAPTER 1

INTRODUCTION

The energy gap for electrons in a periodic potential has been well-known and extensively studied. Since the first realization of the existence of a photonic band gap, people started to design and fabricate optical devices using the ability of photonic crystals to confine light. The working idea behind photon propagation in materials rely on the electron motion in conductor and semi-conductor theory. In conductors and semi-conductors, electron motion is governed by the Coulomb potential. While in photonic crystals photon propagation is governed by the dielectric function. Many researchers have contributed to this field with their studies after the first publications on photonic bandgaps by (John (1987)), (Yablonovitch (1987)), and (Ho et al. (1990)). After these three papers, people in this area have been working on manipulating light propagation in materials. The main goal in this area is to design and manufacture novel optical applications in addition to design optical elements that will be used to complement and/or replace today's electronic components.

Confining light in a region in space or guiding light in a direction or even bending light at a corner is possible with help of photonic crystals(PhCs). This property of PhCs allows their use as circuit elements in optoelectronic applications.

In an optical circuit, components would be made of materials possibly with different dielectric properties and different geometry. As a result, their dispersion relation will be different so the response of material to light will be different. For this reason, transferring light from one circuit element to another one without loss is a potential problem. This difficulty arises from sudden changes in geometry and optical properties of the structure. To be able to use photonic crystals (PhCs) as circuit elements, one needs to devise efficient ways to transfer light between different optical components with little loss.

Efficient coupling of electromagnetic energy between photonic crystal waveguides (PhCWGs) that have different geometric parameters is a challenging problem. Because of group velocity and mode profile mismatch between the input and output waveguides, the coupling loss would be unacceptably high. Early work by (Xu et al., 2000) suggests that by slowly changing the conventional dielectric waveguide geometry, called adiabatic transformation, it is possible to achieve high coupling efficiency of light into and out

of waveguides with different discrete translational symmetry. To minimize coupling loss, a slab waveguide was connected to a photonic crystal waveguide using an intermediate taper. High transmission values over a wide frequency range was achieved using this approach. Another solution for efficient coupling between optical components is suggested by (Baba and Ohsaki, 2001). In this work, an interface made by using small air holes and another interface that is made by projecting air holes is used to achieve high transmission of light. In another work, optical power losses when a guided mode couples from a conventional waveguide to a PhCWG is studied and it is shown that the losses are due to mode mismatch, (Palamaru and Lalanne, 2001). A taper structure is used between the conventional waveguide and the PhCWG to reduce the power loss. To improve coupling efficiency between single-slab waveguide and PhCWG, an adiabatic transition region is used in (Happ et al., 2001) who show that the insertion loss due to mode mismatch can be minimized over a relatively short taper length. In another study, tapered waveguide junction for coupling light from a dielectric slab waveguide to photonic crystal waveguides is investigated by (Mekis and Joannopoulos, 2001). In this work it is shown that using taper region between dielectric waveguide and photonic crystal waveguide can significantly enhance coupling efficiency compared to direct coupling. Theoretical work on adiabatic transition done by (Johnson et al., 2002) shows that an efficient transition is possible provided that the transition region is chosen to be gradual enough. In another work by (Bienstman et al., 2003) it is shown that to transform mode from a slab waveguide to a line defect photonic crystal waveguide, a taper structure geometry can be used to make transition from dielectric waveguide to coupled cavity, and in a second stage it is shown that an index-guided mode can be transformed into a gap-guided mode by using taper structure. Another work by (Witzens et al., 2004) suggests mode matching interface for coupling efficiency of light into planar photonic crystals. In this work it is shown that using a multilayered grating between slab and planar photonic crystal, the insertion efficiency can be enhanced. Adiabatic matching stage for coupling of light between two different PhCWG is studied in (Momeni and Adibi, 2005). Efficient coupling between two different photonic crystal waveguides is studied and they showed that using adiabatic coupling is wideband in frequency, results in a wide acceptance angle and is quite robust against fabrication imperfections. Coupling from a strip waveguide into the flatband slow mode of a photonic crystal waveguide with ring-shaped holes is studied in (Säynätjoki et al., 2008). Highly efficient coupling from a strip waveguide to a slot waveguide is studied by (Wang et al., 2009) theoretically and experimentally. It is shown that highly efficient coupling is achieved and the proposed coupler has relatively high tolerance to

fabrication errors. Group velocity independent coupling from a strip waveguide to a photonic crystal waveguide is studied experimentally by (Lin et al., 2010). A photonic crystal taper structure is used to couple light efficiently. The effect of group index on coupling efficiency between strip waveguide and photonic crystal waveguide is studied both numerically and experimentally by (Hosseini et al., 2011). It is shown that using taper region between strip waveguide and photonic crystal waveguide dramatically improves coupling efficiency. Another experimental work on adiabatic transition of light is reported by (Lin et al., 2012), in this work a continuous group index taper is used to achieve high coupling.

In this thesis, to improve coupling efficiency of optical power we have studied adiabatic transitions between a variety of different dielectric waveguides. Direct coupling transmission value of optical power and adiabatic transmission value of optical power calculated by using the finite-difference time-domain method. Comparison of direct coupling transmission values and adiabatic transmission values shows that highly efficient coupling can be achieved.

The thesis is structured as follows;

In Chapter 2 we begin by outlining the theoretical background of ordinary slab waveguides. Starting from Maxwell's equations, detailed solutions of second order differential equations subject to boundary conditions for the electric and magnetic fields are shown. Again, starting from Maxwell's equations, theory of one-dimensional photonic crystals, two-dimensional photonic crystals, one-dimensional PhCWGs, and two-dimensional PhCWGs using plane wave expansion is given. Also a short introduction to adiabatic coupling is presented, while the reader can find detailed derivations in referenced material. In the last section, a brief discussion of the finite-difference time-domain method that is used to simulate the electromagnetic wave propagation is given.

In Chapter 3 we have focused on coupling process between single-slab waveguides of different thickness. Coupling of modes with direct transition from single-slab to single-slab waveguide is compared with adiabatic coupling case, which is done by gradually changing the thickness of the waveguide. We show that, for adiabatically coupled waveguides, besides converting the mode, it is possible to prevent the excitation of higher order modes. In the last section, we calculate the transmission coefficient for excited modes with and without taper region.

In Chapter 4 coupling efficiency from single-slab waveguide to single-slab waveguide is studied. We have used finite-difference time-domain simulation to find transmission values for both direct coupling, also called butt-coupling, and adiabatic coupling. The effect of transition region length on transmission values is investigated.

In Chapter 5 coupling from single-slab waveguides to 1D photonic crystal waveguides is investigated. Two types of transition are used to improve coupling efficiency from slab WG to PhCWG. The first design used is gradually changing slab WG thickness to the defect line thickness of PhCWG. In the second design we also gradually changed cladding slab thickness of PhCWG. We also show a situation where using taper region, rather than increasing transmission, results in a complete loss of all optical power. We investigate the reasons behind this seemingly paradoxical behavior.

In Chapter 6 coupling between two 1D photonic crystal waveguides that have different geometric parameters (different core thickness, cladding thickness and lattice constant) are investigated. The effect of introducing taper region and the effect of the length of taper on transmission is studied using finite-difference time-domain calculation.

In Chapter 7 coupling from single-slab waveguide to a 2D line defect photonic crystal is studied. One stage coupling, coupling from single slab waveguide to 2D line defect PhCWG, and two stage coupling, coupling from single slab waveguide to 2D line defect PhCWG and coupling back to single slab waveguide, is investigated. Photonic crystal taper and line defect taper transition type is used to convert optical mode. The effect of taper length on transmission value is studied using finite-difference time-domain calculation.

And finally the last chapter, Chapter 8, we sum up our results and include a conclusion.

CHAPTER 2

THEORY OF PHOTONIC CRYSTALS AND WAVEGUIDES

Photonic Crystals (PhCs) are periodically arranged materials in which index of refraction changes in space periodically, in analogy with periodicity of potential in solid state physics. PhCs are classified according to dielectric modulation in space: if this modulation is in one dimension then they are called one-dimensional PhCs, and if this modulation is in two- or three-dimensions, they are called two- or three-dimensional PhCs respectively. This periodicity of the dielectric material governs the propagation of light. The propagation of light of a given frequency depends on the propagation direction within the photonic crystal. The change of dielectric in space will result in the inhibition of propagation of light with certain ranges of frequencies and directions. The frequency interval where the photonic crystal does not allow light to propagate in *any* direction is called a photonic band gap.

2.1. Ordinary Slab Waveguide

The ray optic representation of electromagnetic field propagation is illustrated in Figure 2.1. Reflection and refraction of light at a boundary between two media is defined by Snell's law, $\theta_i = \theta_r$, and $n_d \sin \theta_i = n_b \sin \theta_t$. When the angle θ_i is larger than a certain angle called the critical angle θ_c , ($\theta_i > \theta_c$), then the light will reflect from upper and lower boundary of slab which will result in a net flow of electromagnetic radiation in the x -direction. This is called total internal reflection (TIR). The critical angle is found by setting θ_t to $\pi/2$ in Snell's law,

$$\begin{aligned}\sqrt{\epsilon_d} \sin(\theta_c) &= \sqrt{\epsilon_b} \sin(\pi/2) \\ \theta_c &= \sin^{-1} \left(\sqrt{\frac{\epsilon_b}{\epsilon_d}} \right)\end{aligned}\tag{2.1}$$

where the refractive index is defined as $n^2 = \mu\epsilon$. μ is close to 1 for most materials, so n is approximately $\sqrt{\epsilon}$.

Propagation of light in ordinary slab waveguides (WGs) can be studied in more

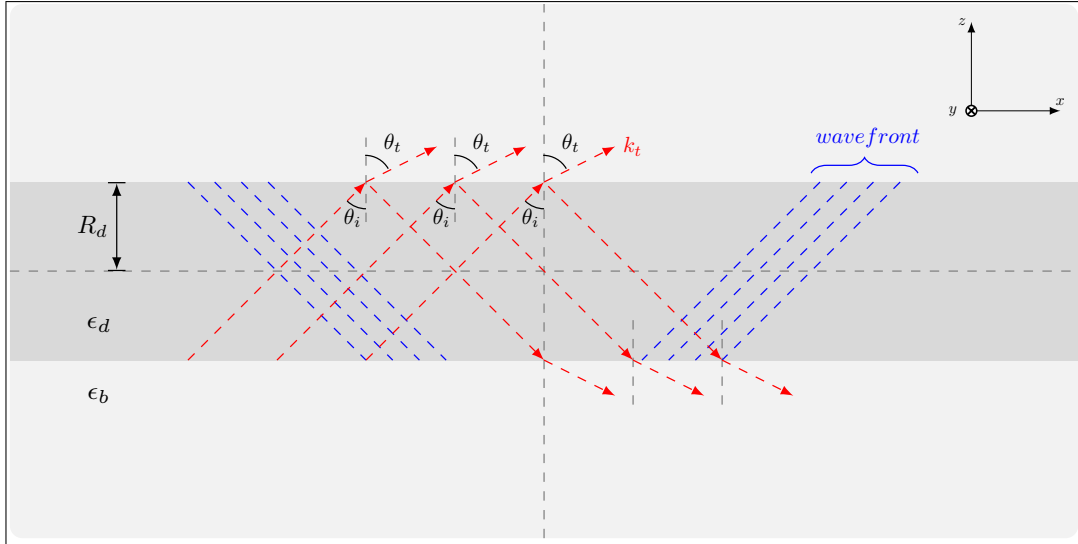


Figure 2.1. Two media with dielectric constants ϵ_d and ϵ_b . The blue dashed lines represent wave fronts. The red dashed arrows represent the propagation vectors. Dark gray region represents a dielectric material with thickness $2R_d$ and with higher dielectric constant, ϵ_d . Light gray represents the background dielectric material with a lower dielectric constant, ϵ_b .

detail by solving Maxwell's equations for this geometry.¹ The slab waveguide structure is shown in Figure 2.1. It consists of a dielectric medium with dielectric constant ϵ_d and thickness $2R_d$. The structure is symmetric about x - y plane. The slab extends to infinity in x - and y -direction. The background material, or the cladding, has a lower dielectric constant, ϵ_b and it extends to infinity in all three directions. The dielectric function of the structure is defined as

$$\epsilon(z) = \begin{cases} \epsilon_d & |z| < R_d \\ \epsilon_b & |z| > R_d \end{cases} \quad (2.2)$$

The equations that govern the propagation of light in a source-free medium are Maxwell's

¹The derivation in this chapter is based on the lecture notes "Photonic structures" given in 2008 at Izmir Institute of technology (Sözüer, 2008), Jackson (1998), Ashcroft and Mermin (1976), Taflove and Hagness (2005), K. (EDT)/ Ohtaka (1980), and Griffiths (1999).

equations, and two curl Equations are written as,

$$\begin{aligned}\nabla \times \mathbf{B} &= \frac{1}{c^2} \frac{\partial \mathbf{D}}{\partial t} \\ \nabla \times \mathbf{E} &= -\frac{\partial \mathbf{B}}{\partial t}\end{aligned}\quad (2.3)$$

to solve these curl equation, Equation 2.3, we assume the solution of the form $\mathbf{E}(\mathbf{r}, t) = \mathbf{E}_0(z)e^{i(\beta x - \omega t)}$ and $\mathbf{B}(\mathbf{r}, t) = \mathbf{B}_0(z)e^{i(\beta x - \omega t)}$ now putting these assumed solution forms into Maxwell's equation, Equation 2.3, we will have,

$$\left(\hat{\mathbf{x}} \frac{\partial}{\partial x} + \hat{\mathbf{y}} \frac{\partial}{\partial y} + \hat{\mathbf{z}} \frac{\partial}{\partial z} \right) \times (B_x \hat{\mathbf{x}} + B_y \hat{\mathbf{y}} + B_z \hat{\mathbf{z}}) = \frac{1}{c^2} \frac{\partial}{\partial t} [\epsilon \mathbf{E}_0(z) e^{i(\beta x - \omega t)}] \quad (2.4)$$

$$\left(\hat{\mathbf{x}} \frac{\partial}{\partial x} + \hat{\mathbf{y}} \frac{\partial}{\partial y} + \hat{\mathbf{z}} \frac{\partial}{\partial z} \right) \times (E_x \hat{\mathbf{x}} + E_y \hat{\mathbf{y}} + E_z \hat{\mathbf{z}}) = -\frac{\partial}{\partial t} [\mathbf{B}_0(z) e^{i(\beta x - \omega t)}] \quad (2.5)$$

We now differentiate right-hand side of Equation 2.4 and Equation 2.5 with respect to time and do the vector product on the left-hand side of both Equation 2.4 and Equation 2.5, then we will have,

$$\begin{aligned}\frac{\partial B_y}{\partial x} (\hat{x} \times \hat{y}) + \frac{\partial B_z}{\partial x} (\hat{x} \times \hat{z}) + \frac{\partial B_x}{\partial y} (\hat{y} \times \hat{x}) + \frac{\partial B_z}{\partial y} (\hat{y} \times \hat{z}) \\ + \frac{\partial B_x}{\partial z} (\hat{z} \times \hat{x}) + \frac{\partial B_y}{\partial z} (\hat{z} \times \hat{y}) = -\frac{i\omega\epsilon}{c^2} \mathbf{E}_0(z) e^{i(\beta x - \omega t)}\end{aligned}\quad (2.6)$$

$$\begin{aligned}\frac{\partial E_y}{\partial x} (\hat{x} \times \hat{y}) + \frac{\partial E_z}{\partial x} (\hat{x} \times \hat{z}) + \frac{\partial E_x}{\partial y} (\hat{y} \times \hat{x}) + \frac{\partial E_z}{\partial y} (\hat{y} \times \hat{z}) \\ + \frac{\partial E_x}{\partial z} (\hat{z} \times \hat{x}) + \frac{\partial E_y}{\partial z} (\hat{z} \times \hat{y}) = i\omega \mathbf{B}_0(z) e^{i(\beta x - \omega t)}\end{aligned}\quad (2.7)$$

After taking cross product of unit vectors in both Equation 2.6 and Equation 2.7, and

collecting same component coefficient, we can rearrange these equations as follows,

$$\hat{\mathbf{x}} \left(\frac{\partial B_z}{\partial y} - \frac{\partial B_y}{\partial z} \right) + \hat{\mathbf{y}} \left(\frac{\partial B_x}{\partial z} - \frac{\partial B_z}{\partial x} \right) + \hat{\mathbf{z}} \left(\frac{\partial B_y}{\partial x} - \frac{\partial B_x}{\partial y} \right) = -\frac{i\omega\epsilon}{c^2} \mathbf{E}_0(z) e^{i(\beta x - \omega t)} \quad (2.8)$$

$$\hat{\mathbf{x}} \left(\frac{\partial E_z}{\partial y} - \frac{\partial E_y}{\partial z} \right) + \hat{\mathbf{y}} \left(\frac{\partial E_x}{\partial z} - \frac{\partial E_z}{\partial x} \right) + \hat{\mathbf{z}} \left(\frac{\partial E_y}{\partial x} - \frac{\partial E_x}{\partial y} \right) = i\omega \mathbf{B}_0(z) e^{i(\beta x - \omega t)} \quad (2.9)$$

where every component of magnetic and electric field are defined as, $B_x = B_{0x}(z) e^{i(\beta x - \omega t)}$, $B_y = B_{0y}(z) e^{i(\beta x - \omega t)}$, $B_z = B_{0z}(z) e^{i(\beta x - \omega t)}$, $E_x = E_{0x}(z) e^{i(\beta x - \omega t)}$, $E_y = E_{0y}(z) e^{i(\beta x - \omega t)}$, and $E_z = E_{0z}(z) e^{i(\beta x - \omega t)}$. Now putting these into Equation 2.8 and Equation 2.9 respectively, we will have,

$$\begin{aligned} & \hat{\mathbf{x}} \left[\frac{\partial}{\partial y} (B_{0z}(z) e^{i(\beta x - \omega t)}) - \frac{\partial}{\partial z} (B_{0y}(z) e^{i(\beta x - \omega t)}) \right] \\ & + \hat{\mathbf{y}} \left[\frac{\partial}{\partial z} (B_{0x}(z) e^{i(\beta x - \omega t)}) - \frac{\partial}{\partial x} (B_{0z}(z) e^{i(\beta x - \omega t)}) \right] \\ & + \hat{\mathbf{z}} \left[\frac{\partial}{\partial x} (B_{0y}(z) e^{i(\beta x - \omega t)}) - \frac{\partial}{\partial y} (B_{0x}(z) e^{i(\beta x - \omega t)}) \right] \\ & = -\frac{i\omega\epsilon}{c^2} (E_{0x} \hat{\mathbf{x}} + E_{0y} \hat{\mathbf{y}} + E_{0z} \hat{\mathbf{z}}) e^{i(\beta x - \omega t)} \end{aligned} \quad (2.10)$$

$$\begin{aligned} & \hat{\mathbf{x}} \left[\frac{\partial}{\partial y} (E_{0z}(z) e^{i(\beta x - \omega t)}) - \frac{\partial}{\partial z} (E_{0y}(z) e^{i(\beta x - \omega t)}) \right] \\ & + \hat{\mathbf{y}} \left[\frac{\partial}{\partial z} (E_{0x}(z) e^{i(\beta x - \omega t)}) - \frac{\partial}{\partial x} (E_{0z}(z) e^{i(\beta x - \omega t)}) \right] \\ & + \hat{\mathbf{z}} \left[\frac{\partial}{\partial x} (E_{0y}(z) e^{i(\beta x - \omega t)}) - \frac{\partial}{\partial y} (E_{0x}(z) e^{i(\beta x - \omega t)}) \right] \\ & = i\omega (B_{0x} \hat{\mathbf{x}} + B_{0y} \hat{\mathbf{y}} + B_{0z} \hat{\mathbf{z}}) e^{i(\beta x - \omega t)} \end{aligned} \quad (2.11)$$

after differentiating these are reduced to;

$$\begin{aligned} \hat{\mathbf{x}} \left[0 - \frac{\partial B_{0y}(z)}{\partial z} e^{i(\beta x - \omega t)} \right] + \hat{\mathbf{y}} \left[\frac{\partial B_{0x}(z)}{\partial z} e^{i(\beta x - \omega t)} - B_{0z}(z)(i\beta) e^{i(\beta x - \omega t)} \right] \\ + \hat{\mathbf{z}} \left[B_{0y}(z)(i\beta) e^{i(\beta x - \omega t)} - 0 \right] = -\frac{i\omega\epsilon}{c^2} (E_{0x}\hat{\mathbf{x}} + E_{0y}\hat{\mathbf{y}} + E_{0z}\hat{\mathbf{z}}) e^{i(\beta x - \omega t)} \end{aligned} \quad (2.12)$$

$$\begin{aligned} \hat{\mathbf{x}} \left[0 - \frac{\partial E_{0y}(z)}{\partial z} e^{i(\beta x - \omega t)} \right] + \hat{\mathbf{y}} \left[\frac{\partial E_{0x}(z)}{\partial z} e^{i(\beta x - \omega t)} - E_{0z}(z)(i\beta) e^{i(\beta x - \omega t)} \right] \\ + \hat{\mathbf{z}} \left[E_{0y}(z)(i\beta) e^{i(\beta x - \omega t)} - 0 \right] = i\omega (B_{0x}\hat{\mathbf{x}} + B_{0y}\hat{\mathbf{y}} + B_{0z}\hat{\mathbf{z}}) e^{i(\beta x - \omega t)} \end{aligned} \quad (2.13)$$

Now we can cancel exponential terms from both sides, since they are common for both sides, and equating the corresponding component in each equation we will have six scalar equations in which three of them are from curl of magnetic field equation and the remaining three of them are from the curl of electric field equation.

$$-\frac{\partial B_{0y}(z)}{\partial z} = -\frac{i\omega\epsilon}{c^2} E_{0x}(z) \quad (2.14)$$

$$\frac{\partial B_{0x}(z)}{\partial z} - i\beta B_{0z}(z) = -\frac{i\omega\epsilon}{c^2} E_{0y}(z) \quad (2.15)$$

$$i\beta B_{0y}(z) = -\frac{i\omega\epsilon}{c^2} E_{0z}(z) \quad (2.16)$$

$$-\frac{\partial E_{0y}(z)}{\partial z} = i\omega B_{0x}(z) \quad (2.17)$$

$$\frac{\partial E_{0x}(z)}{\partial z} - i\beta E_{0z}(z) = i\omega B_{0y}(z) \quad (2.18)$$

$$i\beta E_{0y}(z) = i\omega B_{0z}(z) \quad (2.19)$$

and rearranging this equations we will get, for y - and z - component of electric and mag-

netic fields in terms of x -components,

$$E_{0y}(z) = \frac{-i\omega}{\beta^2 - \frac{\omega^2\epsilon}{c^2}} \frac{\partial B_{0x}(z)}{\partial z} \quad (2.20)$$

$$E_{0z}(z) = \frac{-i\beta}{\beta^2 - \frac{\omega^2\epsilon}{c^2}} \frac{\partial E_{0x}(z)}{\partial z} \quad (2.21)$$

$$B_{0y}(z) = \frac{\frac{i\omega\epsilon}{c^2}}{\beta^2 - \frac{\omega^2\epsilon}{c^2}} \frac{\partial E_{0x}(z)}{\partial z} \quad (2.22)$$

$$B_{0z}(z) = \frac{-i\beta}{\beta^2 - \frac{\omega^2\epsilon}{c^2}} \frac{\partial B_{0x}(z)}{\partial z} \quad (2.23)$$

or alternatively we can rearrange Equation 2.14-2.19 to find x - and z - component of electric and magnetic fields in terms of y -components,

$$E_{0x}(z) = \frac{-ic^2}{\omega\epsilon} \frac{\partial B_{0y}(z)}{\partial z} \quad (2.24)$$

$$E_{0z}(z) = \frac{-c^2\beta}{\omega\epsilon} B_{0y}(z) \quad (2.25)$$

$$B_{0x}(z) = \frac{i}{\omega} \frac{\partial E_{0y}(z)}{\partial z} \quad (2.26)$$

$$B_{0z}(z) = \frac{\beta}{\omega} E_{0y}(z) \quad (2.27)$$

we can either use Equation 2.20-2.23 to write second order differential equation in terms of x -component of electric and magnetic field or we can use Equation 2.24-2.27 to write second order differential equation in terms of y -component of electric and magnetic field. We will use the second way since it is easier to deal with the coefficients. So the y -component of electric field satisfying ordinary differential equation,

$$\frac{\partial^2 E_{0y}(z)}{\partial z^2} - \left(\beta^2 - \frac{\omega^2\epsilon}{c^2} \right) E_{0y}(z) = 0 \quad (2.28)$$

the y -component of magnetic field satisfying ordinary differential equation,

$$\frac{\partial^2 B_{0y}(z)}{\partial z^2} - \left(\beta^2 - \frac{\omega^2\epsilon}{c^2} \right) B_{0y}(z) = 0 \quad (2.29)$$

We have written x - and z -component of electric and magnetic fields in terms of y -component

of the corresponding fields, Equation 2.24-2.27. The y -components of electric and magnetic fields are given by second order differential equations, Equation 2.28 and Equation 2.29. To solve the problem completely all we need to do is solve these two differential equations and the other four components will be easier to calculate by using Equation 2.24-2.27. To solve Equation 2.28 and Equation 2.29 we are free to choose either $E_{0y} = 0$ or $B_{0y} = 0$, but not both, and still satisfy Maxwell's equations. For transverse electric solutions, we set $E_{0x} = 0$ and from Equation 2.21 and Equation 2.22 we see that $B_{0y} = 0$ and $E_{0z} = 0$. For transverse magnetic solutions, we set $B_{0x} = 0$ and from Equation 2.20 and Equation 2.23 we see that $E_{0y} = 0$ and $B_{0z} = 0$. Thus the solution to the problem split into two categories:

- Transverse Electric (TE) Modes, with $E_{0x} = B_{0y} = E_{0z} = 0$
- Transverse Magnetic (TM) Modes, with $B_{0x} = E_{0y} = B_{0z} = 0$

The boundary conditions in a source-free ($\rho_f = 0$, $\mathbf{J}_f = 0$) dielectric medium are,

$$\begin{aligned} \nabla \cdot \mathbf{D} = \rho_f, \quad \rho_f = 0 &\implies D_{\perp} = \text{continuous} \\ \epsilon_d \neq \epsilon_b &\implies E_{\perp} = \text{discontinuous} \end{aligned} \quad (2.30)$$

$$\nabla \cdot \mathbf{B} = 0 \implies B_{\perp} = \text{continuous} \quad (2.31)$$

$$\begin{aligned} \nabla \times \mathbf{H} = \mathbf{J}_f + \frac{\partial \mathbf{D}}{\partial t}, \quad \mathbf{J}_f = 0 &\implies \mathbf{H}_{\parallel} = \text{continuous} \\ \mu_d = \mu_b &\implies \mathbf{B}_{\parallel} = \text{continuous} \end{aligned} \quad (2.32)$$

$$\nabla \times \mathbf{E} = -\frac{\partial \mathbf{B}}{\partial t} \implies \mathbf{E}_{\parallel} = \text{continuous} \quad (2.33)$$

so in our problem the boundary conditions for the component of electric and magnetic fields at the interface between two media are,

$$\begin{array}{ll} E_{0x} = \text{continuous} & B_{0x} = \text{continuous} \\ E_{0y} = \text{continuous} & B_{0y} = \text{continuous} \\ E_{0z} = \text{discontinuous} & B_{0z} = \text{continuous} \end{array}$$

2.1.1. Transverse Electric (TE) Modes

For TE mode solutions we set magnetic field component in the y -direction to zero, $B_{0y} = 0$. From Equation 2.24 and Equation 2.25 we see that E_{0x} , and E_{0z} are also zero. So the only non-zero field components for TE solutions are B_{0x} , E_{0y} and B_{0z} .

$$B_{0x}(z) = \frac{i}{\omega} \frac{\partial E_{0y}(z)}{\partial z} \quad (2.34)$$

$$B_{0z}(z) = \frac{\beta}{\omega} E_{0y}(z) \quad (2.35)$$

and the field component that is transverse to the propagation direction, E_{0y} , is given by the second order differential equation found in the previous section,

$$\frac{\partial^2 E_{0y}(z)}{\partial z^2} - \left(\beta^2 - \frac{\omega^2 \epsilon}{c^2} \right) E_{0y}(z) = 0 \quad (2.36)$$

The solutions to this equation are either sinusoidal or exponential depending on the quantities β^2 and $\omega^2 \epsilon / c^2$. If $\omega^2 \epsilon / c^2 > \beta^2$ then the solutions are sinusoidal. If $\beta^2 > \omega^2 \epsilon / c^2$ then we have exponential solutions. To have mode localized around $z = 0$, solution for region $|z| < R_d$ must be sinusoidal, and solution for $|z| > R_d$ must be exponential. In addition as z goes to infinity the solutions must go to zero. We now will solve the differential equation for $E_{0y}(z)$ in two regions separately and call the solutions $E_{0y,d}(z)$ and $E_{0y,b}(z)$,

$$E_{0y}(z) = \begin{cases} E_{0y,d}(z) & |z| < R_d \\ E_{0y,b}(z) & |z| > R_d \end{cases} \quad (2.37)$$

then the differential equation will be as follows,

$$\left[\frac{\partial^2}{\partial z^2} + \left(\epsilon_d \frac{\omega^2}{c^2} - \beta^2 \right) \right] E_{0y,d}(z) = 0 \quad |z| < R_d \quad (2.38)$$

$$\left[\frac{\partial^2}{\partial z^2} - \left(\beta^2 - \epsilon_b \frac{\omega^2}{c^2} \right) \right] E_{0y,b}(z) = 0 \quad |z| > R_d \quad (2.39)$$

defining $\gamma_d^2 = \epsilon_d \frac{\omega^2}{c^2} - \beta^2$ and $\gamma_b^2 = \beta^2 - \epsilon_b \frac{\omega^2}{c^2}$ and plugging them into partial differential equations then the equation now takes the form,

$$\left[\frac{\partial^2}{\partial z^2} + \gamma_d^2 \right] E_{0y,d}(z) = 0 \quad |z| < R_d \quad (2.40)$$

$$\left[\frac{\partial^2}{\partial z^2} - \gamma_b^2 \right] E_{0y,b}(z) = 0 \quad |z| > R_d \quad (2.41)$$

finally the solutions are,

$$E_{0y}(z) = \begin{cases} A \cos(\gamma_d z) + B \sin(\gamma_d z) & |z| < R_d \\ C e^{-\gamma_b |z|} e^{i(\beta x - \omega t)} & |z| > R_d \end{cases} \quad (2.42)$$

to find the constants A , B , and C , we will use boundary conditions at interface, $z = R_d$, to match the solutions. And the solutions can be separated into even and odd solutions by setting constant A or B to zero.

2.1.1.1. Even Transverse Electric (TE) Modes

The solution of the partial differential equation with dependence on x -coordinate and on the time we have found in previous section is,

$$E_{y,d}(x, y, z, t) = A \cos(\gamma_d z) e^{i(\beta x - \omega t)} + B \sin(\gamma_d z) e^{i(\beta x - \omega t)} \quad (2.43)$$

$$E_{y,b}(x, y, z, t) = C e^{-\gamma_b |z|} e^{i(\beta x - \omega t)} \quad (2.44)$$

for even TE solutions we set the constant B to zero, $B = 0$, then the solution will be as follows,

$$E_{y,d}(x, y, z, t) = A \cos(\gamma_d z) e^{i(\beta x - \omega t)} \quad (2.45)$$

$$E_{y,b}(x, y, z, t) = C e^{-\gamma_b |z|} e^{i(\beta x - \omega t)} \quad (2.46)$$

since there is no free charge in the medium, the parallel component of electric field, E_y , is continuous across the interface. This continuity of electric field at $z = R_d$ gives,

$$\begin{aligned} E_{y,d}(z)|_{z=R_d} &= E_{y,b}(z)|_{z=R_d} \\ A \cos(\gamma_d R_d) e^{i(\beta x - \omega t)} &= C e^{-\gamma_b R_d} e^{i(\beta x - \omega t)} \\ A \cos(\gamma_d R_d) &= C e^{-\gamma_b R_d} \end{aligned} \quad (2.47)$$

The condition B_{0x} be continuous at $z = R_d$ gives, which is the Equation 2.34,

$$\begin{aligned} \frac{i}{\omega} \frac{\partial E_{y,d}(z)}{\partial z} &= \frac{i}{\omega} \frac{\partial E_{y,b}(z)}{\partial z} \\ \frac{\partial}{\partial z} [A \cos(\gamma_d z) e^{i(\beta x - \omega t)}] &= \frac{\partial}{\partial z} [C e^{-\gamma_b |z|} e^{i(\beta x - \omega t)}] \\ -A \gamma_d \sin(\gamma_d z)|_{z=R_d} &= -C \gamma_b e^{-\gamma_b |z|}|_{z=R_d} \\ A \gamma_d \sin(\gamma_d R_d) &= C \gamma_b e^{-\gamma_b R_d} \end{aligned} \quad (2.48)$$

now dividing the Equation 2.48 with Equation 2.47 we will have,

$$\gamma_d \tan(\gamma_d R_d) = \gamma_b \quad (2.49)$$

and defining new parameters $\tilde{\gamma}_d = R_d \gamma_d$ and $\tilde{\gamma}_b = R_d \gamma_b$ then we finally have,

$$\tan \tilde{\gamma}_d = \frac{\tilde{\gamma}_b}{\tilde{\gamma}_d} \quad (2.50)$$

The solution to Equation 2.50 gives the allowed values of $\tilde{\gamma}_d$ for a given value of $\tilde{\gamma}_b$. Graphical solution of Equation 2.50 is plotted in Figure 2.2. The solution is intersection

of function $\tan(\tilde{\gamma}_d)$ and function $\frac{\tilde{\gamma}_b}{\tilde{\gamma}_d}$. For a given $\tilde{\gamma}_b$, Equation 2.50 gives several values

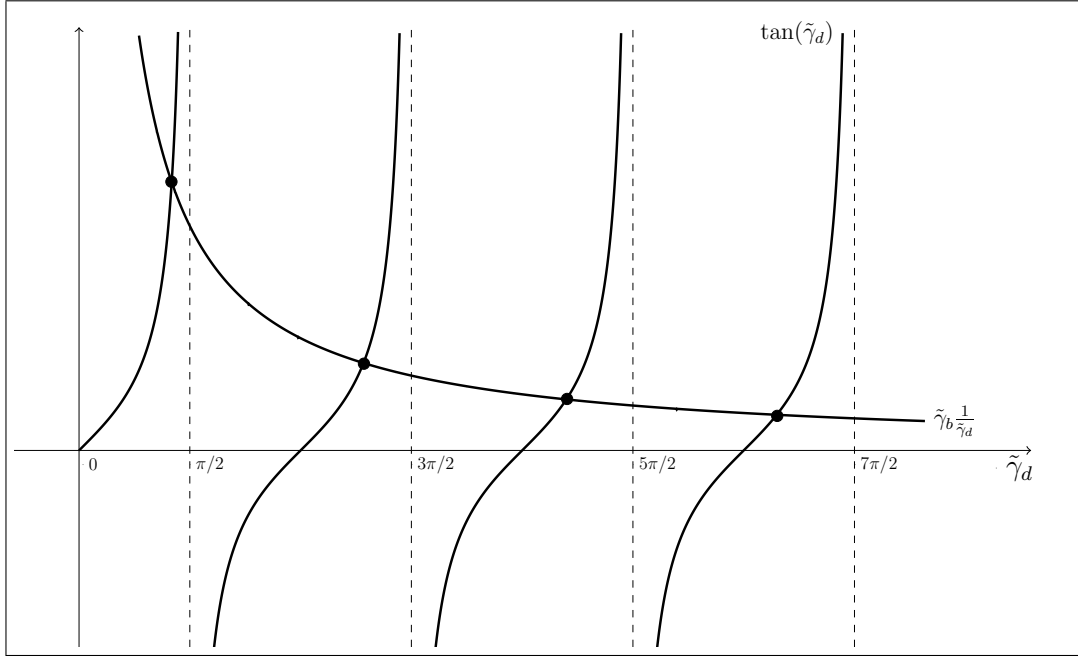


Figure 2.2. Graph of $\tan(\tilde{\gamma}_d)$ and $\tilde{\gamma}_b/\tilde{\gamma}_d$ for even TE modes.

for $\tilde{\gamma}_d$. To find the roots we use the iteration method defined as,

$$(\tilde{\gamma}_d)_{n+1} = \arctan\left(\frac{\tilde{\gamma}_b}{(\tilde{\gamma}_d)_n}\right) \quad n = 0, 1, 2, 3, \dots \quad (2.51)$$

and by using the initial guesses $(\tilde{\gamma}_d)_0 = n\pi$, we can calculate $\tilde{\omega}$ and $\tilde{\beta}$ from the the values of $\tilde{\gamma}_d$ and $\tilde{\gamma}_b$ using,

$$\tilde{\omega}^2 = \left(\frac{\omega R_d}{c}\right)^2 = \frac{\tilde{\gamma}_d^2 + \tilde{\gamma}_b^2}{\epsilon_d - \epsilon_b} \quad (2.52)$$

$$\tilde{\beta}^2 = (\beta R_d)^2 = \frac{\epsilon_b \tilde{\gamma}_d^2 + \epsilon_d \tilde{\gamma}_b^2}{\epsilon_d - \epsilon_b} \quad (2.53)$$

The equation we defined for $\tilde{\gamma}_b$, $\tilde{\gamma}_b^2 = \tilde{\beta}^2 - \epsilon_b \tilde{\omega}^2$, defines hyperbolic curves. For every given $\tilde{\gamma}_b$, ϵ_b and ϵ_d we find $\tilde{\gamma}_d$ by using the iteration method, Equation 2.51. Once we have found $\tilde{\gamma}_d$ then we use Equation 2.52 and Equation 2.53 to calculate $\tilde{\omega}$ and $\tilde{\beta}$.

In Figure 2.3 we plot $\tilde{\beta}$ versus $\tilde{\omega}$ values for even TE modes. Each blue line corresponds to a mode starting from lower order (fundamental mode, TE_0) to higher order modes (TE_2, TE_4, \dots). These modes are even guided mode solutions of slab waveguide structure and as can be seen from the figure the solutions are discrete.

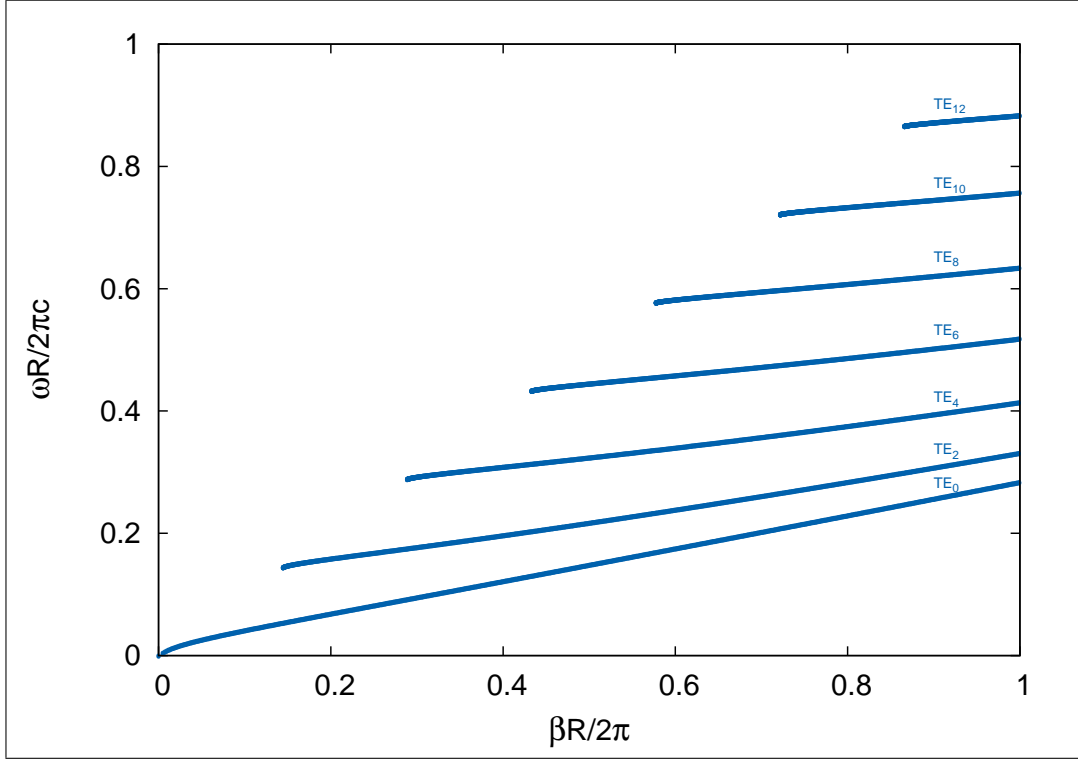


Figure 2.3. $\tilde{\omega} = \omega R/2\pi c$ versus $\tilde{\beta} = \beta R/2\pi$ plotted for even TE modes for a slab waveguide of thickness $2R_d$. The slab waveguide and the background has dielectric constant of $\epsilon_d = 13$ and $\epsilon_b = 1$ respectively.

Now we will find the mode profiles of each field component for even TE modes. The solution for the component of electric field is found as, E_y ,

$$E_y(x, y, z, t) = \begin{cases} A \cos(\gamma_d z) e^{i(\beta x - \omega t)} & |z| < R_d \\ C e^{-\gamma_b |z|} e^{i(\beta x - \omega t)} & |z| > R_d \end{cases} \quad (2.54)$$

where A and C are constants. To find the constant C in terms of the constant A we use

the continuity of parallel component of electric field E_y at the interface, $z = R_d$,

$$\begin{aligned} E_{y,d}(x, y, z, t)|_{z=R_d} &= E_{y,b}(x, y, z, t)|_{z=R_d} \\ A \cos(\gamma_d R_d) e^{i(\beta x - \omega t)} &= C e^{-\gamma_b R_d} e^{i(\beta x - \omega t)} \\ A \cos(\gamma_d R_d) &= C e^{-\gamma_b R_d} \end{aligned} \quad (2.55)$$

solving this equation for C , then we will have $C = A \cos(\gamma_d R_d) e^{\gamma_b R_d}$, and putting this expression into the Equation 2.54 for C then we have,

$$E_y(x, y, z, t) = \begin{cases} A \cos(\gamma_d z) e^{i(\beta x - \omega t)} & |z| < R_d \\ A \cos(\gamma_d R_d) e^{\gamma_b R_d} e^{-\gamma_b |z|} e^{i(\beta x - \omega t)} & |z| > R_d \end{cases} \quad (2.56)$$

Once we find E_y then it is easy to find the other field components, which are B_x and B_z . This two field component are defined by Equation 2.34 and Equation 2.35. The x -component of magnetic field is given by $B_x = (i/\omega) \partial E_y / \partial z$,

$$B_x(x, y, z, t) = \begin{cases} -\frac{i\gamma_d}{\omega} A \sin(\gamma_d z) e^{i(\beta x - \omega t)} & |z| < R_d \\ -\frac{i\gamma_b}{\omega} A \cos(\gamma_d R_d) e^{\gamma_b R_d} e^{-\gamma_b |z|} e^{i(\beta x - \omega t)} & |z| > R_d \end{cases} \quad (2.57)$$

The z -component of magnetic field is given by $B_z = (\beta/\omega) E_y$,

$$B_z(x, y, z, t) = \begin{cases} \frac{\beta}{\omega} A \cos(\gamma_d z) e^{i(\beta x - \omega t)} & |z| < R_d \\ \frac{\beta}{\omega} A \cos(\gamma_d R_d) e^{\gamma_b R_d} e^{-\gamma_b |z|} e^{i(\beta x - \omega t)} & |z| > R_d \end{cases} \quad (2.58)$$

We have found all three field components for even TE mode, B_x , E_y , and B_z . We now will find energy density, and we also will find energy flow rate in each direction. Energy density of electromagnetic field in linear media is defined as,

$$u_{em} = \frac{1}{4} \Re \{ \mathbf{E} \cdot \mathbf{D}^* + \mathbf{H} \cdot \mathbf{B}^* \} \quad (2.59)$$

where \mathbf{E} is related to \mathbf{D} as, $\mathbf{D} = \epsilon_0\epsilon(\mathbf{r})\mathbf{E}$ and \mathbf{B} is related to \mathbf{H} as, $\mathbf{H} = \frac{1}{\mu_0\mu(\mathbf{r})}\mathbf{B}$. Putting these back into Equation 2.59 then we will get,

$$u_{em} = \frac{1}{4}\Re e \left\{ \epsilon_0\epsilon(\mathbf{r})\mathbf{E} \cdot \mathbf{E}^* + \frac{1}{\mu_0\mu(\mathbf{r})}\mathbf{B} \cdot \mathbf{B}^* \right\} \quad (2.60)$$

and taking the dot product in Equation 2.60,

$$u_{em} = \frac{1}{4}\Re e \left\{ \epsilon_0\epsilon(\mathbf{r}) (|E_x|^2 + |E_y|^2 + |E_z|^2) + \frac{1}{\mu_0\mu(\mathbf{r})} (|B_x|^2 + |B_y|^2 + |B_z|^2) \right\} \quad (2.61)$$

for TE modes, E_x , E_z and B_y are zero. The dielectric function varies only in z -direction, so we can write $\epsilon(\mathbf{r}) = \epsilon(z)$. For linear and non-magnetic medium $\mu(\mathbf{r}) = 1$, and using $c^2 = 1/\epsilon_0\mu_0$ for speed of light in free space, the energy density for TE modes can be written as,

$$u_{em} = \frac{1}{4\mu_0}\Re e \left\{ \frac{1}{c^2}\epsilon(z)|E_y|^2 + |B_x|^2 + |B_z|^2 \right\} \quad (2.62)$$

putting field components into Equation 2.62, then the energy density for even TE modes in both region, inside the slab and outside of the slab, will be,

$$u_{em} = \begin{cases} \frac{A^2}{4\mu_0} \left[\left(\frac{\epsilon_d}{c^2} + \frac{\beta^2}{\omega^2} \right) \cos^2(\gamma_d z) + \frac{\gamma_d^2}{\omega^2} \sin^2(\gamma_d z) \right] & |z| < R_d \\ \frac{A^2}{4\mu_0} \left[\frac{\epsilon_b}{c^2} + \frac{\beta^2}{\omega^2} + \frac{\gamma_b^2}{\omega^2} \right] \cos^2(\gamma_d R_d) e^{2\gamma_b R_d} e^{-2\gamma_b |z|} & |z| > R_d \end{cases} \quad (2.63)$$

The flow of electromagnetic energy is defined by Poynting vector. For even TE modes three of the field components are zero, $E_x = 0$, $E_z = 0$, and $B_y = 0$,

$$\mathbf{S} = \frac{1}{2}\Re e \{ \mathbf{E} \times \mathbf{H}^* \} = \frac{1}{2\mu_0}\Re e \{ \mathbf{E} \times \mathbf{B}^* \} = \frac{1}{2\mu_0}\Re e \left\{ \begin{vmatrix} \hat{\mathbf{x}} & \hat{\mathbf{y}} & \hat{\mathbf{z}} \\ 0 & E_y & 0 \\ B_x^* & 0 & B_z^* \end{vmatrix} \right\} \quad (2.64)$$

after taking the determinant then we will have,

$$\mathbf{S} = \frac{1}{2\mu_0} \Re e \{ E_y B_z^* \hat{\mathbf{x}} - E_y B_x^* \hat{\mathbf{z}} \} \quad (2.65)$$

as we see from Equation 2.65 Poynting vector has no component in the y -direction, $S_y = 0$. The x -component of Poynting vector is $S_x = 1/2\mu_0 \Re e \{ E_y B_z^* \}$, using the field components, E_y and B_z , then we will have,

$$S_x = \begin{cases} \frac{A^2 \beta}{2\mu_0 \omega} \cos^2(\gamma_d z) & |z| < R_d \\ \frac{A^2 \beta}{2\mu_0 \omega} \cos^2(\gamma_d R_d) e^{2\gamma_b R_d} e^{-2\gamma_b |z|} & |z| > R_d \end{cases} \quad (2.66)$$

The z - component of Poynting vector is $S_z = -1/2\mu_0 \Re e \{ E_y B_x^* \}$. Using B_x and E_y , then we will have for z -direction,

$$S_z = \begin{cases} -i \frac{A^2 \gamma_d}{2\mu_0 \omega} \cos(\gamma_d z) \sin(\gamma_d z) & |z| < R_d \\ -i \frac{A^2 \gamma_b}{2\mu_0 \omega} \cos^2(\gamma_d R_d) e^{2\gamma_b R_d} e^{-2\gamma_b |z|} & |z| > R_d \end{cases} \quad (2.67)$$

the real part of z -component of Poynting vector is zero so the Poynting vector in the z -direction is zero, $S_z = 0$. This means that in the z - direction there is no net energy flow.

To find the power that is propagating in the slab, $|z| < R_d$, and in the background, $|z| > R_d$, in the x -direction we need to integrate Poynting vector along the z -direction.

$$P_{in} = \int_{-R_d}^{R_d} S_x dz = \frac{A^2 \beta}{2\mu_0 \omega} \int_{-R_d}^{R_d} \cos^2(\gamma_d z) dz \quad (2.68)$$

after taking the integral then we will have,

$$P_{in} = \frac{A^2 \beta}{2\mu_0 \omega} \left[R_d + \frac{1}{2\gamma_d} \sin(2\gamma_d R_d) \right] \quad (2.69)$$

where P_{in} is power passing through unit length in x -direction. And the power that propa-

gates in background is,

$$\begin{aligned}
P_{out} &= \int_{-\infty}^{-R_d} S_x dz + \int_{R_d}^{\infty} S_x dz \\
&= \frac{A^2 \beta}{2\mu_0 \omega} \cos^2(\gamma_d R_d) e^{2\gamma_b R_d} \left\{ \int_{-\infty}^{-R_d} e^{2\gamma_b z} dz + \int_{R_d}^{\infty} e^{-2\gamma_b z} dz \right\} \quad (2.70)
\end{aligned}$$

after taking the integrals then we will have,

$$P_{out} = \frac{A^2 \beta}{2\mu_0 \omega} \frac{1}{\gamma_b} \cos^2(\gamma_d R_d) \quad (2.71)$$

the total power is $P = P_{in} + P_{out}$,

$$P = \frac{A^2 \beta}{2\mu_0 \omega} \left[R_d + \frac{1}{2\gamma_d} \sin(2\gamma_d R_d) + \frac{1}{\gamma_b} \cos^2(\gamma_d R_d) \right] \quad (2.72)$$

2.1.1.2. Odd Transverse Electric (TE) Modes

For odd TE modes we set the coefficient A to zero in Equation 2.42 and then the odd TE solutions are given by,

$$E_{y,d}(x, y, z, t) = B \sin(\gamma_d z) e^{i(\beta x - \omega t)} \quad (2.73)$$

$$E_{y,b}(x, y, z, t) = C e^{-\gamma_b |z|} e^{i(\beta x - \omega t)} \quad (2.74)$$

the condition that E_y be continuous across the interface at $z = R_d$ gives,

$$\begin{aligned}
E_{y,d}(z)|_{z=R_d} &= E_{y,b}(z)|_{z=R_d} \\
B \sin(\gamma_d R_d) e^{i(\beta x - \omega t)} &= C e^{-\gamma_b R_d} e^{i(\beta x - \omega t)} \\
B \sin(\gamma_d R_d) &= C e^{-\gamma_b R_d} \quad (2.75)
\end{aligned}$$

the second boundary condition must be imposed is that B_x be continuous at $z = R_d$, which gives,

$$\begin{aligned}
\frac{i}{\omega} \frac{\partial E_{y,d}(z)}{\partial z} &= \frac{i}{\omega} \frac{\partial E_{y,b}(z)}{\partial z} \\
\frac{\partial}{\partial z} [B \sin(\gamma_d z) e^{i(\beta x - \omega t)}] &= \frac{\partial}{\partial z} [C e^{-\gamma_b |z|} e^{i(\beta x - \omega t)}] \\
B \gamma_d \cos(\gamma_d z)|_{R_d} &= -C \gamma_b e^{-\gamma_b |z|}|_{R_d} \\
B \gamma_d \cos(\gamma_d R_d) &= -C \gamma_b e^{-\gamma_b R_d}
\end{aligned} \tag{2.76}$$

dividing Equation 2.75 with Equation 2.76 will give,

$$\frac{1}{\gamma_d} \tan(\gamma_d R_d) = -\frac{1}{\gamma_b} \tag{2.77}$$

and defining $\tilde{\gamma}_d = \gamma_d R_d$, and $\tilde{\gamma}_b R_d$, then we will have

$$\tan(\tilde{\gamma}_d) = -\frac{\tilde{\gamma}_d}{\tilde{\gamma}_b} \tag{2.78}$$

The graphical solutions of this equation is shown in Figure 2.4 and the solutions are the intersections of both function on the left hand side and right hand side.

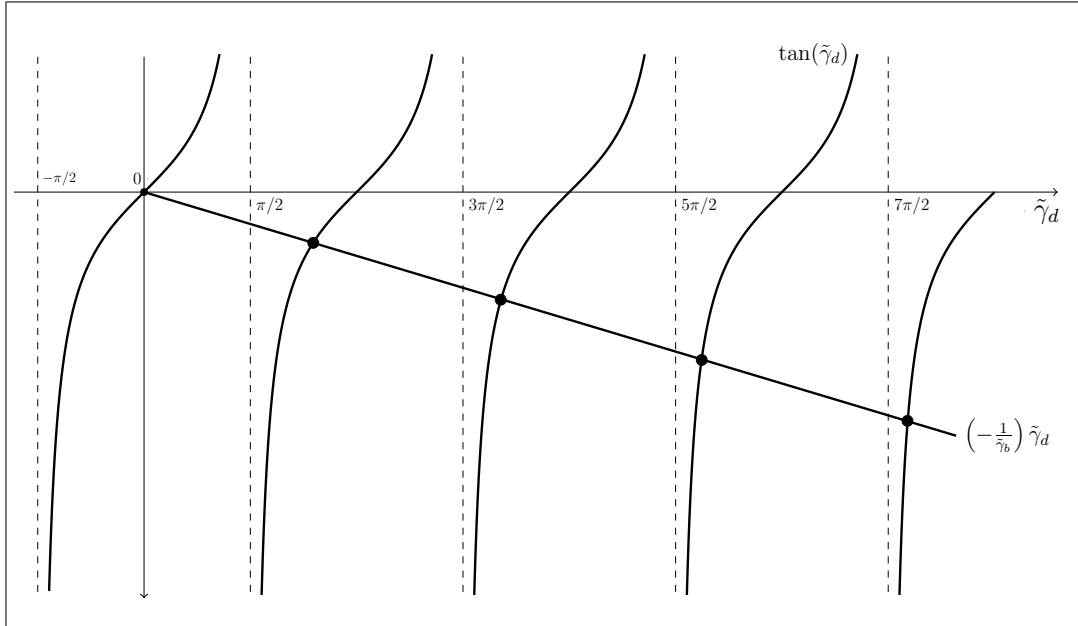


Figure 2.4. Graph of the functions $\tan(\tilde{\gamma}_d)$ and $(-1/\tilde{\gamma}_b) \tilde{\gamma}_d$ for even TE modes.

For a given $\tilde{\gamma}_b$, this equation yields several values for $\tilde{\gamma}_d$. The roots can again be found by using the iteration method.

$$(\tilde{\gamma}_d)_{n+1} = \arctan \left(\frac{\tilde{\gamma}_b}{(\tilde{\gamma}_d)_n} \right) \quad n = 1, 2, 3, \dots \quad (2.79)$$

by using the initial guess $(\tilde{\gamma}_d)_0 = n\pi$. We can then calculate ω and β from the values of $\tilde{\gamma}_d$ and $\tilde{\gamma}_b$ using,

$$\tilde{\omega}^2 = \left(\frac{\omega R_d}{c} \right)^2 = \frac{\tilde{\gamma}_d^2 + \tilde{\gamma}_b^2}{\epsilon_d - \epsilon_b} \quad (2.80)$$

$$\tilde{\beta}^2 = (\beta R_d)^2 = \frac{\epsilon_b \tilde{\gamma}_d^2 + \epsilon_d \tilde{\gamma}_b^2}{\epsilon_d - \epsilon_b} \quad (2.81)$$

as we have done of even TE modes, for every chosen $\tilde{\gamma}_b$, ϵ_b and ϵ_d we use the Equation 2.79 to find $\tilde{\gamma}_d$. Once we find $\tilde{\gamma}_d$ then we use Equation 2.80 and Equation 2.81 to find $\tilde{\omega}$ and $\tilde{\beta}$.

In Figure 2.5 we show $\tilde{\beta}$ versus $\tilde{\omega}$ for odd TE modes. The lowest mode for odd TE solution is indicated with TE_1 and the higher modes are indicated with TE_3, TE_5, \dots

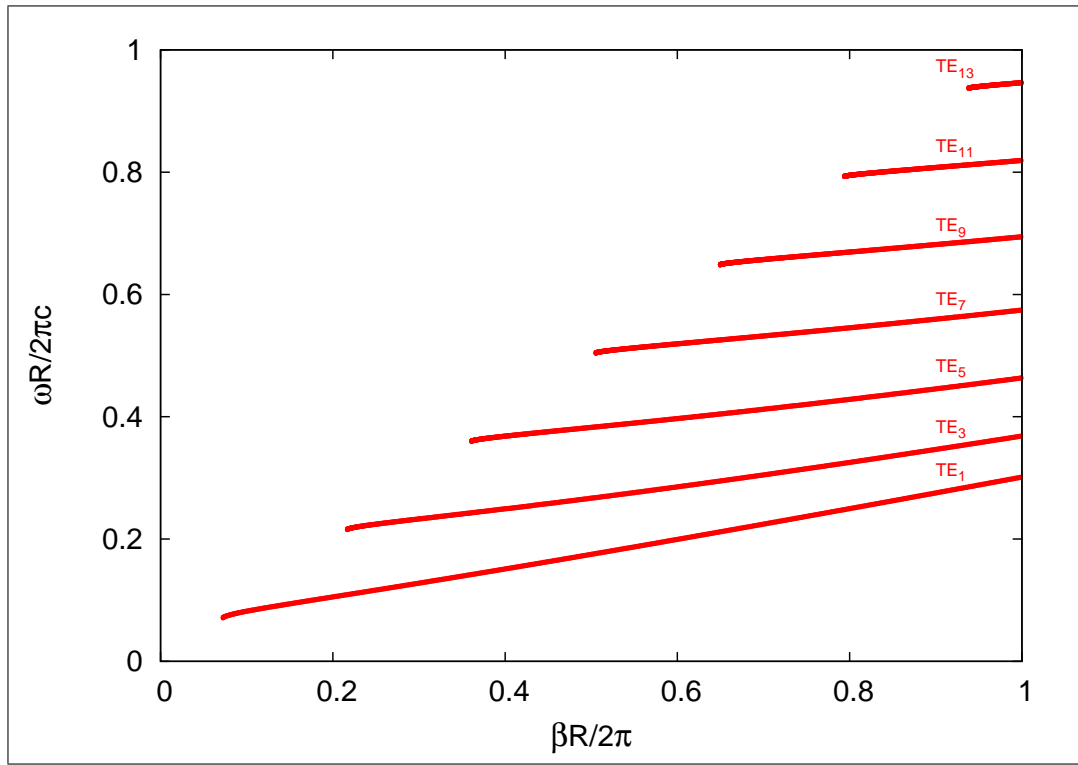


Figure 2.5. $\tilde{\omega} = \omega R_d/2\pi c$ versus $\tilde{\beta} = \beta R_d/2\pi$ plotted for odd TE modes of a slab waveguide with thickness of $2R_d$. The slab waveguide and the background materials have dielectric constant of ϵ_d and ϵ_b respectively.

In Figure 2.6 we plot $\tilde{\omega}$ versus $\tilde{\beta}$ for both even TE and odd TE modes on same graph. These are guided solutions of waveguide. These solutions are obtained by solving second order differential equation with boundary conditions imposed on field components. The guided region in the Figure 2.6 is represented by $\epsilon_d \tilde{\omega} > \tilde{\beta} > \epsilon_b \tilde{\omega}$. In these case solutions are sinusoidal in the region of higher dielectric, and in the lower dielectric region we have exponential decay solutions. For $\epsilon_d \tilde{\omega} > \epsilon_b \tilde{\omega} > \tilde{\beta}$ the solutions are sinusoidal in both region. In this case we get radiation modes.

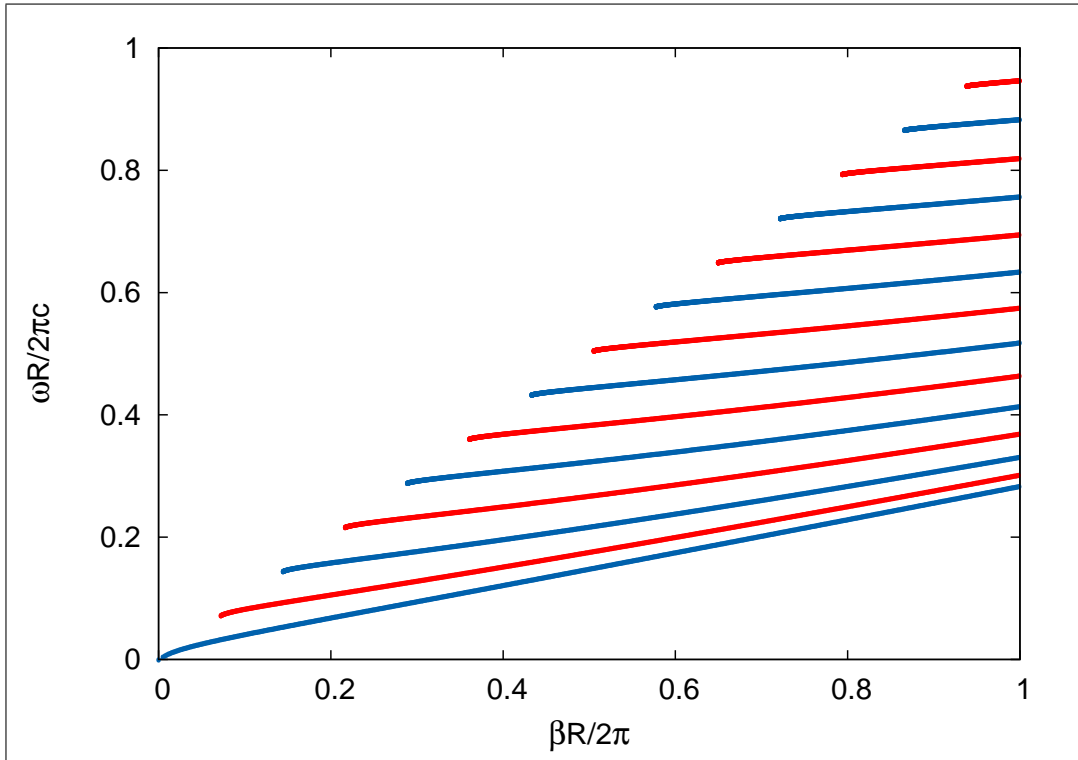


Figure 2.6. $\tilde{\omega}$ versus $\tilde{\beta}$ plotted for even TE (Blue lines) and odd TE modes (Red lines) of a slab waveguide with thickness $2R_d$.

For odd TE mode solutions, the electric field component that is in the y -direction, E_y , is found as,

$$E_y(x, y, z, t) = \begin{cases} B \sin(\gamma_d z) e^{i(\beta x - \omega t)} & |z| < R_d \\ C e^{-\gamma_b |z|} e^{i(\beta x - \omega t)} & |z| > R_d \end{cases} \quad (2.82)$$

where B and C are constants. By using the continuity of electric field, E_y , at $z = R_d$,

$$\begin{aligned} E_{y,d}(x, y, z, t)|_{z=R_d} &= E_{y,b}(x, y, z, t)|_{z=R_d} \\ B \sin(\gamma_d R_d) e^{i(\beta x - \omega t)} &= C e^{-\gamma_b R_d} e^{i(\beta x - \omega t)} \\ B \sin(\gamma_d R_d) &= C e^{-\gamma_b R_d} \end{aligned} \quad (2.83)$$

solving this equation for C , then we will have, $C = B \sin(\gamma_d R_d) e^{\gamma_b R_d}$. Putting this expression for C into the Equation 2.82 then we will have,

$$E_y(x, y, z, t) = \begin{cases} B \sin(\gamma_d z) e^{i(\beta x - \omega t)} & |z| < R_d \\ B \sin(\gamma_d R_d) e^{\gamma_b R_d} e^{-\gamma_b |z|} e^{i(\beta x - \omega t)} & |z| > R_d \end{cases} \quad (2.84)$$

The x -component of magnetic field, B_x , is given by $B_x = (i/\omega) \partial E_y / \partial z$,

$$B_x(x, y, z, t) = \begin{cases} \frac{i\gamma_d}{\omega} B \cos(\gamma_d z) e^{i(\beta x - \omega t)} & |z| < R_d \\ -\frac{i\gamma_b}{\omega} B \sin(\gamma_d R_d) e^{\gamma_b R_d} e^{-\gamma_b |z|} e^{i(\beta x - \omega t)} & |z| > R_d \end{cases} \quad (2.85)$$

the z component of magnetic field, B_z , is given by $B_z = (\beta/\omega) E_y$.

$$B_z(x, y, z, t) = \begin{cases} \frac{\beta}{\omega} B \sin(\gamma_d z) e^{i(\beta x - \omega t)} & |z| < R_d \\ \frac{\beta}{\omega} B \sin(\gamma_d R_d) e^{\gamma_b R_d} e^{-\gamma_b |z|} e^{i(\beta x - \omega t)} & |z| > R_d \end{cases} \quad (2.86)$$

In Figure 2.7 we plotted first two even TE mode profiles, TE_0 and TE_2 , and first two odd TE mode profiles, TE_1 and TE_3 for $\tilde{\beta} = 0.6$. The blue line is the electric field component, $E_y(z)$ that is transverse to propagation direction. The orange line indicates the magnetic field component, $B_z(z)$, that is perpendicular to propagation direction and it is in the z -direction. The red line indicates the magnetic field component, $B_x(z)$, in the propagation direction, x -direction.

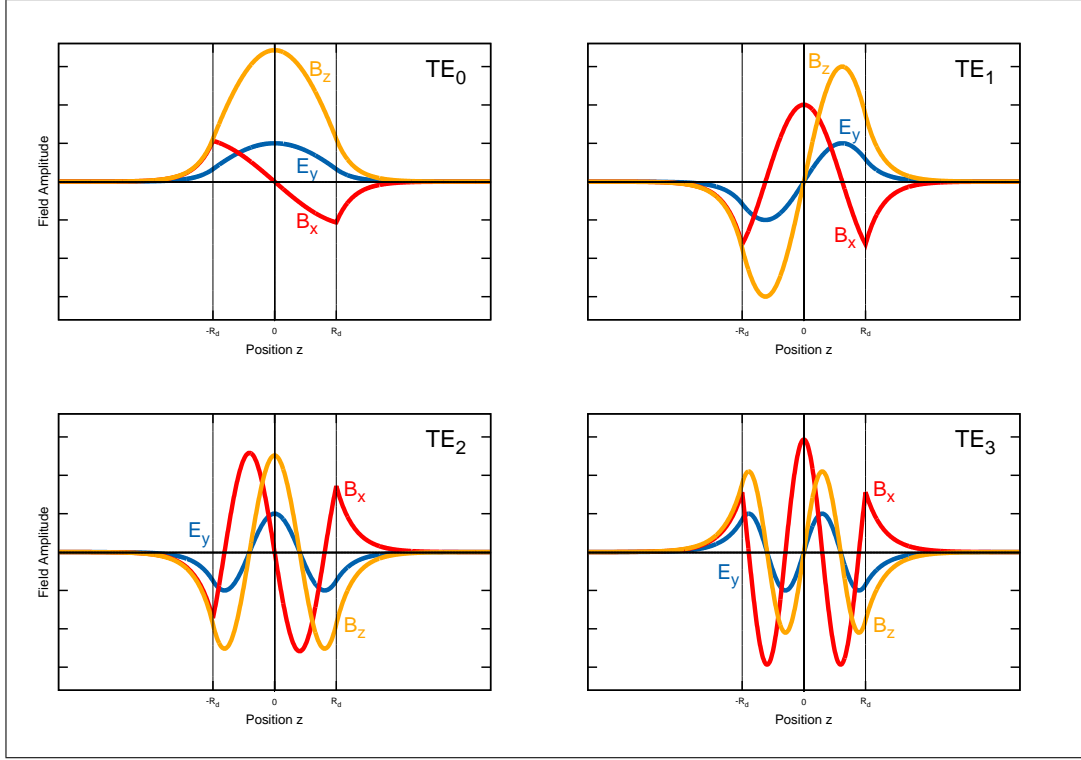


Figure 2.7. First two even TE mode profiles, TE_0 and TE_2 , and First two odd TE mode profiles, TE_1 and TE_3 . The propagation constant is $\tilde{\beta} = 0.6$. The dielectric constant of slab is $\epsilon_d = 13$ and the dielectric constant of back-ground is $\epsilon_b = 1$. The thickness of slab is $2R_d$.

The energy density of TE modes is given by Equation 2.62,

$$u_{em} = \frac{1}{4\mu_0} \Re e \left\{ \frac{1}{c^2} \epsilon(z) |E_y|^2 + |B_x|^2 + |B_z|^2 \right\} \quad (2.87)$$

putting the field components we have found for odd TE solutions into Equation 2.87, then the energy density of odd TE modes will be,

$$u_{em} = \begin{cases} \frac{B^2}{4\mu_0} \left[\left(\frac{\epsilon_d}{c^2} + \frac{\beta^2}{\omega^2} \right) \sin^2(\gamma_d z) + \frac{\gamma_d^2}{\omega^2} \cos^2(\gamma_d z) \right] & |z| < R_d \\ \frac{B^2}{4\mu_0} \left[\frac{\epsilon_b}{c^2} + \frac{\beta^2}{\omega^2} + \frac{\gamma_b^2}{\omega^2} \right] \sin^2(\gamma_d R_d) e^{2\gamma_b R_d} e^{-2\gamma_b |z|} & |z| > R_d \end{cases} \quad (2.88)$$

In Figure 2.8 we plotted electromagnetic energy density for first two even TE and first two odd TE modes for $\tilde{\beta} = 0.6$.

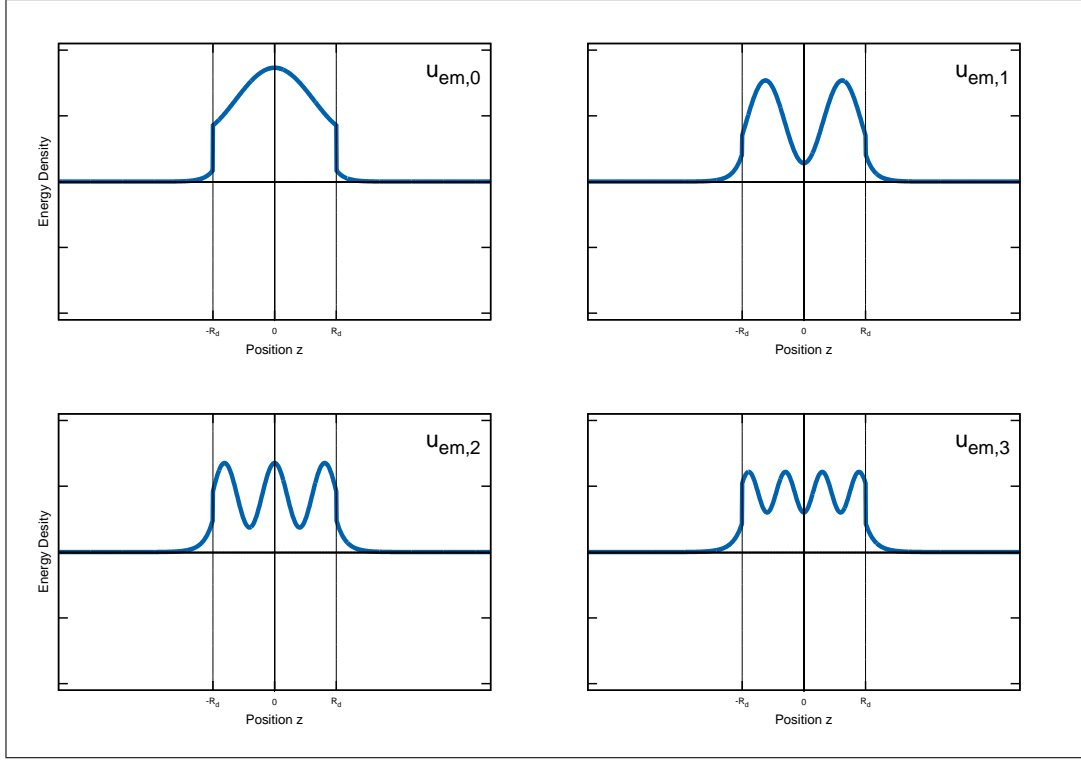


Figure 2.8. Energy density profiles for first two even TE modes, TE_0 and TE_2 , and first two odd TE modes, TE_1 and TE_3 . The propagation constant is $\tilde{\beta} = 0.6$. The dielectric constant of slab is $\epsilon_d = 13$ and the dielectric constant of background is $\epsilon_b = 1$. The thickness of slab is $2R_d$.

The flow of electromagnetic energy for odd TE modes is given by,

$$\mathbf{S} = \frac{1}{2\mu_0} \Re \{ E_y B_z^* \hat{\mathbf{x}} - E_y B_x^* \hat{\mathbf{z}} \} \quad (2.89)$$

As in the even TE mode solution the y -component is zero, $S_y = 0$. The x -component of Poynting vector is $S_x = 1/2\mu_0 \Re \{ E_y B_z^* \}$. Putting the field components, E_y , and B_z , into this expression then we will have for x -direction,

$$S_x = \begin{cases} \frac{B^2}{2\mu_0} \frac{\beta}{\omega} \sin^2(\gamma_d z) & |z| < R_d \\ \frac{B^2}{2\mu_0} \frac{\beta}{\omega} \sin^2(\gamma_d R_d) e^{2\gamma_b R_d} e^{-2\gamma_b |z|} & |z| > R_d \end{cases} \quad (2.90)$$

for the z -direction Poynting vector is $S_z = -1/2\mu_0 \Re \{ E_y B_x^* \}$. Putting the components

of the fields, E_y and B_z , then we will have,

$$S_z = \begin{cases} -i \frac{B^2}{2\mu_0} \frac{\gamma_d}{\omega} \sin(\gamma_d z) \cos(\gamma_d z) & |z| < R_d \\ i \frac{B^2}{2\mu_0} \frac{\gamma_b}{\omega} \sin^2(\gamma_d R_d) e^{2\gamma_b R_d} e^{-2\gamma_b |z|} & |z| > R_d \end{cases} \quad (2.91)$$

as we see the z -component is purely imaginary so the net energy flow in this direction is zero.

The amount of power propagating in the region, $|z| < R_d$, and in the background, $|z| > R_d$, along x -direction is given by integrating x -component of Poynting vector along the z -direction,

$$P_{in} = \int_{-R_d}^{R_d} S_x dz = \frac{A^2}{2\mu_0} \frac{\beta}{\omega} \int_{-R_d}^{R_d} \sin^2(\gamma_d z) dz \quad (2.92)$$

taking the integral will gives,

$$P_{in} = \frac{A^2}{2\mu_0} \frac{\beta}{\omega} \left[R_d - \frac{1}{2\gamma_d} \sin(2\gamma_d R_d) \right] \quad (2.93)$$

where P_{in} is power passing through unit length in x -direction. And the power that propagates in background is,

$$\begin{aligned} P_{out} &= \int_{-\infty}^{-R_d} S_x dz + \int_{R_d}^{\infty} S_x dz \\ &= \frac{A^2}{2\mu_0} \frac{\beta}{\omega} \sin^2(\gamma_d R_d) e^{2\gamma_b R_d} \left\{ \int_{-\infty}^{-R_d} e^{2\gamma_b z} dz + \int_{R_d}^{\infty} e^{-2\gamma_b z} dz \right\} \end{aligned} \quad (2.94)$$

which will give,

$$P_{out} = \frac{A^2}{2\mu_0} \frac{\beta}{\omega} \frac{1}{\gamma_b} \sin^2(\gamma_d R_d) \quad (2.95)$$

the total power is $P = P_{in} + P_{out}$,

$$P = \frac{A^2 \beta}{2\mu_0 \omega} \left[R_d - \frac{1}{2\gamma_d} \sin(2\gamma_d R_d) + \frac{1}{\gamma_b} \sin^2(\gamma_d R_d) \right] \quad (2.96)$$

Table. 2.1 shows confinement factor, $\Gamma_{in,i} = P_{in,i}/P$ and $\Gamma_{out,i} = P_{out,i}/P$ for TE modes where i indicates the mode index. As can be seen from the table confinement factor decreases with increasing mode index .

| Mode | Confinement Factor, $\Gamma_{in,i}$ (%) | Confinement Factor, $\Gamma_{out,i}$ (%) |
|--------|---|--|
| TE_0 | 0.97710935492732665 | 2.2890645072673337E-002 |
| TE_1 | 0.92661327275081484 | 7.3386727249185088E-002 |
| TE_2 | 0.87536185537805455 | 0.12463814462194547 |
| TE_3 | 0.83421130108392050 | 0.16578869891607964 |
| TE_4 | 0.79964427991633102 | 0.20035572008366903 |
| TE_5 | 0.76677251583164507 | 0.23322748416835493 |
| TE_6 | 0.72669642112467925 | 0.27330357887532075 |
| TE_7 | 0.66235543289114807 | 0.33764456710885193 |

Table 2.1. Confinement factors for even and odd TE modes for $\tilde{\beta} = 0.6$.

In Figure 2.9 we see plot of Poynting vector of first two even TE, TE_0 and TE_2 , and first two odd TE, TE_1 and TE_3 , modes for $\tilde{\beta} = 0.6$. In the figure $S_{x,0}$, $S_{x,1}$, $S_{x,2}$, and $S_{x,3}$ represent the Poynting vector of the modes TE_0 , TE_1 , TE_2 , and TE_3 respectively.

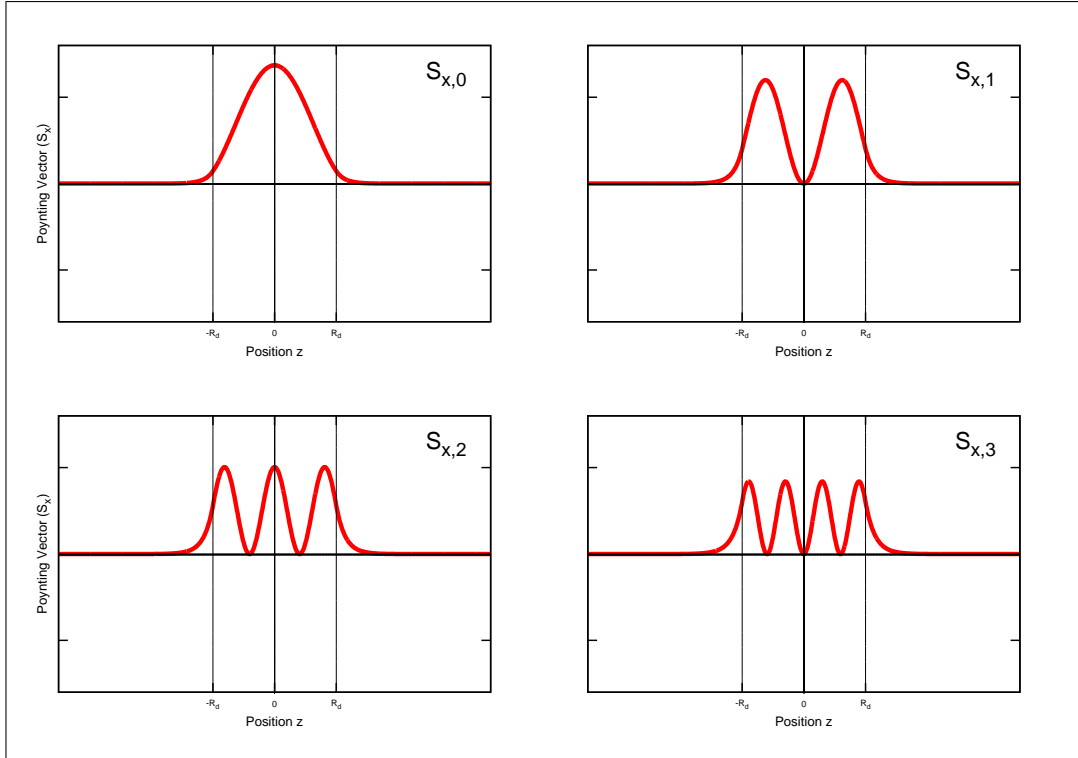


Figure 2.9. Poynting vector for both even and odd TE modes. The dielectric constant of slab is ϵ_d and the dielectric constant of background is ϵ_b . The thickness of slab is $2R_d$. The propagation constant is $\tilde{\beta} = 0.6$

2.1.2. Transverse Magnetic (TM) Modes

To calculate TM modes, we solve the differential equation for E_{0y} in two regions separately and impose boundary conditions on the solutions. By setting E_{0y} to zero we see that B_{0x} and B_{0z} are also zero, and we have left with field component that are non-zero, E_{0z} , B_{0y} , and E_{0x} and which are defined as,

$$E_{0x} = -\frac{ic^2}{\omega\epsilon} \frac{\partial B_{0y}}{\partial z} \quad (2.97)$$

$$E_{0z} = -\frac{c^2\beta}{\omega\epsilon} B_{0y} \quad (2.98)$$

and the second order differential equation for y -component of magnetic field, B_y , is,

$$\frac{\partial^2 B_{0y}(z)}{\partial z^2} - \left(\beta^2 - \frac{\omega^2\epsilon}{c^2} \right) B_{0y} = 0 \quad (2.99)$$

we solve the differential equation for $B_{0y}(z)$ in the two regions separately, and call the solutions $B_{0y,d}(z)$ and $B_{0y,b}(z)$.

$$B_{0y}(z) = \begin{cases} B_{0y,d}(z) & |z| < R_d \\ B_{0y,b}(z) & |z| > R_d \end{cases} \quad (2.100)$$

As we did for TE mode solutions, solutions for the region $|z| < R_d$ must have the form of sinusoidal function, and the solution for the region $|z| > R_d$ must have the form of exponential decay function. This will guaranty the field localization.

$$\left[\frac{\partial^2}{\partial z^2} + \left(\epsilon_d \frac{\omega^2}{c^2} - \beta^2 \right) \right] B_{0y,d}(z) = 0 \quad (2.101)$$

$$\left[\frac{\partial^2}{\partial z^2} - \left(\beta^2 - \epsilon_b \frac{\omega^2}{c^2} \right) \right] B_{0y,b}(z) = 0 \quad (2.102)$$

Now we define $\gamma_d^2 = \epsilon_d \frac{\omega^2}{c^2} - \beta^2$ and $\gamma_b^2 = \beta^2 - \epsilon_b \frac{\omega^2}{c^2}$. Plugging these into partial differential equations, Equation 2.101 and Equation 2.102 then these equations now take the form of,

$$\left[\frac{\partial^2}{\partial z^2} + \gamma_d^2 \right] B_{0y,d}(z) = 0 \quad (2.103)$$

$$\left[\frac{\partial^2}{\partial z^2} - \gamma_b^2 \right] B_{0y,b}(z) = 0 \quad (2.104)$$

and the solutions are, as required by the localization conditions around $|z| < R_d$ and being finite or going to zero as z goes to infinity,

$$B_{0y,d}(x, y, z, t) = A \cos(\gamma_d z) + B \sin(\gamma_d z) \quad (2.105)$$

$$B_{0y,b}(x, y, z, t) = C e^{-\gamma_b |z|} \quad (2.106)$$

where A , B , and C are the constants and they can be found by matching the boundary conditions. Now we can separate the solutions in two categories, one is called even TM and the other is called odd TM modes.

- Even Transverse Magnetic (TM) Modes, with the constant $B = 0$
- Odd Transverse Magnetic (TM) Modes, with the constant $A = 0$

2.1.2.1. Even Transverse Magnetic (TM) Modes

To find even TM solution, we will impose the boundary conditions to the solutions, Equation 2.105 and Equation 2.106. The solutions we found are in the form of,

$$B_{y,d}(x, y, z, t) = A \cos(\gamma_d z) e^{i(\beta x - \omega t)} + B \sin(\gamma_d z) e^{i(\beta x - \omega t)} \quad (2.107)$$

$$B_{y,b}(x, y, z, t) = C e^{-\gamma_b |z|} e^{i(\beta x - \omega t)} \quad (2.108)$$

for even TM solutions, we set the coefficient B to zero,

$$B_{y,d}(x, y, z, t) = A \cos(\gamma_d z) e^{i(\beta x - \omega t)} \quad (2.109)$$

$$B_{y,b}(x, y, z, t) = C e^{-\gamma_b |z|} e^{i(\beta x - \omega t)} \quad (2.110)$$

the boundary condition for the field component B_y be continuous across the interface at $z = R_d$ gives,

$$\begin{aligned} B_{y,d}(z)|_{z=R_d} &= B_{y,b}(z)|_{z=R_d} \\ A \cos(\gamma_d R_d) e^{i(\beta x - \omega t)} &= C e^{-\gamma_b R_d} e^{i(\beta x - \omega t)} \\ A \cos(\gamma_d R_d) &= C e^{-\gamma_b R_d} \end{aligned} \quad (2.111)$$

the condition E_x be continuous at $z = R_d$ will give, which is the Equation 2.26,

$$\begin{aligned} -\frac{ic^2}{\omega \epsilon_d} \frac{\partial B_{y,d}(z)}{\partial z} &= -\frac{ic^2}{\omega \epsilon_b} \frac{\partial B_{y,b}(z)}{\partial z} \\ \frac{1}{\epsilon_d} \frac{\partial}{\partial z} [A \cos(\gamma_d z) e^{i(\beta x - \omega t)}] &= \frac{1}{\epsilon_b} \frac{\partial}{\partial z} [C e^{-\gamma_b |z|} e^{i(\beta x - \omega t)}] \\ \frac{1}{\epsilon_d} (-A \gamma_d \sin(\gamma_d z))|_{z=R_d} &= \frac{1}{\epsilon_b} (-C \gamma_b e^{-\gamma_b |z|})|_{z=R_d} \\ \frac{\gamma_d}{\epsilon_d} A \sin(\gamma_d R_d) &= \frac{\gamma_b}{\epsilon_b} C e^{-\gamma_b R_d} \end{aligned} \quad (2.112)$$

we now have two equations, Equation 2.111 and Equation 2.112, to solve them for $\tilde{\gamma}_d$ we divide the Equation 2.112 with Equation 2.111 then we will have,

$$\frac{\gamma_d}{\epsilon_d} \tan(\gamma_d R_d) = \frac{\gamma_b}{\epsilon_b} \quad (2.113)$$

we can write the Equation 2.113 more simply by defining new parameters $\tilde{\gamma}_d = R_d \gamma_d$ and $\tilde{\gamma}_b = R_d \gamma_b$, then we finally will have,

$$\tan \tilde{\gamma}_d = \frac{\epsilon_d \tilde{\gamma}_b}{\epsilon_b \tilde{\gamma}_d} \quad (2.114)$$

at this point all we need to do is solve this equation for $\tilde{\gamma}_b$. In order to solve Equation 2.114, we plot both $\tan(\tilde{\gamma}_d)$ and $\left(\frac{\epsilon_d \tilde{\gamma}_b}{\epsilon_b}\right) \frac{1}{\tilde{\gamma}_d}$ on same graph, and their intersections are shown. These intersections are the solutions we are looking for, Figure 2.10.

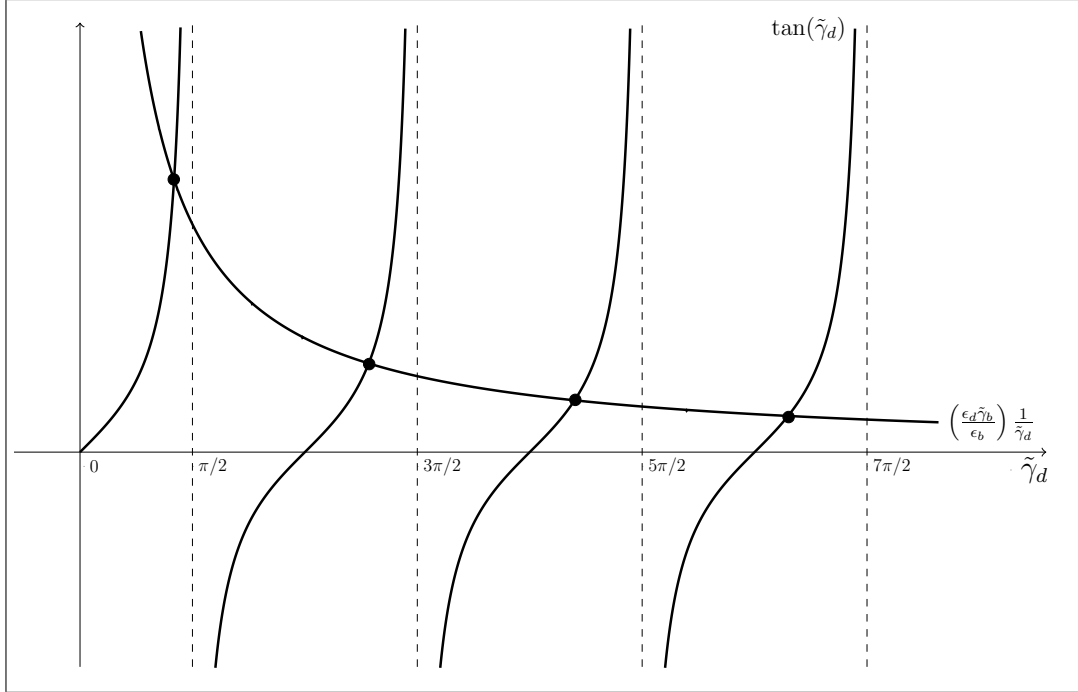


Figure 2.10. Graph of $\tan(\tilde{\gamma}_d)$ and $\left(\frac{\epsilon_d \tilde{\gamma}_b}{\epsilon_b}\right) \frac{1}{\tilde{\gamma}_d}$ for a chosen $\left(\frac{\epsilon_d \tilde{\gamma}_b}{\epsilon_b}\right)$ and their intersection.

For a given $\tilde{\gamma}_b$, ϵ_b and ϵ_d Equation 2.114 gives several values for $\tilde{\gamma}_d$. To find the roots we use the iteration method,

$$(\tilde{\gamma}_d)_{n+1} = \arctan\left(\frac{\epsilon_d \tilde{\gamma}_b}{\epsilon_b (\tilde{\gamma}_d)_n}\right) \quad n = 0, 1, 2, 3, \dots \quad (2.115)$$

and by using the initial guesses $(\tilde{\gamma}_d)_0 = n\pi$, we can calculate $\tilde{\omega}$ and $\tilde{\beta}$ from the values of $\tilde{\gamma}_d$ and $\tilde{\gamma}_b$ that we found by the iteration method by using,

$$\tilde{\omega}^2 = \left(\frac{\omega R_d}{c}\right)^2 = \frac{\tilde{\gamma}_d^2 + \tilde{\gamma}_b^2}{\epsilon_d - \epsilon_b} \quad (2.116)$$

$$\tilde{\beta}^2 = (\beta R_d)^2 = \frac{\epsilon_b \tilde{\gamma}_d^2 + \epsilon_d \tilde{\gamma}_b^2}{\epsilon_d - \epsilon_b} \quad (2.117)$$

The expression for $\tilde{\gamma}_b$ we defined earlier, $\tilde{\gamma}_b^2 = \tilde{\beta}^2 - \epsilon_b \tilde{\omega}^2$, expresses a hyperbola. For a give values of $\tilde{\gamma}_b$, ϵ_d and ϵ_b we first find $\tilde{\gamma}_d$ by using the iteration method that is defined as in Equation 2.115 and then using those values we find $\tilde{\omega}$ and $\tilde{\beta}$ from Equation 2.116 and Equation 2.117. The plot of $\tilde{\omega}$ versus $\tilde{\beta}$ is shown in Figure 2.11

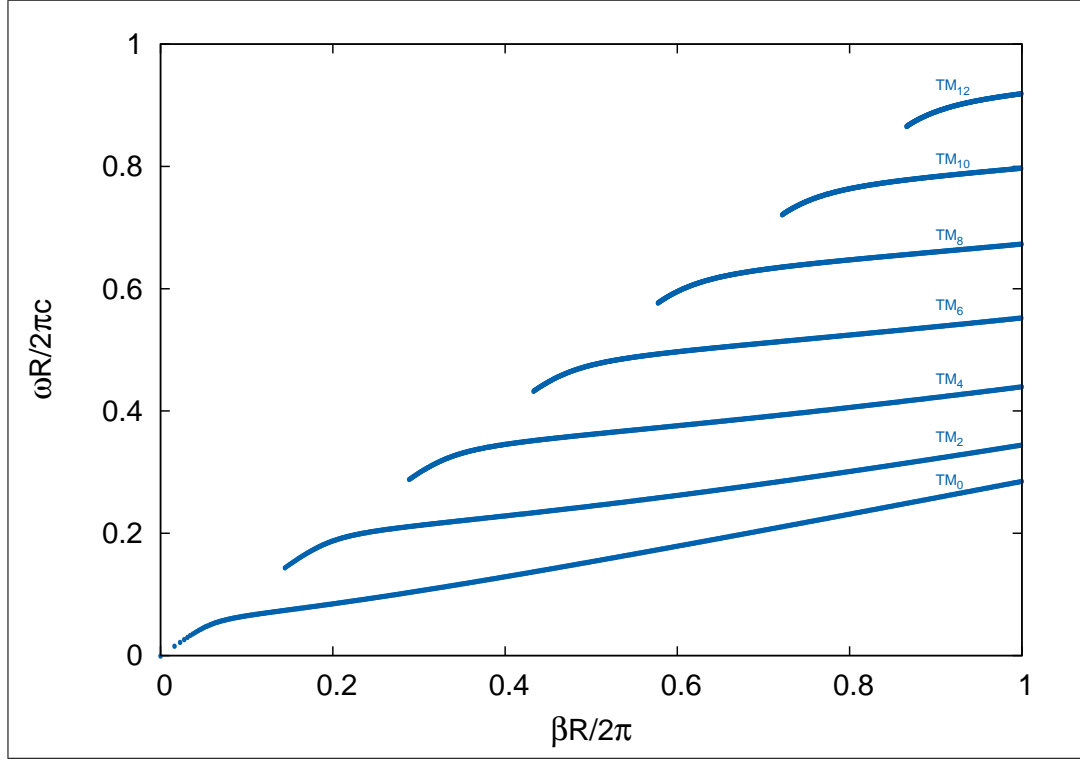


Figure 2.11. $\tilde{\omega}$ versus $\tilde{\beta}$ plotted for even TM modes of a slab waveguide with thickness $2R_d$.

Even TM modes solutions we have found for the magnetic field component is, B_y ,

$$B_y(x, y, z, t) = \begin{cases} A \cos(\gamma_d z) e^{i(\beta x - \omega t)} & |z| < R_d \\ C e^{-\gamma_b |z|} e^{i(\beta x - \omega t)} & |z| > R_d \end{cases} \quad (2.118)$$

we now use the continuity of B_y at the interface between two media to find the constant C in terms of the constant A ,

$$\begin{aligned} B_{y,d}(x, y, z, t)|_{z=R_d} &= B_{y,b}(x, y, z, t)|_{z=R_d} \\ A \cos(\gamma_d R_d) e^{i(\beta x - \omega t)} &= C e^{-\gamma_b R_d} e^{i(\beta x - \omega t)} \\ A \cos(\gamma_d R_d) &= C e^{-\gamma_b R_d} \end{aligned} \quad (2.119)$$

solving this equation for the constant C we will get, $C = A \cos(\gamma_d R_d) e^{\gamma_b R_d}$. Putting this expression into Equation 2.118 for C , then we will get,

$$B_y(x, y, z, t) = \begin{cases} A \cos(\gamma_d z) e^{i(\beta x - \omega t)} & |z| < R_d \\ A \cos(\gamma_d R_d) e^{\gamma_b R_d} e^{-\gamma_b |z|} e^{i(\beta x - \omega t)} & |z| > R_d \end{cases} \quad (2.120)$$

The x -component of electric field, E_x , is given by $E_x = (-ic^2/\omega\epsilon) \partial B_y/\partial z$

$$E_x(x, y, z, t) = \begin{cases} \frac{ic^2\gamma_d}{\omega\epsilon_d} A \sin(\gamma_d z) e^{i(\beta x - \omega t)} & |z| < R_d \\ \frac{ic^2\gamma_b}{\omega\epsilon_b} A \cos(\gamma_d R_d) e^{\gamma_b R_d} e^{-\gamma_b |z|} e^{i(\beta x - \omega t)} & |z| > R_d \end{cases} \quad (2.121)$$

The z -component of electric field, E_z , is given by $E_z = (-c^2\beta/\omega\epsilon) B_y$

$$E_z(x, y, z, t) = \begin{cases} -\frac{c^2\beta}{\omega\epsilon_d} A \cos(\gamma_d z) e^{i(\beta x - \omega t)} & |z| < R_d \\ -\frac{c^2\beta}{\omega\epsilon_b} A \cos(\gamma_d R_d) e^{\gamma_b R_d} e^{-\gamma_b |z|} e^{i(\beta x - \omega t)} & |z| > R_d \end{cases} \quad (2.122)$$

Energy density of electromagnetic field is given by,

$$u_{em} = \frac{1}{4} \Re e \left\{ \epsilon_0 \epsilon(\mathbf{r}) \mathbf{E} \cdot \mathbf{E}^* + \frac{1}{\mu_0 \mu(\mathbf{r})} \mathbf{B} \cdot \mathbf{B}^* \right\} \quad (2.123)$$

for TM modes, E_x , B_y and E_z are the non-zero components. The other three field components are zero, B_x , E_y , and B_z , so the energy density for TM modes can be written

as,

$$u_{em} = \frac{1}{4\mu_0} \Re e \left\{ \frac{1}{c^2} \epsilon(z) (|E_x|^2 + |E_z|^2) + |B_y|^2 \right\} \quad (2.124)$$

Using field components that we have found previously in Equation 2.124 then the energy density will be,

$$u_{em} = \begin{cases} \frac{A^2}{4\mu_0} \left[\left(\frac{c^2\beta^2}{\omega^2\epsilon_d} + 1 \right) \cos^2(\gamma_d z) + \frac{c^2\gamma_d^2}{\omega^2\epsilon_d} \sin^2(\gamma_d z) \right] & |z| < R_d \\ \frac{A^2}{4\mu_0} \left[\frac{c^2\gamma_b^2}{\omega\epsilon_b} + \frac{c^2\beta^2}{\omega^2\epsilon_b} + 1 \right] \cos^2(\gamma_d R_d) e^{2\gamma_b R_d} e^{-2\gamma_b |z|} & |z| > R_d \end{cases} \quad (2.125)$$

The flow of electromagnetic energy for even TM modes is, where three of the field components are zero, $E_y = 0$, $B_x = 0$, and $B_z = 0$,

$$\mathbf{S} = \frac{1}{2} \Re e \{ \mathbf{E} \times \mathbf{H}^* \} = \frac{1}{2\mu_0} \Re e \{ \mathbf{E} \times \mathbf{B}^* \} = \frac{1}{2\mu_0} \Re e \left\{ \begin{vmatrix} \hat{\mathbf{x}} & \hat{\mathbf{y}} & \hat{\mathbf{z}} \\ E_x & 0 & E_z \\ 0 & B_y^* & 0 \end{vmatrix} \right\} \quad (2.126)$$

after taking the determinant then we will have,

$$\mathbf{S} = \frac{1}{2\mu_0} \Re e \{ -E_z B_y^* \hat{\mathbf{x}} + E_x B_y^* \hat{\mathbf{z}} \} \quad (2.127)$$

as we see from this equation Poynting vector has no component in the y -direction, $S_y = 0$. Putting the field components, E_x , B_y , and E_z , into Equation 2.127 then we will have for x -direction,

$$S_x = \begin{cases} \frac{A^2}{2\mu_0} \frac{c^2\beta}{\omega\epsilon_d} \cos^2(\gamma_d z) & |z| < R_d \\ \frac{A^2}{2\mu_0} \frac{c^2\beta}{\omega\epsilon_b} \cos^2(\gamma_d R_d) e^{2\gamma_b R_d} e^{-2\gamma_b |z|} & |z| > R_d \end{cases} \quad (2.128)$$

for the z -direction we will have,

$$S_z = \begin{cases} i \frac{A^2}{2\mu_0} \frac{c^2 \gamma_d}{\omega \epsilon_d} \sin(\gamma_d z) \cos(\gamma_d z) & |z| < R_d \\ i \frac{A^2}{2\mu_0} \frac{c^2 \gamma_b}{\omega \epsilon_b} \cos^2(\gamma_d R_d) e^{2\gamma_b R_d} e^{-2\gamma_b |z|} & |z| > R_d \end{cases} \quad (2.129)$$

the real part of z -component of Poynting vector is zero so the Poynting vector in this direction is zero, $S_z = 0$, there is no net energy flow in this direction.

The power that is propagating in the slab, $|z| < R_d$, is given by,

$$P_{in} = \int_{-R_d}^{R_d} S_x dz = \frac{A^2 c^2}{2\mu_0} \frac{\beta}{\omega \epsilon_d} \int_{-R_d}^{R_d} \cos^2(\gamma_d z) dz \quad (2.130)$$

the integration gives,

$$P_{in} = \frac{A^2 c^2}{2\mu_0} \frac{\beta}{\omega \epsilon_d} \left[R_d + \frac{1}{2\gamma_d} \sin(2\gamma_d R_d) \right] \quad (2.131)$$

the power that propagates in background, $|z| > R_d$, along the x -direction is,

$$\begin{aligned} P_{out} &= \int_{-\infty}^{-R_d} S_x dz + \int_{R_d}^{\infty} S_x dz \\ &= \frac{A^2 c^2}{2\mu_0} \frac{\beta}{\omega \epsilon_b} \cos^2(\gamma_d R_d) e^{2\gamma_b R_d} \left\{ \int_{-\infty}^{-R_d} e^{2\gamma_b z} dz + \int_{R_d}^{\infty} e^{-2\gamma_b z} dz \right\} \end{aligned} \quad (2.132)$$

after taking the integrals then we will have,

$$P_{out} = \frac{A^2 c^2}{2\mu_0} \frac{\beta}{\omega \epsilon_b} \frac{1}{\gamma_b} \cos^2(\gamma_d R_d) \quad (2.133)$$

the total power is $P = P_{in} + P_{out}$,

$$P = \frac{A^2 c^2}{2\mu_0} \frac{\beta}{\omega} \left[\frac{R_d}{\epsilon_d} + \frac{1}{2\gamma_d \epsilon_d} \sin(2\gamma_d R_d) + \frac{1}{\gamma_b \epsilon_b} \cos^2(\gamma_d R_d) \right] \quad (2.134)$$

2.1.2.2. Odd Transverse Magnetic (TM) Modes

Odd TM modes are found by setting the coefficient A to zero in Equation 2.105. So the odd TM solutions are,

$$B_{y,d}(x, y, z, t) = B \sin(\gamma_d z) e^{i(\beta x - \omega t)} \quad (2.135)$$

$$B_{y,b}(x, y, z, t) = C e^{-\gamma_b |z|} e^{i(\beta x - \omega t)} \quad (2.136)$$

the boundary condition requires that B_y be continuous across the interface at $z = R_d$. Which will give,

$$\begin{aligned} B_{y,d}(z)|_{z=R_d} &= B_{y,b}(z)|_{z=R_d} \\ B \sin(\gamma_d R_d) e^{i(\beta x - \omega t)} &= C e^{-\gamma_b R_d} e^{i(\beta x - \omega t)} \\ B \sin(\gamma_d R_d) &= C e^{-\gamma_b R_d} \end{aligned} \quad (2.137)$$

the second boundary condition must be imposed is that B_x be continuous at $z = R_d$, the interface between two media, which will give,

$$\begin{aligned} \frac{c^2}{i\omega\epsilon_d} \frac{\partial B_{y,d}(z)}{\partial z} &= \frac{c^2}{i\omega\epsilon_b} \frac{\partial B_{y,b}(z)}{\partial z} \\ \frac{1}{\epsilon_d} \frac{\partial}{\partial z} [B \sin(\gamma_d z) e^{i(\beta x - \omega t)}] &= \frac{1}{\epsilon_b} \frac{\partial}{\partial z} [C e^{-\gamma_b |z|} e^{i(\beta x - \omega t)}] \\ \frac{1}{\epsilon_d} (B \gamma_d \cos(\gamma_d z)) |_{z=R_d} &= \frac{1}{\epsilon_b} (-C \gamma_b e^{-\gamma_b |z|}) |_{z=R_d} \\ \frac{\gamma_d}{\epsilon_d} B \cos(\gamma_d R_d) &= -\frac{\gamma_b}{\epsilon_b} C e^{\gamma_b R_d} \end{aligned} \quad (2.138)$$

again we have two equations, one from the continuity of B_y and the other is from the continuity of E_x at the interface, $z = R_d$. By dividing Equation 2.137 with Equation 2.138 we will have,

$$\frac{\epsilon_d}{\gamma_d} \tan(\gamma_d R_d) = -\frac{\epsilon_b}{\gamma_b} \quad (2.139)$$

and defining $\tilde{\gamma}_d = \gamma_d R_d$, and $\tilde{\gamma}_b = \gamma_b R_d$, then we will have

$$\tan(\tilde{\gamma}_d) = -\frac{\epsilon_b \tilde{\gamma}_d}{\epsilon_d \tilde{\gamma}_b} \quad (2.140)$$

The graph of functions $\tan(\tilde{\gamma}_d)$ and $(-\frac{\epsilon_b}{\epsilon_d \tilde{\gamma}_b})\tilde{\gamma}_d$ is shown in Figure 2.12. The intersections of two functions indicated are the solutions to the Equation 2.140.

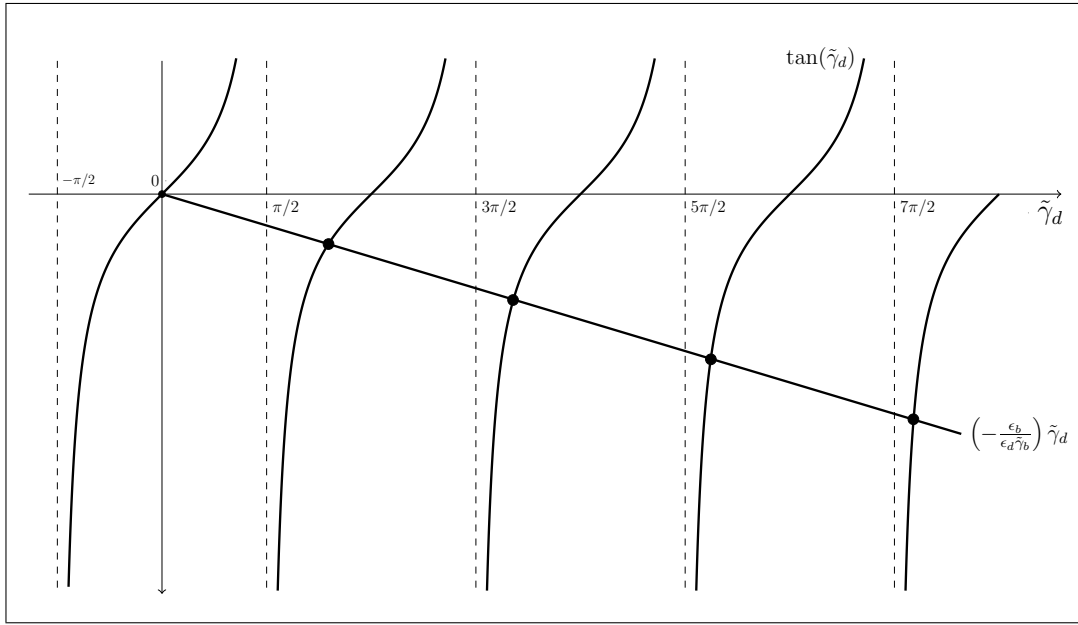


Figure 2.12. Graph of $\tan(\tilde{\gamma}_d)$ and $(-\epsilon_b/(\epsilon_d \tilde{\gamma}_b)) \tilde{\gamma}_d$ functions for a chosen $-\epsilon_b/(\epsilon_d \tilde{\gamma}_b)$ value and their intersections.

For a given $\tilde{\gamma}_b$, ϵ_b and ϵ_d Equation 2.140 gives several values for $\tilde{\gamma}_d$. The roots can again be found by using the iteration method.

$$(\tilde{\gamma}_d)_{n+1} = \arctan\left(-\frac{\epsilon_b(\tilde{\gamma}_d)_n}{\epsilon_d \tilde{\gamma}_b}\right) \quad n = 1, 2, 3, \dots \quad (2.141)$$

by using the initial guess $(\tilde{\gamma}_d)_0 = n\pi$. We can then calculate ω and β from the values of $\tilde{\gamma}_d$ and $\tilde{\gamma}_b$ using,

$$\tilde{\omega}^2 = \left(\frac{\omega R_d}{c}\right)^2 = \frac{\tilde{\gamma}_d^2 + \tilde{\gamma}_b^2}{\epsilon_d - \epsilon_b} \quad (2.142)$$

$$\tilde{\beta}^2 = (\beta R_d)^2 = \frac{\epsilon_b \tilde{\gamma}_d^2 + \epsilon_d \tilde{\gamma}_b^2}{\epsilon_d - \epsilon_b} \quad (2.143)$$

again by looking back to the definition we defined earlier for $\tilde{\gamma}_b, \tilde{\gamma}_b^2 = \tilde{\beta}^2 - \epsilon_b \tilde{\omega}^2$, we see that it defines hyperbolic curves. For every chosen $\tilde{\gamma}_b$ and ϵ_b values we have a different curve defined by $\tilde{\gamma}_b^2 = \tilde{\beta}^2 - \epsilon_b \tilde{\omega}^2$, and we can define infinite number of curves defined by this expression, so for every values of chosen $\tilde{\gamma}_b$ and ϵ_b we have infinitely many values of $\tilde{\omega}$ and $\tilde{\beta}$. By solving this equation and plotting them on a graph we will have Figure 2.13. This graphic gives us the band structure.

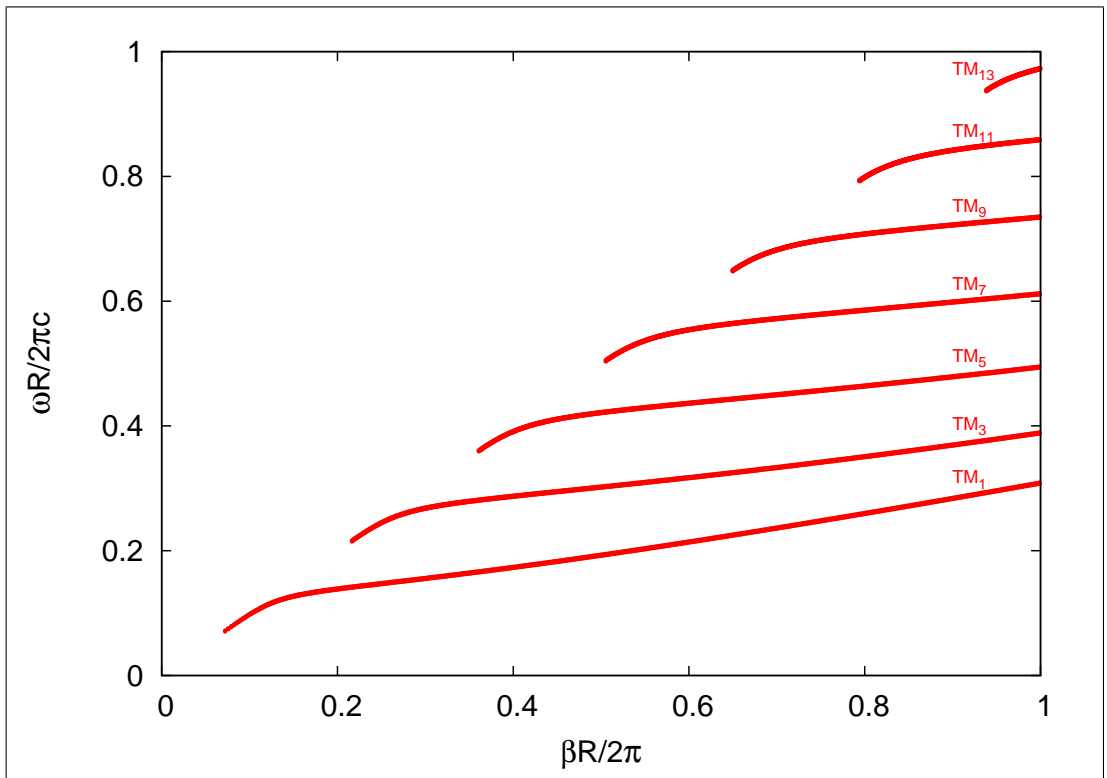


Figure 2.13. $\tilde{\beta}$ versus $\tilde{\omega}$ graph of odd TM modes of a single slab waveguide with dielectric constant $\epsilon_d = 13$ and thickness $2R_d$. The dielectric constant of the background is $\epsilon_b = 1$.

In the Figure 2.14 we show $\tilde{\beta}$ versus $\tilde{\omega}$ of slab waveguide for even and odd TM solutions. Blue lines indicate even modes while red lines indicate odd modes. As it is seen from the figure the fundamental mode, (lowest mode) is even.

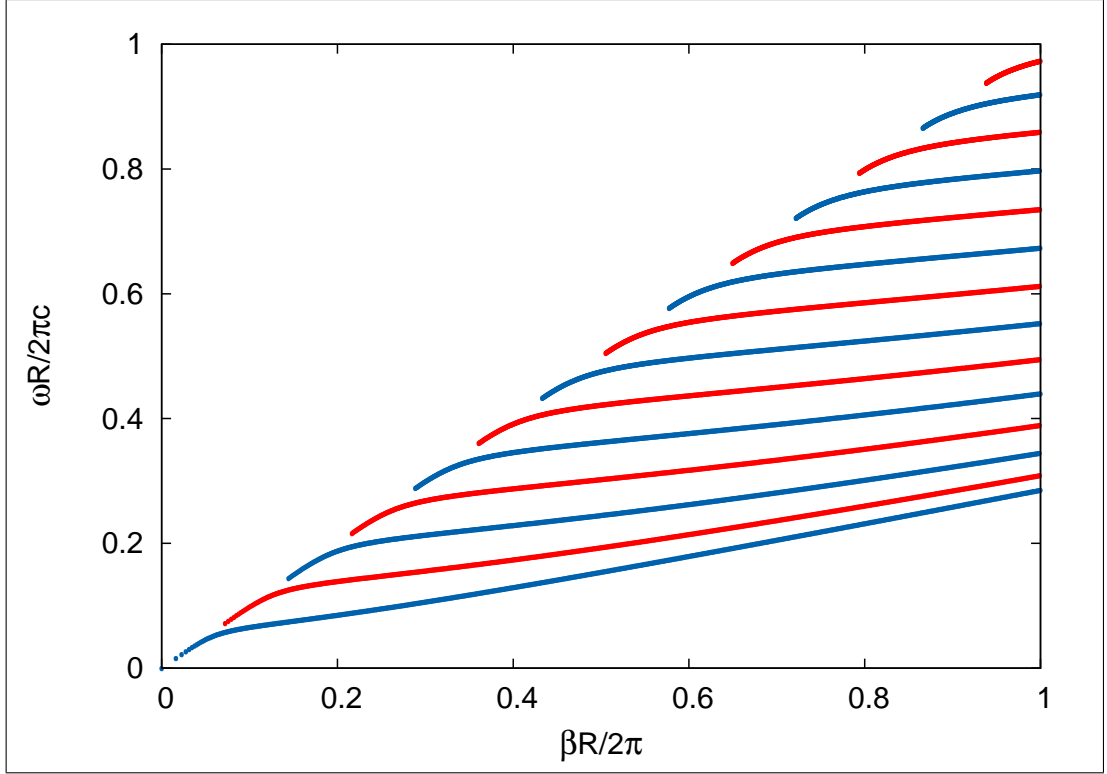


Figure 2.14. Graph of $\tilde{\beta}$ versus $\tilde{\omega}$ plotted for both even TM (Blue lines), and odd TM (Red lines) modes for single slab waveguide with thickness $2R_d$ and dielectric constant of slab and background are $\epsilon_d = 13$ and $\epsilon_b = 1$ respectively.

For odd TM modes, the solution for the field component in the propagation direction of odd TM modes, B_y , are found as,

$$B_y(x, y, z, t) = \begin{cases} B \sin(\gamma_d z) e^{i(\beta x - \omega t)} & |z| < R_d \\ C e^{-\gamma_b |z|} e^{i(\beta x - \omega t)} & |z| > R_d \end{cases} \quad (2.144)$$

to find the constant C in terms of the constant B we use the continuity of B_y at the

interface between two media, then we have,

$$\begin{aligned}
B_{y,d}(x, y, z, t)|_{z=R_d} &= B_{y,b}(x, y, z, t)|_{z=R_d} \\
B \sin(\gamma_d R_d) e^{i(\beta x - \omega t)} &= C e^{-\gamma_b R_d} e^{i(\beta x - \omega t)} \\
B \sin(\gamma_d R_d) &= C e^{-\gamma_b R_d}
\end{aligned} \tag{2.145}$$

solving this equation for the constant C we get $C = B \sin(\gamma_d R_d) e^{\gamma_b R_d}$ and putting this back for the constant C , then we will get,

$$B_y(x, y, z, t) = \begin{cases} B \sin(\gamma_d z) e^{i(\beta x - \omega t)} & |z| < R_d \\ B \sin(\gamma_d R_d) e^{\gamma_b R_d} e^{-\gamma_b |z|} e^{i(\beta x - \omega t)} & |z| > R_d \end{cases} \tag{2.146}$$

the x -component of electric field is, $E_x = (-ic^2/\omega\epsilon)\partial B_y/\partial z$,

$$E_x(x, y, z, t) = \begin{cases} -\frac{ic^2\gamma_d}{\omega\epsilon_d} B \cos(\gamma_d z) e^{i(\beta x - \omega t)} & |z| < R_d \\ \frac{ic^2\gamma_b}{\omega\epsilon_b} B \sin(\gamma_d R_d) e^{\gamma_b R_d} e^{-\gamma_b |z|} e^{i(\beta x - \omega t)} & |z| > R_d \end{cases} \tag{2.147}$$

the electric field component that is perpendicular to the interface is, $E_{0z} = (-ic^2\beta/\omega\epsilon)B_y$,

$$E_z(x, y, z, t) = \begin{cases} -\frac{c^2\beta}{\omega\epsilon_d} B \sin(\gamma_d z) e^{i(\beta x - \omega t)} & |z| < R_d \\ -\frac{c^2\beta}{\omega\epsilon_b} B \sin(\gamma_d R_d) e^{\gamma_b R_d} e^{-\gamma_b |z|} e^{i(\beta x - \omega t)} & |z| > R_d \end{cases} \tag{2.148}$$

In Figure 2.15 We plotted first two odd TM mode profiles and their energy density for $\tilde{\beta} = 0.6$. The blue mode is the magnetic field component in the propagation direction, $B_x(z)$. The red line indicates the electric field component, $E_y(z)$, that is perpendicular to propagation direction and it is in the y -direction. The orange mode indicates the magnetic field component, $B_z(z)$, that is in the z -direction.

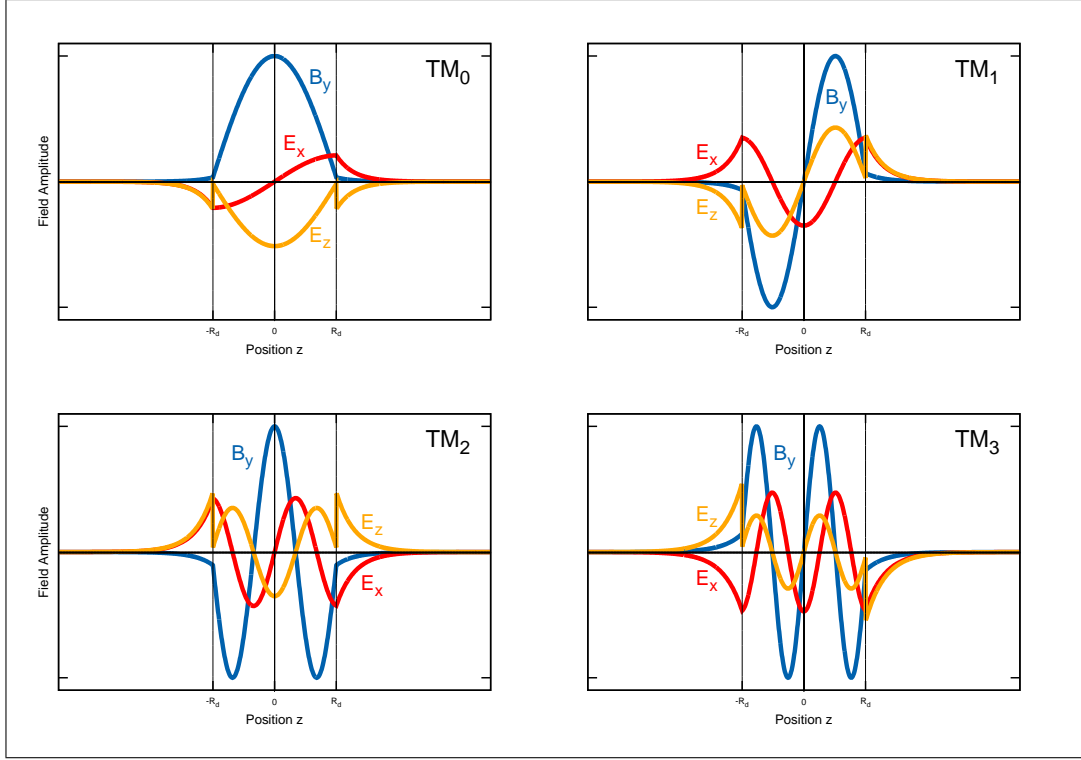


Figure 2.15. First two even TM mode profiles (TM0 and TM2) and energy densities of each modes of slab waveguide. The dielectric constant of slab is ϵ_d and the dielectric constant of background is ϵ_b . The thickness of slab is $2R_d$. The propagation constant is

Energy density of electromagnetic field is given by,

$$u_{em} = \frac{1}{4} \Re e \left\{ \epsilon_0 \epsilon(\mathbf{r}) \mathbf{E} \cdot \mathbf{E}^* + \frac{1}{\mu_0 \mu(\mathbf{r})} \mathbf{B} \cdot \mathbf{B}^* \right\} \quad (2.149)$$

for TM modes, E_x , B_y and E_z are the non-zero component so the energy density for TM modes can be written as,

$$u_{em} = \frac{1}{4\mu_0} \Re e \left\{ \frac{1}{c^2} \epsilon(z) (|E_x|^2 + |E_z|^2) + |B_y|^2 \right\} \quad (2.150)$$

Using field components that we have found previously, then the energy density for two

region, inside and the outside of the slab waveguide will be,

$$u_{em} = \begin{cases} \frac{B^2}{4\mu_0} \left[\left(\frac{c^2\beta^2}{\omega^2\epsilon_d} + 1 \right) \sin^2(\gamma_d z) + \frac{c^2\gamma_d^2}{\omega^2\epsilon_d} \cos^2(\gamma_d z) \right] & |z| < R_d \\ \frac{B^2}{4\mu_0} \left[\frac{c^2\gamma_b^2}{\omega^2\epsilon_b} + \frac{c^2\beta^2}{\omega^2\epsilon_b} + 1 \right] \sin^2(\gamma_d R_d) e^{2\gamma_b R_d} e^{-2\gamma_b |z|} & |z| > R_d \end{cases} \quad (2.151)$$

In Figure 2.16 we see electromagnetic energy density distribution along z -direction. The propagation constant for all four modes is taken as $\tilde{\beta} = 0.6$. In this figure $u_{em,0}$, $u_{em,1}$, $u_{em,2}$, and $u_{em,3}$ represent the electromagnetic energy densities of TM_0 , TM_1 , TM_2 , and TM_3 respectively.

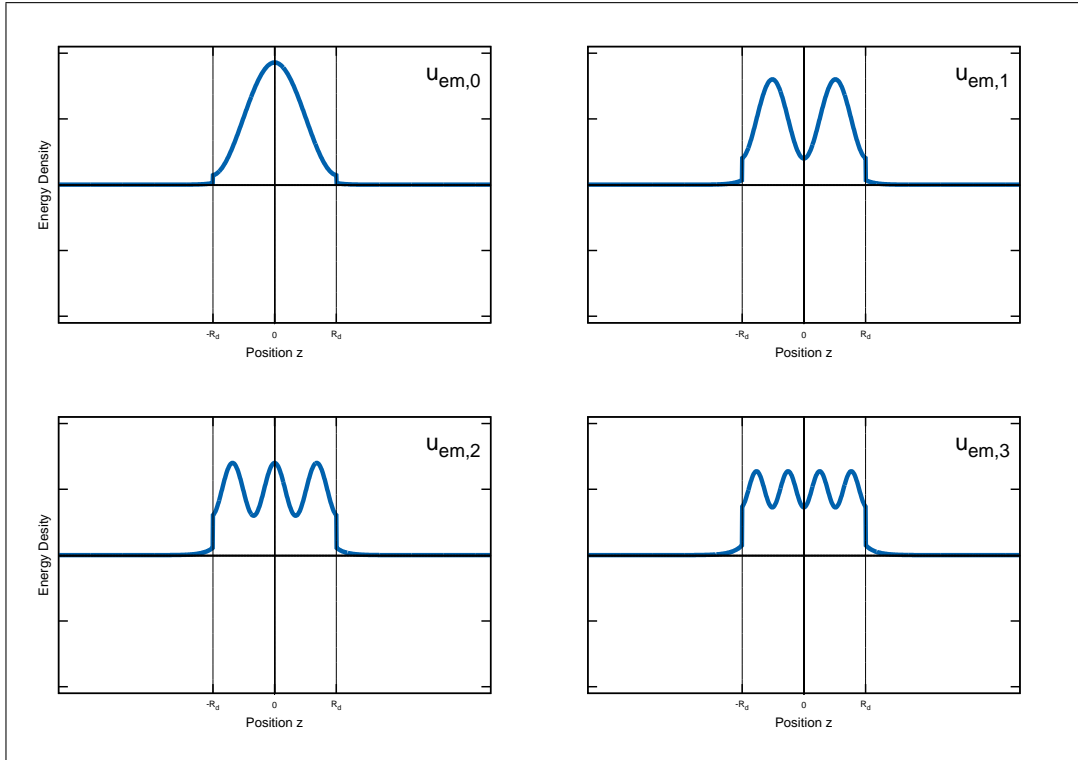


Figure 2.16. Electromagnetic energy density distribution of even TM modes, ($u_{em,0}$ and $u_{em,2}$), and odd TM modes, ($u_{em,1}$ and $u_{em,3}$), along z -coordinate. The dielectric constant of slab is $\epsilon_d = 13$ and the dielectric constant of background is $\epsilon_b = 1$. The thickness of slab is $2R_d$.

The Poynting vector, \mathbf{S} , for TM mode solutions is given by,

$$\mathbf{S} = \frac{1}{2\mu_0} \Re e \{ -E_z B_y^* \hat{\mathbf{x}} + E_x B_y^* \hat{\mathbf{z}} \} \quad (2.152)$$

as we see from Equation 2.152 Poynting vector has no component in the y -direction, $S_y = 0$. This means that there is no energy flow in y -direction. The flow of electromagnetic energy is restricted in the $x - z$ plane. Putting the field components, B_x , E_y , and B_z , into Equation 2.152 then we will have for x -direction, $S_x = (1/2\mu_0) \Re e \{ -E_z B_y^* \}$

$$S_x = \begin{cases} \frac{B^2}{2\mu_0} \frac{c^2 \beta}{\omega \epsilon_d} \sin^2(\gamma_d z) & |z| < R_d \\ \frac{B^2}{2\mu_0} \frac{c^2 \beta}{\omega \epsilon_b} \sin^2(\gamma_d R_d) e^{2\gamma_b R_d} e^{-2\gamma_b |z|} & |z| > R_d \end{cases} \quad (2.153)$$

for z -direction the Poynting vector is $S_z = (1/2\mu_0) \Re e \{ E_x B_y^* \}$

$$S_z = \begin{cases} -i \frac{B^2}{2\mu_0} \frac{c^2 \gamma_d}{\omega \epsilon_d} \cos(\gamma_d z) \sin(\gamma_d z) & |z| < R_d \\ i \frac{B^2}{2\mu_0} \frac{c^2 \gamma_b}{\omega \epsilon_b} \sin^2(\gamma_d R_d) e^{2\gamma_b R_d} e^{-2\gamma_b |z|} & |z| > R_d \end{cases} \quad (2.154)$$

as can be seen the real part of S_z is zero. This means that no net energy flow in this direction. The electromagnetic energy oscillates between electric and magnetic field.

The amount of power propagating in the region, $|z| < R_d$, and in the background, $|z| > R_d$, along x -direction is given by integrating x -component of Poynting vector along the z -direction,

$$P_{in} = \int_{-R_d}^{R_d} S_x dz = \frac{B^2 c^2}{2\mu_0} \frac{\beta}{\omega \epsilon_d} \int_{-R_d}^{R_d} \sin^2(\gamma_d z) dz \quad (2.155)$$

taking the integral will gives,

$$P_{in} = \frac{B^2 c^2}{2\mu_0} \frac{\beta}{\omega \epsilon_d} \left[R_d - \frac{1}{2\gamma_d} \sin(2\gamma_d R_d) \right] \quad (2.156)$$

where P_{in} is power passing through unit length in x -direction. And the power that propagates in background is,

$$\begin{aligned} P_{out} &= \int_{-\infty}^{-R_d} S_x dz + \int_{R_d}^{\infty} S_x dz \\ &= \frac{B^2 c^2}{2\mu_0} \frac{\beta}{\omega \epsilon_b} \sin^2(\gamma_d R_d) e^{2\gamma_b R_d} \left\{ \int_{-\infty}^{-R_d} e^{2\gamma_b z} dz + \int_{R_d}^{\infty} e^{-2\gamma_b z} dz \right\} \end{aligned} \quad (2.157)$$

which will give,

$$P_{out} = \frac{B^2 c^2}{2\mu_0} \frac{\beta}{\omega \epsilon_b} \frac{1}{\gamma_b} \sin^2(\gamma_d R_d) \quad (2.158)$$

the total power is $P = P_{in} + P_{out}$,

$$P = \frac{B^2 c^2}{2\mu_0} \frac{\beta}{\omega} \left[\frac{R_d}{\epsilon_d} - \frac{1}{2\gamma_d \epsilon_d} \sin(2\gamma_d R_d) + \frac{1}{\gamma_b \epsilon_b} \sin^2(\gamma_d R_d) \right] \quad (2.159)$$

In Table. 2.2 we show confinement factor, $\Gamma_{in,i} = P_{in,i}/P$, $\Gamma_{out,i} = P_{out,i}/P$ for TM modes where i represents mode index. As we see confinement factor for the fundamental mode, $i = 0$, has highest value and it decreases as mode index increases.

| Mode | Confinement Factor, $\Gamma_{in,i}$ (%) | Confinement Factor, $\Gamma_{out,i}$ (%) |
|--------|---|--|
| TM_0 | 0.99620041870754428 | 3.7995812924557278E-003 |
| TM_1 | 0.98414634565626546 | 1.5853654343734556E-002 |
| TM_2 | 0.96101576805358679 | 3.8984231946413088E-002 |
| TM_3 | 0.92205481633522113 | 7.7945183664778844E-002 |
| TM_4 | 0.85733309547630632 | 0.14266690452369371 |
| TM_5 | 0.74820770690306504 | 0.25179229309693502 |
| TM_6 | 0.56203703788655657 | 0.43796296211344338 |
| TM_7 | 0.28310495087480991 | 0.71689504912519009 |

Table 2.2. Confinement factors for even and odd TM modes for $\tilde{\beta} = 0.6$.

In Figure 2.17 we plotted Poynting vector for first four TM modes for $\tilde{\beta} = 0.6$. $S_{x,0}$, $S_{x,1}$, $S_{x,2}$, and $S_{x,3}$ are the x -component of Poynting vector for TM_0 , TM_1 , TM_2 , and TM_3 modes respectively.

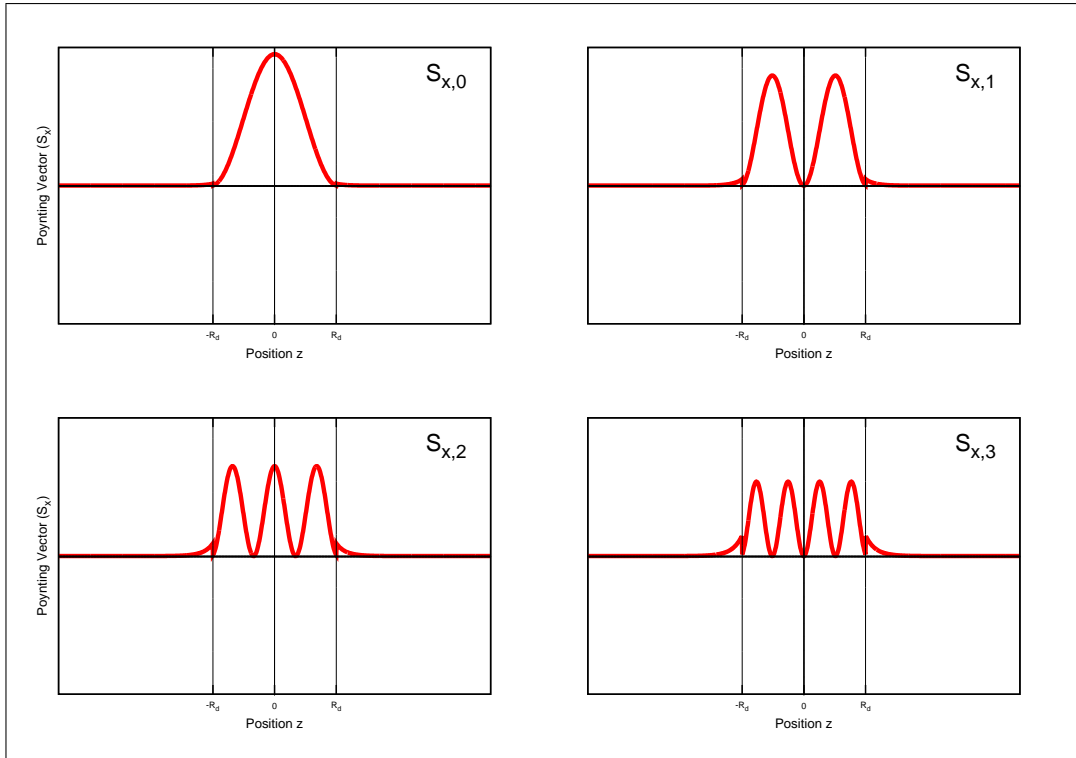


Figure 2.17. Poynting vector profile along z -direction for even, (TM_0 and TM_2), and odd, (TM_1 and TM_3) TM modes of slab waveguide. The dielectric constant of slab is ϵ_d and the dielectric constant of background is ϵ_b . The thickness of slab is $2R_d$.

2.2. Photonic Crystal Theory

To understand propagation of light in dielectric medium we start with microscopic Maxwell's equations,

$$\nabla \cdot \mathbf{E} = \rho/\epsilon_0 \quad (2.160)$$

$$\nabla \cdot \mathbf{B} = 0 \quad (2.161)$$

$$\nabla \times \mathbf{B} = \mu_0 \mathbf{J} + \epsilon_0 \frac{\partial \mathbf{E}}{\partial t} \quad (2.162)$$

$$\nabla \times \mathbf{E} = -\frac{\partial \mathbf{B}}{\partial t} \quad (2.163)$$

where ρ and \mathbf{J} represent charge density and current density. Permittivity of free space and permeability of free space are defined by ϵ_0 and μ_0 . In a material medium \mathbf{D} and \mathbf{H} are defined as,

$$\mathbf{D} \equiv \epsilon_0 \mathbf{E} + \mathbf{P} \quad (2.164)$$

$$\mathbf{H} \equiv \frac{1}{\mu_0} \mathbf{B} - \mathbf{M} \quad (2.165)$$

where \mathbf{P} is the electric polarization of the medium and \mathbf{M} is the magnetization of the medium. Using this definitions, Maxwell's equations for the microscopic fields takes the form of,

$$\nabla \cdot \mathbf{D} = \rho_f \quad (2.166)$$

$$\nabla \cdot \mathbf{B} = 0 \quad (2.167)$$

$$\nabla \times \mathbf{H} = \mathbf{J}_f + \frac{\partial \mathbf{D}}{\partial t} \quad (2.168)$$

$$\nabla \times \mathbf{E} = -\frac{\partial \mathbf{B}}{\partial t} \quad (2.169)$$

which are called Maxwell's equation for macroscopic fields and ρ_f and \mathbf{J}_f are free charge and current density. In a medium with no free charges and current, $\rho_f = 0$, $\mathbf{J}_f = 0$,

Maxwell's equations takes the form of,

$$\nabla \cdot \mathbf{D} = 0 \quad (2.170)$$

$$\nabla \cdot \mathbf{B} = 0 \quad (2.171)$$

$$\nabla \times \mathbf{H} = \frac{\partial \mathbf{D}}{\partial t} \quad (2.172)$$

$$\nabla \times \mathbf{E} = -\frac{\partial \mathbf{B}}{\partial t} \quad (2.173)$$

For non-dispersive and non-lossy materials \mathbf{D} and \mathbf{B} are defined as,

$$\mathbf{D} = \epsilon_0 \epsilon(\mathbf{r}) \mathbf{E} \quad (2.174)$$

$$\mathbf{B} = \mu_0 \mu(\mathbf{r}) \mathbf{H} \quad (2.175)$$

where $\epsilon(\mathbf{r})$ and $\mu(\mathbf{r})$ are permittivity and permeability of space that are functions of position. Now using Equation 2.174 in Equation 2.172 for \mathbf{D} , and taking $\epsilon(\mathbf{r})$ to left-hand side

$$\nabla \times \mathbf{H} = \frac{\partial \mathbf{D}}{\partial t} = \frac{\partial}{\partial t} [\epsilon_0 \epsilon(\mathbf{r}) \mathbf{E}] = \epsilon_0 \epsilon(\mathbf{r}) \frac{\partial \mathbf{E}}{\partial t} \quad (2.176)$$

$$\frac{1}{\epsilon(\mathbf{r})} \nabla \times \mathbf{H} = \epsilon_0 \frac{\partial \mathbf{E}}{\partial t} \quad (2.177)$$

Now taking curl of both side of Equation 2.177 then we have,

$$\nabla \times \left[\frac{1}{\epsilon(\mathbf{r})} \nabla \times \mathbf{H} \right] = \epsilon_0 \frac{\partial}{\partial t} [\nabla \times \mathbf{E}] \quad (2.178)$$

using Equation 2.173 for curl of \mathbf{E} and Equation 2.175 for \mathbf{B} then we will have,

$$\nabla \times \left[\frac{1}{\epsilon(\mathbf{r})} \nabla \times \mathbf{H} \right] = -\epsilon_0 \mu_0 \mu(\mathbf{r}) \frac{\partial^2 \mathbf{H}}{\partial t^2} \quad (2.179)$$

and using $\mu_0\epsilon_0 = 1/c^2$, where c is speed of light in free space, the we finally have

$$\nabla \times \left[\frac{1}{\epsilon(\mathbf{r})} \nabla \times \mathbf{H} \right] + \frac{1}{c^2} \mu(\mathbf{r}) \frac{\partial^2 \mathbf{H}}{\partial t^2} = 0 \quad (2.180)$$

In the same way, we now use Equation 2.175 in Equation 2.173 for B and taking $\mu(\mathbf{r})$ to left-hand side,

$$\nabla \times \mathbf{E} = -\frac{\partial \mathbf{B}}{\partial t} = -\frac{\partial}{\partial t} [\mu_0 \mu(\mathbf{r}) \mathbf{H}] = -\mu_0 \mu(\mathbf{r}) \frac{\partial \mathbf{H}}{\partial t} \quad (2.181)$$

$$\frac{1}{\mu(\mathbf{r})} \nabla \times \mathbf{E} = -\mu_0 \frac{\partial \mathbf{H}}{\partial t} \quad (2.182)$$

Now taking curl of both side of Equation 2.182 then we have,

$$\nabla \times \left[\frac{1}{\mu(\mathbf{r})} \nabla \times \mathbf{E} \right] = -\mu_0 \frac{\partial}{\partial t} [\nabla \times \mathbf{H}] \quad (2.183)$$

using Equation 2.172 for curl of \mathbf{H} and Equation 2.174 for \mathbf{D} then we will have,

$$\nabla \times \left[\frac{1}{\mu(\mathbf{r})} \nabla \times \mathbf{E} \right] = -\epsilon_0 \mu_0 \epsilon(\mathbf{r}) \frac{\partial^2 \mathbf{E}}{\partial t^2} \quad (2.184)$$

and using $\mu_0\epsilon_0 = 1/c^2$, where c is speed of light in free space, the we finally have,

$$\nabla \times \left[\frac{1}{\mu(\mathbf{r})} \nabla \times \mathbf{E} \right] + \frac{1}{c^2} \epsilon(\mathbf{r}) \frac{\partial^2 \mathbf{E}}{\partial t^2} = 0 \quad (2.185)$$

Now we have written Maxwell's equations for magnetic field, \mathbf{H} , and electric field, \mathbf{E} , which are,

$$\nabla \times \left[\frac{1}{\epsilon(\mathbf{r})} \nabla \times \mathbf{H} \right] + \frac{1}{c^2} \mu(\mathbf{r}) \frac{\partial^2 \mathbf{H}}{\partial t^2} = 0 \quad (2.186)$$

$$\nabla \times \left[\frac{1}{\mu(\mathbf{r})} \nabla \times \mathbf{E} \right] + \frac{1}{c^2} \epsilon(\mathbf{r}) \frac{\partial^2 \mathbf{E}}{\partial t^2} = 0 \quad (2.187)$$

Now we need to solve Equation 2.186 and Equation 2.186 for a give periodic dielectric medium to find the magnetic field, \mathbf{H} , and the electric field \mathbf{E} and the corresponding frequencies. A periodic function, $f(\mathbf{r})$ is defined as,

$$f(\mathbf{r}) = f(\mathbf{r} + \mathbf{R}) \quad (2.188)$$

where \mathbf{R} is lattice vector defined as $\mathbf{R} = n_1\mathbf{a}_1 + n_2\mathbf{a}_2 + n_3\mathbf{a}_3$ where \mathbf{a}_1 , \mathbf{a}_2 , and \mathbf{a}_3 are real space basis vectors and n_1 , n_2 , and n_3 are integers.

The Fourier transform of any periodic function, $f(\mathbf{r}) = f(\mathbf{r} + \mathbf{R})$ is defined as,

$$f(\mathbf{r}) = \sum_{\mathbf{G}} f(\mathbf{G})e^{i\mathbf{G}\cdot\mathbf{r}} \quad (2.189)$$

where \mathbf{G} is reciprocal lattice vector defined as $\mathbf{G} = m_1\mathbf{b}_1 + m_2\mathbf{b}_2 + m_3\mathbf{b}_3$ where \mathbf{b}_1 , \mathbf{b}_2 , and \mathbf{b}_3 are reciprocal space basis vectors and m_1 , m_2 , and m_3 are integers. The relation between real lattice vector and reciprocal lattice vector is given by $\mathbf{G} \cdot \mathbf{R} = 2\pi N$. And by using the relation $\mathbf{b}_i \cdot \mathbf{a}_j = 2\pi\delta_{ij}$. The reciprocal basis vectors are found by,

$$\mathbf{b}_1 = 2\pi \frac{\mathbf{a}_2 \times \mathbf{a}_3}{\mathbf{a}_1 \cdot (\mathbf{a}_2 \times \mathbf{a}_3)} \quad (2.190)$$

$$\mathbf{b}_2 = 2\pi \frac{\mathbf{a}_3 \times \mathbf{a}_1}{\mathbf{a}_2 \cdot (\mathbf{a}_3 \times \mathbf{a}_1)} \quad (2.191)$$

$$\mathbf{b}_3 = 2\pi \frac{\mathbf{a}_1 \times \mathbf{a}_2}{\mathbf{a}_3 \cdot (\mathbf{a}_1 \times \mathbf{a}_2)} \quad (2.192)$$

since we have defined reciprocal basis vectors in terms of real space basis vector, we can write reverse Fourier transform of any periodic function as,

$$f(\mathbf{G}) = \frac{1}{V_{cell}} \int_{cell} f(\mathbf{r})e^{-i\mathbf{G}\cdot\mathbf{r}} \quad (2.193)$$

2.2.1. 1D Photonic Crystals

In 1D photonic crystals, the dielectric function depends only one coordinate, and we choose the dielectric function to alternate along z -direction, so $\epsilon(\mathbf{r}) = \epsilon(z)$. The electric field is taken along x -axis, $\mathbf{E}(\mathbf{r}, t) = E_x(z, t)\mathbf{i}$ and magnetic field is taken along y -axis, $\mathbf{H}(\mathbf{r}, t) = H_y(z, t)\mathbf{j}$. The rest of the field components are taken to be zero, $E_y = E_z = H_x = H_z = 0$, putting those in Equation 2.187 we will have,

$$\frac{\partial^2 E_x}{\partial z^2} = \epsilon(z) \frac{1}{c^2} \frac{\partial^2 E_x}{\partial t^2} \quad (2.194)$$

to get rid of time dependence we write

$$E_x(z, t) = \int_{-\infty}^{\infty} E_x(z, \omega) e^{-i\omega t} d\omega \quad (2.195)$$

substituting Equation 2.195 into Equation 2.194 the we have,

$$\int_{-\infty}^{\infty} e^{-i\omega t} \left\{ \frac{\partial^2 E_x}{\partial z^2} + \frac{\omega^2}{c^2} \epsilon(z) E_x \right\} d\omega = 0 \quad (2.196)$$

the The Equation 2.196 is the Fourier transform of the term in curly braces, so this term must be zero for all possible possible ω ,

$$\frac{\partial^2 E_x(z)}{\partial z^2} + \frac{\omega^2}{c^2} \epsilon(z) E_x(z) = 0 \quad (2.197)$$

Now we write electric field $E_x(\mathbf{r})$ as,

$$E_x(\mathbf{r}) = \int_{all \mathbf{q}} E_x(\mathbf{q}) e^{i\mathbf{q} \cdot \mathbf{r}} \quad (2.198)$$

putting this equation into Equation 2.197 then we have,

$$\int_{all\mathbf{q}} d\mathbf{q} E_x(\mathbf{q}) \frac{\partial^2}{\partial z^2} e^{i\mathbf{q}\cdot\mathbf{r}} + \frac{\omega^2}{c^2} \left[\sum_{\mathbf{G}} \epsilon(\mathbf{G}) e^{i\mathbf{G}\cdot\mathbf{r}} \right] \int_{all\mathbf{q}} d\mathbf{q} E_x(\mathbf{q}) e^{i\mathbf{q}\cdot\mathbf{r}} = 0 \quad (2.199)$$

The integral is over the entire reciprocal space. This space can be broken up into cells defined by the basis vectors \mathbf{b}_i ,

$$\int_{all\mathbf{q}} d\mathbf{q} f(\mathbf{q}) \longrightarrow \int_{cell} d\mathbf{k} \sum_{\mathbf{G}} f(\mathbf{k} + \mathbf{G}) \quad (2.200)$$

where \mathbf{k} spans only a unit cell in the reciprocal space, and \mathbf{G} is the set of all reciprocal lattice vectors. Using this in Equation 2.199 we will have,

$$\begin{aligned} & \int_{cell} d\mathbf{k} \sum_{\mathbf{G}} E_x(\mathbf{k} + \mathbf{G}) (-|\mathbf{k} + \mathbf{G}|^2) e^{i(\mathbf{k} + \mathbf{G})\cdot\mathbf{r}} \\ & + \frac{\omega^2}{c^2} \sum_{\mathbf{G}''} \epsilon(\mathbf{G}'') e^{i\mathbf{G}''\cdot\mathbf{r}} \int_{cell} d\mathbf{k} \sum_{\mathbf{G}'} E_x(\mathbf{k} + \mathbf{G}') e^{i(\mathbf{k} + \mathbf{G}')\cdot\mathbf{r}} = 0 \end{aligned} \quad (2.201)$$

and letting $\mathbf{G} = \mathbf{G}' + \mathbf{G}''$ in the second term we will have,

$$\begin{aligned} & \int_{cell} d\mathbf{k} \sum_{\mathbf{G}} e^{i(\mathbf{k} + \mathbf{G})\cdot\mathbf{r}} \\ & \times \left\{ -|\mathbf{k} + \mathbf{G}|^2 E_x(\mathbf{k} + \mathbf{G}) + \frac{\omega^2}{c^2} \sum_{\mathbf{G}'} \epsilon(\mathbf{G} - \mathbf{G}') E_x(\mathbf{k} + \mathbf{G}') \right\} = 0 \end{aligned} \quad (2.202)$$

and using Equation 2.200 in this, then we will get,

$$\int_{all\mathbf{q}} d\mathbf{q} f(\mathbf{q}) \left\{ -|\mathbf{k} + \mathbf{G}|^2 E_x(\mathbf{k} + \mathbf{G}) + \frac{\omega^2}{c^2} \sum_{\mathbf{G}'} \epsilon(\mathbf{G} - \mathbf{G}') E_x(\mathbf{k} + \mathbf{G}') \right\} = 0 \quad (2.203)$$

this is Fourier transform of function in curly braces. To vanish for all \mathbf{k} and \mathbf{G} the expression in curly braces must vanish it self,

$$|\mathbf{k} + \mathbf{G}|^2 E_x(\mathbf{k} + \mathbf{G}) = \frac{\omega^2}{c^2} \sum_{\mathbf{G}'} \epsilon(\mathbf{G} - \mathbf{G}') E_x(\mathbf{k} + \mathbf{G}') \quad (2.204)$$

which is an eigenvalue problem of the form,

$$Ax = \lambda Bx \quad (2.205)$$

where A , B , x , and λ are defined as,

$$\begin{aligned} A_{nm} &= \delta_{nm} |k + \frac{2\pi n}{a}|^2 \\ B_{nm} &= \epsilon(\mathbf{G}_n - \mathbf{G}_m) = \frac{1}{V_{cell}} \int_{cell} \epsilon(\mathbf{r}) e^{-i(\mathbf{G}_n - \mathbf{G}_m) \cdot \mathbf{r}} \\ x_n &= E_{\mathbf{k}}(\mathbf{G}) \\ \lambda &= \frac{\omega^2}{c^2} \end{aligned}$$

now we can solve this eigenvalue problem for a given value of \mathbf{k} to find the eigenvalue $\lambda = \omega^2/c^2$.

2.2.2. 2D Photonic Crystals

In 2-Dimension, electric and magnetic properties of materials defined as $\epsilon(\boldsymbol{\rho})$ and $\mu(\boldsymbol{\rho})$ where $\boldsymbol{\rho} = x\mathbf{i} + y\mathbf{j}$. The electric and magnetic fields are defined as,

$$\mathbf{H}(\boldsymbol{\rho}, t) = \int_{-\infty}^{\infty} \mathbf{H}(\boldsymbol{\rho}, \omega) e^{-i\omega t} d\omega \quad (2.206)$$

$$\mathbf{E}(\boldsymbol{\rho}, t) = \int_{-\infty}^{\infty} \mathbf{E}(\boldsymbol{\rho}, \omega) e^{-i\omega t} d\omega \quad (2.207)$$

Putting this two equation into Equation 2.186 and Equation 2.187 then we have,

$$\int_{-\infty}^{\infty} e^{-i\omega t} d\omega \left\{ \nabla \times \left[\frac{1}{\epsilon(\boldsymbol{\rho})} \nabla \times \mathbf{H} \right] - \frac{\omega^2}{c^2} \mu(\boldsymbol{\rho}) \mathbf{H} \right\} = 0 \quad (2.208)$$

$$\int_{-\infty}^{\infty} e^{-i\omega t} d\omega \left\{ \nabla \times \left[\frac{1}{\mu(\boldsymbol{\rho})} \nabla \times \mathbf{E} \right] - \frac{\omega^2}{c^2} \epsilon(\boldsymbol{\rho}) \mathbf{E} \right\} = 0 \quad (2.209)$$

These two equations are FT of the term in curly braces, to satisfy these this two equation the terms in curly braces must vanish, then we have,

$$\nabla \times \left[\frac{1}{\epsilon(\boldsymbol{\rho})} \nabla \times \mathbf{H} \right] - \frac{\omega^2}{c^2} \mu(\boldsymbol{\rho}) \mathbf{H} = 0 \quad (2.210)$$

$$\nabla \times \left[\frac{1}{\mu(\boldsymbol{\rho})} \nabla \times \mathbf{E} \right] - \frac{\omega^2}{c^2} \epsilon(\boldsymbol{\rho}) \mathbf{E} = 0 \quad (2.211)$$

Now we write $\mathbf{E}(\boldsymbol{\rho})$ and $\mathbf{H}(\boldsymbol{\rho})$ as,

$$\mathbf{H}(\boldsymbol{\rho}) = \int_{all \mathbf{q}} \mathbf{H}(\mathbf{q}) e^{i\mathbf{q} \cdot \boldsymbol{\rho}} \quad (2.212)$$

$$\mathbf{E}(\boldsymbol{\rho}) = \int_{all \mathbf{q}} \mathbf{E}(\mathbf{q}) e^{i\mathbf{q} \cdot \boldsymbol{\rho}} \quad (2.213)$$

and we write periodic functions, $\epsilon(\boldsymbol{\rho})$, $\mu(\boldsymbol{\rho})$, $\eta(\boldsymbol{\rho})$, and $\zeta(\boldsymbol{\rho})$ as,

$$\begin{aligned} \epsilon(\boldsymbol{\rho}) &= \sum_{\mathbf{G}} \epsilon(\mathbf{G}) e^{i\mathbf{G} \cdot \boldsymbol{\rho}} \\ \mu(\boldsymbol{\rho}) &= \sum_{\mathbf{G}} \mu(\mathbf{G}) e^{i\mathbf{G} \cdot \boldsymbol{\rho}} \\ \eta(\boldsymbol{\rho}) &= \sum_{\mathbf{G}} \eta(\mathbf{G}) e^{i\mathbf{G} \cdot \boldsymbol{\rho}} \\ \zeta(\boldsymbol{\rho}) &= \sum_{\mathbf{G}} \zeta(\mathbf{G}) e^{i\mathbf{G} \cdot \boldsymbol{\rho}} \end{aligned} \quad (2.214)$$

where $\eta(\boldsymbol{\rho}) = 1/\epsilon(\boldsymbol{\rho})$ and $\zeta(\boldsymbol{\rho}) = 1/\mu(\boldsymbol{\rho})$. Now we put Equation 2.212, Equation 2.213 and Equation 2.214 into Equation 2.210 and Equation 2.211 and using the equation,

$$\int_{all\mathbf{q}} d\mathbf{q}f(\mathbf{q}) \longrightarrow \int_{cell} d\mathbf{k} \sum_{\mathbf{G}} f(\mathbf{k} + \mathbf{G}) \quad (2.215)$$

then we will finally have, for magnetic field solution and electric field solution,

$$\begin{aligned} \sum_{\mathbf{G}'} \eta(\mathbf{G} - \mathbf{G}')(\mathbf{k} - \mathbf{G}) \times [(\mathbf{k} - \mathbf{G}') \times \mathbf{H}(\mathbf{k} + \mathbf{G}')] \\ + \frac{\omega^2}{c^2} \sum_{\mathbf{G}'} \mu(\mathbf{G} - \mathbf{G}')\mathbf{H}(\mathbf{k} + \mathbf{G}') = 0 \end{aligned} \quad (2.216)$$

$$\begin{aligned} \sum_{\mathbf{G}'} \zeta(\mathbf{G} - \mathbf{G}')(\mathbf{k} - \mathbf{G}) \times [(\mathbf{k} - \mathbf{G}') \times \mathbf{E}(\mathbf{k} + \mathbf{G}')] \\ + \frac{\omega^2}{c^2} \sum_{\mathbf{G}'} \epsilon(\mathbf{G} - \mathbf{G}')\mathbf{E}(\mathbf{k} + \mathbf{G}') = 0 \end{aligned} \quad (2.217)$$

These two equations are generalized eigenvalue problems, and we can solve these equations for a given value of \mathbf{k} to get eigenvalue λ .

2.3. Photonic Crystal Waveguides

Photonic crystal waveguides are formed by breaking symmetry of perfectly periodic photonic crystals. To find band structure of photonic crystal waveguides we need to modify the results that we have found for perfect structure to account for this broken symmetry.

2.3.1. 1D Photonic Crystal Waveguides

We start with Equation 2.186 and Equation 2.187 and substituting,

$$\mathbf{H}(\mathbf{r}, t) = \int_{-\infty}^{\infty} e^{-i\omega t} d\omega \int e^{i\boldsymbol{\beta} \cdot \boldsymbol{\rho}} d^2\boldsymbol{\beta} \left[\int e^{iq_z z} \mathbf{H}(\boldsymbol{\beta}, q_z, \omega) dq_z \right] \quad (2.218)$$

$$\mathbf{E}(\mathbf{r}, t) = \int_{-\infty}^{\infty} e^{-i\omega t} d\omega \int e^{i\boldsymbol{\beta} \cdot \boldsymbol{\rho}} d^2\boldsymbol{\beta} \left[\int e^{iq_z z} \mathbf{E}(\boldsymbol{\beta}, q_z, \omega) dq_z \right] \quad (2.219)$$

where $\boldsymbol{\beta}(x, y)$ is the propagation constant, and $\mathbf{q} = q_z \hat{\mathbf{z}}$ then we will have,

$$\begin{aligned} \sum_{\mathbf{G}'} \eta(\mathbf{G} - \mathbf{G}')(\boldsymbol{\beta} + \mathbf{k} + \mathbf{G}) \times [(\boldsymbol{\beta} + \mathbf{k} + \mathbf{G}') \times \mathbf{H}(\boldsymbol{\beta}, \mathbf{k} + \mathbf{G}')] \\ + \frac{\omega^2}{c^2} \sum_{\mathbf{G}'} \mu(\mathbf{G} - \mathbf{G}') \mathbf{H}(\boldsymbol{\beta}, \mathbf{k} + \mathbf{G}') = 0 \end{aligned} \quad (2.220)$$

$$\begin{aligned} \sum_{\mathbf{G}'} \zeta(\mathbf{G} - \mathbf{G}')(\boldsymbol{\beta} + \mathbf{k} + \mathbf{G}) \times [(\boldsymbol{\beta} + \mathbf{k} + \mathbf{G}') \times \mathbf{E}(\boldsymbol{\beta}, \mathbf{k} + \mathbf{G}')] \\ + \frac{\omega^2}{c^2} \sum_{\mathbf{G}'} \epsilon(\mathbf{G} - \mathbf{G}') \mathbf{E}(\boldsymbol{\beta}, \mathbf{k} + \mathbf{G}') = 0 \end{aligned} \quad (2.221)$$

We finally get a generalized eigenvalue equation in the form of $Ax = \lambda Bx$ for both electric field and magnetic field. These two equation can be solved to find eigenvalue, λ where we defined eigenvalue as $\lambda = \omega^2/c^2$.

2.3.2. 2D Photonic Crystal waveguides

Again we start with Equation 2.186 and Equation 2.187 and substituting the following two equation for the fields,

$$\mathbf{H}(\mathbf{r}, t) = \int_{-\infty}^{\infty} e^{-i\omega t} d\omega \int e^{i\beta z} d\beta \left[\int e^{i\mathbf{q}\cdot\boldsymbol{\rho}} \mathbf{H}(\mathbf{q}, \beta, \omega) d^2\mathbf{q} \right] \quad (2.222)$$

$$\mathbf{E}(\mathbf{r}, t) = \int_{-\infty}^{\infty} e^{-i\omega t} d\omega \int e^{i\beta z} d\beta \left[\int e^{i\mathbf{q}\cdot\boldsymbol{\rho}} \mathbf{E}(\mathbf{q}, \beta, \omega) d^2\mathbf{q} \right] \quad (2.223)$$

where $\boldsymbol{\rho}(x, y) = x\hat{\mathbf{i}} + y\hat{\mathbf{j}}$, and $\mathbf{q} = \mathbf{q} + \mathbf{G} = q_x\hat{\mathbf{i}} + q_y\hat{\mathbf{j}}$. The structure is periodic in x - and y -direction so the dielectric and magnetic property function are defined as,

$$\begin{aligned} \epsilon(\boldsymbol{\rho}) &= \sum_{\mathbf{G}} \epsilon(\mathbf{G}) e^{i\mathbf{G}\cdot\boldsymbol{\rho}} \\ \mu(\boldsymbol{\rho}) &= \sum_{\mathbf{G}} \mu(\mathbf{G}) e^{i\mathbf{G}\cdot\boldsymbol{\rho}} \end{aligned} \quad (2.224)$$

after substitution, we will have, for magnetic field and electric field,

$$\begin{aligned} \sum_{\mathbf{G}'} \eta(\mathbf{G} - \mathbf{G}') (\boldsymbol{\beta} + \mathbf{k} + \mathbf{G}) \times [(\boldsymbol{\beta} + \mathbf{k} + \mathbf{G}') \times \mathbf{H}(\boldsymbol{\beta}, \mathbf{k} + \mathbf{G}')] \\ + \frac{\omega^2}{c^2} \sum_{\mathbf{G}'} \mu(\mathbf{G} - \mathbf{G}') \mathbf{H}(\boldsymbol{\beta}, \mathbf{k} + \mathbf{G}') = 0 \end{aligned} \quad (2.225)$$

$$\begin{aligned} \sum_{\mathbf{G}'} \zeta(\mathbf{G} - \mathbf{G}') (\boldsymbol{\beta} + \mathbf{k} + \mathbf{G}) \times [(\boldsymbol{\beta} + \mathbf{k} + \mathbf{G}') \times \mathbf{E}(\boldsymbol{\beta}, \mathbf{k} + \mathbf{G}')] \\ + \frac{\omega^2}{c^2} \sum_{\mathbf{G}'} \epsilon(\mathbf{G} - \mathbf{G}') \mathbf{E}(\boldsymbol{\beta}, \mathbf{k} + \mathbf{G}') = 0 \end{aligned} \quad (2.226)$$

where $\mathbf{k} = k_x\hat{x} + k_y\hat{y}$, $\boldsymbol{\beta} = \beta\hat{z}$, and $\eta = 1/\eta$, $\zeta = 1/\mu$. This two equations are again generalized eigenvalue problem in the form of $Ax = \lambda Bx$. For purely dielectric medium, setting $\mu(\mathbf{r}) = 1/\zeta = 1$, we can solve these two equation for a given value of $\boldsymbol{\beta}$ and \mathbf{k} to find eigenvalue, λ .

2.4. Adiabatic Coupling

In this section we want to give a short explanation about adiabatic theorem that will be the main idea used in this thesis. Suppose the Hamiltonian changes gradually from an initial state H_i to a final state H_f . The adiabatic theorem states that if the particle was initially in the n th eigenstate of H_i , it will be carried into the n th eigenstate of H_f . If the Hamiltonian is independent of time, then a particle which starts in the n th eigenstate, ψ_n , (Griffiths (2004))

$$H\psi_n = E_n\psi_n \quad (2.227)$$

remains in the n th eigenstate with picking a phase factor,

$$\Psi_n(t) = \psi_n e^{(-E_n t/\hbar)} \quad (2.228)$$

Now if the Hamiltonian changes with time, then the eigenfunctions and the eigenvalues will be time dependent,

$$H(t)\psi_n(t) = E_n(t)\psi_n(t) \quad (2.229)$$

so the general solution to time-dependent Schrödinger equation

$$i\hbar \frac{\partial}{\partial t} \Psi(t) = H(t)\Psi(t) \quad (2.230)$$

can be expressed as a linear combination of them,

$$\Psi(t) = \sum_n c_n(t) \psi_n(t) e^{i\theta_n(t)} \quad (2.231)$$

where $\theta_n(t)$ is,

$$\theta_n(t) = -\frac{1}{\hbar} \int_0^t E_n(t') dt' \quad (2.232)$$

Using time-dependent perturbation theory, substituting time-dependent solutions into Schrödinger equation, we finally will have,

$$\dot{c}_m(t) = -c_m \langle \psi_m | \dot{\psi}_m \rangle - \sum_{nm} c_n \frac{\langle \psi_m | \dot{H} | \psi_n \rangle}{E_n - E_m} e^{-\frac{i}{\hbar} \int_0^t [E_n(t') - E_m(t')] dt'} \quad (2.233)$$

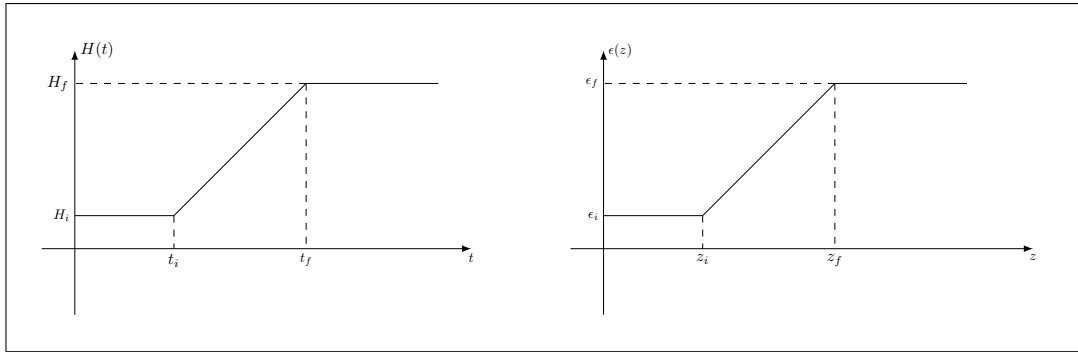


Figure 2.18. A graphical representation of adiabatic transition of the Hamiltonian from H_i to H_f . The graph on the left hand represents adiabatic transition of a particle. The graph on the right-hand side represents the adiabatic transition of a electromagnetic mode coupling from an initial state to a final state.

In the Figure 2.18 we have shown a model to represent the adiabatic transition of state that is its Hamiltonian gradually changing from an initial state H_i to a final state H_f . In quantum mechanics for the systems that the Hamiltonian is changing with time, $H(t)$ (left graph), rate of change of Hamiltonian is $\frac{dH(t)}{dt} = \frac{H_f(t_f) - H_i(t_i)}{t_f - t_i}$. As the time interval goes to zero, $\Delta t \rightarrow 0$, the rate of change of Hamiltonian will be infinite, the system will be in a superposition of all possible eigenstate. As the time interval increases the rate of change is decreasing. In the limit $\Delta t \rightarrow \infty$ the time derivative of Hamiltonian goes to zero. In this way the eigenstate will remain same as the Hamiltonian changes. As an example, suppose we have a particle trapped in infinite square well with well width a and the particle start in the ground state wave function ψ_0 , if we suddenly increase the well width to $2a$ then the new wave function will be the the superposition of all possible

eigenstate. If the wall width is gradually changed from a to $2a$ then the particle will remain in the same eigenstate. Now turning back to Equation 2.233, the adiabatic approximation says if \dot{H} is too small then we can drop the second term in Equation 2.233 and leaving

$$\dot{c}_m(t) = -c_m \langle \psi_m | \dot{\psi}_m \rangle \quad (2.234)$$

and this equation has the solution

$$c_m(t) = c_m(0) e^{i\gamma_m(t)} \quad (2.235)$$

where $\gamma_m(t)$ is

$$\gamma_m(t) = i \int_0^t \langle \psi_m(t') | \frac{\partial}{\partial t'} \psi_m(t') \rangle dt' \quad (2.236)$$

this equation states that if the particle starts in the n th eigenstate, then,

$$\Psi_n(t) = e^{i\theta_n(t)} e^{i\gamma_n(t)} \psi_n(t) \quad (2.237)$$

so it remains in the n th eigenstate, picking up only a couple of phase factors, (Griffiths, 2004).

In electromagnetic, source free Maxwell's equation can be written in the form of Schrödinger equation used in quantum mechanics, (Johnson et al. (2002)),

$$\hat{A}|\psi\rangle = -i\frac{\partial}{\partial z}\hat{B}|\psi\rangle \quad (2.238)$$

where $|\psi\rangle$ is the column vector,

$$|\psi\rangle = \begin{pmatrix} \mathbf{E}_t(x, y, z) \\ \mathbf{H}_t(x, y, z) \end{pmatrix} e^{-i\omega t} \quad (2.239)$$

where \hat{A} and \hat{B} are defined as,

$$\hat{A} = \begin{pmatrix} \frac{\omega\epsilon}{c} - \frac{c}{\omega}\nabla_t \times \frac{1}{\mu}\nabla_t \times & 0 \\ 0 & \frac{\omega\mu}{c} - \frac{c}{\omega}\nabla_t \times \frac{1}{\epsilon}\nabla_t \times \end{pmatrix} \quad (2.240)$$

$$\hat{B} = \begin{pmatrix} 0 & -\hat{\mathbf{z}} \times \\ \hat{\mathbf{z}} \times & 0 \end{pmatrix} \quad (2.241)$$

If we compare Equation 2.238 with Schrödinger equation,

$$H(t)\Psi(t) = i\hbar\frac{\partial}{\partial t}\Psi(t) \quad (2.242)$$

we see that in quantum mechanic the wave function is a complex scalar function while in electrodynamic the wave function is a vector field with a real part that is meaningful physically and an imaginary part. In quantum and electrodynamic, both system are determined by an eigenvalue equation. The Hamiltonian operator \hat{H} in quantum mechanics is a function of potential and the differential operator \hat{A} in electrodynamic is a function of dielectric function. In electrodynamic, time derivative wave function is now taken with respect to space.

As derived in (Johnson et al., 2002), suppose we have coupled linear differential

equation in $c_n(z)$ describing the solution of a system that is changing with position, z ,

$$\frac{dc_n(z)}{dz} = \sum_{m \neq n} C_{mn}(z) \left\langle \frac{\partial \hat{X}}{\partial z} \right\rangle \exp \left(i \int^z \Delta\beta_{mn}(z') dz' \right) c_m(z) \quad (2.243)$$

where C_{nm} is coefficient matrix, \hat{X} is an operator, and $\Delta\beta_{nm}$ is phase mismatch. To see L dependence of this equation as the length of taper becomes too large, we introduce a scaled coordinate $s = z/L$, in this case the equation becomes,

$$\frac{dc_n(s)}{ds} = \sum_{m \neq n} C_{mn}(s) \left\langle \frac{\partial \hat{X}}{\partial s} \right\rangle \exp \left(iL \int^s \Delta\beta_{mn}(s') ds' \right) c_m(s) \quad (2.244)$$

As we have shown on the right-hand side of Figure 2.18, for electromagnetic case this time the Hamiltonian of the system depends on the position. When a propagating mode come across a medium that has different dielectric properties, the rate of change of dielectric function is given by $\frac{d\epsilon(z)}{dz} = \frac{\epsilon_f(z_f) - \epsilon_i(z_i)}{z_f - z_i}$. As can be seen from the right diagram of Figure 2.18, in the direct transition case $\Delta z \rightarrow 0$ the rate of change of dielectric function goes to infinity, in this case the electromagnetic state will not have enough time to respond this sudden change, so the excited mode in the final state will be the superposition of all possible modes. In the adiabatic transition case $\Delta z \rightarrow \infty$, the rate of change of dielectric function goes to zero. So the system will remain in its initial eigenstate.

Now turning back to the Equation 2.244, as we see the only L dependence appears in the exponent. Taking the $L \rightarrow \infty$ limit, because in that limit the integration in exponent goes to zero. As we move toward the adiabatic limit the solution to the generalized differential equation is constant, $c_n(z) = c_n(0)$.

So to keep the solution of generalized differential equation constant we need to change the waveguide geometry slowly enough to keep mode profile constant to couple light without loss.

2.5. Finite Difference Time Domain Method

In this thesis we used finite-difference time-domain (FDTD) method (Taflove and Hagness, 2005) to simulate the propagation of electromagnetic field in a dielectric medium using a freely available software package MEEP (Oskooi et al., 2010). So we will give a short introduction of FDTD method. Finite-difference time-domain method is a numerical method that is used to solve Maxwell's curl equations by dividing space and time into small grid. The solution method introduced by (Yee, 1966) is based on discretizing Maxwell's curl equation in time and space. And the discretized differential equations are solved by evolving both time and space.

We start with two Maxwell's curl equations for electric field and magnetic fields,

$$\frac{\partial \mathbf{H}}{\partial t} = -\frac{1}{\mu_0 \mu} \nabla \times \mathbf{E} \quad (2.245)$$

$$\frac{\partial \mathbf{E}}{\partial t} = \frac{1}{\epsilon_0 \epsilon} \{ \nabla \times \mathbf{H} - \mathbf{J}_{source} \} \quad (2.246)$$

where \mathbf{J}_{source} is current source. After taking the curl of both field then we will have six scalar equation for each component,

$$\frac{\partial H_x}{\partial t} = \frac{1}{\mu_0 \mu} \left\{ \frac{\partial E_y}{\partial z} - \frac{\partial E_z}{\partial y} \right\} \quad (2.247)$$

$$\frac{\partial H_y}{\partial t} = \frac{1}{\mu_0 \mu} \left\{ \frac{\partial E_z}{\partial x} - \frac{\partial E_x}{\partial z} \right\} \quad (2.248)$$

$$\frac{\partial H_z}{\partial t} = \frac{1}{\mu_0 \mu} \left\{ \frac{\partial E_x}{\partial y} - \frac{\partial E_y}{\partial x} \right\} \quad (2.249)$$

$$\frac{\partial E_x}{\partial t} = \frac{1}{\epsilon_0 \epsilon} \left\{ \frac{\partial H_z}{\partial y} - \frac{\partial H_y}{\partial z} - J_{x,source} \right\} \quad (2.250)$$

$$\frac{\partial E_y}{\partial t} = \frac{1}{\epsilon_0 \epsilon} \left\{ \frac{\partial H_x}{\partial z} - \frac{\partial H_z}{\partial x} - J_{y,source} \right\} \quad (2.251)$$

$$\frac{\partial E_z}{\partial t} = \frac{1}{\epsilon_0 \epsilon} \left\{ \frac{\partial H_y}{\partial x} - \frac{\partial H_x}{\partial y} - J_{z,source} \right\} \quad (2.252)$$

and for one-dimension, lets consider the electromagnetic field is travelling in the x -direction and we set electric field in the z -direction and we set magnetic field in the y -direction. So the partial derivative of field component with respect to y - and z -direction

vanishes leaving only two equations,

$$\frac{\partial H_y}{\partial t} = \frac{1}{\mu_0 \mu} \frac{\partial E_z}{\partial x} \quad (2.253)$$

$$\frac{\partial E_z}{\partial t} = \frac{1}{\epsilon_0 \epsilon} \left\{ \frac{\partial H_y}{\partial x} - J_{z,source} \right\} \quad (2.254)$$

now we need to understand notation that is used by Yee. A point in discretized space is represented by $(i, j, k) = (i\Delta x, j\Delta y, k\Delta z)$ where i, j, k are integers, $\Delta x, \Delta y, \Delta z$ are increments in coordinates x, y, z . Keeping time step constant, the finite-difference expression for space derivative in the x -direction of electric field and magnetic field can be written as,

$$\frac{\partial E_z}{\partial x}(i\Delta x, j\Delta y, k\Delta z, n\Delta t) = \frac{E_z|_{i+1/2,j,k}^n - E_z|_{i-1/2,j,k}^n}{\Delta x} \quad (2.255)$$

$$\frac{\partial H_y}{\partial x}(i\Delta x, j\Delta y, k\Delta z, n\Delta t) = \frac{H_y|_{i+1/2,j,k}^n - H_y|_{i-1/2,j,k}^n}{\Delta x} \quad (2.256)$$

where n is integer and Δt is increment in time t . This time keeping space constant, partial derivative with respect to time of electric field and magnetic field are defined as,

$$\frac{\partial E_z}{\partial t}(i\Delta x, j\Delta y, k\Delta z, n\Delta t) = \frac{E_z|_{i,j,k}^{n+1/2} - E_z|_{i,j,k}^{n-1/2}}{\Delta t} \quad (2.257)$$

$$\frac{\partial H_y}{\partial t}(i\Delta x, j\Delta y, k\Delta z, n\Delta t) = \frac{H_y|_{i,j,k}^{n+1/2} - H_y|_{i,j,k}^{n-1/2}}{\Delta t} \quad (2.258)$$

now putting Equation 2.255 and Equation 2.258 into Equation 2.253 and putting Equation 2.256 and Equation 2.257 into Equation 2.254 then we will have,

$$\frac{H_y|_{i,j,k}^{n+1/2} - H_y|_{i,j,k}^{n-1/2}}{\Delta t} = \frac{1}{\mu_0 \mu_{i+1/2,j,k}} \frac{E_z|_{i+1/2,j,k}^n - E_z|_{i-1/2,j,k}^n}{\Delta x} \quad (2.259)$$

$$\frac{E_z|_{i,j,k}^{n+1/2} - E_z|_{i,j,k}^{n-1/2}}{\Delta t} = \frac{1}{\epsilon_0 \epsilon_{i+1/2,j,k}} \left\{ \frac{H_y|_{i+1/2,j,k}^n - H_y|_{i-1/2,j,k}^n}{\Delta x} - J_z|_{i+1/2,j,k} \right\} \quad (2.260)$$

or more clearly,

$$H_y|_{i,j,k}^{n+1/2} = H_y|_{i,j,k}^{n-1/2} + \frac{\Delta t}{\mu_0 \mu_{i+1/2,j,k} \Delta x} \{ E_z|_{i+1/2,j,k}^n - E_z|_{i-1/2,j,k}^n \} \quad (2.261)$$

$$E_z|_{i,j,k}^{n+1/2} = E_z|_{i,j,k}^{n-1/2} + \frac{\Delta t}{\epsilon_0 \epsilon_{i+1/2,j,k} \Delta x} \{ H_y|_{i+1/2,j,k}^n - H_y|_{i-1/2,j,k}^n - J_z|_{i+1/2,j,k} \} \quad (2.262)$$

Where J_z is the current source in the z -direction. As can be seen from Equation 2.261 to find magnetic field at time step $n + 1/2$ and space point i, j, k we need to know electric field at space point $i + 1/2, j, k$ and $i - 1/2, j, k$ and time step n , in addition we need to know magnetic field at time step $n - 1/2$ and space point i, j, k . In similar way, as can be seen from Equation 2.262 to find the electric field at time step $n + 1/2$ and space point i, j, k we need to know magnetic field at space point $i + 1/2, j, k$ and $i - 1/2, j, k$ and time step n , in addition we need to know electric field at time step $n - 1/2$ and space point i, j, k .

CHAPTER 3

IMPROVING COUPLING EFFICIENCY

In this chapter we are going to study coupling process between dielectric structures made by single-slab waveguides also called strip waveguides. The chapter is structured as follows: in the first section we will study coupling process from a thin single-slab waveguide to a thick single-slab waveguide and coupling process from thick single-slab waveguide to thin single-slab waveguide. For both transition type, we will couple mode directly which is also called butt-coupling and we will couple mode by using a transition region which is called adiabatic transition. In both cases the effect of introducing transition region on excited mode profile will be studied. In the second section the coupling coefficient of excited modes will be calculated for both butt-coupling and adiabatic coupling case with continuous source. The mode profiles generated by Gaussian source will be given for both butt-coupling and adiabatic coupling cases.

3.1. Coupling Process

How does a guided mode behave when it comes to an interface of two different waveguides that have different geometric parameters? Another question about the coupling process is which parameters affect the coupling efficiency? Ideally one, of course, would like to have completely lossless coupling between the two waveguides for optoelectronic applications.

The transition from the input to the output waveguide can be made by two different ways. The first one is an abrupt transition in which the two waveguides are simply brought in contact with each other with their symmetry axes aligned. The second way is a gradual transition in which the input waveguide profile gradually morphs into that of the output waveguide. As the transition length becomes larger, this would approach the so-called adiabatic transition, provided certain conditions are met in the intermediate transition region. As the adiabatic theorem states (Griffiths, 2004), slowly changing a physical system (the thickness of waveguide in this case) will transform the mode so that the coupling without loss can be achieved.

To understand the guided mode behaviour when it comes across an interface, and

to find out which parameters are responsible for coupling efficiency, we investigated the simplest possible case: two simple waveguide structures with different core thickness. We will use the finite-difference time-domain (FDTD) simulation and look at the mode profiles along the input and output waveguides.

3.1.1. Coupling from Thin to Thick Waveguides

We start by exploring the coupling of electromagnetic (EM) modes between two different single-slab waveguides. The waveguide structure is shown in the Figure 3.1 which is made by two single-slab waveguides that are butt-joined. The single slab on the left hand side has thickness of $d_{in} = 2$ with dielectric constant $\epsilon_a = 13$. The single-slab on the right hand side has thickness of $d_{out} = 12$ with dielectric constant $\epsilon_a = 13$. Both single-slabs are immersed in a background that has a dielectric constant of $\epsilon_b = 2.25$. All lengths are in units of $a/2\pi$, where a is the lattice constant, and all frequencies are in units of $2\pi c/a$.

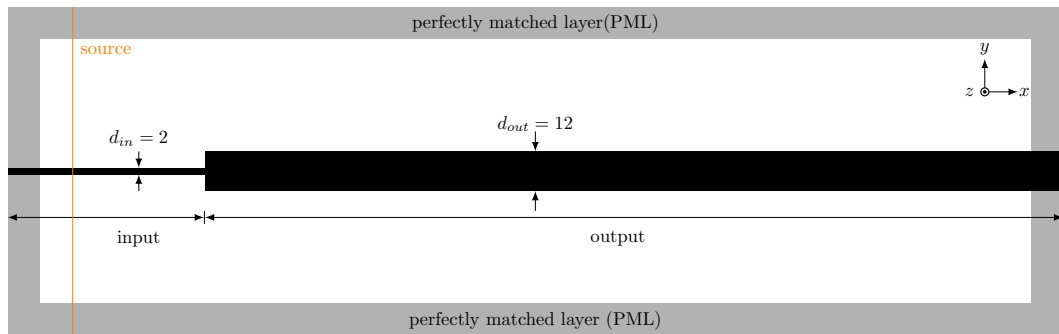


Figure 3.1. The single-slab waveguide on the left-hand side has thickness of $d_{in} = 2$ with $\epsilon_a = 13$, the single-slab waveguide on the right-hand side has thickness of $d_{out} = 12$ with $\epsilon_a = 13$. Background has dielectric constant of $\epsilon_b = 2.25$. Two slabs are butt joined.

In Figure 3.2 we see the band structure of single-slab waveguide calculated for transverse electric (TE) modes. Black solid lines represent the band structure of waveguide with thickness $d_{out} = 12$, and dielectric constant $\epsilon_a = 13$. The background material has dielectric constant of $\epsilon_b = 2.25$.

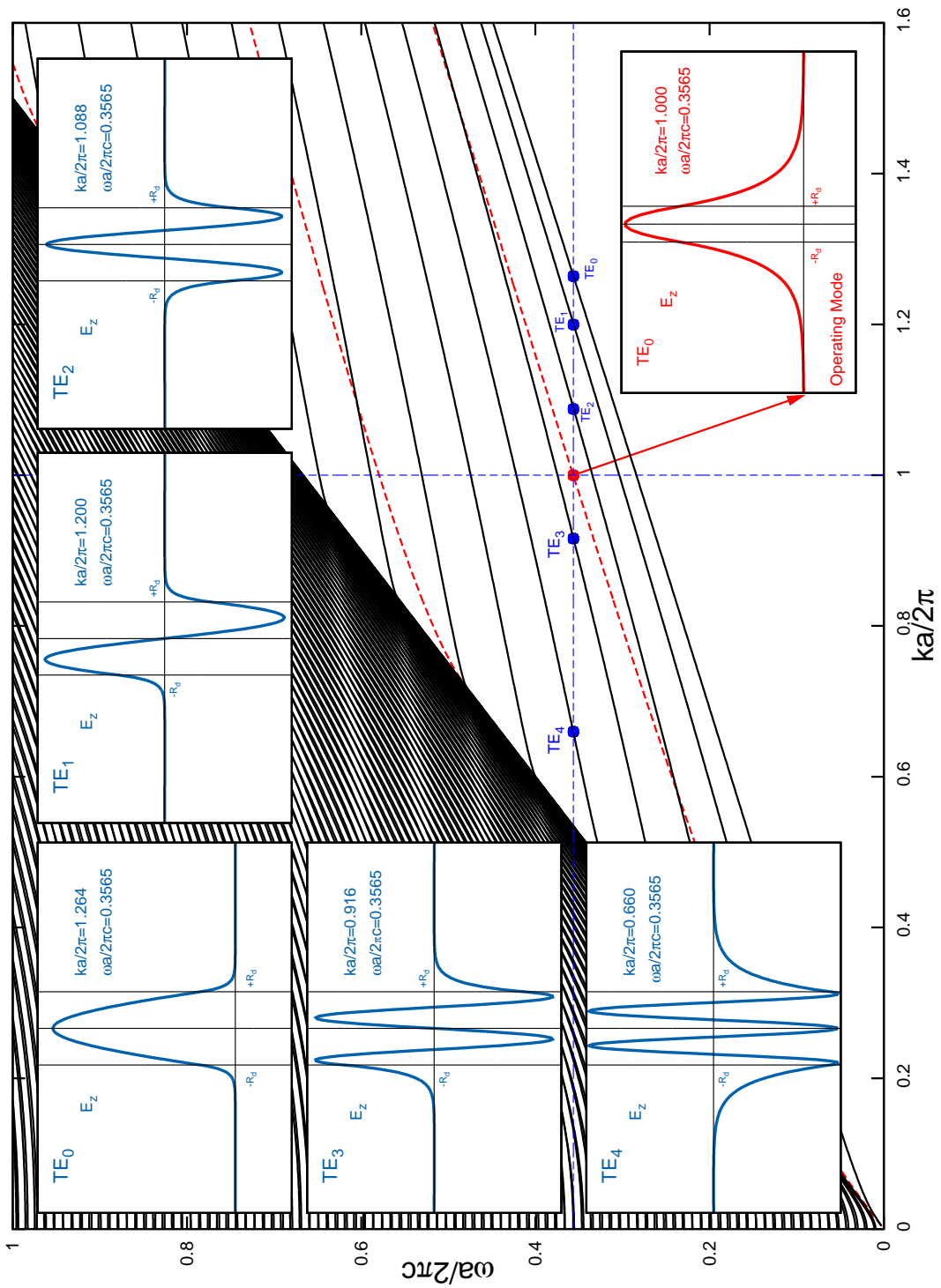


Figure 3.2. Single-slab waveguide band structure for transverse electric (TE) mode. Red dashed lines represent the first three guided modes of single-slab of thickness $d_{in} = 2$ and dielectric constant of $\epsilon_a = 13$, black solid lines represent the band structure of waveguide that has thickness of $d_{out} = 12$ and dielectric constant $\epsilon_a = 13$. The background for both waveguide has dielectric constant of $\epsilon_b = 2.25$.

The red dashed lines represent the first three guided modes of the input single-slab waveguide with thickness $d_{in} = 2$, and dielectric constant $\epsilon_a = 13$. In the same figure (Figure 3.2), the intersection of horizontal and vertical blue dashed lines indicate our operating mode. The operating mode profile of input waveguide is shown on the right lower corner of Figure 3.2. At the operating frequency, $\tilde{\omega} = \frac{\omega a}{2\pi c} = 0.3565$, we also show first five guided mode profiles, (E_z) , of the output waveguide. At the operating frequency $\tilde{\omega} = 0.3565$ with wave vector $\tilde{k} = 1.000$ in the input region, there are five guided modes in the output region. Their wave vectors are, starting from the lowest order mode, $\tilde{k}_0 = 1.264$, $\tilde{k}_1 = 1.200$, $\tilde{k}_2 = 1.088$, $\tilde{k}_3 = 0.916$, and $\tilde{k}_4 = 0.660$. Three of them are even, TE_0 , TE_2 , TE_4 , and two, TE_1 , TE_3 , are odd modes. If we send first guided mode from input part (lowest red curve), which has frequency $\tilde{\omega} = 0.3565$ and wave vector $\tilde{k} = 1.000$, it will propagate along input part without any loss because its propagation along other directions is forbidden. When it comes to interface this mode can excite all guided modes below the light line. Coupling of those modes depends on the spatial symmetry of the incident mode. If the incident mode is odd, it will couple to the two odd modes supported by the output waveguide at that frequency, and if the incident mode is even, then it will couple to three guided even modes TE_0 , TE_2 , TE_4 supported by the output waveguide.

Now we will send the first guided mode of input waveguide and find modes that it excites in the output waveguide. The first simulation is done with an abrupt transition between the two waveguides. Then we will introduce a taper region between two waveguides and look at the effect of this intermediate region on modes excited in the output waveguide. In the case of an abrupt transition, the sudden change in waveguide geometry results in the some reflection at the interface and some scattering to the background, resulting in loss in the energy transmitted to the guided mode in the second waveguide. When the intermediate region is introduced, this transition will be more smooth, thereby preventing most of the energy loss at the interface. By linearly changing the waveguide thickness from d_{in} to d_{out} over a transition length L of a few wavelengths, the transmission losses can be drastically reduced.

In Figure 3.3 we see z -component of electric field, E_z , distribution along waveguide structure for TE mode. A continuous mode source is used to excite the the operation mode. The mode profile is taken at a time step when the propagation of mode reaches steady state. We first run simulation without taper region and find field distribution along waveguide. As we see from mode profile, some of the mode is radiated to background of the waveguide structure and some is reflected back at the interface. The excited propaga-

tion mode profile in output waveguide is multi-mode, which is the superposition of three guided even modes.

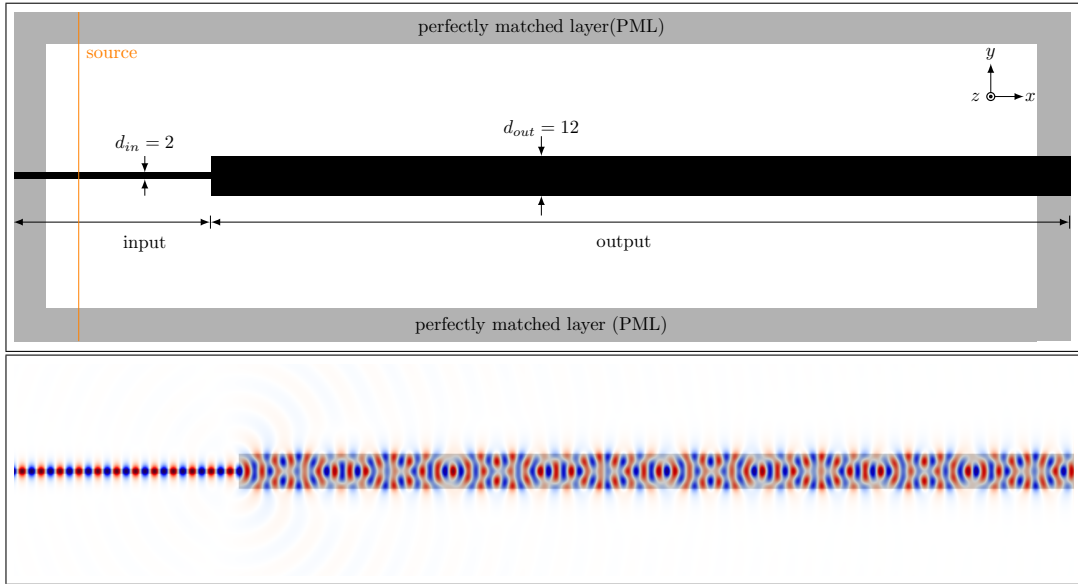


Figure 3.3. The single-slab waveguide on the left-hand side has thickness of $d_{in} = 2$ with $\epsilon_a = 13$, the single-slab waveguide on the right-hand side has thickness of $d_{out} = 12$ with $\epsilon_a = 13$. Background has dielectric constant of $\epsilon_b = 2.25$. FDTD simulation of z - component of electric field E_z of TE mode profile along waveguide without taper region.

In Figure 3.4 we see the dielectric profile of waveguide shown in Figure 3.1. In this figure, we introduced a transition region, a linear taper with $L = 20a$ between input and output waveguides. This time we want to demonstrate the effect of using taper region whose thickness is gradually changing from $d_{in} = 2$, to $d_{out} = 12$.

In Figure 3.4 we see the FDTD simulation of z -component of electric field (E_z) for TE mode profile. As we clearly see, the propagating mode in output region is single mode. By introducing the taper region, we force the incoming fundamental mode to couple to the outgoing fundamental mode, which is the first guided mode of output waveguide. The mode profile remain essentially the same as it propagates from input region to output region. The mode size is also converted slowly. Coupling to a single mode is important because it will prevent signal distortion as different modes will likely have different group velocities, resulting in modal dispersion.

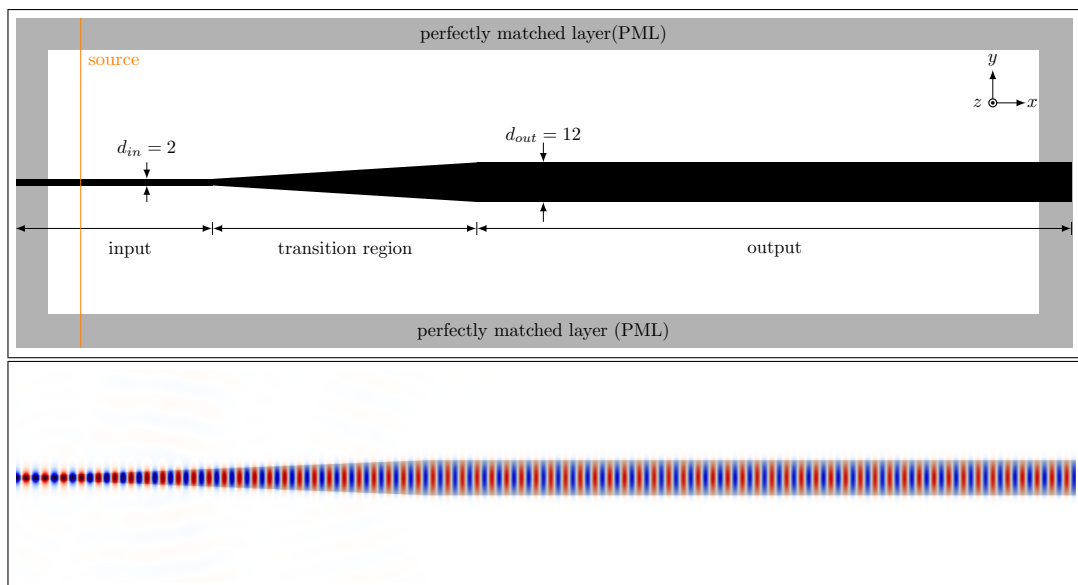


Figure 3.4. The slab on the left-hand side has thickness of $d_{in} = 2$ with dielectric constant of $\epsilon_a = 13$, the slab waveguide on the right-hand side has thickness of $d_{out} = 12$ with dielectric constant of $\epsilon_a = 13$. Background has dielectric constant of $\epsilon_b = 2.25$. FDTD simulation of z -component of electric field E_z of TE mode profile along waveguide with taper region introduced.

3.1.2. Coupling from Thick to Thin Waveguides

Coupling from a thick single-slab waveguide to a thin single-slab waveguide can give us a more clear explanation about the coupling process. In this waveguide structure at the operating frequency, there is only one guided mode supported by output waveguide. So we will use this waveguide structure to show how modes couple to each other, and under what conditions this coupling process take place. To see how coupling of modes work we will use the waveguide structure shown in Figure 3.5. This waveguide consist of an input part with thickness of $d_{in} = 12$ and dielectric constant of $\epsilon_a = 13$, and output part with thickness of $d_{out} = 2$ with dielectric constant of $\epsilon_a = 13$. Both waveguides are immersed in a background material with dielectric constant $\epsilon_b = 2.25$.

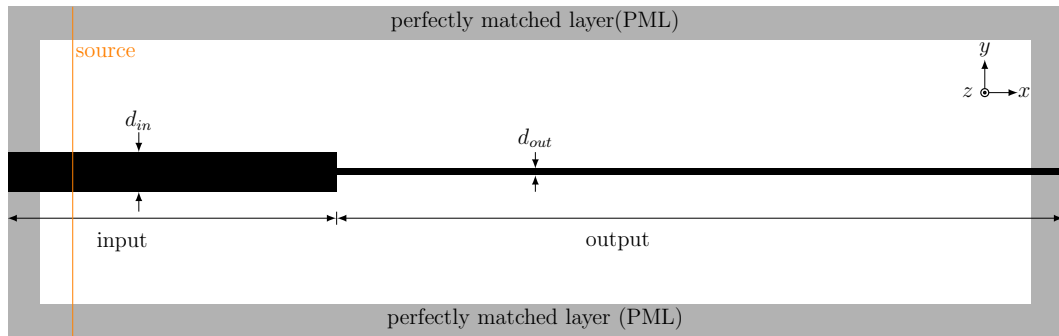


Figure 3.5. Dielectric structure of butt joined single-slab waveguide, input part thickness $d_{in} = 12$ with $\epsilon_a = 13$, output part thickness is $d_{out} = 2$ with $\epsilon_a = 13$. Background has dielectric constant of $\epsilon_b = 2.25$.

The band structure of both single-slab waveguides is shown on the same graph in Figure 3.6. In this figure, black solid lines represent the band structure of single-slab waveguide with thickness of $d_{out} = 2$ and dielectric constant of $\epsilon_a = 13$. We also show first guided mode (the operating mode) of single-slab waveguide with thickness of $d_{in} = 12$ and dielectric constant of $\epsilon_a = 13$, which is shown by red dashed lines. The intersection of horizontal and vertical blue dashed lines represent our operating frequency $\tilde{\omega} = 0.3565$ and wave vector $\tilde{k} = 1.264$. At this frequency the output waveguide has only one guided mode, and it is the fundamental mode (TE_0) of output waveguide. On the right lower corner of this graph we showed the operating mode profile. On the left upper corner we showed the guided mode profile of output waveguide at the operating frequency. Zoomed section around operating frequency and wave vector is also shown on the upper right corner.

As can be seen in Figure 3.6, the operating mode will excite the first guided mode (TE_0) of output waveguide which has frequency $\tilde{\omega} = 0.3565$ and wave vector $\tilde{k} = 1.000$. And the radiation modes will also be excited at the interface between two waveguides. To illustrate this we will send input guided mode and look at the excited mode profile that is propagating in output waveguide and the radiation mode that are propagating in background and the modes that are reflected back at interface for both structure without and with taper region introduced.

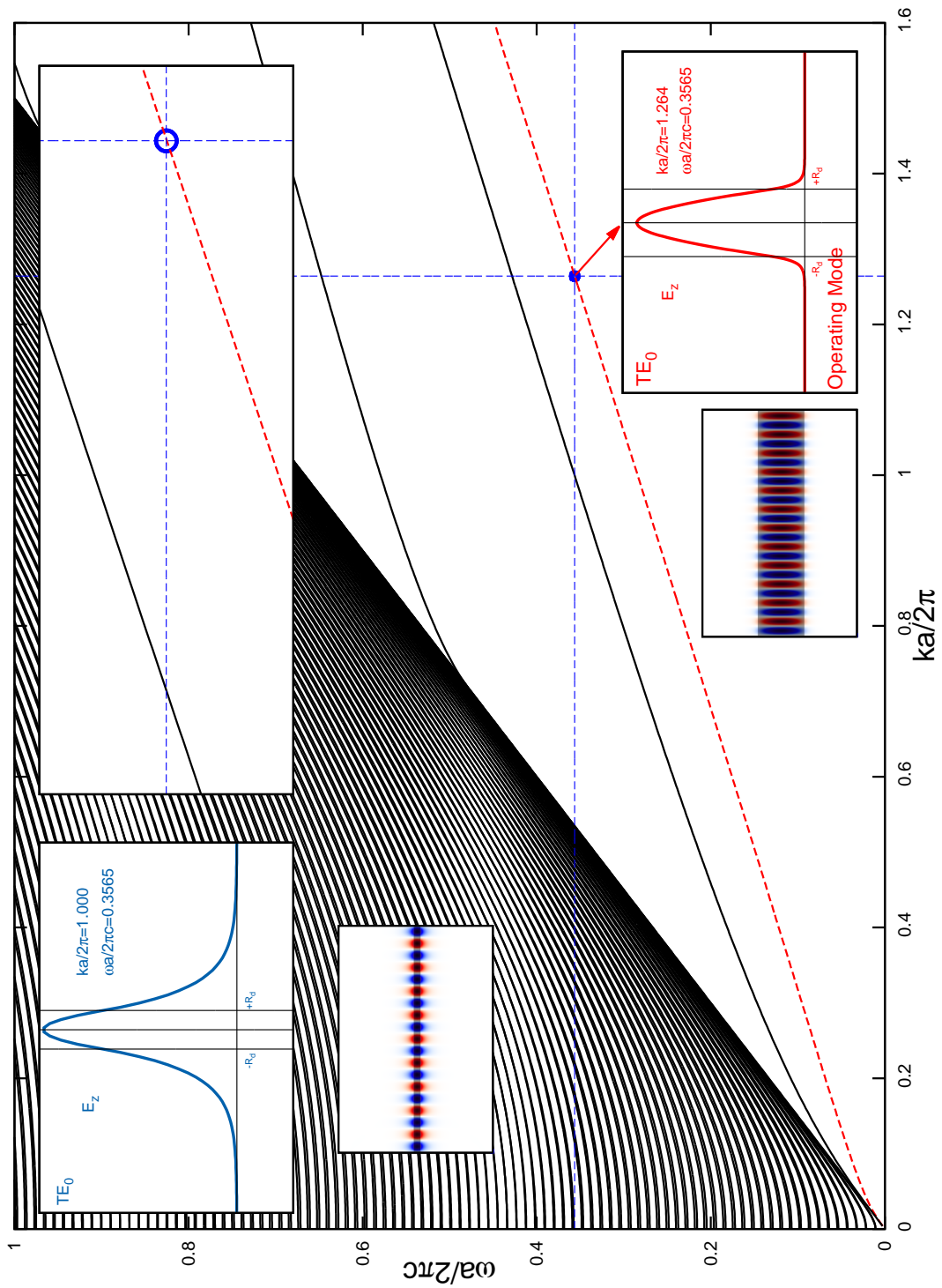


Figure 3.6. Band structure of single slab waveguide calculated for TE modes. Black lines represent band structure of single-slab with thickness $d_{out} = 2$ and dielectric constant of $\epsilon_a = 13$. Red line is the guided mode of single-slab waveguide with thickness $d_{in} = 12$ and dielectric constant of $\epsilon_a = 13$. The background of both waveguide has the same dielectric constant of $\epsilon_b = 2.25$.

In the Figure 3.7 we see dielectric profile of waveguide without transition region introduced. This direct transition also called butt-coupling or abrupt coupling. In the Figure 3.7 we see z -component of electric field (E_z) of TE mode propagating in the x -direction. The time snapshot of the field profile is taken when the field reached to steady state. The guided operating mode is generated by a continuous source with operating frequency, $\tilde{\omega} = 0.3565$ and wave vector $\tilde{k} = 1.264$. At operating frequency the single-slab (output) waveguide has only one guided mode with wave vector $\tilde{k} = 1.000$.

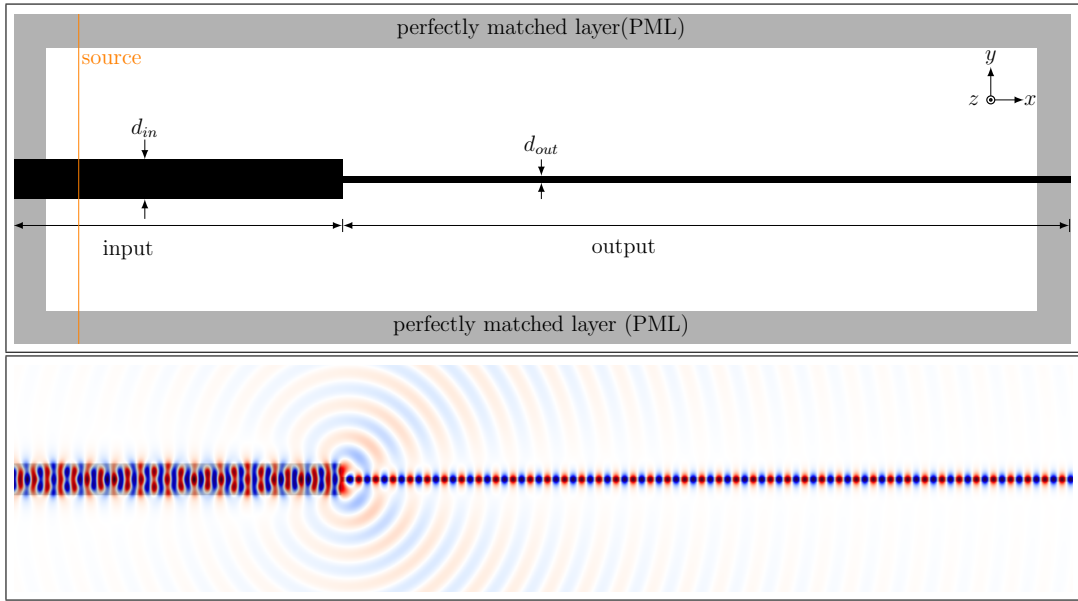


Figure 3.7. Dielectric structure, input part thickness $d_{in} = 12$ with $\epsilon_a = 13$, output part thickness $d_{out} = 2$ with $\epsilon_a = 13$. Background has dielectric constant of $\epsilon_b = 2.25$. FDTD simulation of TE mode, operating mode is even with frequency $\tilde{\omega} = 0.3565$ and wave vector $\tilde{k} = 1.264$, and there is no taper region introduced.

In this simulation transition from input waveguide to output waveguide is sudden. As can be seen from the simulation this abrupt transition of waveguide geometry will cause some of the mode to radiate to background and some of the mode to reflect back at interface. The mode profile in the input part is the superposition of forward propagating wave and those are reflected back from the interface. The excited mode profile that is propagating in the output part is the first guided mode supported by this region. Both mode profiles are same except their width. Another difference is that their group velocity are different for both modes. And their wave vector are also different. These parameters are the reasons for the reflection and the radiation.

In the adiabatic transition case, in which the geometry of waveguide is changed slowly, the mode is carried from the input waveguide to the output waveguide in a series of intermediate single-slab waveguide. This can be visualized as transition region consists of single-slab waveguide that is thickness of input waveguide gradually decreasing and finally reaches the output waveguide thickness. To see how this mode transferred along the transition region, we need to look at the band structure of waveguides with thickness between input and output waveguides. The Figure 3.8 is the same band structure shown in the Figure: 3.6. The only difference here is that we also showed first guided mode of intermediate thickness waveguides, which are ranged from $d_{out} = 12, 10, 8, 6, 5.8, \dots, 4, 3.8, \dots, 2.2, 2$. The black lines are the band structure of output region, while the red line is the operating mode of input region. The green lines represents the first guided mode of single-slab waveguide of the intermediate thickness. The structure is continuous along propagation direction but we only showed for some selected slab thickness to illustrate how coupling between input region and output region takes place along the taper.

As seen from the zoomed figure shown in the upper-right corner of Figure 3.8, introducing taper region will transfer the operating mode from input region to output region in such a way that it couples through intermediate states. In the abrupt transition case mode is coupled directly. In the case of adiabatic transition the operating mode transferred to output waveguide in a series of intermediate thickness. This slow change in thickness shift the operating mode branch up until it reaches the output region's mode. This situation is shown on the Figure 3.8. The first guided modes of slabs with thickness $d_{out} = 10, d_{out} = 8, d_{out} = 6, d_{out} = 4$, and $d_{out} = 2$ are shown by green solid lines.

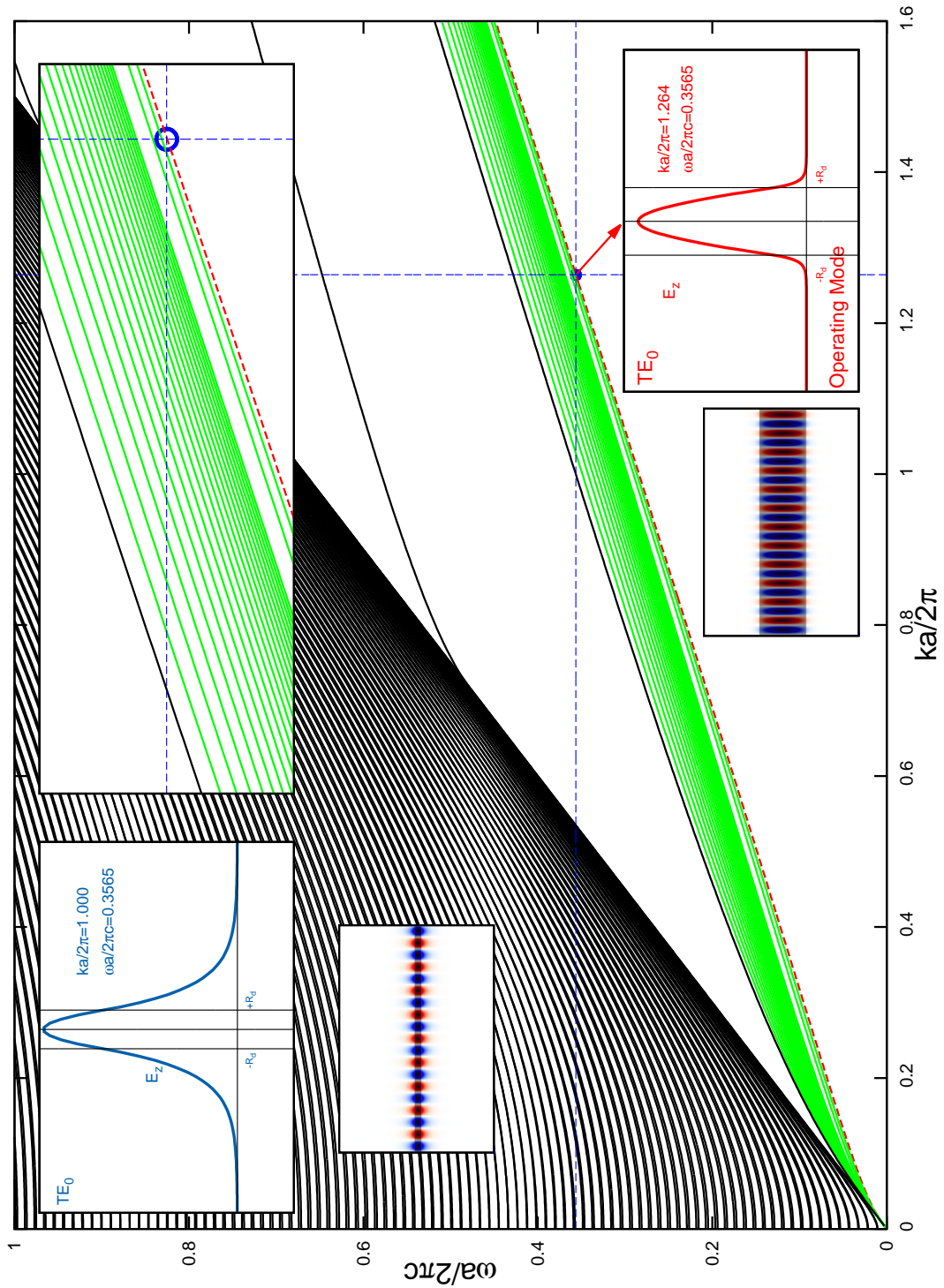


Figure 3.8. Band structure of single slab waveguide calculated for TE modes. Black lines represent band structure of single slab with thickness $d_{out} = 2$ and dielectric constant of $\epsilon_a = 13$. Red line is the guided modes of single slab waveguide with thickness $d_{in} = 12$ and dielectric constant of $\epsilon_a = 13$. The background of both waveguide has dielectric constant of $\epsilon_b = 2.25$. The green lines are the first guided modes of single-slab with intermediate thickness of $d_{out} = 10, 8, 6, 5.8, \dots 2.2$

Now we want to see what will happen to mode propagation along the structure if we introduce taper region. In Figure 3.9 we see dielectric structure with taper region introduced. Taper region thickness gradually changes from input thickness, $d_{in} = 12$ to output thickness $d_{out} = 2$. Time snapshot of electric field distribution is taken at a time when the field propagation reaches a steady state. FDTD simulation of z -component of electric field (E_z) of TE mode profile that is propagating in the x -direction is shown in Figure 3.9. We used a continuous mode source to generate first even guided mode with wave vector $\tilde{k} = 1.264$ and frequency $\tilde{\omega} = 0.3565$.

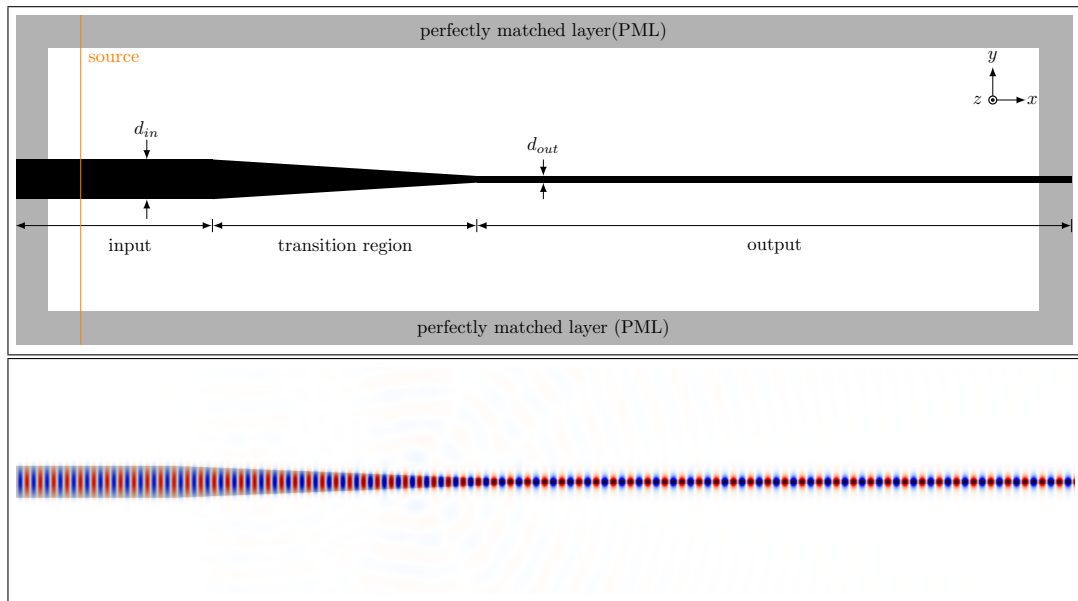


Figure 3.9. Dielectric profile of structure, the waveguide on the left hand side has thickness of $d_{in} = 12$ and the waveguide on right hand side has thickness of $d_{out} = 2$ with taper region introduced. FDTD simulation of TE mode, operating mode is odd, and in this simulation we introduce taper region.

By gradually decreasing the input waveguide thickness, we transform the guided mode profile of input waveguide to guided mode of output waveguide. Taper region converts the incoming guided mode to the guided mode of output region. Taper region is also serve as mode size converter. This chapter only covers the coupling process, so the transmission values will be studied in the upcoming chapters.

In Figure 3.10 we see band structure of single slab waveguide calculated for TE modes. The thickness of single-slab waveguide (output) is $d_{out} = 2$ and dielectric constant is $\epsilon_a = 13$ (black lines). The two dashed red lines are first (TE_0) and second (TE_1) guided modes of single-slab waveguide with thickness of $d_{in} = 12$ and dielectric constant of $\epsilon_a = 13$. Background for both waveguide is made by same dielectric medium with dielectric constant of $\epsilon_b = 2.25$. We also showed the operating mode profile (lower right corner) with frequency $\tilde{\omega} = 0.3565$ and wave vector $\tilde{k} = 1.200$. At the operating frequency the output waveguide has only one guided mode with wave vector $\tilde{k} = 1.000$. The guided mode profile of output waveguide is shown on the upper left corner. On the upper right corner we see a zoomed picture taken around operating frequency and wave vector. On the same graph we showed second guided modes of slab waveguides with intermediate thickness (green solid lines). The intermediate thickness are ranged from $d_{out} = 10, 8, \dots, 1.8$.

As can be seen from the band structure the output waveguide has only one guided mode at operating frequency, and this mode is orthogonal with the operating mode. Because of orthogonality the coupling to guided mode of output waveguide is not possible. In the case of butt coupling, when operating mode come to interface between input and output waveguides it will couple to radiation mode. All electromagnetic wave will be lost. In the case of adiabatic transition, operating mode will couple or excite the guided mode of intermediate thickness keeping the mode profile same and slowly converting mode size. Since there is no guided mode with same symmetry supported buy output part eventually the mode will couple to radiation mode when the thickness of taper reaches to a certain value.

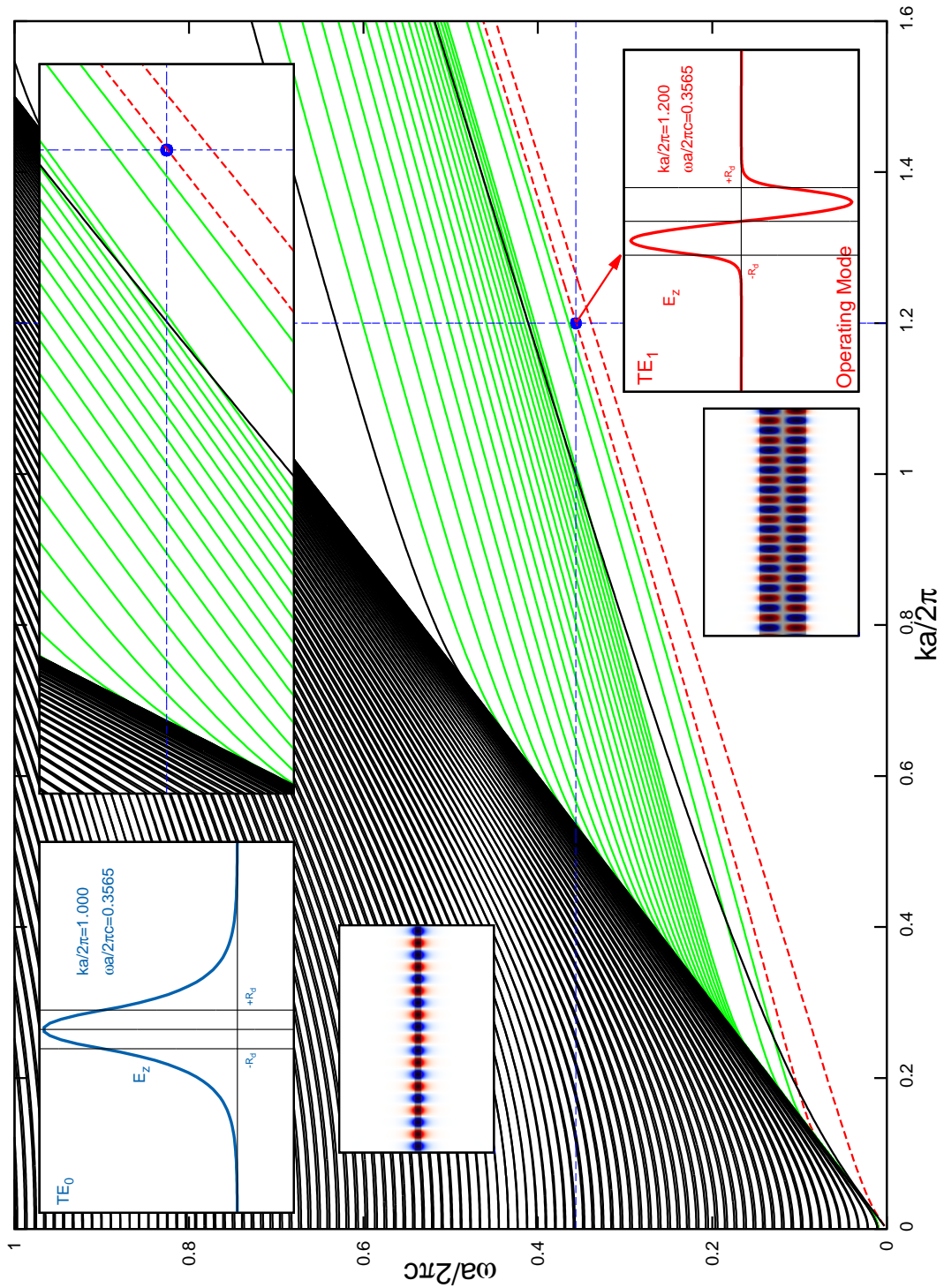


Figure 3.10. Band structure of single slab waveguide with thickness of $d_{out} = 2$, which has dielectric constant of $\epsilon_a = 13$ (black lines). The first two guided modes of input waveguide which has thickness $d_{in} = 12$ and dielectric constant $\epsilon_a = 13$ (red dashed lines). Both waveguides are immersed in the same region with dielectric constant $\epsilon_b = 2.25$. The green lines represent the second guided modes of waveguides with intermediate thickness $d_{out} = 10, 8, 6, 5.8, \dots 2.2$.

Now we will send the second guided mode of input waveguide, which we labelled as TE_1 , and we will look at the mode profile in output part. As seen from Figure 3.10 there is only one guided mode at operating frequency supported by output waveguide which has even symmetry. The operating mode has odd symmetry about the center of waveguide along x -direction. The orthogonality requirement imposes that the overlap integral of this two mode vanishes. So this mode will couple to radiation mode and some of the mode will be reflected back at the interface.

FDTD simulation z -component of electric field (E_z) of TE mode is shown in Figure 3.11 for four different output waveguide thickness. The first odd operating mode is generated by continuous mode source. The mode profiles are taken at a time when mode propagation of wave reached a steady state flow rate along waveguide. In this simulation we kept input slab waveguide constant while the output thickness is changed, ($d_{out} = 8$, $d_{out} = 6$, $d_{out} = 4$, and $d_{out} = 2$). In the pictures labelled as (a), (b), and (c) we show mode profiles of output slabs with input thickness $d_{out} = 8$, $d_{out} = 6$, and $d_{out} = 4$. For these three output thickness the slabs have odd guided mode. In the picture labelled as (d) we see mode profile of slab with output thickness $d_{out} = 2$. At the operating frequency the output waveguide only one guided mode which is even so all incoming mode radiated to background. It is clearly seen that there is no mode propagating in second medium (output part). All incoming mode are coupled to background and some of the electromagnetic radiation are reflected back at interface.

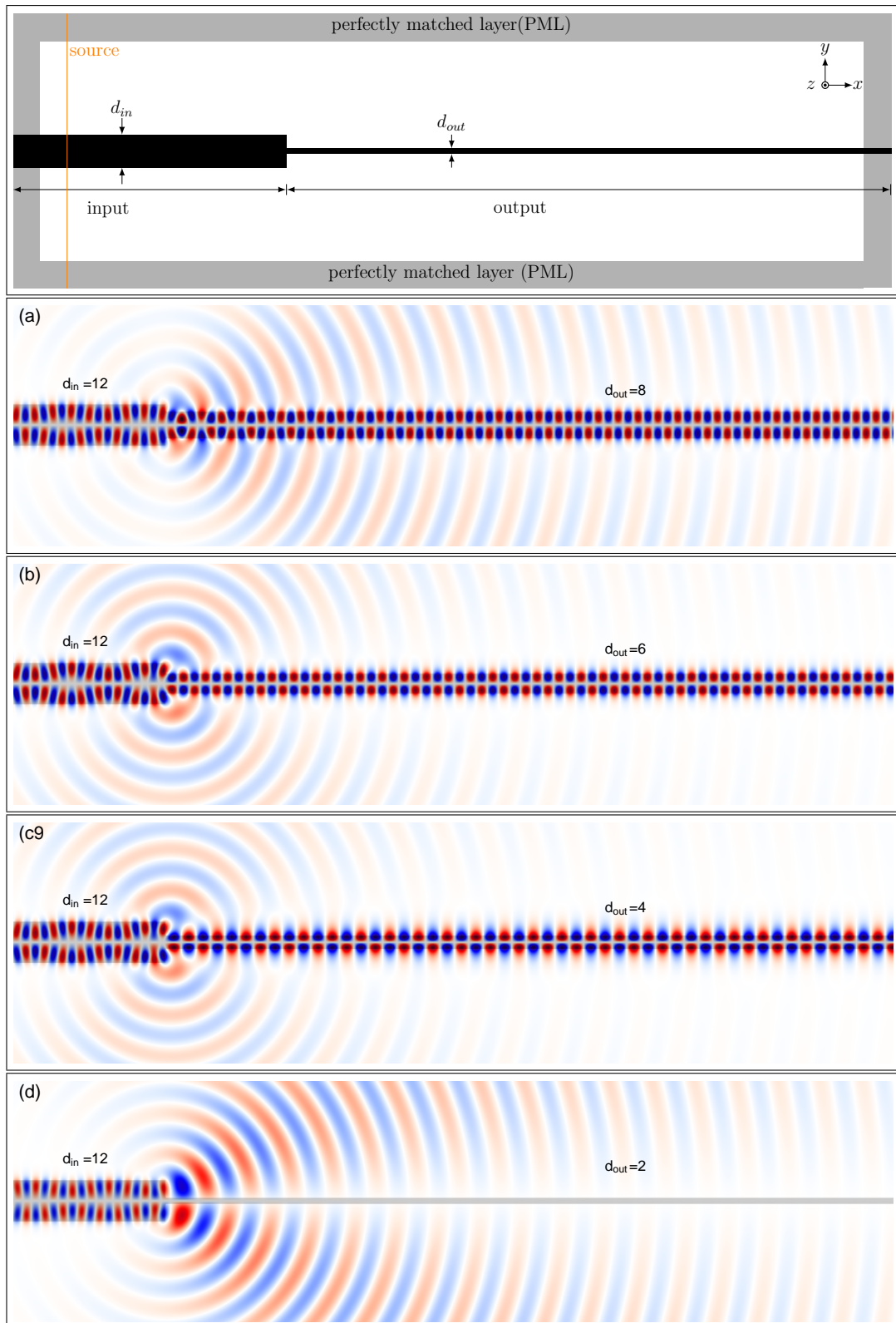


Figure 3.11. Dielectric profile of waveguide structure without taper region introduced. FDTD simulation of z -component of electric field (E_z) of TE mode taken for four different output slab thickness, $d_{out} = 8$, $d_{out} = 6$, $d_{out} = 4$, and $d_{out} = 2$, while keeping the input slab thickness constant $d_{in} = 12$. The operating mode has odd symmetry with frequency $\tilde{\omega} = 0.3565$ and wave vector $\hat{k} = 1.200$.

Now we want to see what will happen to mode propagation along the structure if we introduce taper region. In Figure 3.12 we see dielectric structure with taper region introduced. Taper region thickness gradually changes from input thickness, $d_{in} = 12$ to output thickness $d_{out} = 2$.

FDTD simulation of z -component of electric field (E_z) profile of TE mode which is propagating in the x -direction is shown in Figure 3.12. Again A continuous source mode is used to generate the first odd guided mode is used as operating frequency $\tilde{\omega} = 0.3565$ and wave vector $\tilde{k} = 1.200$. The time snapshots are taken when the field reaches a steady state. In this simulation we kept input slab waveguide constant while the output thickness is changed, ($d_{out} = 8$, $d_{out} = 6$, $d_{out} = 4$, and $d_{out} = 2$). And the connection between input and output slabs are made by taper. In the pictures labelled as (a), (b), and (c) we show mode profiles of output slabs with input thickness $d_{out} = 8$, $d_{out} = 6$, and $d_{out} = 4$. For these three output thickness smooth mode conversion is seen when we use taper region. In the picture labelled as (d) we see mode profile of slab with output thickness $d_{out} = 2$. At the operating frequency the output waveguide does not support any odd guided mode so all incoming mode radiated to background.

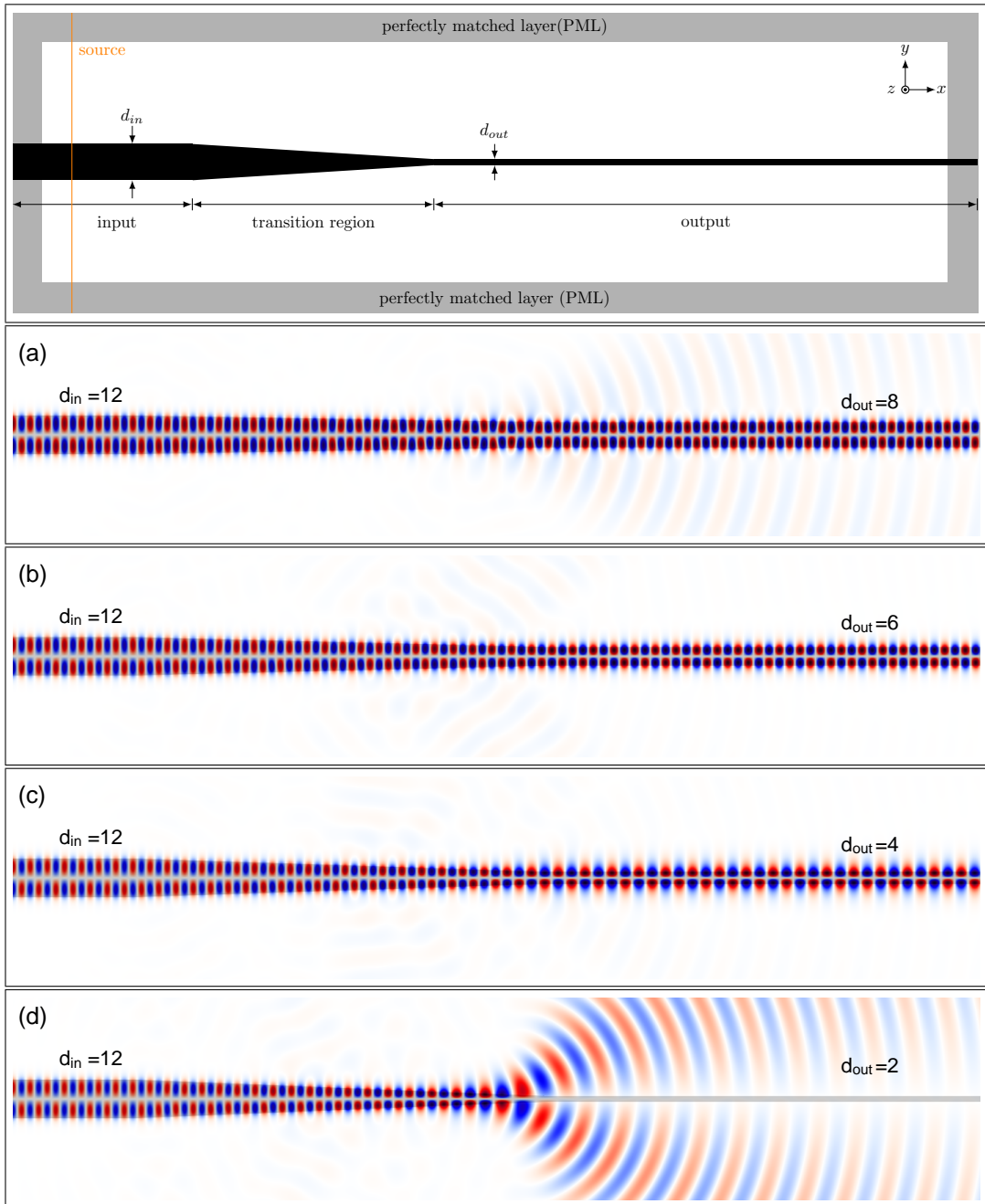


Figure 3.12. Dielectric profile of structure with taper region introduced. FDTD simulation of z -component of electric field for TE mode. Mode profiles are taken for four different output slab thickness, $d_{out} = 8$, $d_{out} = 6$, $d_{out} = 4$, and $d_{out} = 2$ while the input slab thickness is kept constant, $d_{in} = 12$

Now we will use the third guided mode (TE_2) of single-slab waveguide (input) as our operating mode. To understand how the the operating mode couples to modes of the output waveguide, we need to look the band structure shown in Figure 3.13. In this figure we see the band structure of a single-slab waveguide (output) which has thickness of $d_{out} = 2$ and dielectric constant $\epsilon_a = 13$, (black lines). On same figure we showed first three guided mode (TE_0, TE_1, TE_2) of single-slab waveguide (input) that has thickness of $d_{in} = 12$ and dielectric constant $\epsilon_a = 13$, (dashed red lines). The operating mode profile which has frequency, $\tilde{\omega} = 0.3565$ and wave vector $\tilde{k} = 1.088$ is shown on lower right corner. The only supported guided mode profile of output waveguide is shown on the left upper corner. The third guided modes of single-slab waveguides with intermediate thickness between $d_{in} = 12$ and $d_{out} = 2$, ($d_{out} = 10, 8, 6, 5.8, \dots, 2.2$) is shown by green lines.

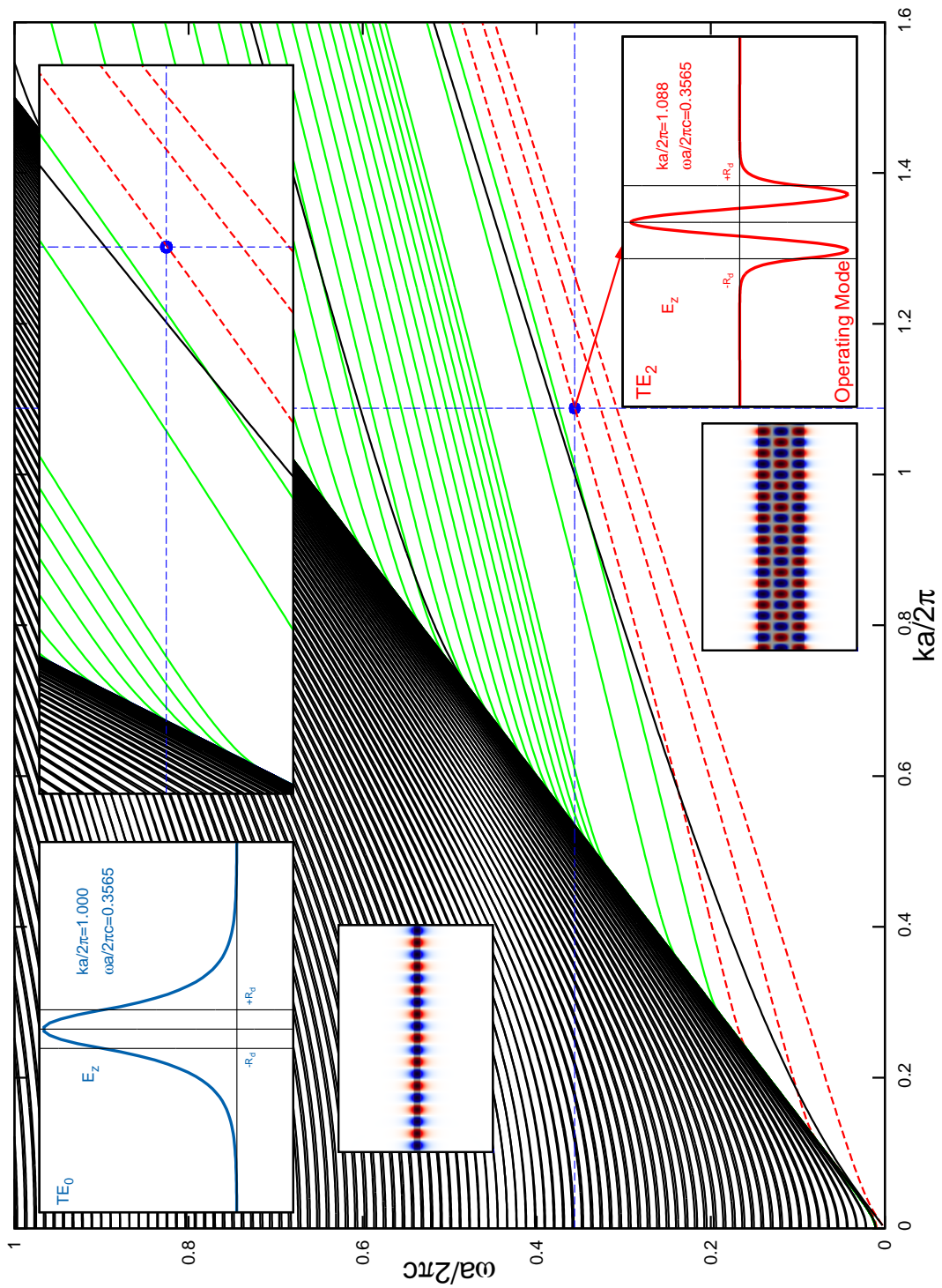


Figure 3.13. Band structure of single-slab waveguide with thickness of $d_{out} = 2$ and dielectric constant of $\epsilon_a = 13$, (black lines). First three guided mode of single-slab waveguide with thickness of $d_{in} = 12$ with dielectric constant of $\epsilon_a = 13$. Both waveguides are immersed in a background with dielectric constant $\epsilon_b = 2.25$. The green lines are the third guided modes of single-slab with core width $d_{out} = 10, 8, 6, 5.8, \dots, 2.2$.

The waveguide structure without transition region introduced is shown in Figure 3.14. Both single-slab waveguide are butt joined to each other. The connection is made directly in such a way that their symmetry axis along x -direction coincide.

FDTD simulation of z -component of electric field (E_z) of TE mode that is propagating in the x -direction is shown in Figure 3.14. In this simulation we send second even guided mode (TE_2) generated by using continuous source with frequency $\tilde{\omega} = 0.3565$ and wave vector $\tilde{k} = 1.088$. The mode profile for four different output waveguide thickness, $d_{out} = 8$, $d_{out} = 6$, $d_{out} = 4$, and $d_{out} = 2$, while the input thickness is kept constant, $d_{in} = 12$. As can be seen from figure labelled as (a) the output waveguide that has thickness $d_{out} = 8$ the excited mode is multi mode, which is superposition of first and second even guided modes. In the figure labelled as (b) the output is a superposition of the first and second even guided modes but as can be seen the second mode is too close to continuum region. In the figures labelled as (d) and (c) the only excited mode is the first even guided mode, the second guided mode is radiated to background and reflected back at the interface between two waveguides.

In the case of butt-coupling (direct coupling), when there is no taper region used, the guided modes of output region are excited directly depending on their symmetry match. some of the incoming mode will excite or couple to the radiation modes.

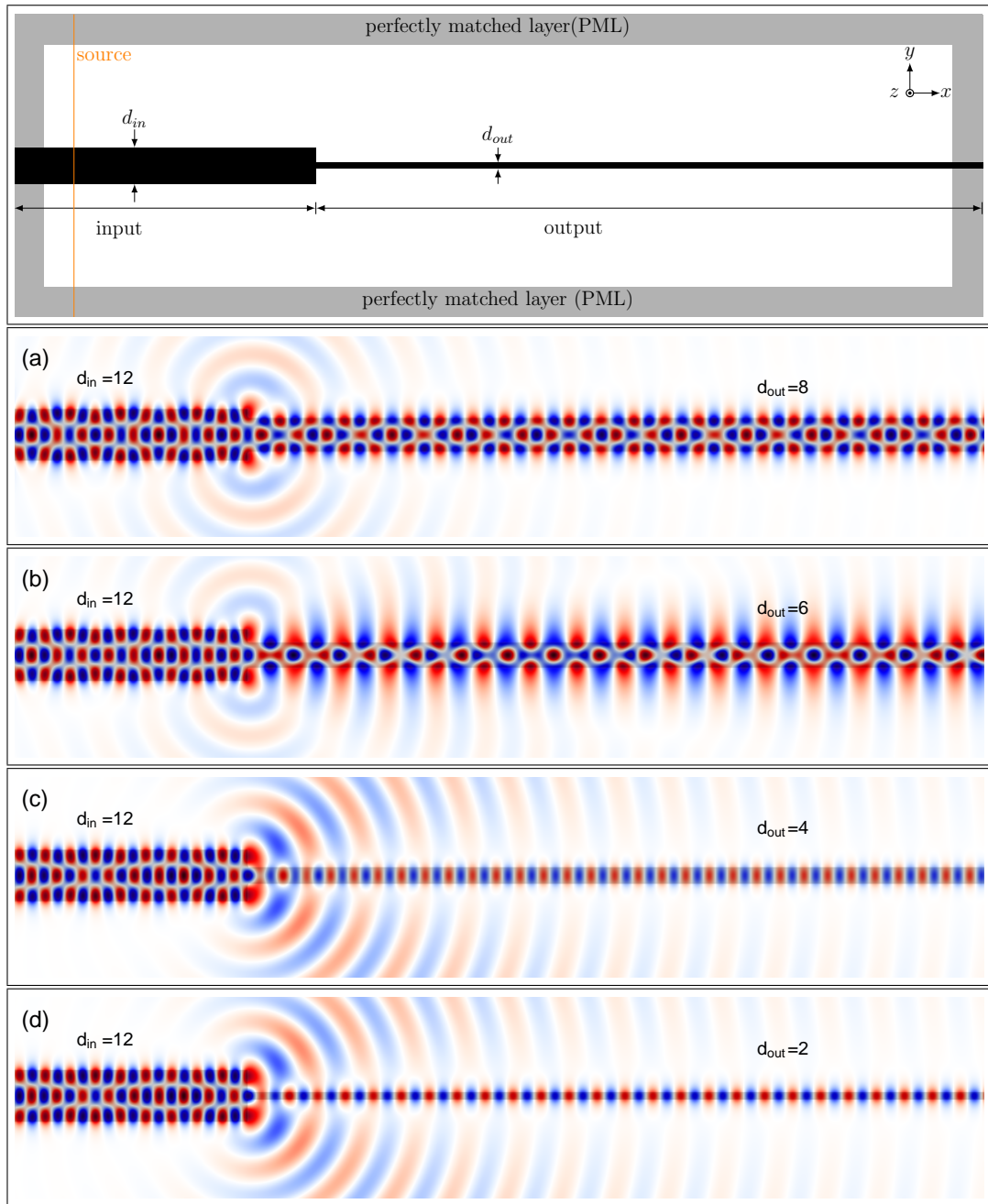


Figure 3.14. Dielectric profile of waveguide structure without taper region introduced. FDTD simulation of z -component of electric field (E_z) of TE mode. The operating mode has even symmetry with frequency $\tilde{\omega} = 0.3565$ and wave vector $\tilde{k} = 1.088$. The mode profiles are taken for four different output slab thickness, $d_{out} = 8$, $d_{out} = 6$, $d_{out} = 4$, and $d_{out} = 2$. Input part thickness is kept constant, $d_{in} = 12$.

To see the effect of introducing taper region between two single-slab waveguide on coupling of modes, we will use the waveguide structure shown in Figure 3.15. Taper region thickness gradually changes from input single-slab waveguide thickness, $d_{in} = 12$ to four different output single-slab waveguide thickness of $d_{out} = 8$, $d_{out} = 6$, $d_{out} = 4$, and $d_{out} = 2$.

FDTD simulation of z -component of electric field (E_z) of TE mode profile at a steady state for four different output waveguide thickness, $d_{out} = 8$, $d_{out} = 6$, $d_{out} = 4$, and $d_{out} = 2$, while keeping the input waveguide thickness constant, $d_{in} = 12$, is shown in the Figure 3.15. In adiabatic coupling case, the mode propagates along taper structure without changing its profile. During this transition the frequency is a conserved quantity, so the only changing parameter is the wave vector. As the operating mode propagate along transition region the wave vector shifts of operating mode shifts toward the radiation mode, and finally it enters the radiation region. As can be seen from the field distribution at a certain value of taper region thickness the guided propagating mode couples to radiation (continuum) modes. And as we also see from this simulation there is no excited wave propagating in the output region.

In the case of adiabatic transition, the operating mode will couple to output waveguides through intermediate thickness as it propagate along taper structure. Since the geometry of waveguide slowly changing the mode profile will be kept constant as it propagate. At a certain thickness, the mode will no longer be guided. It will eventually couple to radiation mode. As stated in the (Johnson et al., 2002), the operating mode must be guided for every point along taper so that adiabatic transition can be achieved.

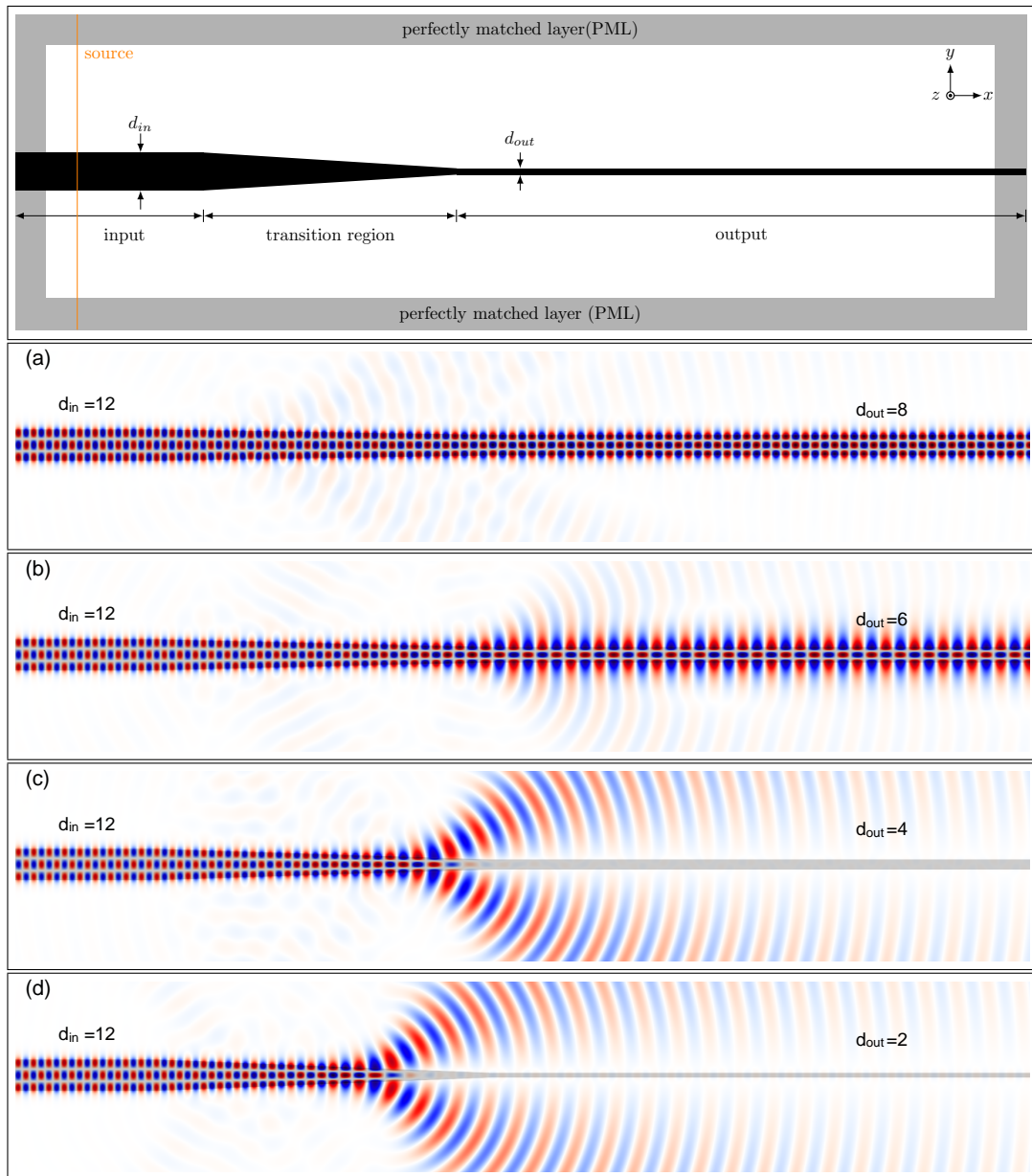


Figure 3.15. Dielectric profile of the waveguide structure with taper region introduced. FDTD simulation of z -component of electric field (E_z) of TE mode, the operating mode is even. The mode profiles are taken for four different output thickness, ($d_{out} = 8$, $d_{out} = 6$, $d_{out} = 4$, and $d_{out} = 2$) while input slab thickness kept constant, $d_{in} = 12$.

3.2. Calculation of Coupling Coefficients

We will use the waveguide structure shown in Figure 3.3 to find the coupling coefficients of excited modes in output part of the structure. As can be seen from band structure shown in Figure 3.2 our operating mode is even. At the operating frequency, the output region has only three guided even modes. When the operating mode comes to the interface between to slab it will excite only these three guided modes. To be able to find which mode is excited in what fraction (amount) we need to find transmission coupling coefficient of these three modes. Since we know the operating mode is even and there is only three even modes for output part, we represent even guided modes as follows,

$$\begin{aligned}
 \psi_0(x, y) &= f_0(y)e^{i(\beta_0x+\alpha_0)} \\
 \psi_2(x, y) &= f_2(y)e^{i(\beta_2x+\alpha_2)} \\
 \psi_4(x, y) &= f_4(y)e^{i(\beta_4x+\alpha_4)}
 \end{aligned} \tag{3.1}$$

using trigonometric identities to expand these equations and taking the real part the we will have,

$$\begin{aligned}
 \psi_0(x, y) &= f_0(y) \cos(\beta_0x + \alpha_0) \\
 \psi_2(x, y) &= f_2(y) \cos(\beta_2x + \alpha_2) \\
 \psi_4(x, y) &= f_4(y) \cos(\beta_4x + \alpha_4)
 \end{aligned} \tag{3.2}$$

and again with the help of trigonometric identities,

$$\begin{aligned}
 \psi_0(x, y) &= f_0(y) [\cos \alpha_0 \cos(\beta_0x) - \sin \alpha_0 \sin(\beta_0x)] \\
 \psi_2(x, y) &= f_2(y) [\cos \alpha_2 \cos(\beta_2x) - \sin \alpha_2 \sin(\beta_2x)] \\
 \psi_4(x, y) &= f_4(y) [\cos \alpha_4 \cos(\beta_4x) - \sin \alpha_4 \sin(\beta_4x)]
 \end{aligned} \tag{3.3}$$

and summation of these three wave is equals to the measured wave that we found by using FDTD method (meep) simulation,

$$\psi_{measured}(x, y) = C_0\psi_0(x, y) + C_2\psi_2(x, y) + C_4\psi_4(x, y) \quad (3.4)$$

putting equation 3.3 in equation 3.4 we get,

$$\begin{aligned} \psi_{measured}(x, y) &= (C_0 \cos \alpha_0) [f_0(y) \cos(\beta_0 x)] + (-C_0 \sin \alpha_0) [f_0(y) \sin(\beta_0 x)] \\ &+ (C_2 \cos \alpha_2) [f_2(y) \cos(\beta_2 x)] + (-C_2 \sin \alpha_2) [f_2(y) \sin(\beta_2 x)] \\ &+ (C_4 \cos \alpha_4) [f_4(y) \cos(\beta_4 x)] + (-C_4 \sin \alpha_4) [f_4(y) \sin(\beta_4 x)] \end{aligned} \quad (3.5)$$

We now introduce new coefficient, $\tilde{C}_j = C_j \cos \alpha_j$, where $j = 0, 2, 4$, and $\tilde{C}_j = -C_j \sin \alpha_j$, where $j = 1, 3, 5$, this equation becomes,

$$\begin{aligned} \psi_{measured}(x, y) &= \tilde{C}_0 [f_0(y) \cos(\beta_0 x)] + \tilde{C}_1 [f_0(y) \sin(\beta_0 x)] \\ &+ \tilde{C}_2 [f_2(y) \cos(\beta_2 x)] + \tilde{C}_3 [f_2(y) \sin(\beta_2 x)] \\ &+ \tilde{C}_4 [f_4(y) \cos(\beta_4 x)] + \tilde{C}_5 [f_4(y) \sin(\beta_4 x)] \end{aligned} \quad (3.6)$$

Now collecting all terms to one side and calling this χ and taking square of both side we get,

$$\begin{aligned} \chi^2 &= \sum_{i=1}^N \left\{ \psi_m(x_i, y_i) - \tilde{C}_0 f_0(y_i) \cos(\beta_0 x_i) - \tilde{C}_1 f_0(y_i) \sin(\beta_0 x_i) \right. \\ &\quad \left. - \tilde{C}_2 f_2(y_i) \cos(\beta_2 x_i) - \tilde{C}_3 f_2(y_i) \sin(\beta_2 x_i) \right. \\ &\quad \left. - \tilde{C}_4 f_4(y_i) \cos(\beta_4 x_i) - \tilde{C}_5 f_4(y_i) \sin(\beta_4 x_i) \right\}^2 \end{aligned} \quad (3.7)$$

using least square method to find coefficients we differentiate χ^2 w.r.t coefficients \tilde{C}_j , where $j = 0, 1, \dots, 5$,

$$\begin{aligned} \frac{\partial \chi^2}{\partial \tilde{C}_j} = \frac{\partial}{\partial \tilde{C}_j} \sum_{i=1}^N \left\{ \psi_m(x_i, y_i) - \tilde{C}_0 f_0(y_i) \cos(\beta_0 x_i) - \tilde{C}_1 f_0(y_i) \sin(\beta_0 x_i) \right. \\ \left. - \tilde{C}_2 f_2(y_i) \cos(\beta_2 x_i) - \tilde{C}_3 f_2(y_i) \sin(\beta_2 x_i) \right. \\ \left. - \tilde{C}_4 f_4(y_i) \cos(\beta_4 x_i) - \tilde{C}_5 f_4(y_i) \sin(\beta_4 x_i) \right\}^2 \end{aligned} \quad (3.8)$$

taking the differentiation then we have,

$$\begin{aligned} \frac{\partial \chi^2}{\partial \tilde{C}_0} = \sum_{i=1}^N (-2) \left\{ \psi_m(x_i, y_i) - \tilde{C}_0 f_0(y_i) \cos(\beta_0 x_i) - \tilde{C}_1 f_0(y_i) \sin(\beta_0 x_i) \right. \\ \left. - \tilde{C}_2 f_2(y_i) \cos(\beta_2 x_i) - \tilde{C}_3 f_2(y_i) \sin(\beta_2 x_i) \right. \\ \left. - \tilde{C}_4 f_4(y_i) \cos(\beta_4 x_i) - \tilde{C}_5 f_4(y_i) \sin(\beta_4 x_i) \right\} f_0(y_i) \cos(\beta_0 x_i) \end{aligned} \quad (3.9)$$

$$\begin{aligned} \frac{\partial \chi^2}{\partial \tilde{C}_1} = \sum_{i=1}^N (-2) \left\{ \psi_m(x_i, y_i) - \tilde{C}_0 f_0(y_i) \cos(\beta_0 x_i) - \tilde{C}_1 f_0(y_i) \sin(\beta_0 x_i) \right. \\ \left. - \tilde{C}_2 f_2(y_i) \cos(\beta_2 x_i) - \tilde{C}_3 f_2(y_i) \sin(\beta_2 x_i) \right. \\ \left. - \tilde{C}_4 f_4(y_i) \cos(\beta_4 x_i) - \tilde{C}_5 f_4(y_i) \sin(\beta_4 x_i) \right\} f_0(y_i) \sin(\beta_0 x_i) \end{aligned} \quad (3.10)$$

$$\begin{aligned} \frac{\partial \chi^2}{\partial \tilde{C}_2} = \sum_{i=1}^N (-2) \left\{ \psi_m(x_i, y_i) - \tilde{C}_0 f_0(y_i) \cos(\beta_0 x_i) - \tilde{C}_1 f_0(y_i) \sin(\beta_0 x_i) \right. \\ \left. - \tilde{C}_2 f_2(y_i) \cos(\beta_2 x_i) - \tilde{C}_3 f_2(y_i) \sin(\beta_2 x_i) \right. \\ \left. - \tilde{C}_4 f_4(y_i) \cos(\beta_4 x_i) - \tilde{C}_5 f_4(y_i) \sin(\beta_4 x_i) \right\} f_2(y_i) \cos(\beta_2 x_i) \end{aligned} \quad (3.11)$$

$$\begin{aligned} \frac{\partial \chi^2}{\partial \tilde{C}_3} = \sum_{i=1}^N (-2) \left\{ \psi_m(x_i, y_i) - \tilde{C}_0 f_0(y_i) \cos(\beta_0 x_i) - \tilde{C}_1 f_0(y_i) \sin(\beta_0 x_i) \right. \\ \left. - \tilde{C}_2 f_2(y_i) \cos(\beta_2 x_i) - \tilde{C}_3 f_2(y_i) \sin(\beta_2 x_i) \right. \\ \left. - \tilde{C}_4 f_4(y_i) \cos(\beta_4 x_i) - \tilde{C}_5 f_4(y_i) \sin(\beta_4 x_i) \right\} f_2(y_i) \sin(\beta_2 x_i) \end{aligned} \quad (3.12)$$

$$\begin{aligned} \frac{\partial \chi^2}{\partial \tilde{C}_4} = \sum_{i=1}^N (-2) \left\{ \psi_m(x_i, y_i) - \tilde{C}_0 f_0(y_i) \cos(\beta_0 x_i) - \tilde{C}_1 f_0(y_i) \sin(\beta_0 x_i) \right. \\ \left. - \tilde{C}_2 f_2(y_i) \cos(\beta_2 x_i) - \tilde{C}_3 f_2(y_i) \sin(\beta_2 x_i) \right. \\ \left. - \tilde{C}_4 f_4(y_i) \cos(\beta_4 x_i) - \tilde{C}_5 f_4(y_i) \sin(\beta_4 x_i) \right\} f_4(y_i) \cos(\beta_4 x_i) \end{aligned} \quad (3.13)$$

$$\begin{aligned} \frac{\partial \chi^2}{\partial \tilde{C}_5} = \sum_{i=1}^N (-2) \left\{ \psi_m(x_i, y_i) - \tilde{C}_0 f_0(y_i) \cos(\beta_0 x_i) - \tilde{C}_1 f_0(y_i) \sin(\beta_0 x_i) \right. \\ \left. - \tilde{C}_2 f_2(y_i) \cos(\beta_2 x_i) - \tilde{C}_3 f_2(y_i) \sin(\beta_2 x_i) \right. \\ \left. - \tilde{C}_4 f_4(y_i) \cos(\beta_4 x_i) - \tilde{C}_5 f_4(y_i) \sin(\beta_4 x_i) \right\} f_4(y_i) \sin(\beta_4 x_i) \end{aligned} \quad (3.14)$$

now we have six linear equation with six unknown. Solving this linear system for coefficients, \tilde{C}_j where $j = 0, 1, \dots, 5$ we can find coupling coefficient of coupled modes. its matrix form is as follows,

$$\begin{bmatrix} S_{11} & S_{12} & S_{13} & S_{14} & S_{15} & S_{16} \\ S_{21} & S_{22} & S_{23} & S_{24} & S_{25} & S_{26} \\ S_{31} & S_{32} & S_{33} & S_{34} & S_{35} & S_{36} \\ S_{41} & S_{42} & S_{43} & S_{44} & S_{45} & S_{46} \\ S_{51} & S_{52} & S_{53} & S_{54} & S_{55} & S_{56} \\ S_{61} & S_{62} & S_{63} & S_{64} & S_{65} & S_{66} \end{bmatrix} \begin{bmatrix} \tilde{C}_0 \\ \tilde{C}_1 \\ \tilde{C}_2 \\ \tilde{C}_3 \\ \tilde{C}_4 \\ \tilde{C}_5 \end{bmatrix} = \begin{bmatrix} \sum_{i=1}^N \psi_m(x_i, y_i) f_0(y_i) \cos(\beta_0 x_i) \\ \sum_{i=1}^N \psi_m(x_i, y_i) f_0(y_i) \sin(\beta_0 x_i) \\ \sum_{i=1}^N \psi_m(x_i, y_i) f_2(y_i) \cos(\beta_2 x_i) \\ \sum_{i=1}^N \psi_m(x_i, y_i) f_2(y_i) \sin(\beta_2 x_i) \\ \sum_{i=1}^N \psi_m(x_i, y_i) f_4(y_i) \cos(\beta_4 x_i) \\ \sum_{i=1}^N \psi_m(x_i, y_i) f_4(y_i) \sin(\beta_4 x_i) \end{bmatrix} \quad (3.15)$$

where S_{kl} with $k, l = 1, 2, \dots, 6$, are coefficients of \tilde{C}_j with $j = 0, 1, \dots, 5$. Once we solve this linear system we can find the coupling coefficient of each excited mode by using,

$$P_0 = \frac{\tilde{C}_0^2 + \tilde{C}_1^2}{\sum_{j=0}^5 \tilde{C}_j^2} \quad P_2 = \frac{\tilde{C}_2^2 + \tilde{C}_3^2}{\sum_{j=0}^5 \tilde{C}_j^2} \quad P_4 = \frac{\tilde{C}_4^2 + \tilde{C}_5^2}{\sum_{j=0}^5 \tilde{C}_j^2} \quad (3.16)$$

3.2.1. Continuous source

Electric field distribution of TE mode for continuous source along the propagation direction, x - axes, is shown in Figure 3.16. This profile is taken at a time when propagating wave reached a steady state. In this figure there is no taper region introduced. In this case, the sudden change in geometry cause the incoming mode to couple all guided mode supported by the output region. The resultant propagating mode is superposition of three guided modes supported by output waveguide.

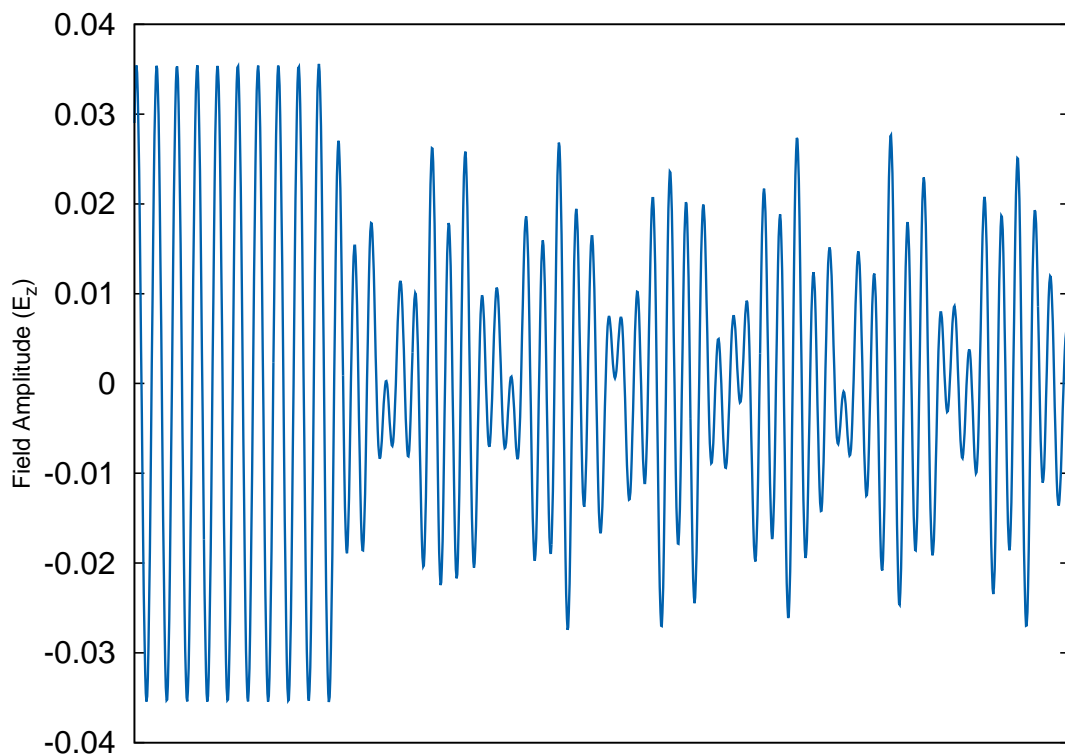


Figure 3.16. Transverse electric mode distribution viewed along x - axes taken at $y = 0$, and there is no taper region, incoming mode couple to three even modes as seen. Drop in amplitude of EM wave is due to back reflection and radiation to background at the interface.

In Figure 3.17 we introduce taper region and as we see incoming mode smoothly converted to single mode in output waveguide. To be able to completely couple to fundamental mode, the transition region need to be made gradual enough.

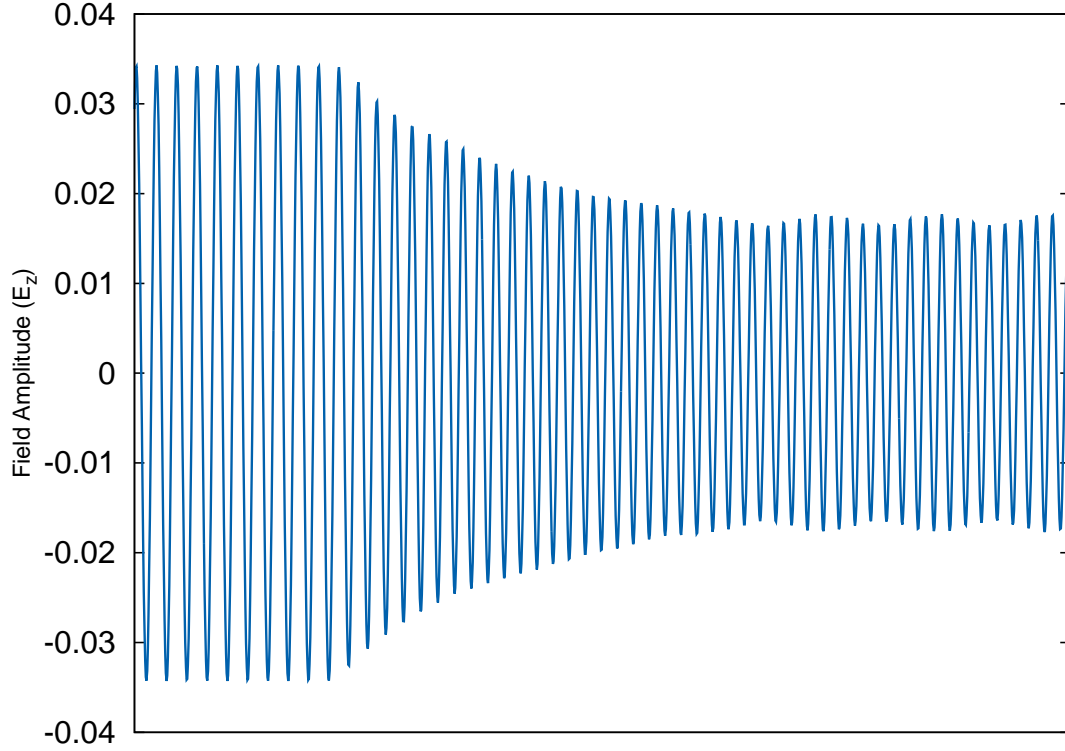


Figure 3.17. TE mode profile viewed along x – axes taken at $y = 0$, we introduce taper region in this structure, taper region force incoming mode to couple first single mode of output part.

The coupling coefficient (coupling coefficient) can be found by using coefficients found from the matrix Equation 3.15 and it is calculated as follows,

$$P_0 = \frac{\tilde{C}_0^2 + \tilde{C}_1^2}{\sum_{j=1}^6 \tilde{C}_j^2} \quad P_2 = \frac{\tilde{C}_2^2 + \tilde{C}_3^2}{\sum_{j=1}^6 \tilde{C}_j^2} \quad P_4 = \frac{\tilde{C}_4^2 + \tilde{C}_5^2}{\sum_{j=1}^6 \tilde{C}_j^2} \quad (3.17)$$

where P_0 is the coupling efficiency of first even guided mode, P_2 is the coupling efficiency of the second even guided mode, and P_4 is the coupling efficiency of third even guided mode.

In Table 3.1 we see the coupling coefficients of modes in the output waveguide for two structure. In one structure, there is no taper region while in the second structure

we introduced taper region. The coupling coefficients of first three even guided modes without taper region are $P_0 = 0.1562$, $P_2 = 0.0639$, and $P_4 = 0.7799$. The coupling coefficient with taper region introduced are $P_0 = 0.9230$, $P_2 = 0.0743$, and $P_4 = 0.0027$. It is clearly seen from coupling coefficients by using such a region almost all operating mode coupled to the fundamental (first guided) mode of output part.

| Coupling coefficient | without taper region | with taper region |
|----------------------|------------------------|------------------------|
| P_0 | 0.156243272481348 | 0.923352346102108 |
| P_2 | 6.390326292546283E-002 | 7.437058370358268E-002 |
| P_4 | 0.779853464593189 | 2.277070194309248E-003 |

Table 3.1. Coupling coefficient of TE mode, in one structure there is no taper region, and in the second structure we introduce taper region in which geometry of waveguide gradually changes and finally reach the output parts dimensions.

3.2.2. Gaussian source

In Figure 3.18 we see the propagation of a Gaussian pulse taken at waveguide center four different time step along waveguide structure which is the x -axis, $t = 25$, $t = 30$, $t = 35$, and $t = 40$. The waveguide structure consists of two single-slab waveguide that are butt joined to each other which is shown in the inset of first figure of Figure 3.18. Zoomed pulse profile around the red rectangular area are also shown in the inset. In the butt coupling case, when the guided mode comes to interface it couples to three guided mode of output part. Propagating mode in output waveguide is superposition of three guided mode supported by output part. As seen at time step $t = 25$, $t = 30$, and $t = 35$ the excited mode in output region is multi mode. When we introduce taper region between two waveguides, as we see from mode profile, the excited mode is the fundamental mode (first guided even mode) supported by output part. The propagating mode is single mode which is desired for signal transfer. In the case of multi mode, each mode has its own group velocity and this will cause mixing data during transfer. TE mode profile is shown in Figure 3.19. By introducing taper region, we slowly convert incoming mode to first guided mode of output part. In the adiabatic coupling case the mode slowly converted from operating mode to first guided mode of output waveguide.

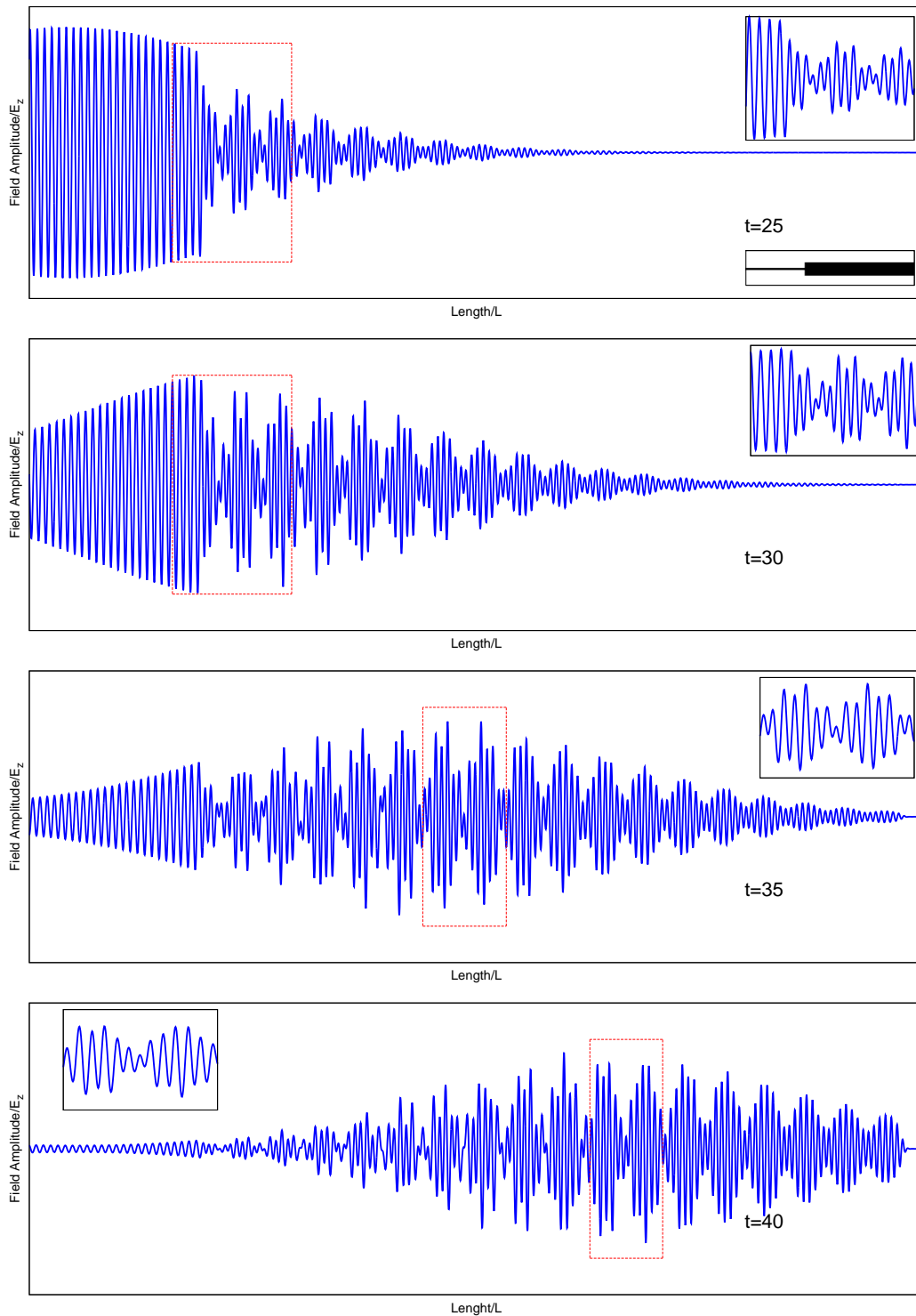


Figure 3.18. z -component of electric field distribution along the center of waveguide structure in the x -direction. Two waveguide are butt joined to each other. The incoming mode couple to three even mode as seen from figure. Drop in amplitude of TE mode is due to back reflection and radiation to background at the interface.

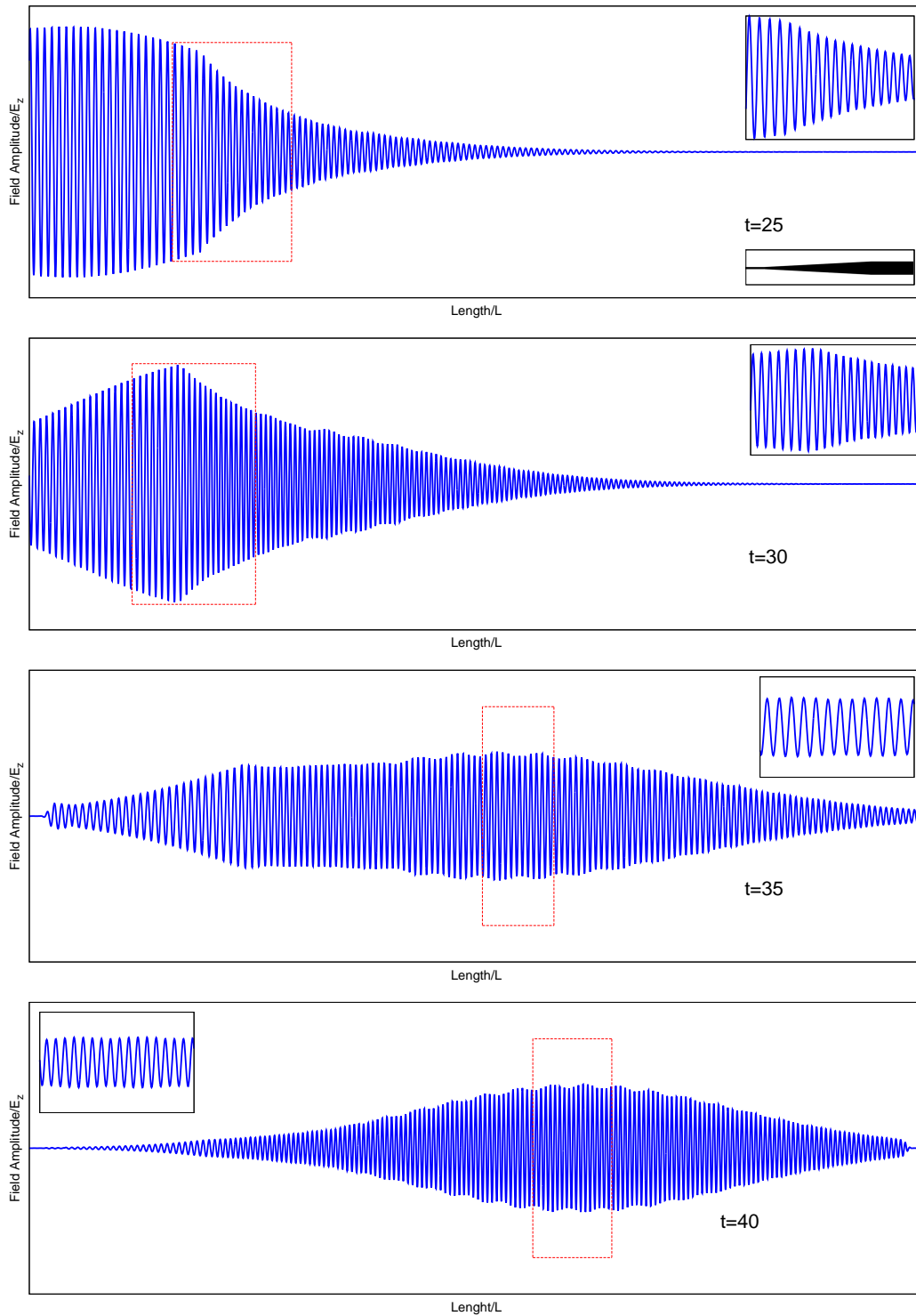


Figure 3.19. Electric field distribution along waveguide in the x -direction at the center of waveguide taken at four different time step ($t = 25$, $t = 30$, $t = 35$, and $t = 40$). Two single-slab waveguides are joined by a taper region

CHAPTER 4

COUPLING SINGLE-SLAB WAVEGUIDES

In this chapter we will study coupling efficiency of electromagnetic mode between single-slab waveguides. In first section we found transmission values for coupling from a single-slab to another single-slab waveguide that have different geometric parameters. This calculation will be performed with and without taper region. In the second section we will study coupling of mode from single-slab (input part) to another single-slab (intermediate region) and again couple it back to a region called output part which has same thickness with the input part.

4.1. Single Slab to Single Slab Waveguide

In order to understand how the taper region improves transmission values, single slab waveguide will be studied in this section. At first we run simulation without taper region. Then we introduce a taper region which gradually changes geometry of waveguide from input region to output region and we will compare transmission values of non-tapered structure with the case of tapered structure. The waveguide structure is shown in Figure 4.1.

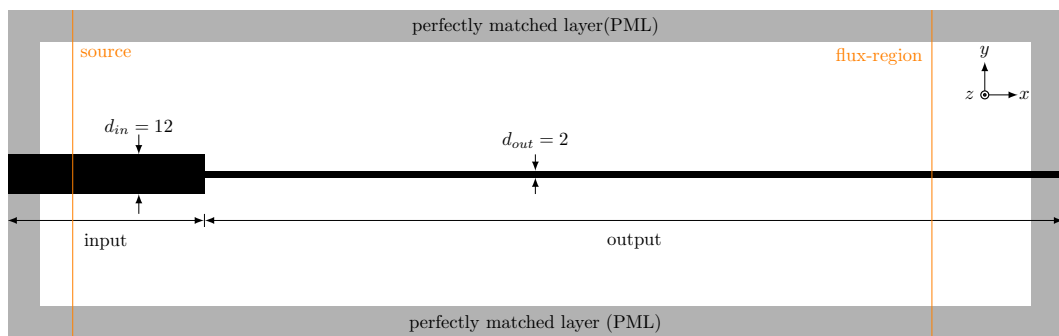


Figure 4.1. Dielectric profile of waveguide structure without taper region introduced. The input waveguide has thickness of $d_{in} = 12$ and the output waveguide has thickness of $d_{out} = 2$. Both waveguide have the same dielectric constant of $\epsilon_a = 13$. The waveguide structure is immersed in a background with dielectric constant of $\epsilon_b = 2.25$.

The slab on the left side of Figure 4.1 has thickness $d_{in} = 12$ with dielectric constant of $\epsilon_a = 13$, (input part). and the slab on the right side has thickness $d_{out} = 2$ with dielectric constant of $\epsilon_a = 13$, (output part). The background has dielectric constant of $\epsilon_b = 2.25$.

The dispersion relation (band structure) of single-slab waveguide calculated for TE mode is shown in Figure 4.2. The red dashed line in the figure is the first guided mode of single-slab waveguide (input) that has thickness of $d_{in} = 12$ with dielectric constant $\epsilon_a = 13$ and the black solid lines in the figure are the band structure of single-slab waveguide that has thickness of $d_{out} = 2$ with dielectric constant $\epsilon_a = 13$. The background has dielectric constant $\epsilon_b = 2.25$. In the Figure 4.2, the intersection of blue lines indicates the operating guided mode of input part. At this point the mode has frequency $\tilde{\omega} = 0.2840$ and the wave vector $\tilde{k} = 1$. At the operating frequency, as we see from band diagram, there is only one guided mode of output part with wave vector $\tilde{k} = 0.740$.

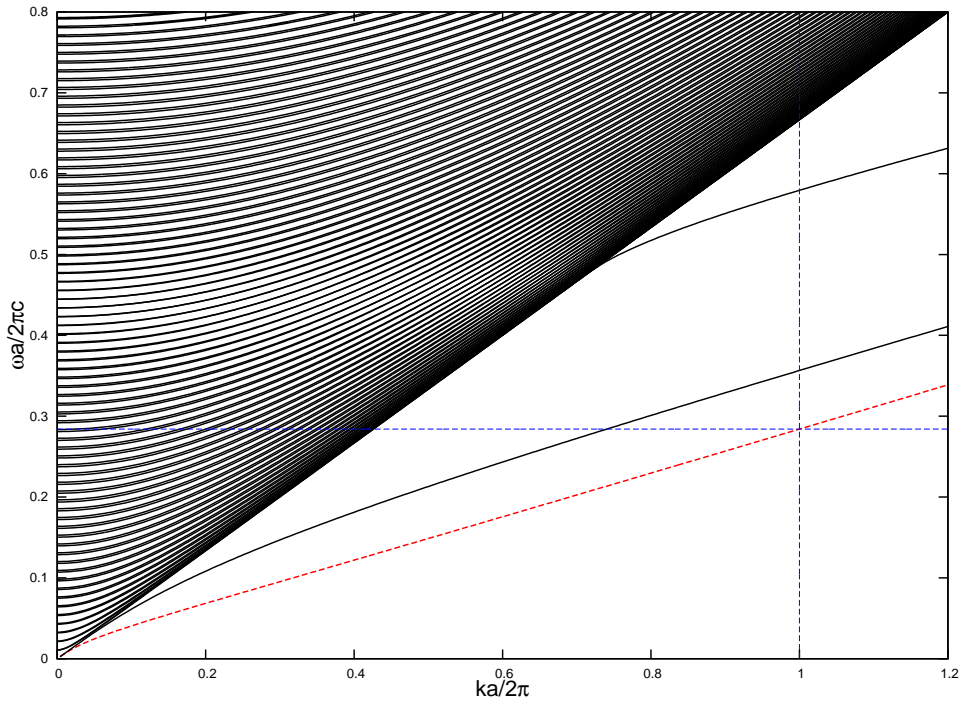


Figure 4.2. Band structures of single-slab waveguides of thickness $d_{out} = 2$ and dielectric $\epsilon_a = 13$ (black solid lines). First guided mode of single-slab waveguide of thickness $d_{in} = 12$ with dielectric $\epsilon_a = 13$ (red dashed lines). The background has dielectric constant of $\epsilon_b = 2.25$.

In Figure 4.3 we see dielectric waveguide structure consist of two single-slab waveguide that are butt joined. Field distribution of z -component of electric field (E_z) for TE mode found by FDTD simulation. The guided mode of input region is generated by a Gaussian mode source. The field distribution is taken at four different time ($t = 25$, $t = 30$, $t = 35$ and $t = 40$). At time step $t = 25$ and $t = 30$ the operating excites the guided mode of output waveguide. At time step $t = 35$ the reflected wave from interface of bot waveguide is clearly seen. And finally after those radiated and reflected wave absorbed by PML region, the guided propagating mode of output waveguide is seen at time step $t = 40$.

The transmission value for that structure, (butt-coupled) is about 77%. This shows that 23% of optical power is lost to background and reflected back at interface during coupling. In the butt coupling case, the the operating (initial) mode with frequency and wave vector $(\tilde{\omega}, \tilde{k}_i)$ converted directly to the final mode with frequency and wave vector $(\tilde{\omega}, \tilde{k}_f)$. The frequency is conserved so it is same for both states but the wave vector of both mode are different.

In Figure 4.4 we see dielectric profile of waveguide structure. In this structure the connection between two single-slab waveguide is made by a trapezoidal waveguide called taper region which will serve as mode converter to improve transmission value. Introducing taper region convert incoming guided TE mode to first guided mode of second region (output part). The operating mode is generated with a gaussian mode source with frequency $\tilde{\omega} = 0.2840$ and wave vector $\tilde{k} = 1$. The distribution of z -component of electric field is (E_z) found by FDTD simulation is shown. The propagation of mode is shown for four different time ($t = 26$, $t = 32$, $t = 38$ and $t = 44$).

In adiabatic coupling case, the calculated transmission value for this waveguide structure is about 98%. Only %2 of optical power is radiated to background or reflected back at interface of two slabs. By introducing a taper geometry between two waveguides the incoming mode converted gradually to guided mode of output waveguide.

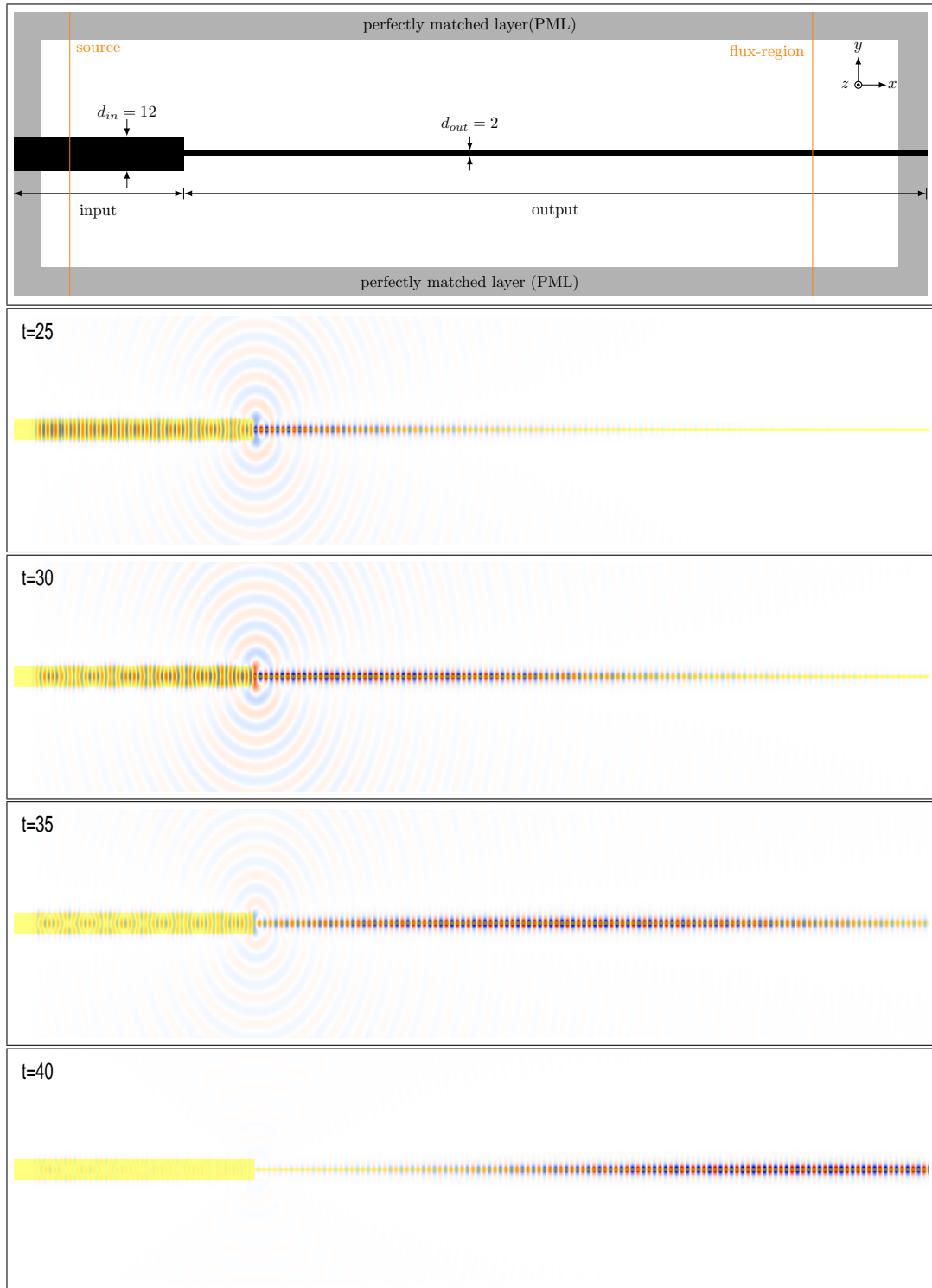


Figure 4.3. Dielectric profile of waveguide structure without taper region introduced. The input waveguide has thickness of $d_{in} = 12$ and the output waveguide has thickness of $d_{out} = 2$. Both waveguide have the same dielectric constant of $\epsilon_a = 13$. The waveguide structure is immersed in a background with dielectric constant of $\epsilon_b = 2.25$. FDTD simulation of z -component of electric field (E_z) profile for TE mode is shown.

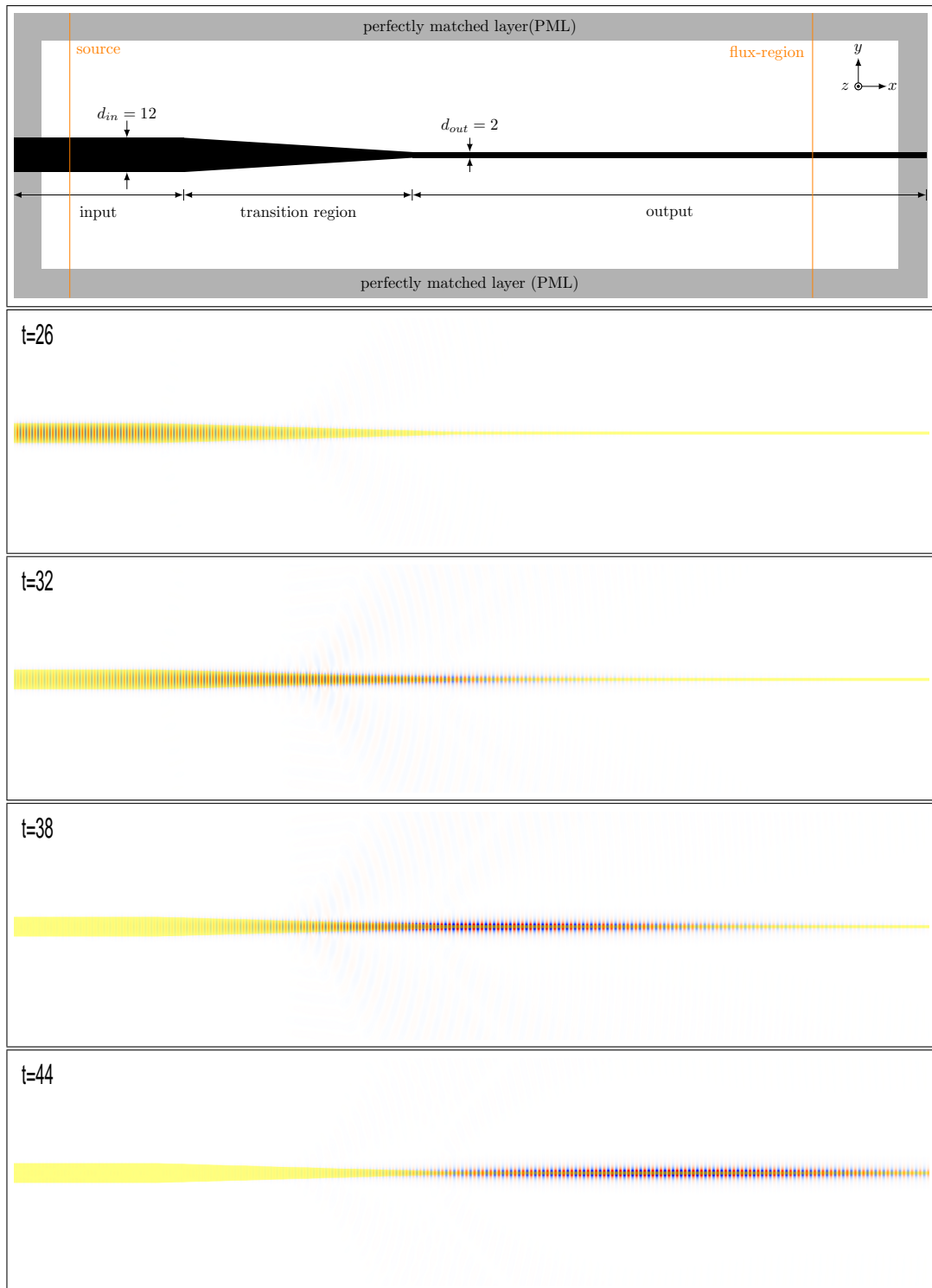


Figure 4.4. Dielectric profile of waveguide structure with taper region introduced. The input and output single slab waveguides thickness are $d_{in} = 12$ and $d_{out} = 2$. The dielectric constant are same for both slab which is $\epsilon_a = 13$. The whole structure is immersed in a background with dielectric constant $\epsilon_b = 2.25$. FDTD simulation of z - component of electric field shown for four different time step. The operating mode is generated by using a Gaussian mode source with frequency and wave vector $\tilde{\omega} = 0.2840$, $\tilde{k} = 1$ respectively.

In Figure 4.5 we show the transmission values versus taper length. As seen from transmission graph, transmission increases significantly with increasing taper length. The transmission reaches its maximum value at about $L = 10a$. Further increase in taper length has no significant improvement on transmission values. Data point on graph are taken by increasing taper length by lattice constant a starting from $L = 0$ to $L = 100$.

The loss in transmission values depends on group velocity mismatch of guided modes of both waveguides. In this structure, without taper region introduced, there is a sudden change in geometry of waveguide. This sudden change cause optical power to radiate to background or reflect back at interface of two slabs.

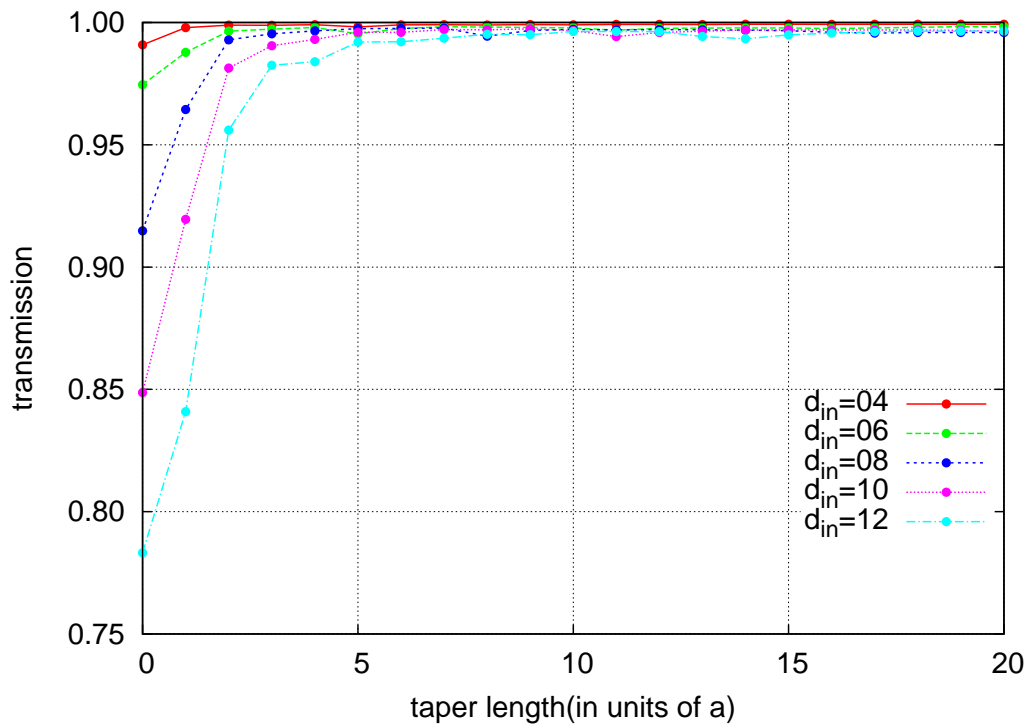


Figure 4.5. Transmission values versus taper length found by FDTD simulation. Butt-coupling case ($L = 0a$) and adiabatic coupling case ($L > 0a$) are shown for five different input waveguide thickness ($d_{in} = 4, 6, 8, 10, 12$) while keeping the output waveguide thickness constant ($d_{out} = 2$).

Besides improving coupling efficiency, adiabatic transition also prevent the operating mode to excite high order modes. To show this effect we will use the waveguide structure shown in Figure 4.6. This structure consist of two single-slab waveguide that are butt joined. Input slab has thickness of $d_{in} = 2$ with dielectric constant of $\epsilon_a = 13$. Output slab has thickness of $d_{out} = 12$ with dielectric constant of $\epsilon_a = 13$. The structure is put in a medium that has dielectric constant $\epsilon_b = 2.25$.

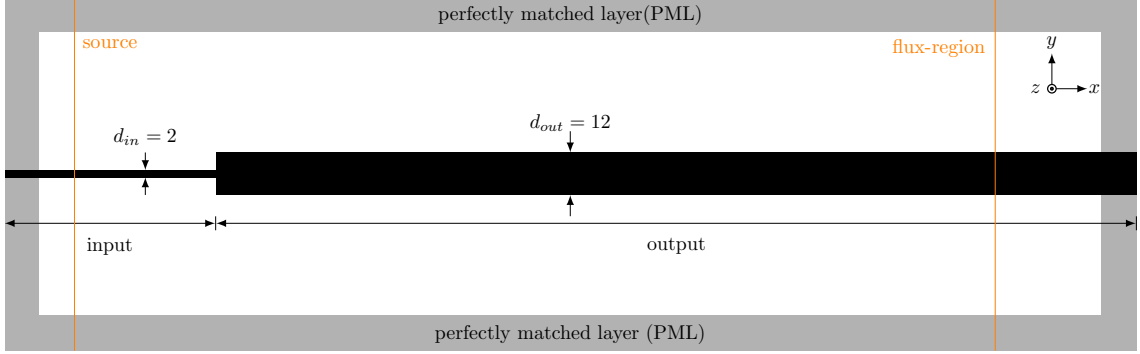


Figure 4.6. Dielectric profile of waveguide structure consisting of two butt joined single-slab. Input slab has thickness of $d_{in} = 2$ with dielectric constant of $\epsilon_a = 13$. Output slab has thickness of $d_{out} = 12$ with dielectric constant of $\epsilon_a = 13$. The background medium has dielectric constant of $\epsilon_b = 2.25$

In Figure 4.7 we showed band structure of single-slab waveguide with thickness $d_{out} = 12$ with dielectric constant $\epsilon_a = 13$, (black solid lines). Dielectric constant of background material is $\epsilon_b = 2.25$. At the operating frequency $\tilde{\omega} = 0.3565$ the guided modes of this single-slab waveguide is shown and they are labelled as TE_0 , TE_1 , TE_2 , TE_3 and TE_4 . The red dashed lines are first two guided mode of single-slab waveguide with thickness $d_{in} = 2$ with dielectric constant $\epsilon_a = 13$. The background has dielectric constant of $\epsilon_b = 2.25$.

In Figure 4.8 we see time snap-shot of z -component of electric field of TE mode distribution. A Gaussian mode source is used to excite the operating frequency $\tilde{\omega} = 0.3565$ and $\tilde{k} = 1$. The mode profiles are taken at four different time, ($t = 35$, $t = 45$, $t = 55$, and $t = 65$). In the butt coupling case as seen from Figure 4.8, since the operating mode is even then the incoming wave coupled to multi mode of output part and resultant propagating mode is superposition of three guided mode supported by output part, (TE_0 , TE_2 , and TE_4). We have zoomed the mode profile to get a clear view. The loss in EM radiation in this structure is not high but now propagating mode is multi-mode. Every mode propagate with its own group velocity.

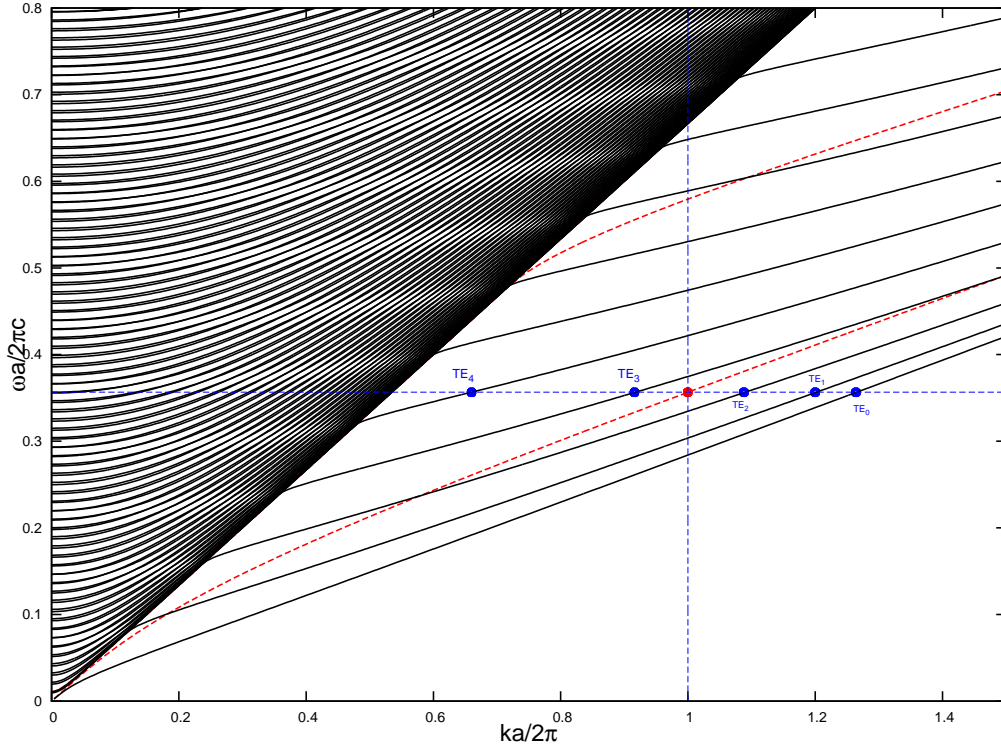


Figure 4.7. Band structure of single-slab waveguide. Black lines represents single-slab waveguide with thickness of $d_{out} = 12$ with dielectric constant $\epsilon_a = 13$ immersed in a background with dielectric constant $\epsilon_b = 2.25$. The two red dashed lines represent first two guided modes of single-slab waveguide with thickness $d_{in} = 2$ and dielectric constant $\epsilon_a = 13$. The background has $\epsilon_b = 2.25$. The intersection of blue dashed lines indicates our operating mode with frequency $\tilde{\omega} = 0.3565$ and wave vector $\tilde{k} = 1$

Now we will introduce a transition (taper) region between this two waveguides and we will look to their mode profile after TE mode pass to output part. The structure and taper region is shown in Figure 4.9. The effect of introducing taper region on mode profile is clearly seen from zoomed portion of the figure that is taken at four different time step. As seen from Figure 4.9 the excited mode is single mode, first mode supported by output part. This shows us that by using proper transition region we can excite (couple) the fundamental mode of output part. The excited mode is no longer multi-mode. So introducing taper region, besides improving coupling efficiency, it can be used to couple light to single mode.



Figure 4.8. Dielectric profile of waveguide structure consisting of two butt joined single-slab. Input slab has thickness of $d_{in} = 2$ with dielectric constant of $\epsilon_a = 13$. Output slab has thickness of $d_{out} = 12$ with dielectric constant of $\epsilon_a = 13$. FDTD simulation of electric field distribution of waveguide structure that is made by butt joined single-slabs.



Figure 4.9. Dielectric profile of waveguide consist of input region with thickness of $d_{in} = 2$, trapezoidal taper region and output region with thickness of $d_{out} = 12$. All waveguide region have same dielectric constant of $\epsilon_a = 13$. The waveguide structure immersed in a background with dielectric constant of $\epsilon_b = 2.25$. Electric field profile of TE mode taken at four different time along waveguide that is adiabatically connected with a transition region.

4.2. Two Stage Coupling of Single Slab Waveguide

Now we will find the transmission values for the structure shown in Figure 4.10. This structure is made of three region which is constructed as follows, first part is the input part with thickness of $d_{in} = 8$, second part which we call intermediate region with thickness of $d_{int} = 2$, and the output part which has same thickness with input part, d_{out} . All three region have same dielectric constant of $\epsilon_a = 13$. The background has dielectric constant of $\epsilon_b = 2.25$.

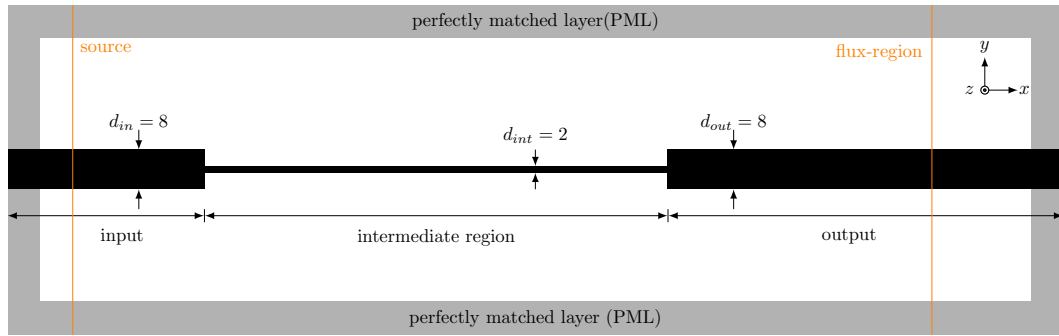


Figure 4.10. The waveguide structure consisting of three single-slab waveguides that are butt joined. The input region thickness is $d_{in} = 8$ with dielectric constant $\epsilon_a = 13$. The intermediate region thickness is $d_{int} = 2$ with dielectric constant $\epsilon = 13$. The output region thickness is $d_{out} = 8$ with dielectric constant $\epsilon_a = 13$. The whole structure is immersed in a background material with dielectric constant of $\epsilon_b = 2.25$.

The band structure of single-slab waveguide, the intermediate region, with thickness $d_{int} = 2$ and dielectric constant $\epsilon_a = 13$ immersed in a medium with dielectric constant $\epsilon_b = 2.25$ is shown in the Figure 4.11, black lines. First three guided mode of single-slab waveguide, the input region, is also shown, red dashed curves. The intersection of vertical and horizontal red dashed lines indicates our operating frequency, $\tilde{\omega} = 0.1027$ and wave vector, $\tilde{k} = 0.3$.

FDTD simulation of z -component of electric field found by using MEEP is shown in Figure 4.12 for butt-coupling case. In this simulation we used a gaussian source with frequency $\tilde{\omega} = 0.1027$ and wave vector $\tilde{k} = 0.3$ to generate the operating mode. The z -component of electric field (E_z) distribution is taken at four different time step, ($t = 20$, $t = 30$, $t = 35$, and $t = 50$) is shown. Operating mode send form input region first couples to intermediate region and then couple back to output region. At this frequency and wave vector there is only one guided mode of intermediate region. Incoming mode

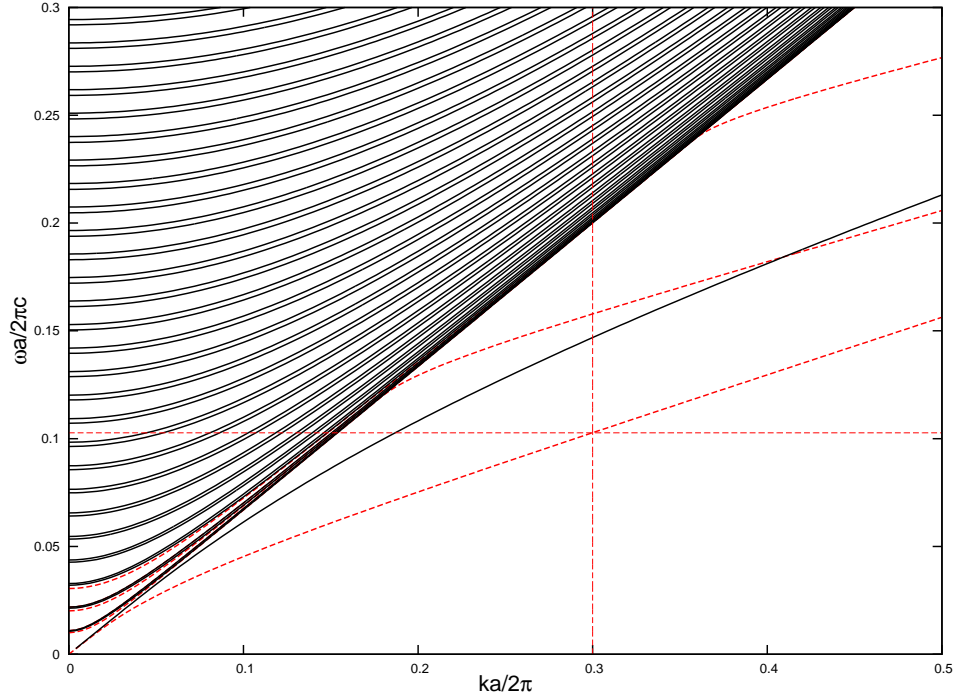


Figure 4.11. Band structure of single-slab waveguide with thickness $d_{int} = 2$ with dielectric constant of $\epsilon = 13$ immersed in a medium with dielectric constant of $\epsilon = 2.25$, black lines. Dashed red lines represents guided modes of single slab waveguide with thickness $d_{in} = 8$ with dielectric constant of $\epsilon = 13$ immersed in a medium with dielectric constant of $\epsilon = 2.25$.

will couple to this mode and this excited mode will propagate along intermediate region and will excite modes of output part which has only one guided mode at this frequency. Transmission value for this structure, without taper region introduced, is 65.7%. The rest of optical power is radiated to background during the coupling at two interface. Radiation to background at the interface between input and intermediate region and the radiation between intermediate region and output region is clearly seen from time snapshots $t = 30$, $t = 35$. At time step $t = 50$ we see the excited propagating mode out output region.

To increase coupling efficiency we now introduce taper region at interface between single-slab waveguides, first taper region is between input part and intermediate region and second taper introduced between intermediate region and output part. In Figure 4.13 we see the waveguide structure.

FDTD simulation of z -component of electric field of TE mode along waveguide is shown in Figure 4.13 for adiabatic coupling case. Time snapshot of electric field distribution that is taken at four time step is shown, $t = 40$, $t = 60$, $t = 70$, and $t = 90$. As seen from the simulation, radiation to background and reflection at interfaces are reduced

by great amount when we use taper region. Transmission value for this simulation is 97.9%. In the adiabatic limit, it is predicted that when this transition gradually enough it is possible to couple all optical power between two different dielectric medium. This simulation run for 20 resolution per period. The taper region length used in this simulation is $L = 50a$, where a is lattice constant.

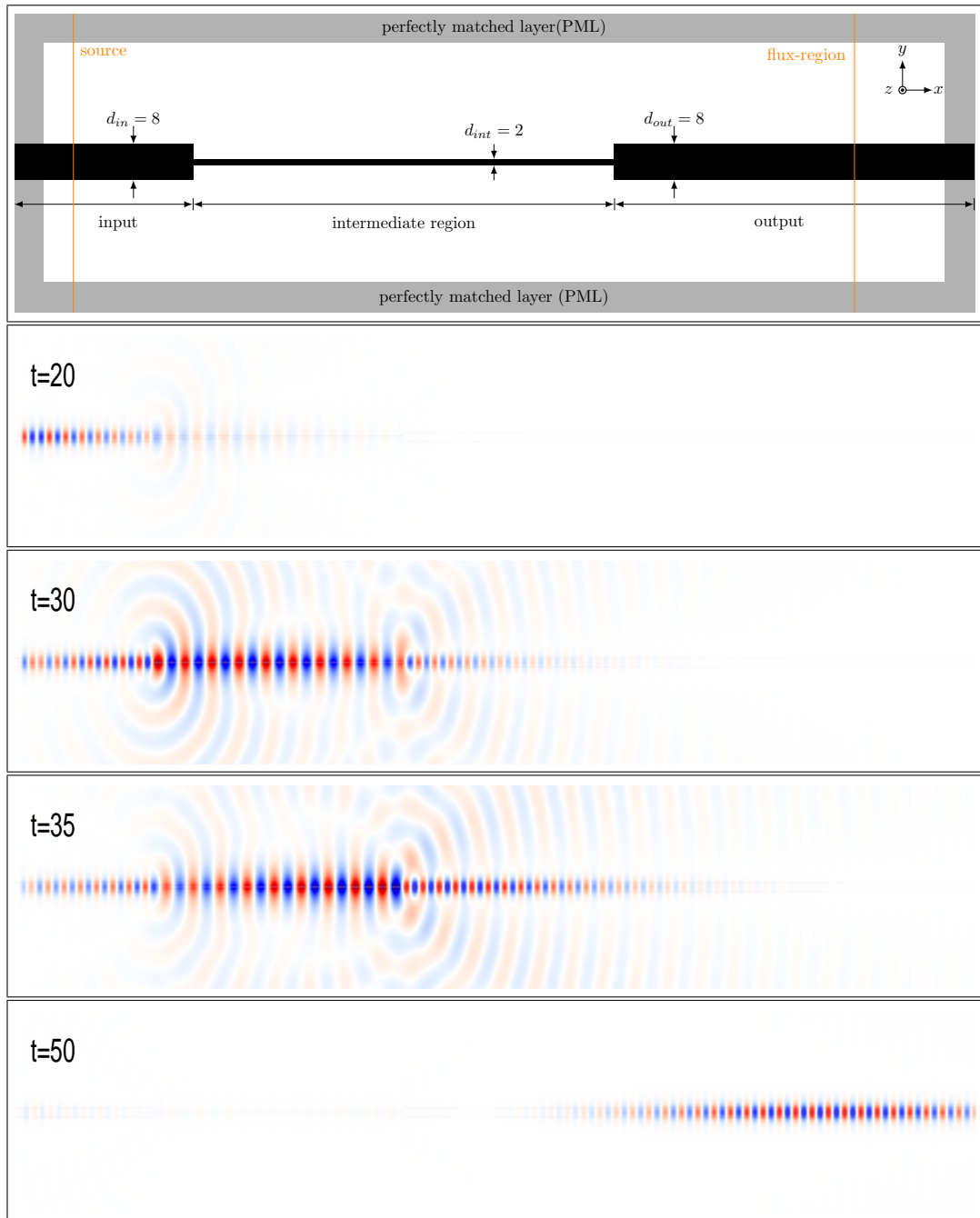


Figure 4.12. Dielectric structure of waveguide without taper region introduced. The waveguide consist of input region, intermediate region, and the output region. FDTD simulation of electric field component, (E_z), of TE mode profile shown for four different time step. The operating frequency and wave vector are $\tilde{\omega} = 0.1027$ and $\tilde{k} = 0.3$ respectively.

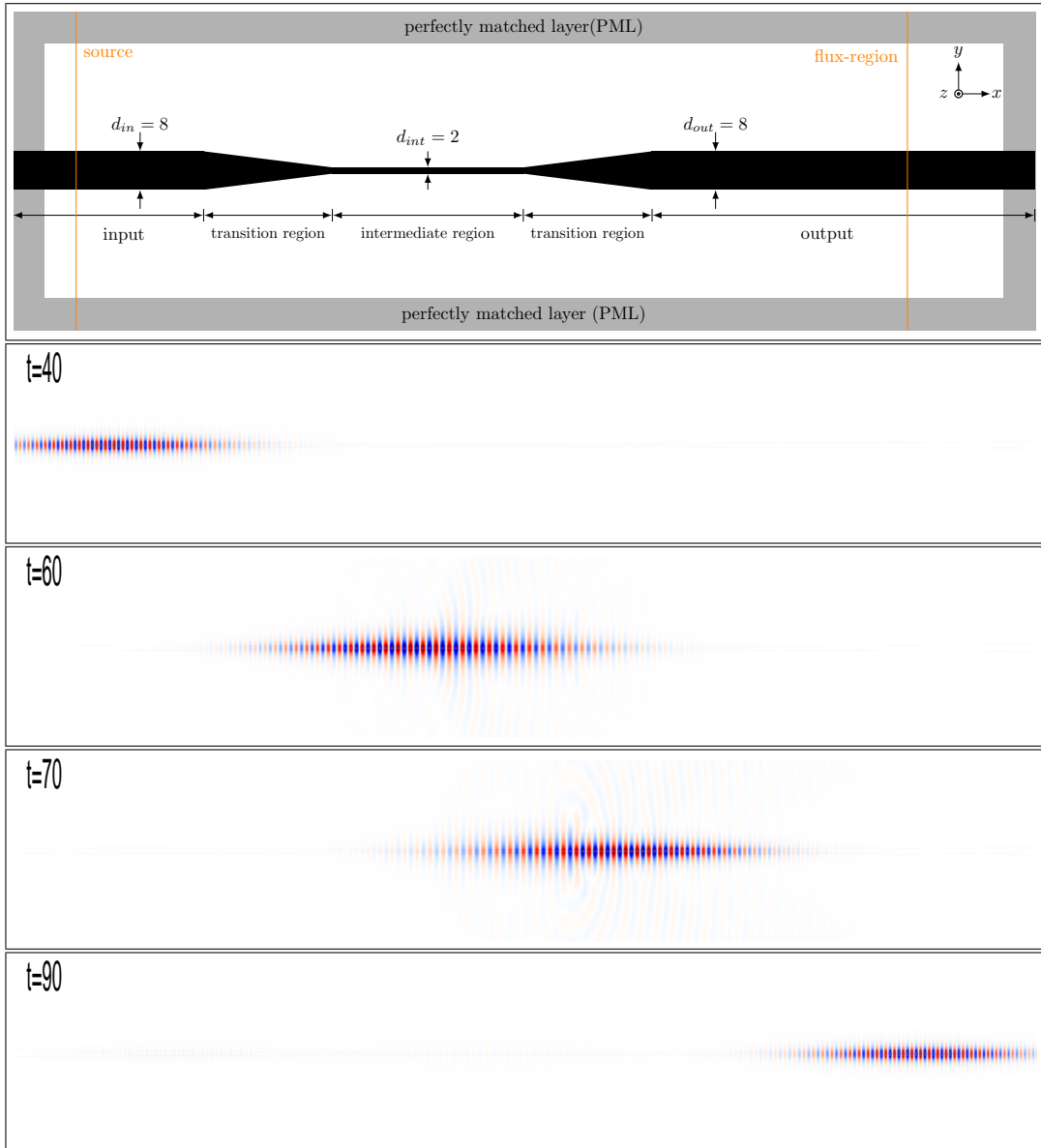


Figure 4.13. Dielectric profile of waveguide structure consisting of an input part, transition region, intermediate region and an output part. FDTD simulation of electric field component (E_z) for TE mode profile for four different time step for frequency $\tilde{\omega} = 0.1027$ and wave vector $\tilde{k} = 0.3$

The transmission values versus taper length is shown in Figure 4.14. Transmission values are plotted for waveguide which made of an input part with thickness $d_{in} = 12$, the intermediate region thickness is $d_{int} = 2$ and the output part with thickness $d_{out} = 12$. All region made of same material with dielectric constant $\epsilon_a = 13$. The background has dielectric constant $\epsilon_a = 2.25$. As it is seen from the transmission graph, after $L = 10a$ the transmission value reaches a steady state value. Further increasing taper length has no effect on increasing the transmission value.

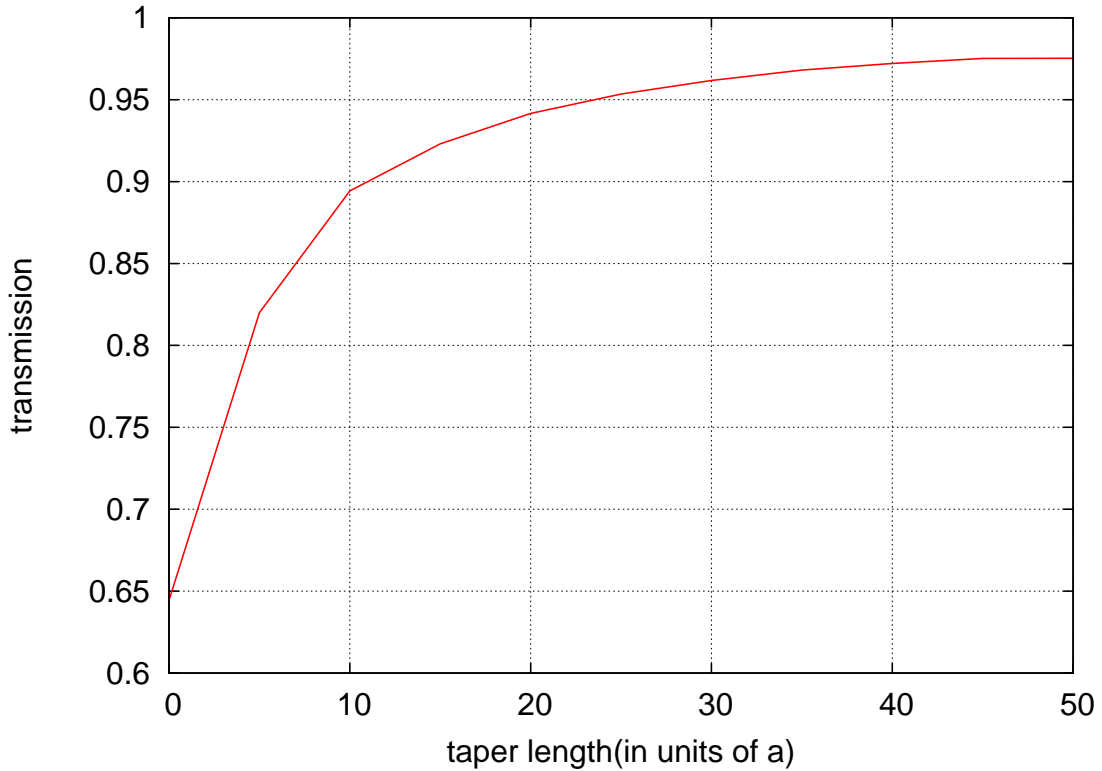


Figure 4.14. Transmission values versus taper length found by using FDTD simulation. Transmission value for butt-coupling ($L = 0a$) and adiabatic coupling ($L > 0a$) is shown.

In the butt-coupling case, the transmission value is found as %65. Direct transition cause %35 of optical power loss during coupling from input waveguide to intermediate waveguide and coupling from intermediate waveguide to output waveguide. This lost optical power either radiated to background fo reflected back at the interface where waveguides with different thickness met. In the adiabatic coupling case, the calculated transmission value is found as %97. This transition type only causes %3 of optical power loss.

CHAPTER 5

COUPLING SINGLE-SLAB TO 1D PHOTONIC CRYSTAL WAVEGUIDES

In this chapter we will study coupling process between single-slab waveguide and multi-slab waveguide. Transmission values for both butt-coupling and adiabatic coupling will be calculated using FDTD method. In the first section we will use taper region between single-slab waveguide and the defect line of multi-slab waveguide. In second section, besides using use taper region between single-slab waveguide and the defect line of multi-slab waveguide, we also will use taper geometry between background of single-slab waveguide to cladding of multi-slab waveguide. In the last section we will study a case when introducing taper region fails.

5.1. Tapering Only Defect Line

In this section we will study the waveguide structure shown in Figure 5.1. The structure consists of a single-slab waveguide with thickness $d_{in} = 8$ with dielectric constant $\epsilon_a = 13$ (called input region). The output region of this structure is made of multi-slab with thickness $d_{clad} = 1$ with dielectric constant $\epsilon_a = 13$, and the defect line is made by removing one slab and replacing it with a slab with thickness $d_{out,def} = 2$ with dielectric constant $\epsilon_d = 13$. The whole structure is placed in air background which has dielectric constant of $\epsilon_b = 1$.

In Figure 5.2 we see the band structure calculated for TE mode of multi-slab waveguide, (Black lines). The geometric parameters for multi-slab waveguide are, cladding thickness $d_{clad} = 1$, defect line thickness $d_{out,def} = 2$. The defect line and cladding dielectric constant is $\epsilon_a = \epsilon_d = 13$. The background dielectric constant is $\epsilon_b = 1$, air. We also show first guided mode of single-slab waveguide on the same graph (red line). The single-slab waveguide thickness is $d_{in} = 8$ with dielectric constant of $\epsilon_a = 13$ and it is immersed in a background with dielectric constant of $\epsilon_b = 1$, air. Intersection of blue dashed lines shows our operating frequency, first guided mode of single-slab waveguide, (input part), $\tilde{\omega} = \left(\frac{a}{2\pi c}\right) \omega = 0.1521$, and wave vector, $\tilde{k} = \left(\frac{a}{2\pi}\right) k = 0.5$. At this frequency, multi-slab waveguide has only one guided mode with wave vector $\tilde{k} = 0.30$.

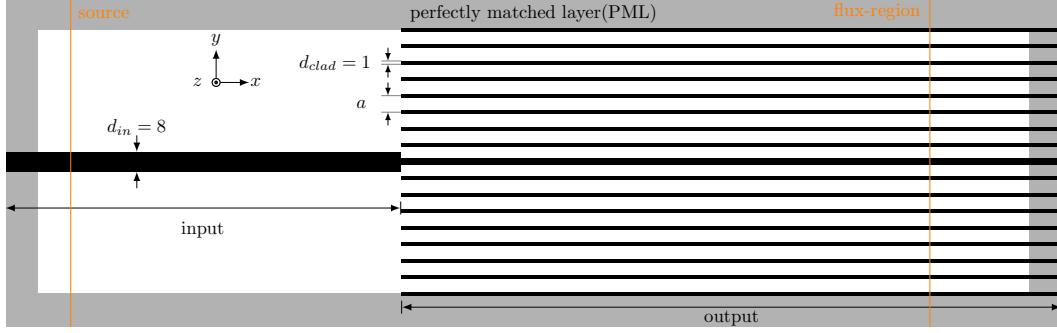


Figure 5.1. Dielectric profile of a waveguide that is made by a single slab waveguide with thickness of $d_{in} = 8$ and dielectric constant of $\epsilon_a = 13$, and a multi-slab waveguide with slab thickness of $d_{clad} = 1$ and dielectric constant $\epsilon_a = 13$ and defect line thickness of $d_{out,def} = 2$ with dielectric constant $\epsilon_d = 13$. The whole waveguide is immersed in air, $\epsilon_b = 1$.

When we send the guided mode of input part it will propagate along input part and when it comes to interface it will excite the first guided mode of output part. At the operating frequency, the guided mode of output region has wave vector of $\tilde{k} = 0.30$. Comparing this value with the operating mode wave vector we see that the difference in wave vectors is $\Delta\tilde{k} = 0.20$. The group velocities at the operating frequency and wave vectors are defined as $v_g = d\tilde{\omega}/d\tilde{k}$. Calculated group velocity, v_g , for multi-slab waveguide is 0.395 and calculated group velocity for single slab waveguide is $v_g = 0.270$. The mode profiles are same, (Both modes have the same even symmetry) except for the mode widths. So the main reasons for the optical power loss is the wave vector mismatch and group velocity mismatch. To be able to couple this two mode efficiently, we need to find a way that match the operating mode profile, group velocity and wave vector with the guided mode of output region.

In Figure 5.3 we see z -component of electric field (E_z) distribution for TE mode found by FDTD simulation. A Gaussian source is used to excite the operating mode with operating frequency and wave vector. An absorbing boundary layer is used to absorb the reflection from the boundary of computational region.

Propagation of electric field (E_z) for TE mode along the structure for four different time step is shown in the Figure 5.3. We send first guided mode of input part which has frequency of $\tilde{\omega} = 0.1521$ at wave vector $\tilde{k} = 0.5$. Transmitted power in the output region is calculated and normalized with the calculated power of single slab waveguide without the output region. The transmission value for this structure is 91.2%. The loss is clearly seen from the FDTD simulation snapshot, the wave that is propagating in the cladding and the wave that is propagating back in the input region.

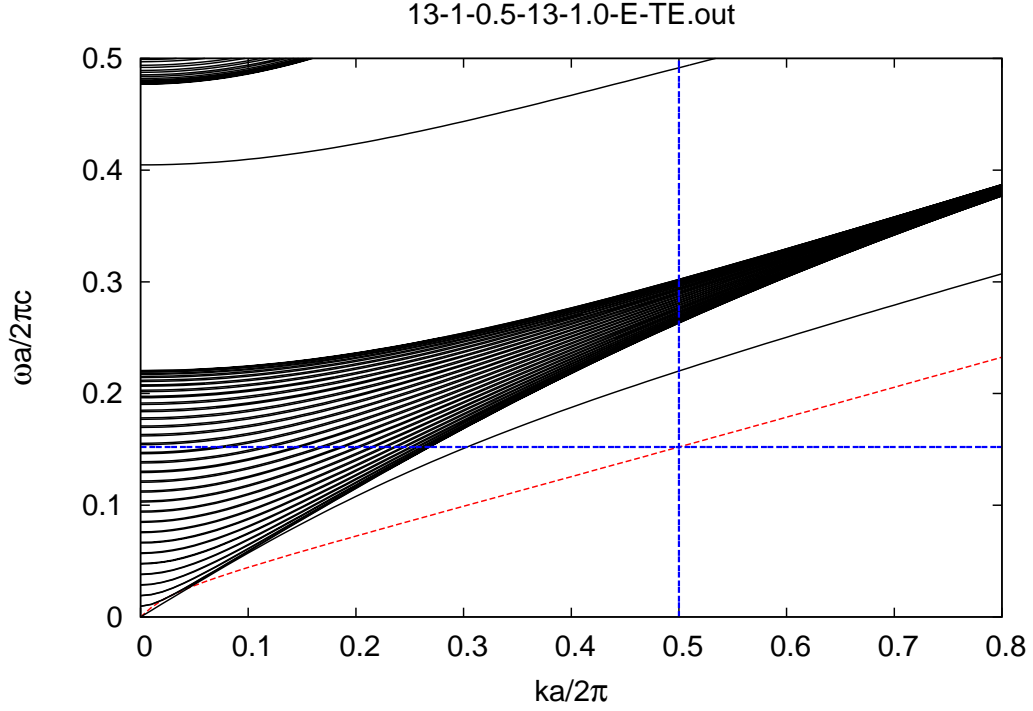


Figure 5.2. Band structure calculated for TE mode of multi-slab waveguide (Black lines). The waveguide is made by slabs of thickness $d_{clad} = 1$ with dielectric constant $\epsilon_a = 13$. The defect line has thickness of $d_{out,def} = 2$ with same dielectric constant with cladding slabs. Red dashed line is first guided mode of input part (single slab waveguide) which has thickness of $d_{in} = 8$ with dielectric constant $\epsilon_a = 13$. The background is air, ($\epsilon_b = 1$).

In the case of butt coupling, when there is no transition region, the guided mode of input region directly coupled from single-slab waveguide to multi-slab waveguide. Direct transition from a dielectric medium to another dielectric medium that have different dielectric properties, as can be seen from the simulation, causes some of the optical power to refract and some of the optical power to reflect back at the interface. As shown in (Mekis and Joannopoulos, 2001), butt-coupling efficiency can be found using, $\eta = \frac{4\tilde{k}_{in}\tilde{k}_{out}}{(\tilde{k}_{in}+\tilde{k}_{out})^2}$ where \tilde{k}_{in} and \tilde{k}_{out} are the wave vector of the single-slab and multi-slab waveguides. As can be seen from the this equation, unity transmission is possible only if the wave vectors of both region are equal, $\tilde{k}_{in} = \tilde{k}_{out}$.

Now we introduce trapezoidal transition region between single-slab waveguide, the input region, and defect line of multi-slab waveguide, the output region. The structure is shown in Figure 5.4. The transition region thickness gradually decreased form input waveguide thickness to thickness of defect line of output waveguide.

In Figure 5.4 we see electric field distribution, E_z , found by FDTD simulation for

TE mode taken at four different time step. In the case of tapered structure, the incoming mode transferred to output guided mode in a series of intermediate thickness. As wave propagate in the taper, it sees dielectric structure that is slowly changing in electromagnetic properties. This slow change in geometry of waveguide serve as a medium that transform wave vectors, group velocity and mode profile as slowly as possible so that the loss of optical power minimized. Transmission value when we introduce taper with length of $20a$ unit cell long is 99.2%. By comparing this with the transmission value for the structure without taper, we see transmission value is increased by 8%. Back reflection and radiation to background are almost no longer exist. The incoming mode is smoothly coupled to output waveguide with almost no loss.

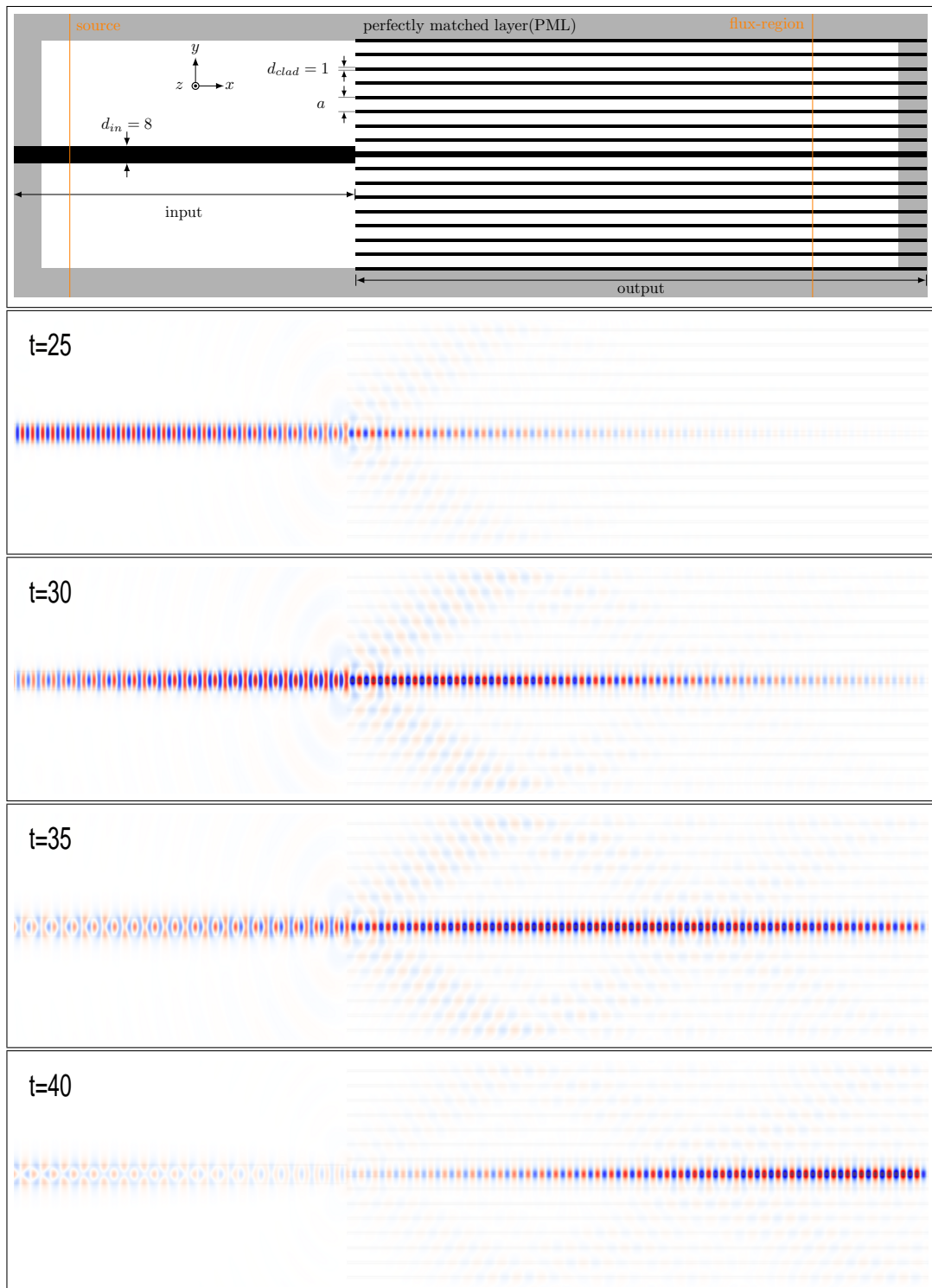


Figure 5.3. Dielectric profile of a single slab waveguide and a multi-slab waveguide. Mode profile of electric field (E_z) found by FDTD simulation. The field profiles are taken at four different time, in this structure there is no taper region introduced.

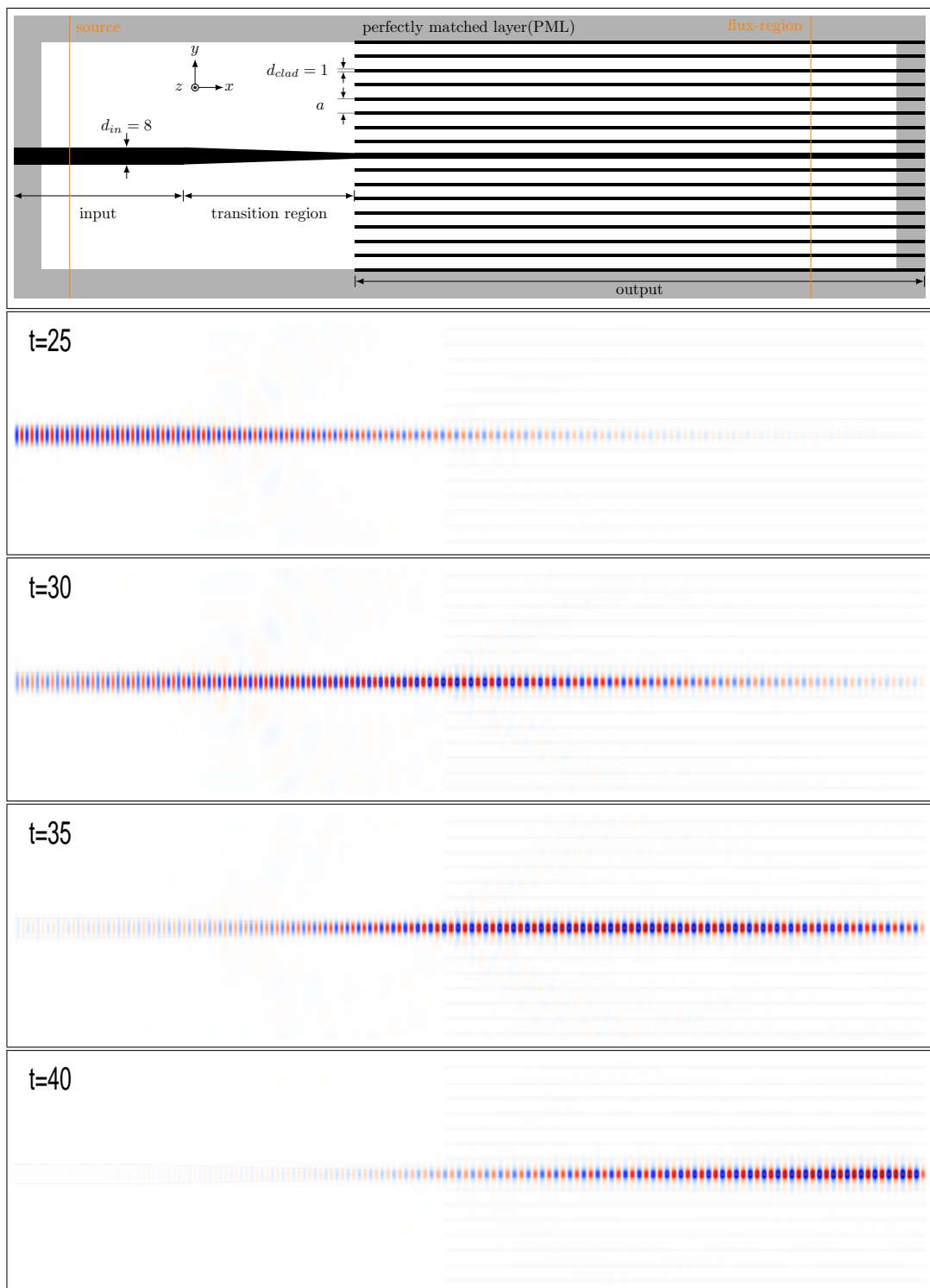


Figure 5.4. FDTD simulation of structure, consist of a single-slab waveguide, a taper region, and multi-slab waveguide. The single-slab waveguide on left called input part we introduce a taper region which gradually change from $d_{in} = 8$ to $d_{out,def} = 2$.

In Figure 5.5 we show transmission versus taper length for four different single slab waveguide thickness (input part) while output part thicknesses are kept constant. The cladding thickness of Multi-slab waveguide is $d_{clad} = 1$ and the defect line thickness of multi-slab waveguide is $d_{out,def} = 2$.

When the thickness of single slab waveguide is taken as $d_{in} = 4$ the transmission value without taper region introduced, $L = 0$, is around 99%. When the thickness of single slab waveguide is taken as $d_{in} = 10$ this time the transmission value is, without taper region, is around 87%. So in the case of butt coupling, $L = 0$, the transmission value decreases with increasing ratio between single slab waveguide thickness to defect line thickness of multi-slab waveguide. When we introduce taper region between two waveguide, as can be seen from transmission graph the transmission values increases with increasing taper length. The transmission values shown in this figure shows that the coupling efficiency between single-slab waveguide and multi-slab waveguide can be increased by using taper region.

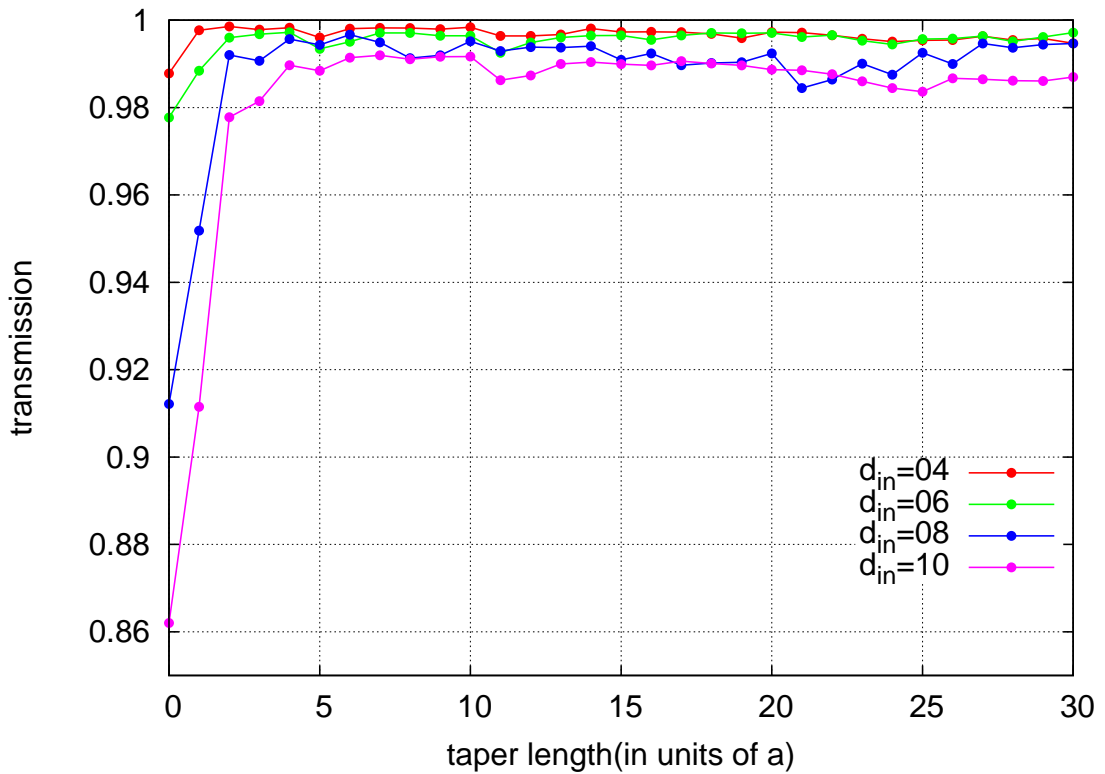


Figure 5.5. Transmission versus taper length. The output thickness are kept constant while we increase the single slab waveguide thickness from $d_{in} = 4$ to $d_{in} = 10$.

5.2. Single slab to Multi Slab Coupling-A different Approach

In previous section we have used trapezoidal shaped taper structure to use as an transition region to convert incoming mode to output mode of multi-slab waveguide. These is one of the possible taper choice. Another possible transition region is that, besides tapering the single-slab and defect line of multi-slab waveguide, we can change the cladding thickness of output waveguide from zero to its final value.

In Figure 5.6 we see dielectric structure of waveguide we are going to work with in this section. Single slab waveguide on the left hand side has thickness of $d_{in} = 10$, the multi-slab waveguide on the right hand side is made of slabs with thickness $d_{clad} = 1$, and the defect line has thickness of $d_{out,def} = 2$. Both single slab and multi slab waveguide have same dielectric constant of $\epsilon_a = 13$. The background has dielectric constant of $\epsilon_b = 1$.

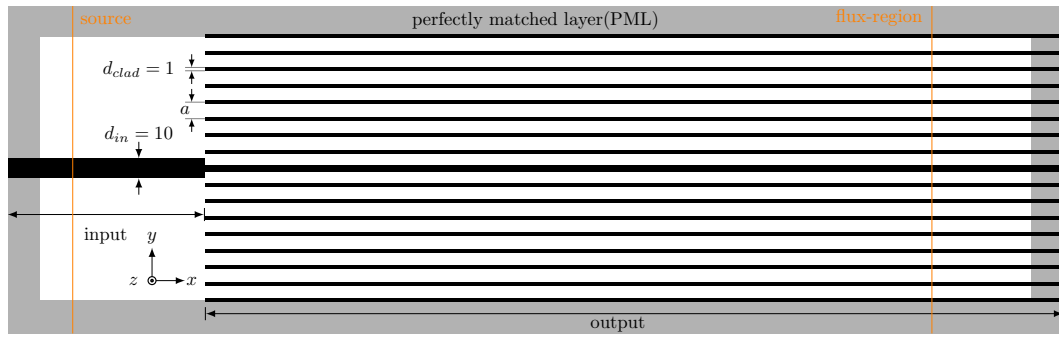


Figure 5.6. Dielectric profile of structure consist of a single-slab waveguide of thickness $d_{in} = 10$ with dielectric constant $\epsilon_a = 13$ (input) and multi-slab waveguide consist of cladding slabs of thickness $d_{clad} = 1$ with dielectric constant $\epsilon_a = 13$ and defect line thickness of $d_{out,def} = 2$ with dielectric constant $\epsilon_a = 13$. The background has dielectric constant of $\epsilon_b = 1$ (output).

In Figure 5.7 We see band structure of multi-slab waveguide calculated for TE mode (black lines) and we also show first guided mode of single slab waveguide (red line). The intersection of blue lines indicate our operating mode with the frequency $\tilde{\omega} = 0.1516$ and wave vector $\tilde{k} = 0.5$. As we see from graph there is only one guided mode of multi-slab waveguide at this frequency. Both modes have same spatial symmetry, but their group velocities and wave vectors are different. These two difference is the main reason for the coupling inefficiency.

The operating mode and the guided mode supported by output region has same spatial symmetry, both modes are even. Another difference between these two mode

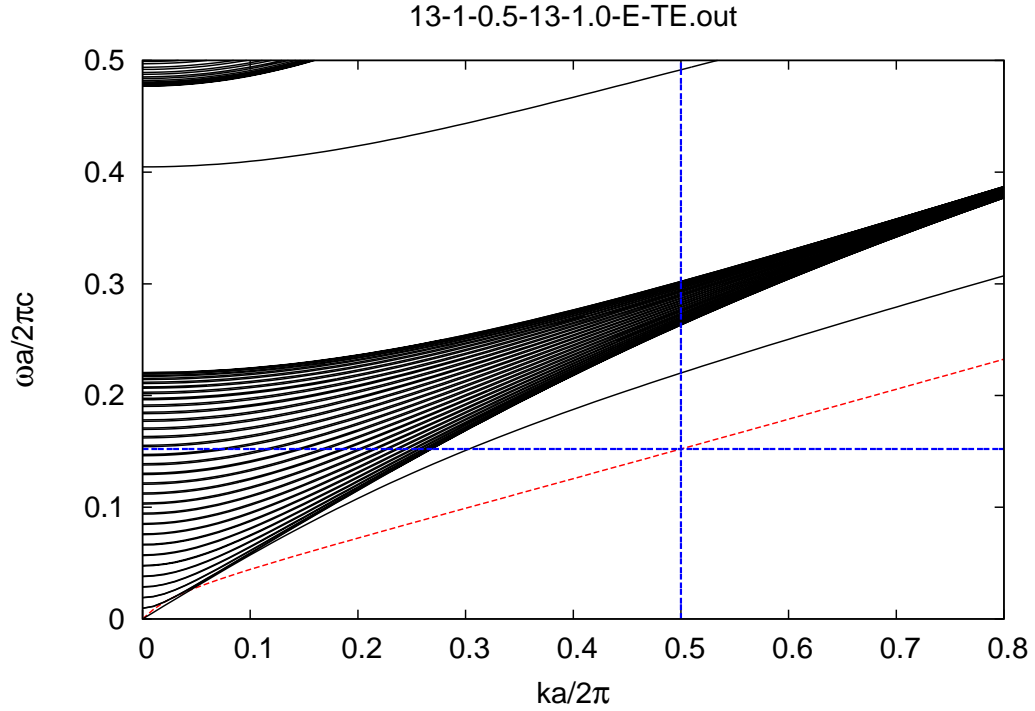


Figure 5.7. Band Structure calculated for TE mode of multi-slab waveguide with cladding and defect line thickness of $d_{clad} = 1$, $d_{out,def} = 2$ respectively. The dielectric constants are $\epsilon_a = 13$ and $\epsilon_d = 13$, black lines. The red dashed line is the first guided mode of input part (single slab waveguide) which has thickness of $d_{in} = 10$ and dielectric constant $\epsilon_a = 13$.

is their group velocity. As we see from the band structure, the operating mode group velocity is smaller than the guided mode of output region. And both mode have different wave vector at the operating frequency.

In Figure 5.8 we see electric field (E_z) distribution of TE mode found by FDTD simulation. Transmission value for this structure is 81.8%. This simulation was run without taper region with 30 resolution per period. As we see without taper region 18.2% of optical power radiated to background and reflection back at the position where two waveguides meet.

Besides tapering only defect line, there is an alternative taper design for the structure we have studied in previous section. Now we will taper the cladding too. The Figure 5.9 shows the structure we are going to work with. The cladding thickness of multi-slab waveguide gradually changes from zero, $d_{clad} = 0$, to its final thickness, $d_{clad} = 1$. And as it is done in the previous section, the thickness of single-slab waveguide is gradually changed to thickness of defect line of multi-slab waveguide.

In Figure 5.9 we see electric field distribution of TE mode calculated by FDTD simulation. The simulation were done with taper region length of $L = 50a$. Simulations are performed with 30 resolution per period. Transmission value for this structure is 98.3%. Comparing this with the transmission found when no taper region used we see that transmission value increased by 16.5%.

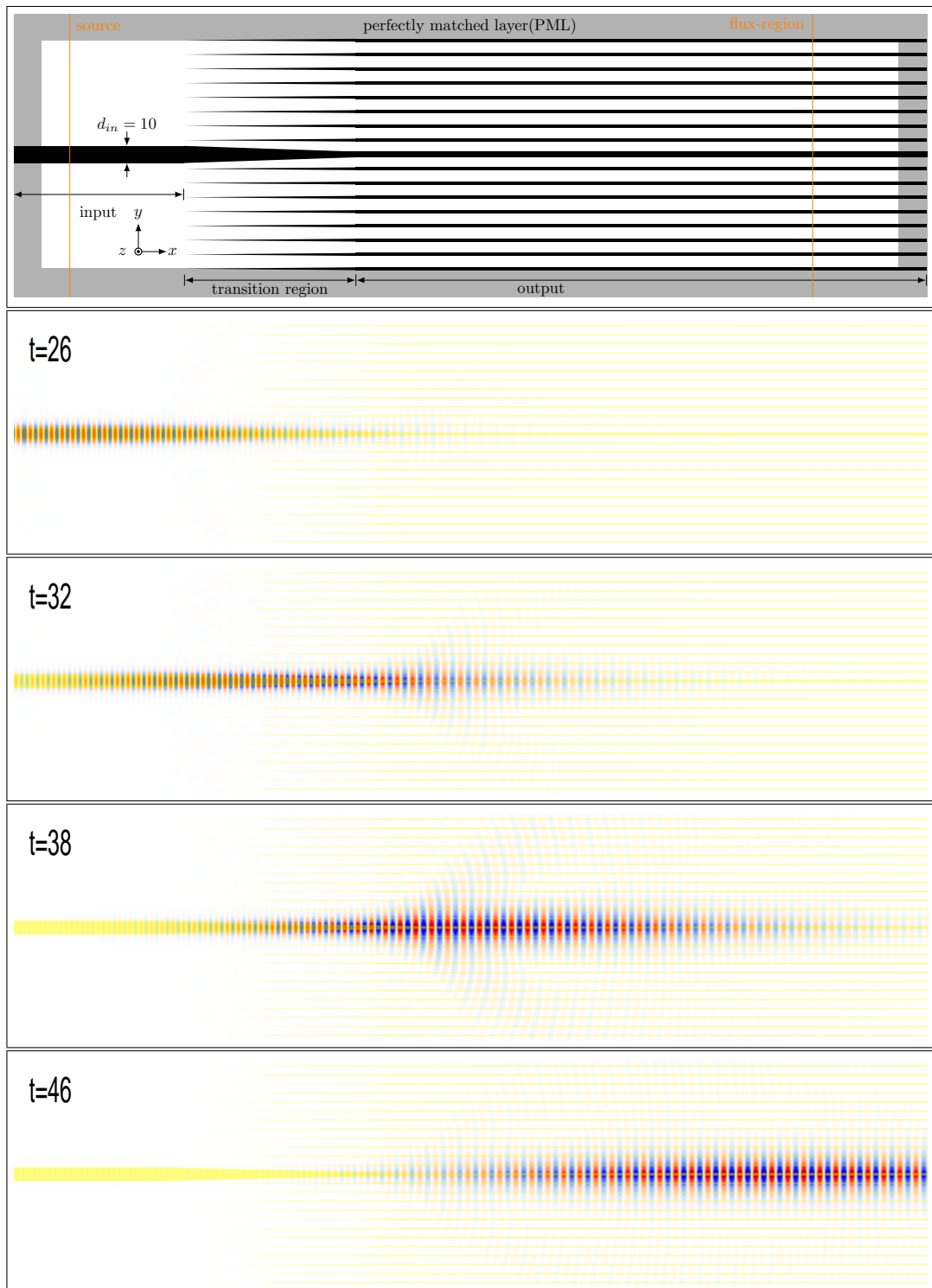


Figure 5.9. FDTD simulation of z -component of electric field of TE mode, in this structure there we introduced taper region with 50 unit cell long. Dielectric structure, which consist of a single- slab waveguide (input), a taper region and multi-slab waveguide (output).

In Figure 5.10 we show transmission versus taper length. In the butt coupling case the transmission value is around 82%. As can be seen from the graph the transmission value increases with increasing taper length, starting from $L = 0a$ to $L = 50a$, and finally it reaches above 98%. The transmission curve for this structure needs longer taper length to reach a steady state value.

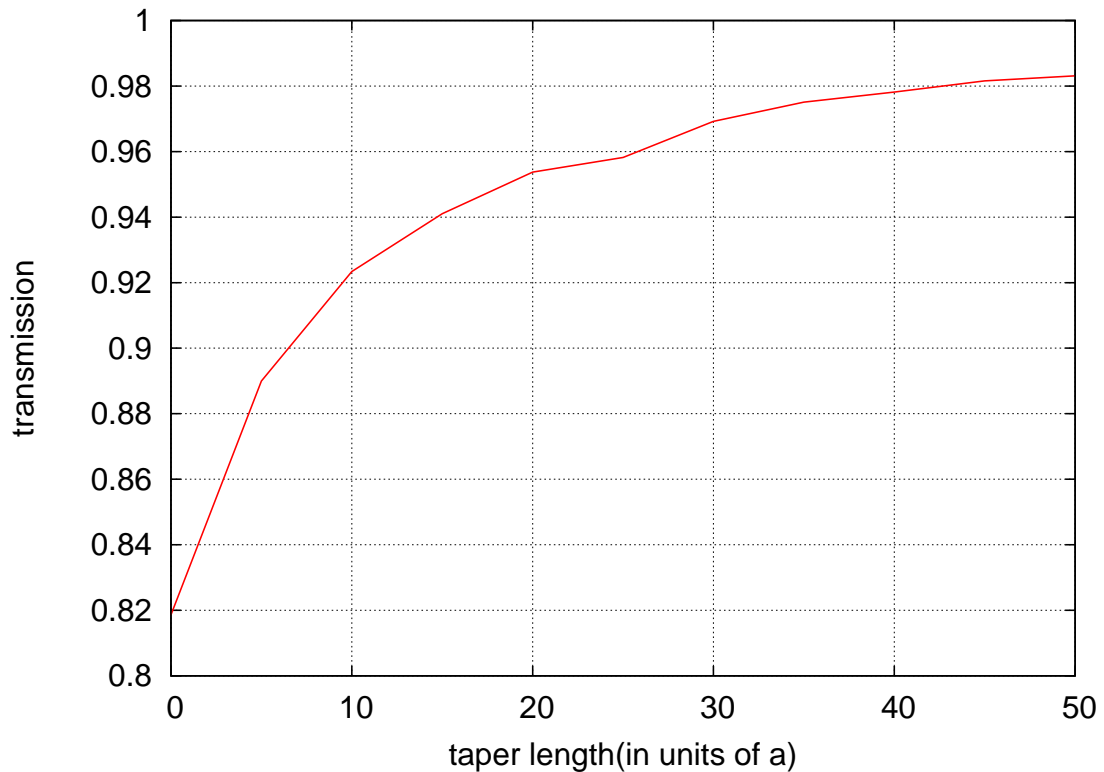


Figure 5.10. Transmission values versus taper length calculated with FDTD method. Butt coupling and adiabatic coupling situations are shown, $L = 0a$ and $L = 50a$.

Comparing this graph with the one we show in Figure 5.2 we can conclude that the first kind of taper geometry is more suitable because of the required adiabatic condition, since the first transition type require shorter taper length to reach the steady state of transmission values.

5.3. Taper Fail

Now we will run our simulation and calculate transmission values without and with taper region introduced to study a case when using taper region does not increase transmission values. An important point that must be taken into account is, as it is stated in (Johnson et al., 2002), besides requirement that the operating mode must not be evanescent for any intermediate point of the taper, the mode must be guided for every intermediate thickness of taper. This is important because if operating mode is a part of continuum then all mode will radiate to background.

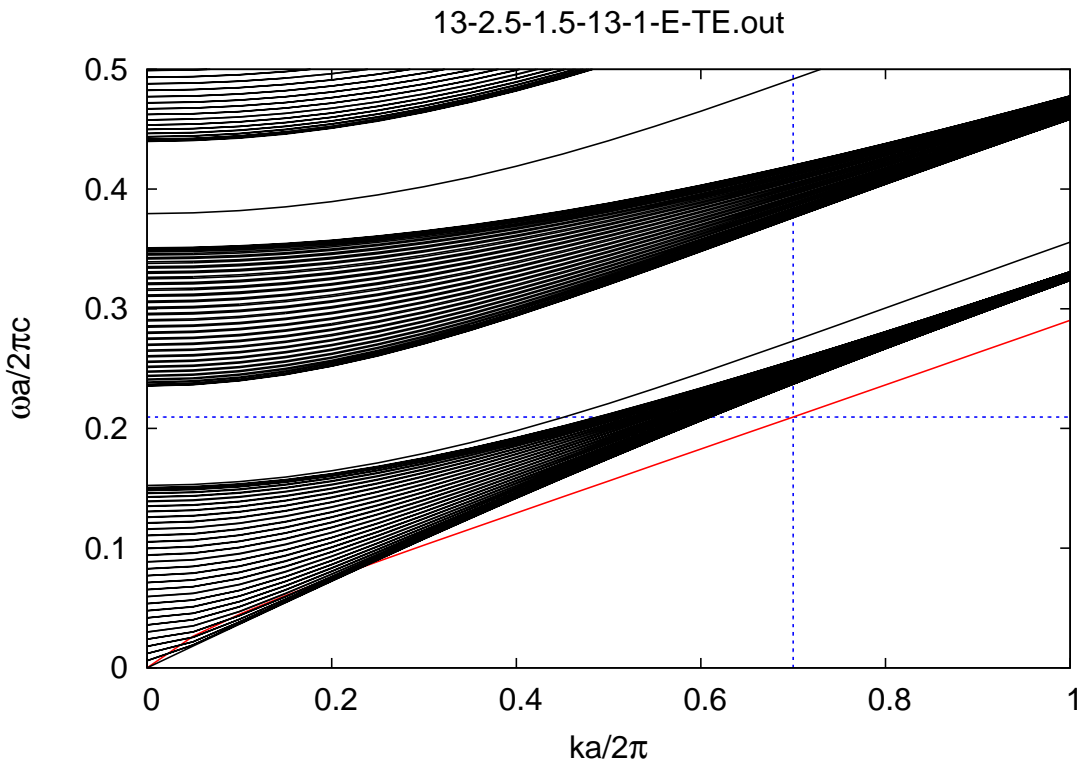


Figure 5.11. Band Structure calculated for TE mode of multi-slab waveguide, cladding thickness is $d_{clad} = 3$, cladding dielectric constant is $\epsilon_a = 13$, defect line thickness is $d_{def} = 2$, defect line dielectric constant is $\epsilon_d = 13$. The background dielectric constant is $\epsilon_b = 2.5$. Red line is first guided mode of input part (single slab waveguide) which has thickness of $d_{in} = 8$ and dielectric constant is $\epsilon_a = 13$ immersed in a background with dielectric constant $\epsilon_b = 2.5$. The intersection of blue lines indicate the operating mode.

In Figure 5.11 we see band structure of multi-slab waveguide (output part), shown by black lines, calculated for TE mode. The thickness of cladding is $d_{clad} = 3$ and the defect line has thickness of $d_{out,def} = 2$. Both cladding and defect line have same

dielectric constant of $\epsilon_a = \epsilon_d = 13$. The background material has dielectric constant of $\epsilon_b = 2.5$. We also show first guided mode of single-slab waveguide (input part), which is indicated by red dashed line. Single slab waveguide thickness is $d_{in} = 8$ and the dielectric constant is $\epsilon_a = 13$. Single-slab waveguide is immersed in a background of dielectric constant of $\epsilon_b = 2.5$. The intersection of blue dashed lines indicate the operating mode with frequency $\tilde{\omega} = 0.2095$, and wave vector, $\tilde{k} = 0.7$. As can be seen from the band graph there is no guided mode of multi-slab waveguide below continuum region. First guided mode of multi slab waveguide is above the continuum region so if we want to excite this mode with the operating mode, we first must move through the continuum region and this will cause optical power to couple those continuum modes as well.

The dielectric structure of waveguide is shown in Figure 5.12. In Figure 5.12 we also see z -component of electric field, E_z , of TE mode found by FDTD simulation. The snapshots are taken for four different time steps. In this simulation there is no taper region introduced. The transmission value for this structure is 52.4%. Which shows that without taper region introduced almost half of the optical power coupled to background and reflected back at interface.

In Figure 5.13 we see dielectric profile of structure with taper region introduced. All geometric parameters and dielectric constant are same with the structure shown in Figure 5.12. The only difference here is the transition region connecting the Single slab waveguide with the defect line of multi-slab waveguide and the transition region connecting the background of single slab waveguide to the multi-slab waveguide cladding. The cladding slab thickness are increased from zero to its final values.

In Figure 5.13 we see FDTD simulation of electric field, E_z , of TE mode. The electric field distributions are taken at four time steps. In this simulation the taper region length is $L = 50a$ where a is lattice constant. The transmission value in this case is 3.1% as seen from simulation, when we increases the taper length 96.9% of incoming mode coupled to radiation modes. In this structure when taper region thickness is gradually changing at intermediate point it forms a perfect structure. Since there is no propagation mode for perfect structure, then all incoming mode radiates to background. This situation is clearly seen from time snapshot taken at $t = 38$ of the Figure 5.13.

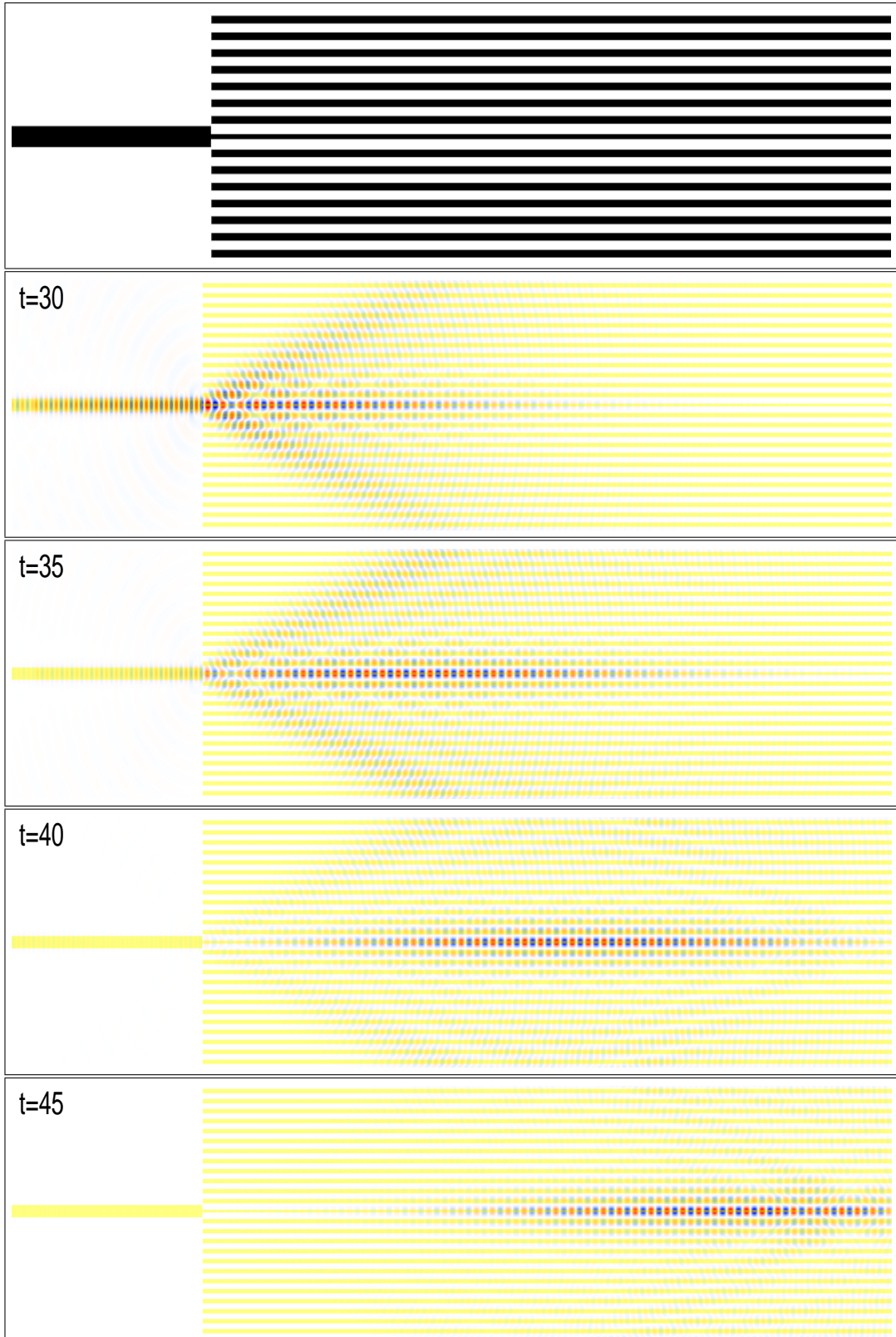


Figure 5.12. Dielectric structure, which consist of a single-slab waveguide (input), multi-slab waveguide (output). Electric field distribution, E_z , of TE mode found by FDTD simulation. In this structure there is no taper region.

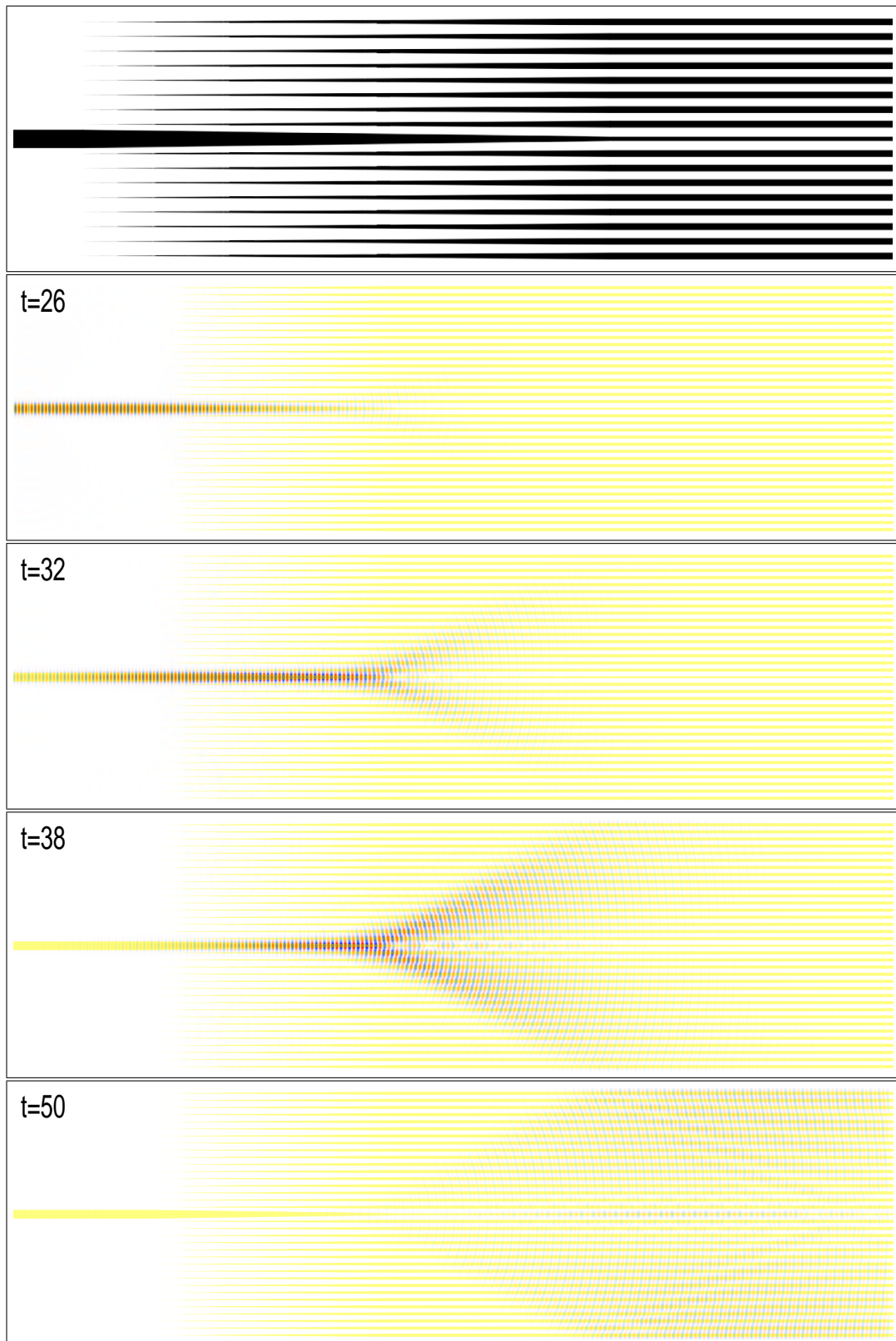


Figure 5.13. FDTD simulation of TE mode, z -component of electric field, E_z , in this structure we introduced taper region which gradually changing their thickness. Dielectric structure, which consist of a single-slab waveguide (input), a taper region and multi-slab waveguide (output).

In Figure 5.14 we show transmission versus taper length. The transmission value for the butt coupling is found as 52.4%. As can be seen from the graph transmission values decreasing as we increase taper length. To be able to excite the first guided mode of multi-slab, the operating mode need to go through continuum region as seen from band structure. This decrease in transition value is explained by turn on bulk crystal. At a certain point along transition region the multi-slab waveguide forms a perfect multi-slab waveguide which has no propagating, guided, modes. At this point all incoming optical power couples to radiation modes. In the adiabatic limit, which is in this case with an infinitely long taper region the transmission value will be zero.

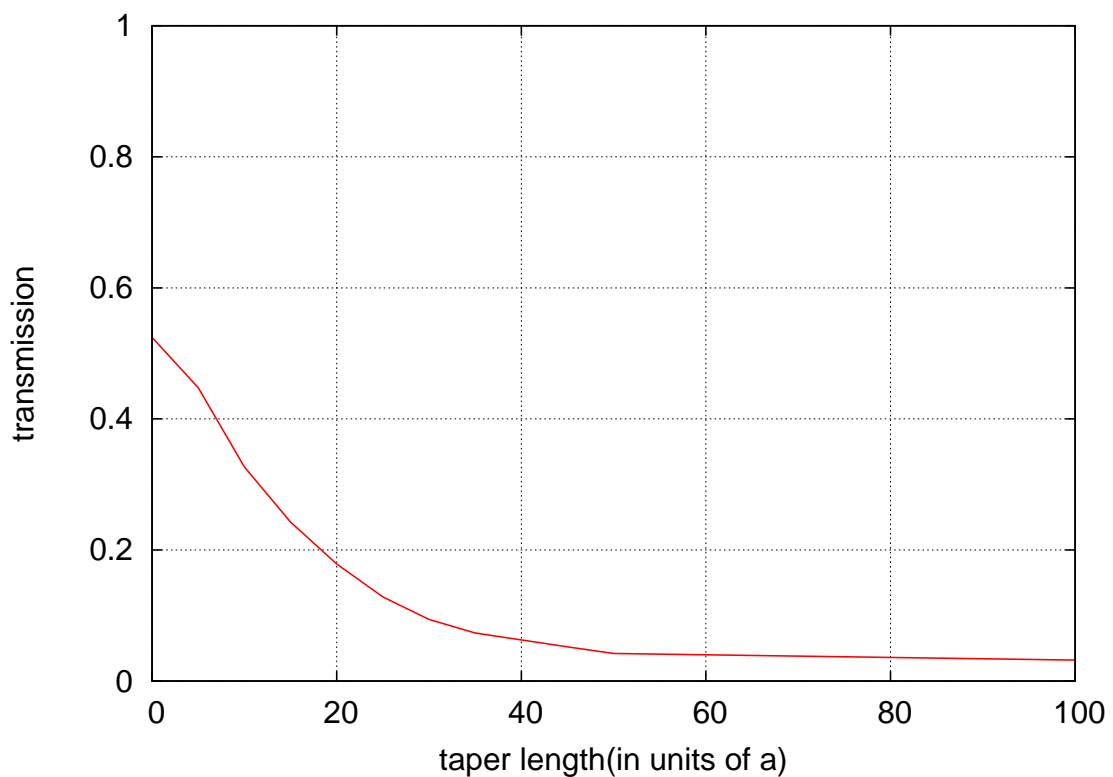


Figure 5.14. Transmission values versus taper length of a waveguide structure that is its guided mode is above continuum region. Taper length changed from $L = 0a$ (without transition region) to $L = 100a$ (with transition region).

CHAPTER 6

COUPLING MULTI-SLAB TO MULTI-SLAB WAVEGUIDE

In this chapter we will study coupling efficiency of light between two multi-slab waveguide. In first section we will work with multi-slab waveguides that have different lattice constant, cladding thickness, and defect line thickness. Simulation will be performed for both untapered and tapered waveguides to find transmission values. In second section the waveguides we will work with have the same lattice constant but different thickness of slabs and line defects. Again the simulation will be performed for untapered and tapered waveguides to calculate transmission values.

6.1. Coupling Between Two Different Waveguide

In Figure 6.1 we see the waveguide structure that is made by two different waveguide. The waveguide on the left-hand side is made by slabs of thickness $d_{in,clad} = 2$ with dielectric constant $\epsilon_a = 13$, the defect line thickness is $d_{in,def} = 6$ with dielectric constant $\epsilon_d = 13$ (input part) and lattice constant a_1 . The waveguide on the right-hand side is made by slabs of thickness $d_{out,clad} = 1$ with dielectric constant $\epsilon_a = 13$, the defect line thickness is $d_{out,def} = 2$ with dielectric constant $\epsilon_d = 13$ (output part) and lattice constant $a_2 = 0.5a_1$. The background of this structure is air ($\epsilon_b = 1$).

In Figure 6.2 we see band structure of multi-slab waveguide calculated for TE mode with lattice constant of $0.5a$, the thickness of slabs are $d_{out,clad} = 1$ and thickness of defect line is $d_{out,def} = 2$, both slabs and defect line have same dielectric constant of $\epsilon_a = \epsilon_d = 13$. The waveguide is placed in air background, ($\epsilon_b = 1$). We also show our operating mode which is the first guided mode of, (red line), the waveguide with lattice constant of a which is made by slabs of thickness $d_{in,clad} = 2$ and the defect line is made by a slab of thickness $d_{in,def} = 6$. Both slabs and defect line has same dielectric constant $\epsilon_a = \epsilon_d = 13$. The background again is air. Intersection of blue dashed lines indicate our operating frequency which is $\tilde{\omega} = 0.1351$ and wave vector $\tilde{k} = 0.4$. At the operating frequency the output waveguide is single mode.

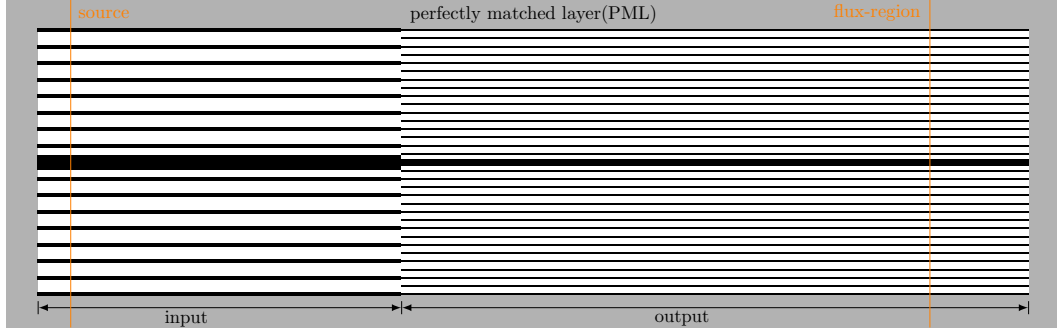


Figure 6.1. The waveguide on the left-hand side has lattice constant a_1 with cladding and defect line thickness of $d_{in,clad} = 2$, $d_{in,def} = 6$ respectively. The waveguide on the right-hand side has lattice constant $a_2 = 0.5a_1$ with cladding and defect line thickness of $d_{out,clad} = 1$, $d_{out,def} = 2$ respectively. Both waveguides are immersed in air background, $\epsilon_b = 1$.

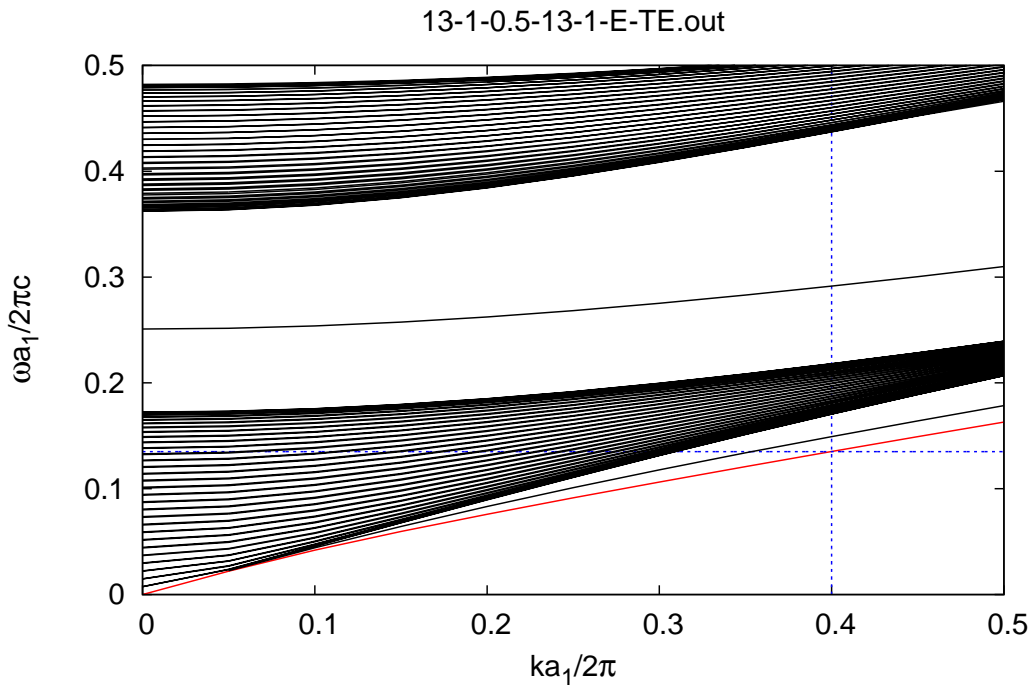


Figure 6.2. Black lines represent the band structure calculated for TE mode of multi-slab waveguide (the output waveguide) made by slabs of thickness $d_{out,clad} = 1$ with dielectric constant $\epsilon_a = 13$. The defect line has thickness of $d_{out,def} = 2$ with same dielectric constant of cladding, $\epsilon_d = 13$. The background is air, ($\epsilon_b = 1$). The red line represents the first guided mode of multi-slab waveguide (the input waveguide) which has geometric parameters, $d_{in,clad} = 2$, $d_{in,def} = 6$, and the dielectric constants of cladding and defect line are, $\epsilon_a = \epsilon_d = 13$. The background is air, $\epsilon_b = 1$.

In Figure 6.3 we see z -component of electric field of TE mode found by FDTD simulation. In this simulation there is no taper region between two waveguides. Our operating mode frequency is $\tilde{\omega} = 0.1351$ and the operating mode wave vector is $\tilde{k} = 0.4$. At the operating frequency the wave vector of output waveguide is $\tilde{k} = ??$. A Gaussian mode source used to generate the operating mode.

As shown in Figure 6.3, we took time snapshot of the electric field propagation (E_z) along the waveguide structure for four different time step. At $t = 26$ the operating mode propagate along the input waveguide since it is the guided mode of this region. At $t = 32$ we see the mode just has arrived to the interface between two waveguides and start to excite some of guided mode of output region, and some of the radiation modes. At $t = 38$ we see the excited mode of output part propagating along the waveguide. Finally, at $t = 45$ we see the excited mode that is propagating along the output waveguide. At this last snapshot we also see some of the wave are propagating in input waveguide which are reflected from the interface.

In Figure 6.4 we see dielectric structure with taper region introduced. The geometric parameters are same with the waveguide structure shown in Figure 6.3. The only difference here is the transition region that is introduced between two waveguides. We connect slabs of input part with slabs of output part in such a way that both cladding slab thickness and lattice constants of input waveguide change slowly from the input waveguide parameters to output waveguide parameters. The defect lines of both waveguides are joined to each other by trapezoids as we did in the previous sections.

In Figure 6.4 we show FDTD simulation of electric field, E_z for TE mode with taper region introduced. Again a Gaussian mode source is used to generate the operating mode. This simulation performed with 30 resolution per period. The taper region length in this structure is $L = 50a$ where a is defined as lattice constant. Calculated transmission value for this structure is 97.5%. Comparing this value with the transmission value we found for the structure that when there is no taper region introduced, we see the coupling efficiency increased by 10.6%.

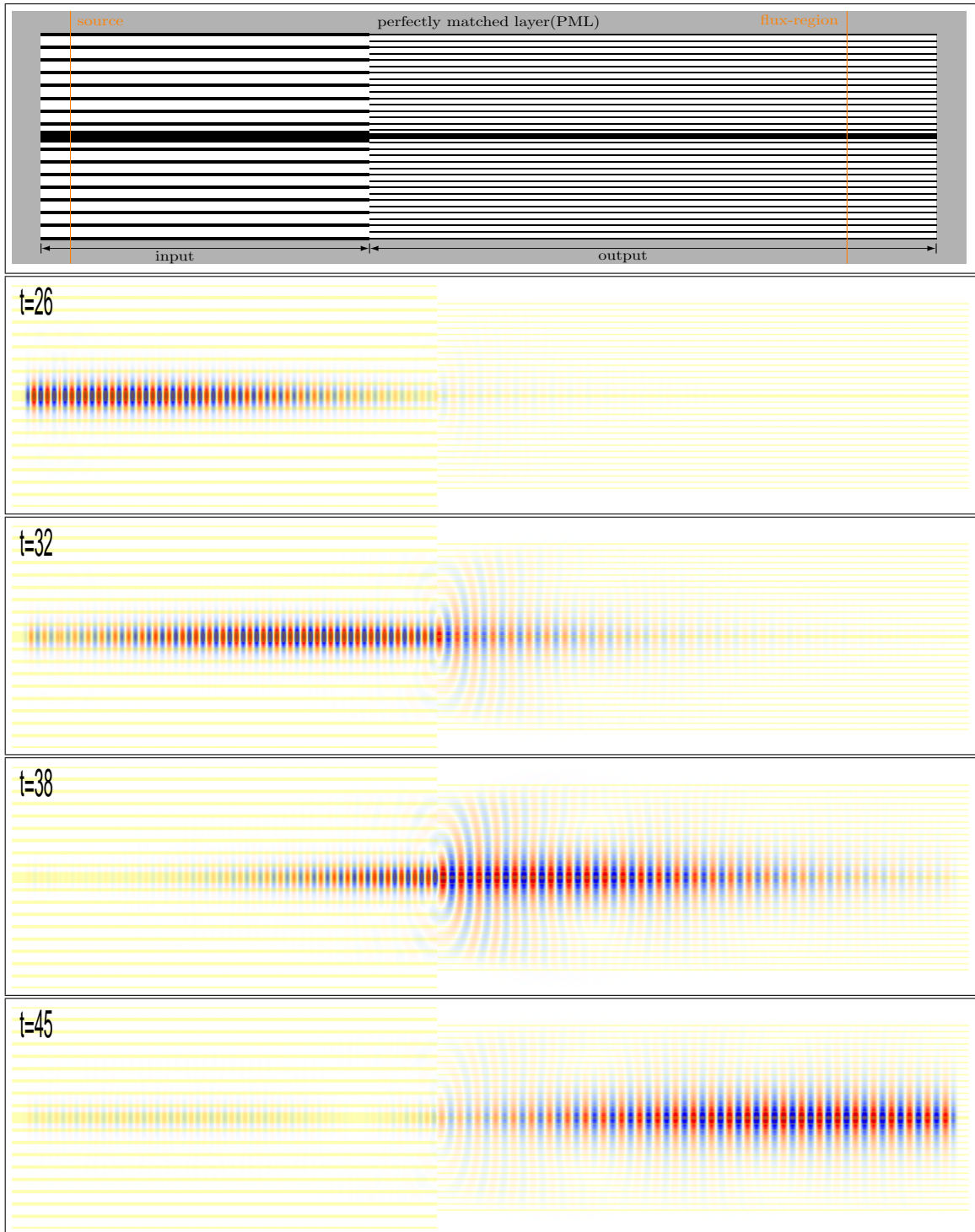


Figure 6.3. Dielectric structure of two multi-slab waveguide. The waveguide on the left-hand side has lattice constant a with cladding and defect line thickness of $d_{in,clad} = 2$, $d_{in,def} = 6$ respectively. The waveguide on the right-hand side has lattice constant $0.5a$ with cladding and defect line thickness of $d_{out,clad} = 1$, $d_{out,def} = 2$ respectively. Both waveguides are immersed in air background, $\epsilon_b = 1$. Both waveguide cladding and defect line have the same dielectric constant of $\epsilon_a = \epsilon_d = 13$. FDTD simulation of z -component of electric field (E_z) for TE mode with frequency $\tilde{\omega} = 0.1351$ and wave vector $\tilde{k} = 0.4$.

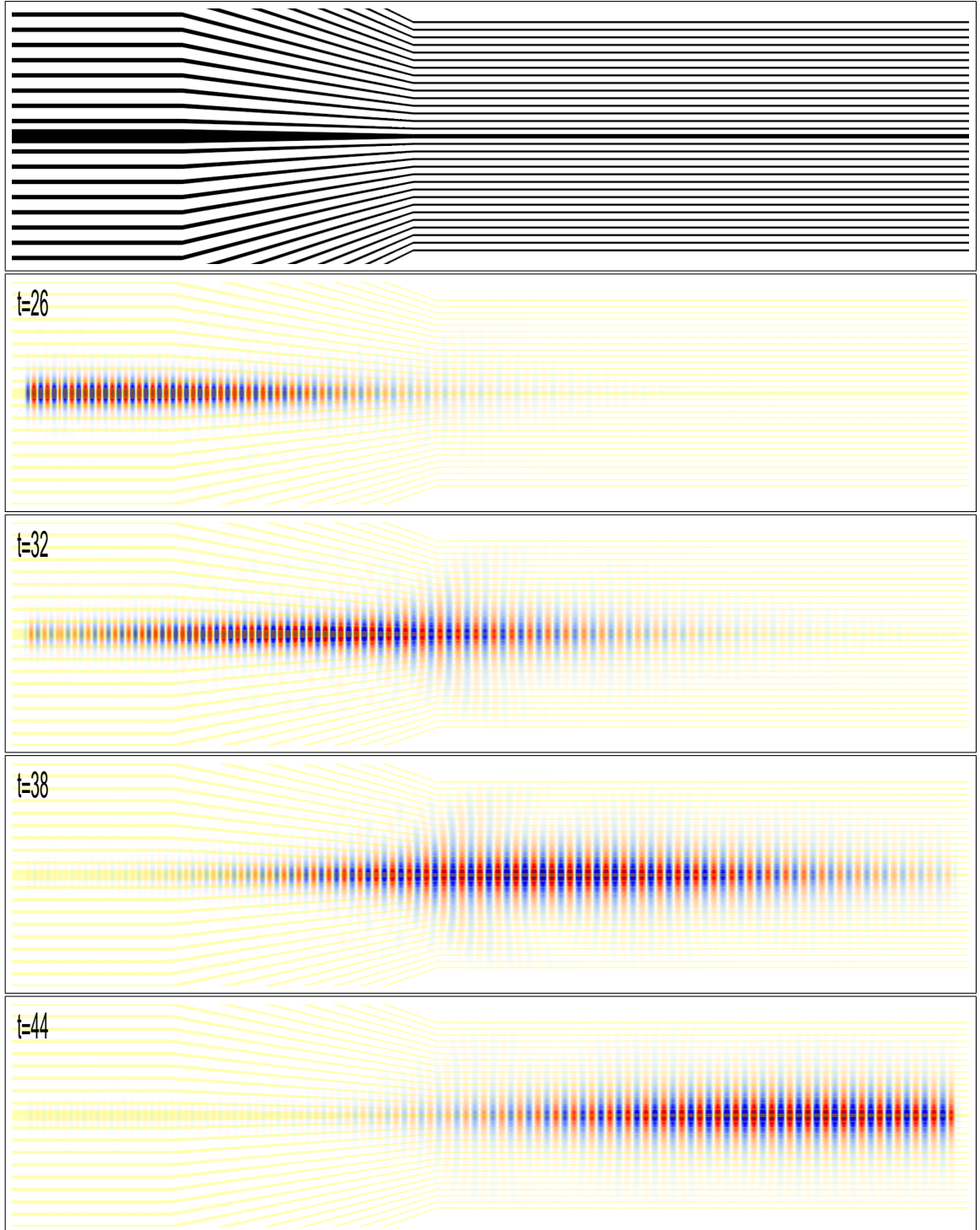


Figure 6.4. Dielectric profile of the waveguide structure with taper region introduced. The waveguide on the left-hand side is made by slabs of thickness $d_{in,clad} = 2$ with dielectric constant $\epsilon_a = 13$ and the defect line of thickness $d_{in,def} = 6$ with dielectric constant $\epsilon_d = 13$. The waveguide on the right-hand side is made by slabs of thickness $d_{out,clad} = 1$ with $\epsilon_b = 13$ and the defect line is made by a slab of thickness $d_{out,def} = 2$ with $\epsilon_a = 13$. The background is air, ($\epsilon_b = 1$). FDTD simulation of z -component of electric field for TE mode with frequency $\tilde{\omega} = 0.1351$ and wave vector $\tilde{k} = 0.4$. In this structure we introduced taper region of $L = 50a$ long.

In Figure 6.5 we see transmission values versus taper length. In the butt coupling case, $L = 0a$, the calculated transmission value is 86.9%. As clearly seen from the graph, transmission values increase with increasing taper length. The calculated transmission value for the taper length $L = 50a$ is found as 97.5%. For approximately $L = 30a$ of the taper length, the transmission value increased to its final value. After this value, increasing the taper length has no effect on the transmission of optical power.

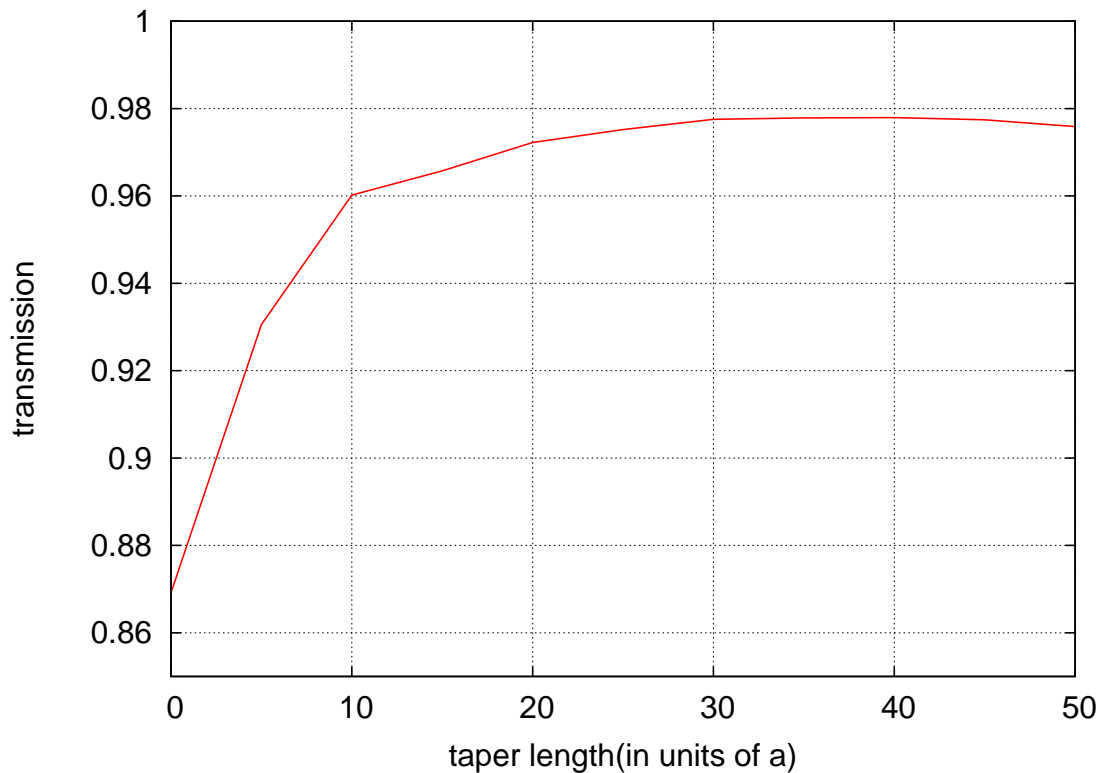


Figure 6.5. Transmission value change versus taper length of two waveguides with different lattice constant and different cladding and core slab thickness. $L = 0a$ represents the direct coupling case where $L > 0$ represents the adiabatic coupling case.

6.2. Multi to Multi slab WG-Same lattice constant

In this section we will study coupling efficiency between two waveguides that have different thickness, the cladding and the defect line thickness, but this time their lattice constants are the same, a . In Figure 6.6 we see the dielectric profile of waveguide structure we are going to work with. The waveguide on the left-hand side is made by slabs of thickness $d_{in,clad} = 2$ with dielectric constant of $\epsilon_a = 13$ and defect line has thickness of $d_{in,def} = 6$ with dielectric constant of $\epsilon_d = 13$. The waveguide on right-hand side is made by slabs of thickness $d_{out,clad} = 1$ and defect line has thickness of $d_{out,def} = 1.4$ both slabs and defect line have the same dielectric constant $\epsilon_a = \epsilon_d = 13$. The waveguide structure is immersed in air which has dielectric constant of $\epsilon_b = 1$.

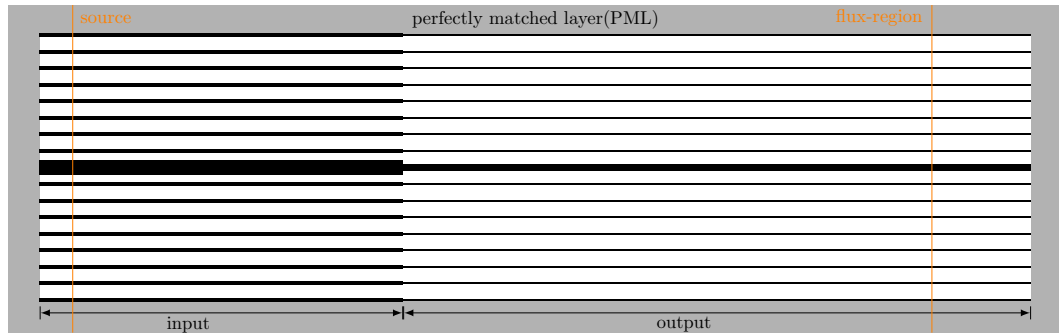


Figure 6.6. Dielectric structure of waveguide. The waveguide on the left-hand side (input part) is made by slabs of thickness $d_{in,clad} = 2$ and the defect line thickness is $d_{in,def} = 6$ with $\epsilon_a = 13$. The waveguide on the right-hand side (output part) is made by slabs of thickness $d_{out,clad} = 1$ and the defect line thickness is $d_{out,def} = 1.4$ with $\epsilon_a = 13$. The background is air, ($\epsilon_b = 1$).

In Figure 6.2 we see band structure of multi-slab waveguide (output part) calculated for TE mode. The cladding thickness is $d_{out,clad} = 1$ and the defect line thickness is $d_{out,def} = 1.4$ (black lines). Both cladding and defect line have same dielectric constant, $\epsilon_a = \epsilon_d = 13$. The waveguide is placed in a background with dielectric constant of $\epsilon_b = 1$, air. In this band structure we also show our operating mode, which is first guided mode of input part (red line). The cladding thickness of input waveguide is $d_{in,clad} = 2$ and the defect line thickness is $d_{in,def} = 6$. Cladding and defect line have same dielectric constant of $\epsilon_a = \epsilon_d = 13$. the background is air, $\epsilon_b = 1$.

Intersection of blue lines indicates our operating frequency and the wave vector. The operating frequency is $\tilde{\omega} = 0.1630$, and the wave vector is $\tilde{k} = 0.5$. At this frequency

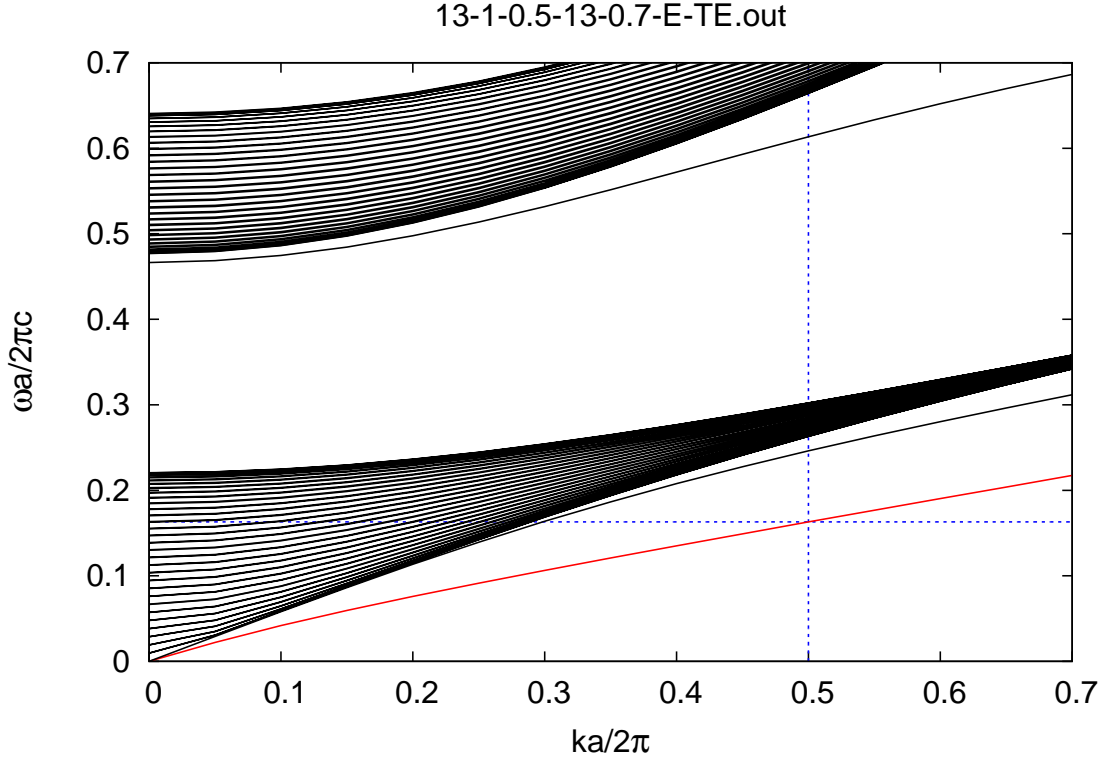


Figure 6.7. Band Structure calculated for TE mode of multi-slab waveguide, Black lines are modes of waveguide with slabs and defect line thickness $d_{out,clad} = 1$, $d_{out,def} = 1.4$ respectively. Red dashed line is first guided mode of waveguide with slabs and defect line thickness $d_{out,clad} = 2$, $d_{out,def} = 6$ respectively. Intersection of the blue line represent our operating mode with frequency and wave vector $\tilde{\omega} = 0.1630$, $\tilde{k} = 0.5$.

there is one guided mode supported by output waveguide, which is first guided mode of output waveguide.

In Figure 6.8 we see FDTD simulation of z -component of electric field (E_z). we run this simulation with 30 resolution per period and 60 resolution per period with Gaussian source. Two waveguide are butt joined to each other in this simulation. The transmission value without taper region for the simulation with 30 resolution is 59.18%, and the transmission value for the simulation with 60 resolution is 63.7%.

At time step $t = 42$ the radiation to background is clearly seen and at time step $t = 52$ and $t = 62$ the wave that is reflected back at interface is propagating backward is clearly seen. At last two time step we see the excited guided mode of the output waveguide.

Now we introduce taper region between two waveguides. The geometric parameters and dielectric constants are the same with the waveguide we used in previous simula-

tion without taper region. The only difference here is the transition region. We gradually change thickness of input waveguide cladding from $d_{in,clad} = 2$ to $d_{out,clad} = 1$, and the thickness of defect line from $d_{in,def} = 6$ to $d_{out,def} = 1.4$. The dielectric constant of transition region are also same with the dielectric constant of corresponding slabs. In Figure 6.9 we see dielectric structure of waveguide with taper region introduced.

In Figure 6.9 we see FDTD simulation of electric field, E_z , for TE mode with taper region. A Gaussian source is used to excite the operating mode. The simulation performed with 30 resolution per period. Two waveguide are joined adiabatically by using an intermediate region called taper. The taper length used for this simulation is $L = 100a$, where a is lattice constant. Transmission value with taper region introduced is 93.3%. By comparing this results with the results of the simulation run without taper region, we found that the transmission value increased by 34.1%.

The taper region serves as a mode converter, which shifts the wave vector of incoming (operating) mode to wave vector of excited mode slowly. During the coupling process the frequency is a conserved quantity and the changing parameter is the wave vector. The initial frequency and wave vector is $\tilde{\omega}_1, \tilde{k}_1$, and the final frequency and the wave vector is $\tilde{\omega}_1, \tilde{k}_2$. The closer values of wave vector values results in the lower loss of optical power. In this way the loss in optical power is minimized depending on the rate of taper change.

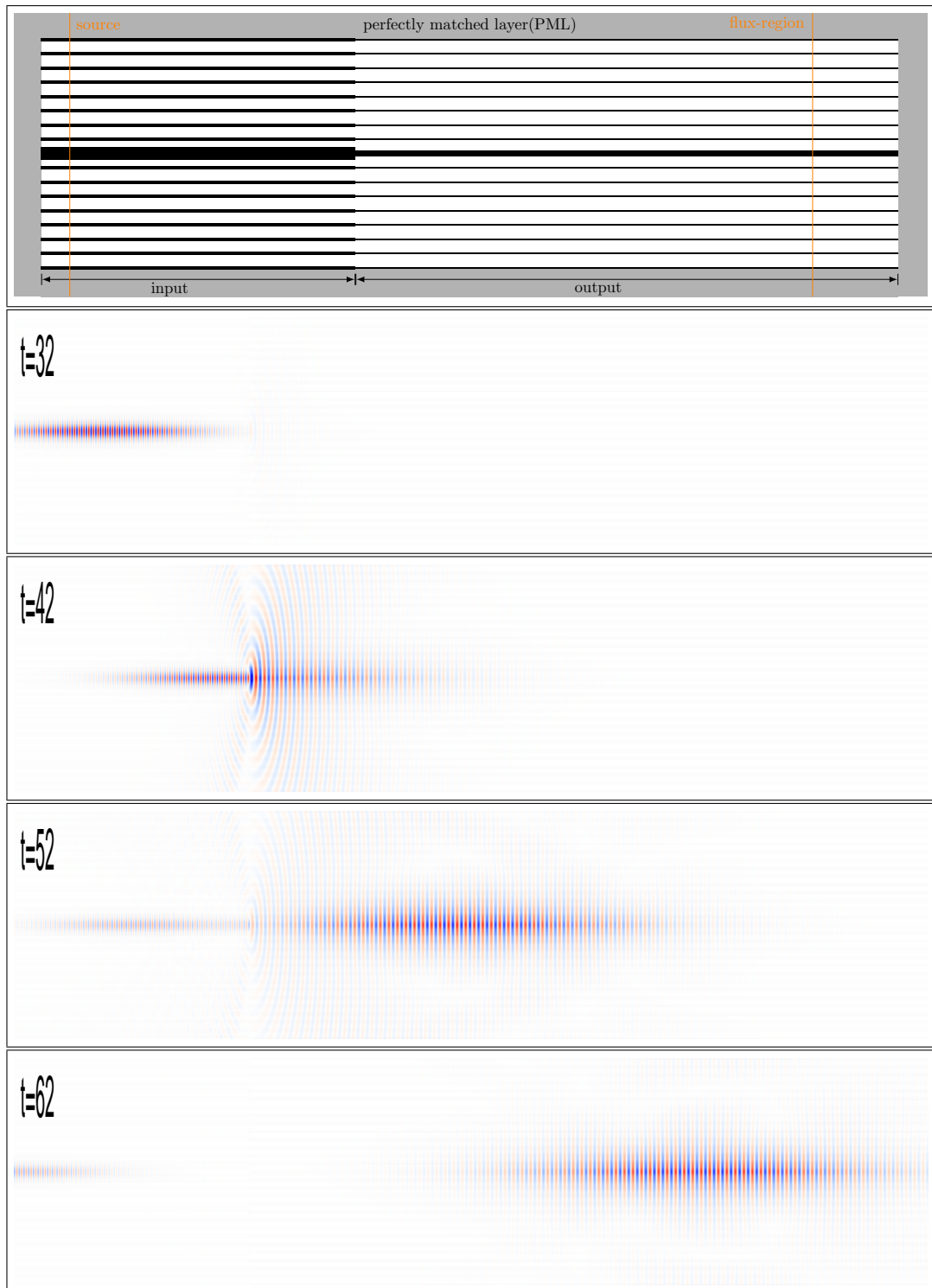


Figure 6.8. Dielectric structure of waveguide without taper region introduced. The waveguide on the left-hand side (input part) is made by slabs of thickness $d_{in,clad} = 2$ with ϵ_a and the defect line thickness is $d_{in,def} = 6$ with $\epsilon_d = 13$. The waveguide on the right-hand side (output part) is made by slabs of thickness $d_{out,clad} = 1$ with $\epsilon_a = 13$ and the defect line thickness is $d_{out,def} = 1.4$ with $\epsilon_d = 13$. The background is air, ($\epsilon_b = 1$). FDTD simulation of electric field that is in the z -direction is shown for the waveguide without taper region.

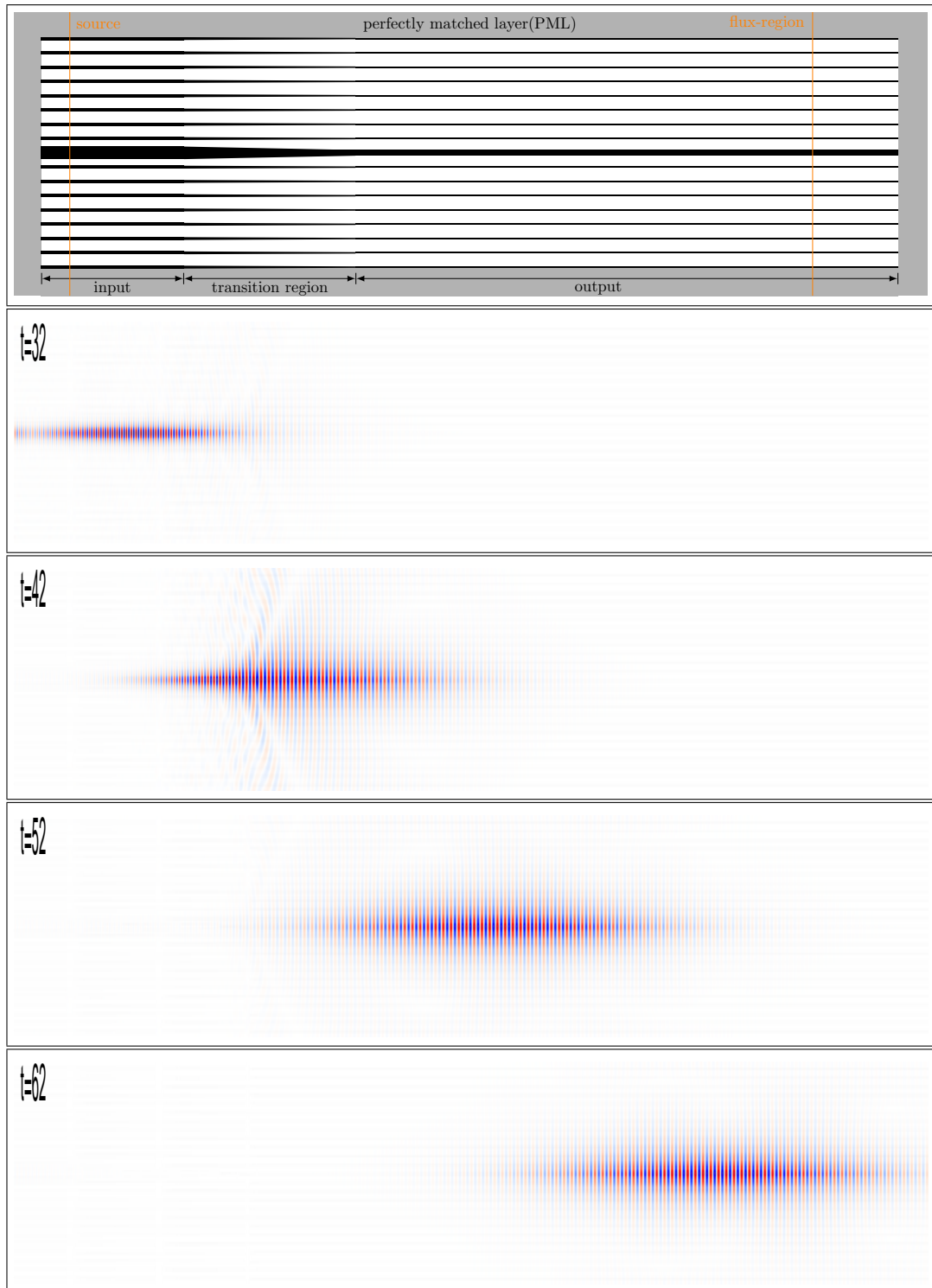


Figure 6.9. Dielectric structure of waveguide with taper region of length $L = 100a$ introduced. FDTD simulation of z -component of electric field in the case of taper region introduced. The waveguide on the left-hand side made by slabs of thickness $d_{in,clad} = 2$, the line defect has thickness of $d_{in,def} = 6$ and the waveguide on the right-hand side is made by slabs of thickness $d_{out,clad} = 1$, the defect line thickness is $d_{out,def} = 1.4$. All slabs have same dielectric constant $\epsilon_a = \epsilon_d = 13$. The background is air, ($\epsilon_b = 1$)

In figure 6.10 we see transmission values versus taper region length. The red line is transmission values obtained by running simulation with 30 resolution per period. Comparing the butt coupling efficiency, where $L = 0a$, with adiabatic coupling efficiency when taper length $L = 100a$, we found that 34.1% enhancement is achieved. The blue line shows transmission value obtained by running the simulation with 60 resolution per period. And the coupling efficiency is increased by 31.5%.

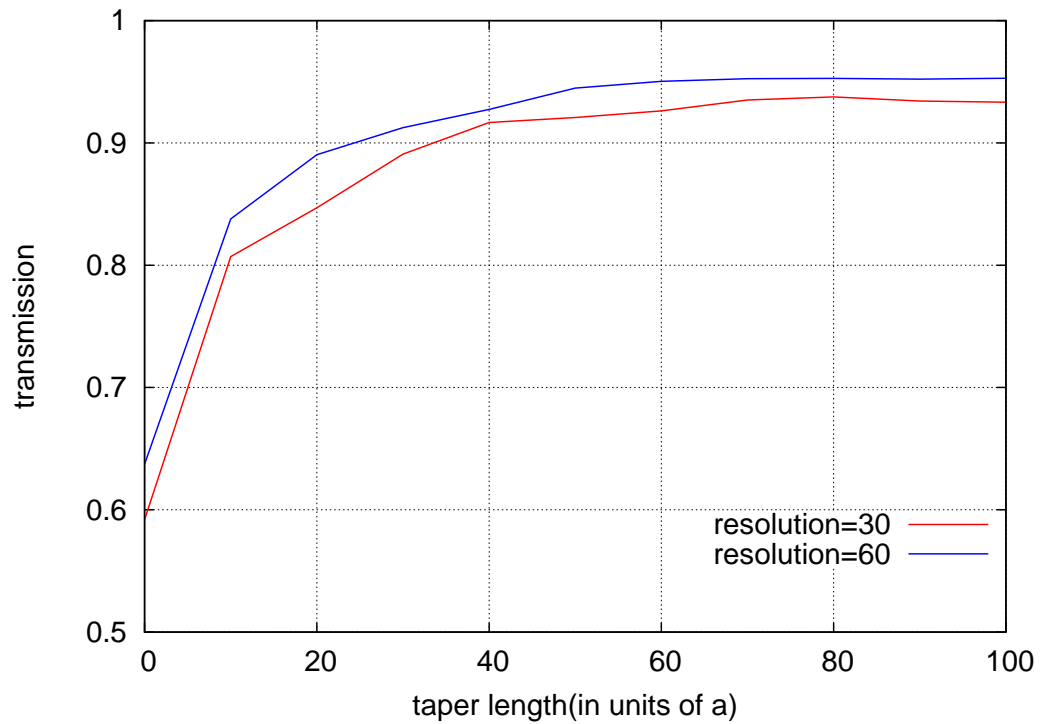


Figure 6.10. Transmission values versus taper length calculate using FDTD method. The red curve shows the transmission value calculated using 30 resolution per period and the blue curve shows the transmission value calculated using 60 resolution per period. The butt-coupling case ($L = 0a$) and adiabatic coupling case ($L > 0a$) is shown.

As seen from the transmission value versus taper length, Figure 6.10, introducing taper region, slowly changing the cladding and the defect line thickness, increases the coupling efficiency.

CHAPTER 7

COUPLING SINGLE-SLAB TO 2D LINE DEFECT PHOTONIC CRYSTAL WAVEGUIDES

In this chapter we will study the coupling process between single-slab waveguide and 2-D line defect photonic crystal waveguide (PhCWG). Transmission values will be calculated using FDTD method with and without taper region introduced. In the first section we will study coupling of light from single slab- waveguide to 2D line defect PhCWG (one-stage coupling). In the second section we will also couple light back from 2-D line defect PhCWG to single-slab waveguide (two-stage coupling). The effect of taper length on transmission value will be studied.

7.1. One-Stage Coupling

Coupling efficiency of electromagnetic mode between single-slab waveguide and 2D line defect photonic crystal waveguide will be studied in this section. The waveguide structure is shown in Figure 7.1. The structure consists of a single-slab waveguide (the input region), and a 2D line defect PhCWG which is made by cylindrical rods arranged in a square lattice (the output region). Two waveguides are butt joined to each other.

Photonic band structure of 2D line defect PhCWG calculated for TE modes using plane wave expansion is shown in Figure 7.2. The photonic crystal waveguide is made by cylindrical rods arranged in a square lattice with lattice constant a . The radius of cylindrical rods is $R = 1$ with dielectric constant of $\epsilon_a = 13$. The defect line is made by removing one row of cylinders along the center of the photonic crystal and replaced by a slab with thickness of $d_{out,def} = 2$ with dielectric constant $\epsilon_d = 13$. The background material has dielectric constant of $\epsilon_b = 2.25$, (black lines). We also showed first guided mode of single-slab waveguide (red line) in Figure 7.2. The single-slab thickness is $d_{in} = 12$ with dielectric constant of $\epsilon_a = 13$ and the background of single-slab has dielectric constant of $\epsilon_b = 2.25$. The intersection of blue dashed lines indicate our operating mode with normalized frequency $\tilde{\omega} = \left(\frac{\omega a}{2\pi c}\right) = 0.1219$, and the normalized wave vector $\tilde{k} = \left(\frac{ka}{2\pi}\right) = 0.4$.

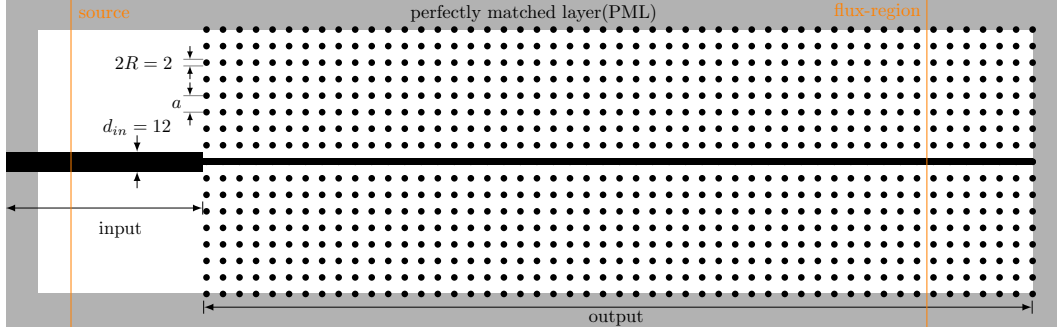


Figure 7.1. Dielectric structure of butt jointed waveguide which is made of a single slab waveguide of thickness $d_{in} = 12$ and 2-D line defect PhCWG made of cylindrical rods of radius $R = 1$ and defect line with thickness $d_{out,def} = 2$. All waveguide parts have same dielectric constant of $\epsilon_a = 13$. The background has dielectric constant $\epsilon_b = 2.25$.

At the operating frequency, as can be seen from Figure 7.2 there is only one propagating (guided) mode of 2-D line defect PhCWG. When we send the operating mode from single-slab waveguide it will propagate along single-slab waveguide and when it comes to interface it will excite all guided mode of 2-D line defect PhCWG, in this structure there is only one guided mode of 2-D line defect PhCWG, and radiation mode will also be excited. Some of the incoming mode will be reflected back from interface.

In Figure 7.3 we see time snapshot of electric field profile (E_z) of TE mode found by using FDTD method. Gaussian source with normalized frequency of $\tilde{\omega} = 0.1219$ and normalized wave vector of $\tilde{k} = 0.4$ is used to excite the operating mode. The simulation is performed with 30 resolution per period. These mode profiles are taken at four different time step. The calculated transmission value when there is no taper region is 81.5%. The loss of optical power is 18.5%. At the interface where both single-slab waveguide and 2-D line defect PhCWG are met, the operating mode coupled directly to the output waveguide

At time step $t = 25$, $t = 30$ and $t = 35$ the incoming wave excited the guided mode of output region, some of the optical power is radiated to background and some of the optical power is reflected back at the interface. These power radiated to background and reflected back at the interface are the loss of electromagnetic energy. At time step $t = 40$ we see the excited guided mode of output region. The coupling efficiency is effected by the group velocity difference and the mode profile difference of both waveguide. The mode profile difference can be seen from wave vector of operating mode and wave vector of excited mode in the output region.

Now we will use taper region between single-slab WG and 2D line defect PhCWG and we will look for transmission values, and compare the transmission values with the

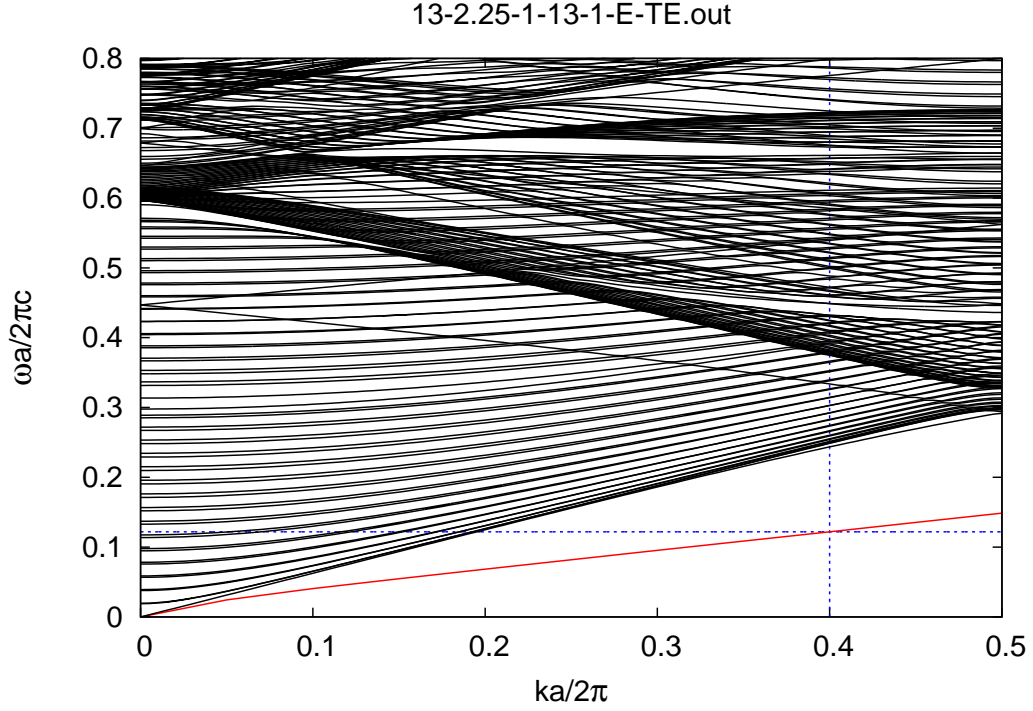


Figure 7.2. Band structure of a 2-D line defect PhCWG calculated for TE modes. The photonic crystal is made by cylindrical rods arranged in a square lattice. The defect line has thickness $d_{out,def} = 2$ with dielectric constant $\epsilon_d = 13$ and the cylindrical rods have radius $R = 1$ with same dielectric constant of defect line. The background has dielectric constant of $\epsilon_b = 2.25$. The red line is the operating mode of single-slab with thickness $d_{in} = 12$ with dielectric constant $\epsilon_a = 13$ immersed in a background with dielectric constant of $\epsilon_b = 2.25$. The intersection of blue dashed lines is the operating frequency and wave vector, $\tilde{\omega} = 0.1219$ and $\tilde{k} = 0.4$ respectively.

case of butt coupling. The transition region for the background of single-slab waveguide of this structure is made by cylindrical rods with an arbitrary small radius and gradually increase their radius until it become same with radius of cylindrical rods of 2D line defect PhCWG. The lattice spacing is kept constant during this gradual change. In this way we gradually taper the structure from background to cylindrical region. The transition from single slab waveguide to defect line of 2-D line defect PhCWG is made by a trapezoidal geometry. The waveguide structure with transition region is shown in Figure 7.4. The geometric parameters are the same with the waveguide shown in Figure 7.3. Single-slab thickness is decreased form $d_{in} = 12$ to the thickness of defect line of PhCWG, $d_{out,def} = 2$. The cylindrical rods of radius are increased from the value of $R = 0$ to $R = 1$. Taper length in this structure is $L = 50a$, where a is lattice constant.

In simulation shown in Figure 7.4 we used first guided mode of single-slab waveguide-

uide (input part). A Gaussian source is used to excite the operating mode with frequency of $\tilde{\omega} = 0.1219$ with wave vector $\tilde{k} = 0.4$. The simulation is performed with 30 resolution per period. FDTD simulations of z -component of electric field for TE mode is shown in Figure 7.4. In this figure we see electric field distribution taken at four different time. At time step $t = 28$, the operating mode propagation along the input waveguide is shown. The excited guided mode and the radiation mode are shown at time steps $t = 35$ and $t = 40$. The transmission value for this simulation is 98.1%. Only 1.9% of optical power is lost. At time step $t = 46$ the guided excited mode of 2-D line defect PhCWG is shown.

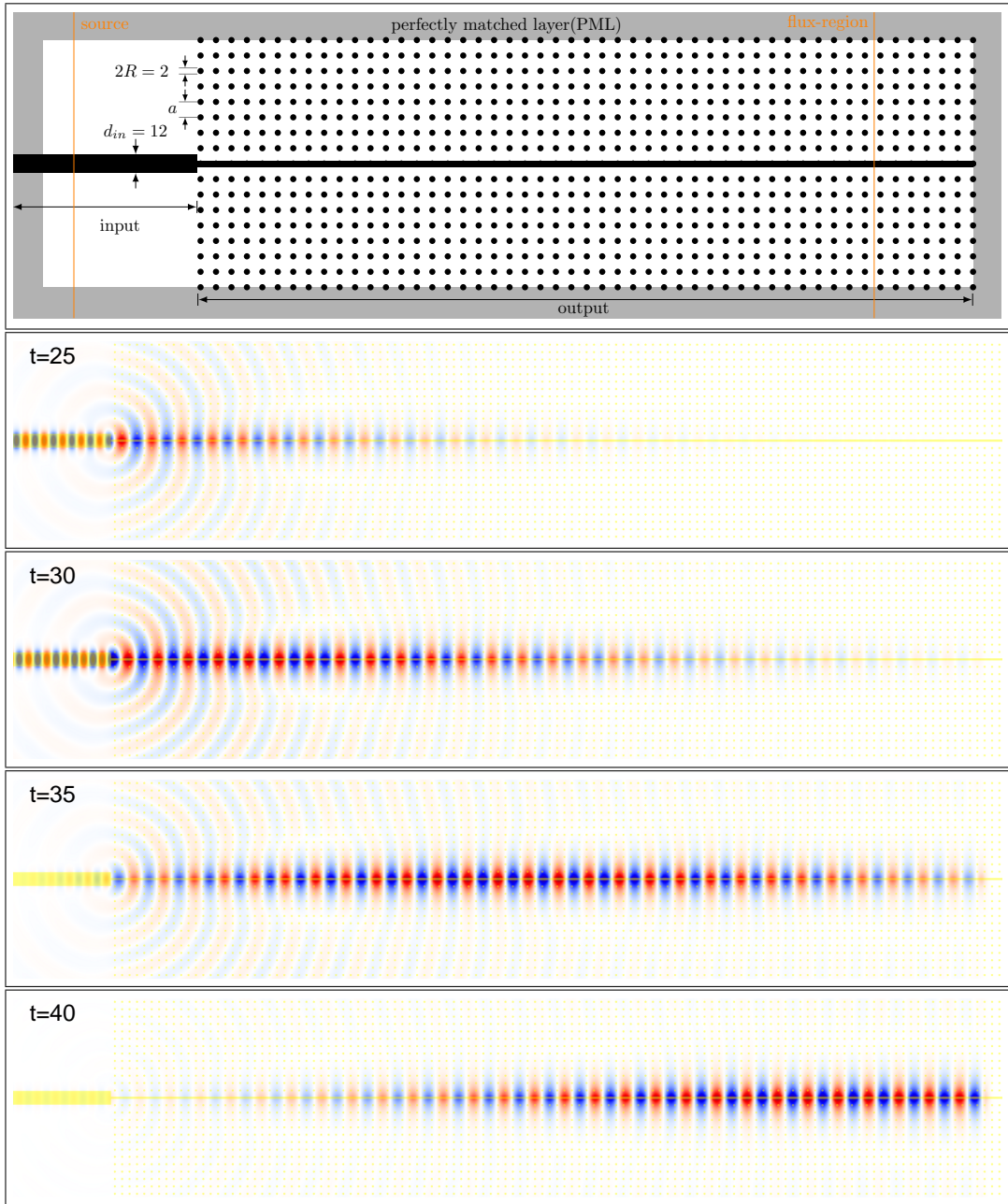


Figure 7.3. Dielectric structure of butt joined waveguide and z -component of electric field profile of TE mode along structure which is made of a single-slab waveguide of thickness $d_{in} = 12$ and 2D line defect PhCWG made of cylindrical rods of radius $R = 1$ and defect line with thickness $d_{out,def} = 2$. All waveguide parts have same dielectric constant of $\epsilon_a = 13$. The background has dielectric constant $\epsilon_b = 2.25$.

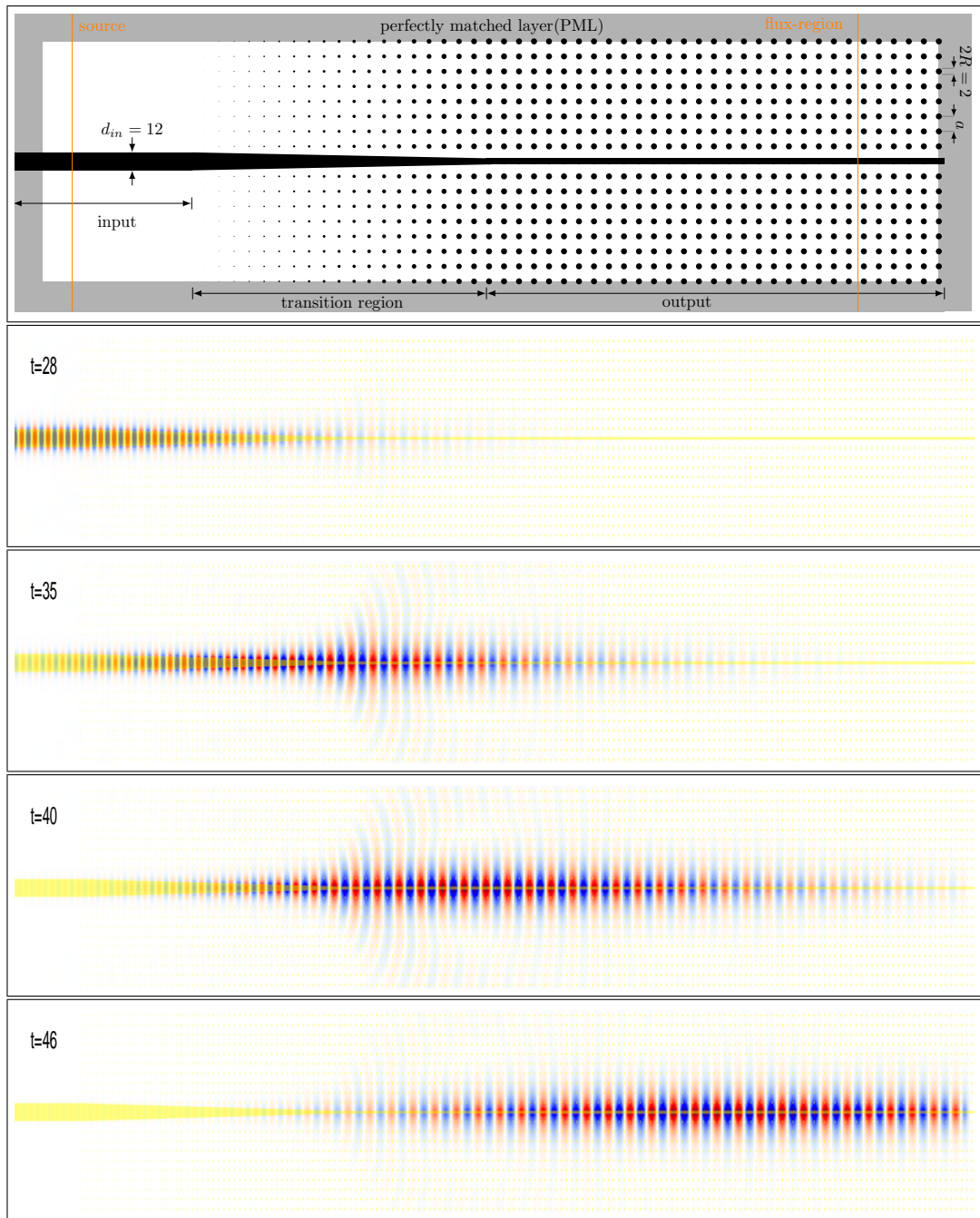


Figure 7.4. The dielectric structure of single-slab WG and 2-D line defect PhCWG joined by a taper region. We introduced cylindrical transition region for the background of single-slab WG. Trapezoidal transition geometry is used between single-slab WG and the defect line of 2-D line defect PhCWG. Electric field distribution, (E_z), found by FDTD simulation. Snapshot of field taken for four different time step.

The transmission values versus taper length is shown in Figure 7.5, as we see from the graph transmission value is increasing with increasing taper length. In the case of butt coupling, $L = 0a$, the transmission value is around 81.5%. When the taper region length start to increase, the transmission value increases smoothly. The figure shows transmission values for $L = 0a$ to $L = 50a$. Transmission value for $L = 50a$ is 98.1%. Comparing this value with the simulation result of the structure without taper we see that transmission value increased by 16.6%.

Using taper region, slowly converting a dielectric medium properties, slowly changes the the response of a dielectric material to electromagnetic radiation.

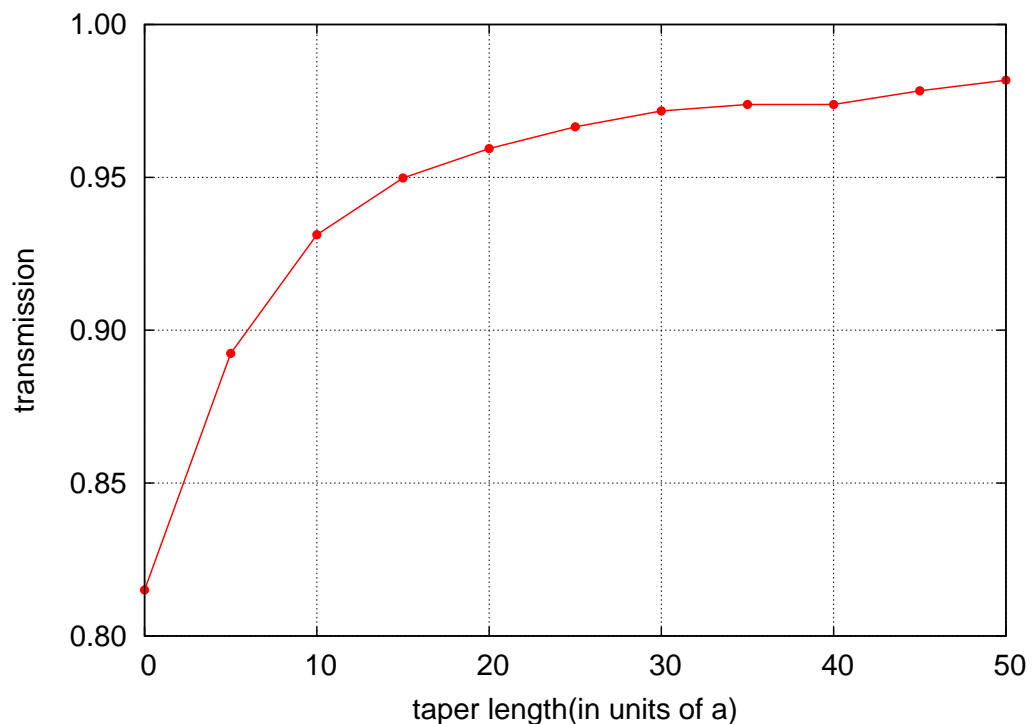


Figure 7.5. Transmission values for TE-polarized electric field, E_z , for the structure of single slab and 2-D line defect PhCWG calculated using FDTD simulation, one stage coupling. Transmission values versus taper length calculated for every $5a$ starting from $L = 0a$, (butt coupling) to $L = 50a$ is shown.

7.2. Two-Stage Coupling

Two-stage coupling will be studied in this section. The waveguide structure is shown in Figure 7.6. Geometric parameters are the same with the waveguide structure we studied in the previous section but this time the output region is made by single-slab waveguide.

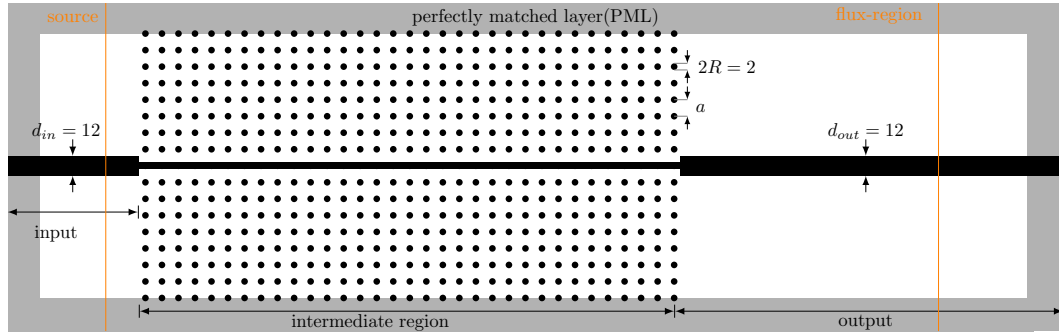


Figure 7.6. Waveguide structure consist of three region, the waveguide on left called input part has thickness of $d_{in} = 12$, intermediate part is 2-D line defect PhCWG has defect line of thickness $d_{int,def} = 2$ and cylindrical rods of radius $R = 1$, and the output part has same thickness with input part. All three part has same dielectric constant $\epsilon_a = 13$. The background has dielectric constant of $\epsilon_b = 2.25$.

The waveguide on left-hand side is called input part has thickness of $d_{in} = 12$, the intermediate part is 2D line defect PhCWG has defect line thickness $d_{int,def} = 2$ and cylindrical rods has radius of $R = 1$, and output part has same thickness with the input part, $d_{out} = 12$. All waveguide part have same dielectric constant of $\epsilon_a = 13$. The background has dielectric constant $\epsilon_b = 2.25$. The guided operating mode of single-slab waveguide will be coupled to 2D line defect PhCWG then the excited mode of 2D line defect PhCWG will propagate along this region and finally it will be coupled back to single-slab waveguide. The band structure of 2D line defect PhCWG and the operating mode of single-slab waveguide is shown in Figure 7.2.

In Figure 7.7 we see FDTD simulation of z -component of electric field (E_z) for TE mode taken for four different time step. A Gaussian source is used to excite the operating mode with frequency $\tilde{\omega} = 0.1219$ and wave vector $\tilde{k} = 0.4$. This mode propagate along the single slab waveguide and when it comes to interface it will excited the guided mode of 2-D line defect PhCWG and after propagating along this medium it excites the guided modes of single slab waveguide in output region. At time step $t = 25$, the operating mode

and the excited mode of both single slab and 2-D line defect PhCWG is clearly seen. At time step $t = 30$ and $t = 35$ we see the electric field of both intermediate region. The radiated and the reflected optical power are clearly seen. At the last time step $t = 45$, the mode is entirely in the output region, single mode and well confined. Butt coupling in this simulation take place twice in this simulation.

In Figure 7.8 we see the dielectric profile of the waveguide structure. The geometric parameters are same with the waveguide structure used in the previous simulation. The only difference here is the two taper region used to make smooth transition from single slab waveguide to 2-D line defect PhCWG and from 2-D line defect PhCWG to single slab waveguide. First taper region introduced between input waveguide and 2-D line defect PhCWG is constructed as the radius of cylindrical rods increased from $R = 0$ to $R = 1$ while keeping the lattice constant same and the single-slab waveguide is connected to defect line of 2-D line defect PhCWG by a trapezoidal slab which thickness is decreased smoothly from $d_{in} = 12$ to $d_{int,def} = 2$. The second taper region is introduced between 2-D line defect PhCWG and the output waveguide which has the the mirror symmetry of the taper used between input waveguide and the 2-D line defect PhCWG.

In Figure 7.8 the z -component of electric field of TE mode profile found by FDTD for four different time step is shown. The simulation were performed with 30 resolution per period by using a Gaussian source to excite the operating mode with frequency $\tilde{\omega} = 0.1219$ and wave vector $\tilde{k} = 0.4$. Taper length for this structure is $L = 100a$, where a is lattice constant. Transmission value for this structure is 98.3%. By comparing this value with the butt-coupling case we see that transmission value increased by 31.7%. Comparing the mode profile at time step $t = 35$ with the mode profile at time step $t = 50$, we see that the operating mode profile is converted smoothly to guided mode of 2-D line defect PhCWG. The reverse smooth conversion is seen clearly at time step $t = 65$.

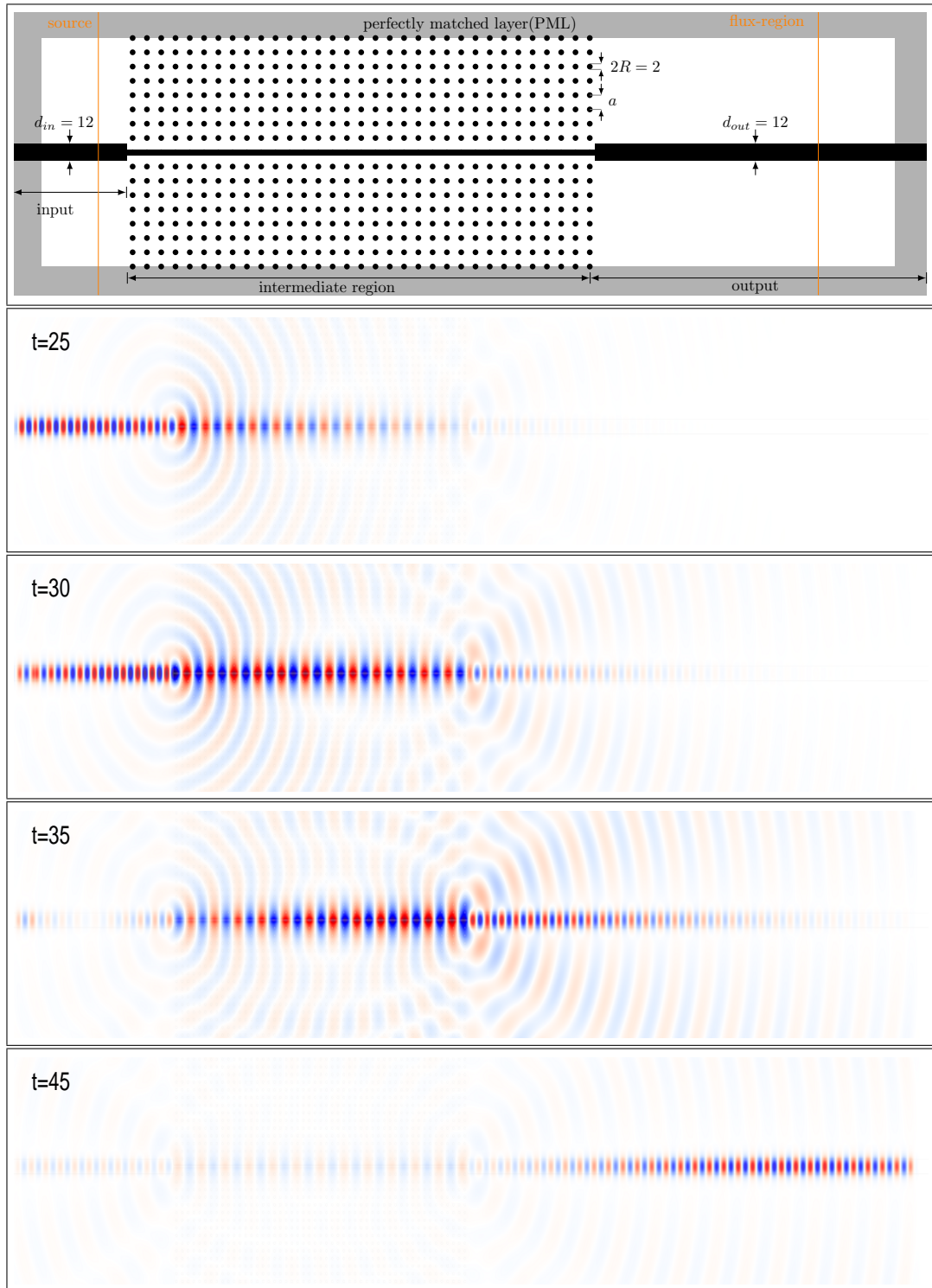


Figure 7.7. FDTD simulation of structure, which consist of three waveguides, the waveguide on left called input part has thickness of $d_{in} = 12$, intermediate part is 2-D line defect PhCWG has defect line of thickness $d_{int,def} = 2$ and cylindrical rods of radius $R = 1$, and the output part has same thickness with input part, $d_{out} = 12$. All three part has same dielectric constant $\epsilon_a = 13$. The background has dielectric constant of $\epsilon_b = 2.25$.

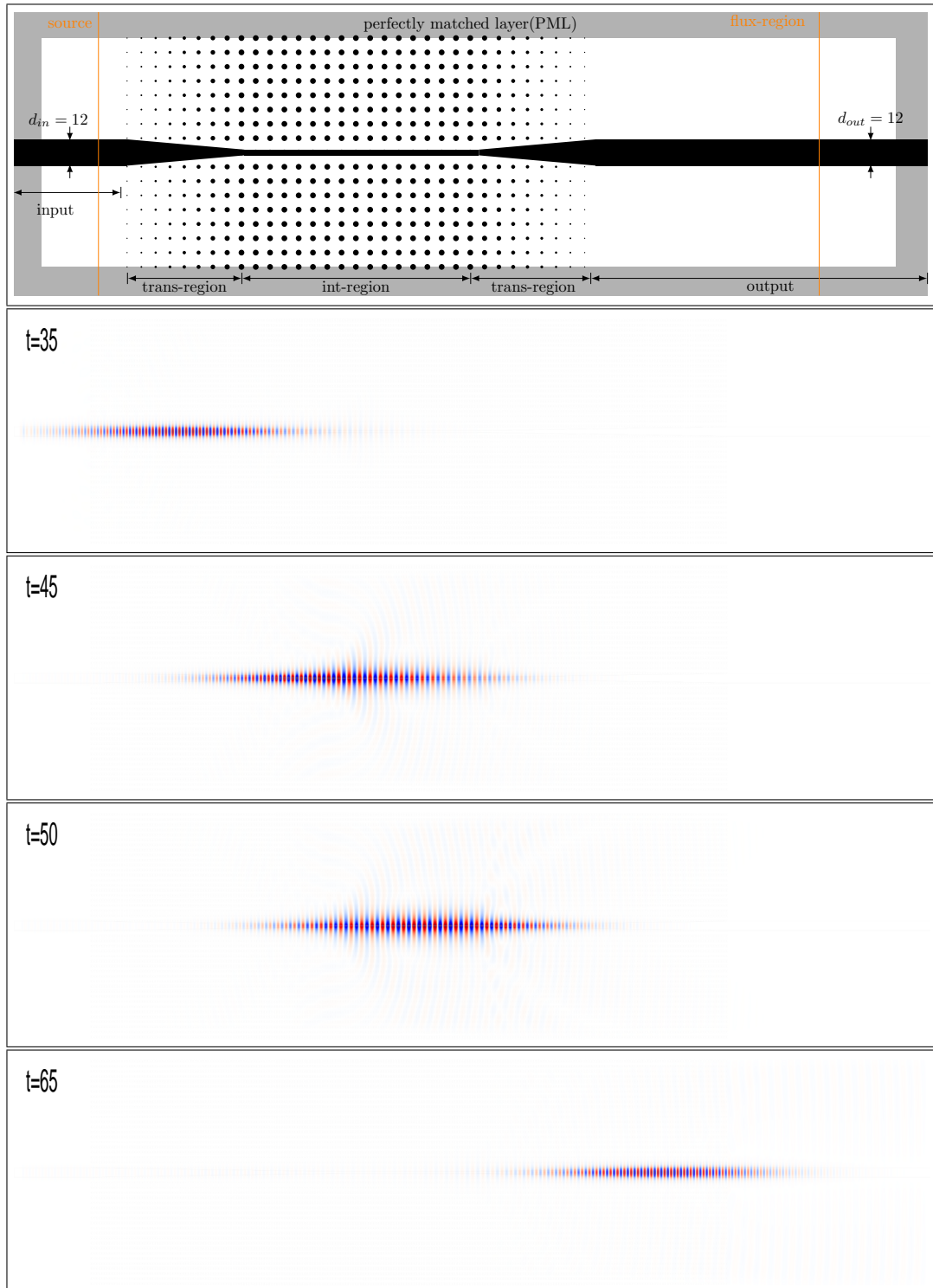


Figure 7.8. Dielectric profile of waveguide with taper region length of $L = 100a$ where a is lattice constant. The structure is constructed with a single-slab waveguide which is called input region, a taper region is introduced between input waveguide and 2-D line defect PhCWG. Between 2-D line defect PhCWG and output region we introduce another taper region. The z -component of electric field (E_z) distribution for TE mode found by FDTD simulation.

The transmission values corresponding to taper length is shown in Figure 7.9, as we see from the figure transmission value is increasing with increasing taper length. In the butt coupling case, the optical mode send from single slab waveguide first couple to 2-D line defect PhCWG. This coupling results in optical power loss. After propagating in 2-D line defect PhCWG for a while then the excited mode couples back to single slab waveguide. This coupling also will cause some optical power loss. The main reason for those loss are the group velocity and wave vector mismatch.

In the case of adiabatic transition, the mode we excite from single-slab waveguide is coupled to 2-D line defect PhCWG by transition region called taper. After this region, the mode transferred to 2-D line defect PhCWG and again tapered back to single slab waveguide. As can be seen from Figure 7.9 using taper region has significant improvement on transmission values.

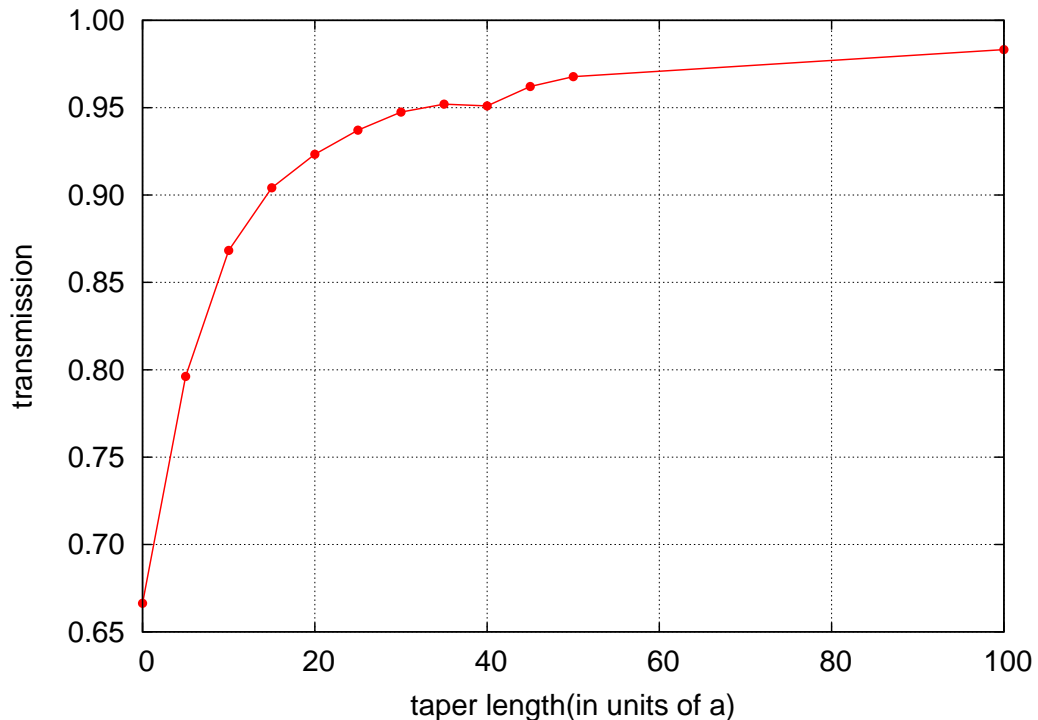


Figure 7.9. Transmission values for TE mode for the structure of single-slab waveguide and 2-D line defect PhCWG calculated using FDTD simulation. In this simulation, the operating mode first coupled form single slab waveguide to 2-D line defect PhCWG and then coupled back to single slab waveguide, two stage-coupling. Transmission values versus taper length calculated for every $5a$ starting from $L = 0a$, (butt coupling) to $L = 100a$, (adiabatic coupling) is shown.

CHAPTER 8

CONCLUSION

In this thesis work we have presented taper region designs for four types of waveguide structure. Coupling from single-slab waveguide to single-slab waveguide, coupling from single-slab waveguide to multi-slab waveguide, coupling from multi slab waveguide to multi slab waveguide, and coupling from single-slab waveguide to 2D line defect photonic crystal waveguide has been studied numerically using finite-different time-domain method. A trapezoidal shaped transition region is used to connect single-slab waveguides. Besides trapezoidal shaped transition region, to make gradual transition from background of single-slab waveguide to 2D line defect photonic crystal we changed dielectric cylinders radius from zero to its final value. Finite-different time- domain simulation has shown that, the guided mode profile can be smoothly converted or transferred from an input waveguide to an output waveguide that have different geometric parameters and different guiding mechanism. In adiabatic transition case, comparing to the butt-coupling case, excitation of higher mode can be prevented. Coupling to multi-mode cause the signal to spread in space along waveguide which is due to mode's group velocity difference. FDTD calculation showed that EM radiation loss due to sudden change in geometry of waveguide can be prevented by using a transition region that designed gradual enough.

According to transmission values that are found by using FDTD method, it is showed that the coupling efficiency is increased by 21% for single-slab waveguide. We also showed that the transmission value for single slab to multi slab waveguide is increased by 8% when we only use taper region between single-slab waveguide and defect line of multi-slab waveguide. The transmission value for the case where we used taper region between single-slab waveguide and defect line of multi-slab waveguide and between background of single slab waveguide and cladding of multi-slab waveguide is increased by 16.5%. Transmission value for coupling light between two multi-slab waveguide that has different geometric parameter, different core, cladding and lattice constant, with taper region introduced increased by 10.6%. In the case of waveguide structures that have same lattice constant and different slab and core thickness, the transmission value is increased by 34.1%. And finally we showed that coupling efficiency between single-slab waveguide and 2D line defect PhCWG is increased for one-stage coupling by 16.6%. For two stage coupling the increase of coupling efficiency is 31.7%.

Our works show that, by properly matching two physically different waveguides we have shown that it's possible to transfer the optical power almost without loss in the adiabatic limit.

REFERENCES

- Ashcroft, N. W. and N. D. Mermin (1976, 1). *Solid State Physics* (1 ed.). Brooks Cole.
- Baba, T. and D. Ohsaki (2001). Interfaces of photonic crystals for high efficiency light transmission. *Japanese Journal of Applied Physics* 40(Part 1, No. 10), 5920–5924.
- Bienstman, P., S. Assefa, S. G. Johnson, J. D. Joannopoulos, G. S. Petrich, and L. A. Kolodziejski (2003, Sep). Taper structures for coupling into photonic crystal slab waveguides. *J. Opt. Soc. Am. B* 20(9), 1817–1821.
- Griffiths, D. J. (1999, 1). *Introduction to Electrodynamics* (3rd ed.). Addison Wesley.
- Griffiths, D. J. (2004, 4). *Introduction to Quantum Mechanics* (2nd ed.). Benjamin Cummings.
- Happ, T. D., M. Kamp, and A. Forchel (2001, Jul). Photonic crystal tapers for ultracompact mode conversion. *Opt. Lett.* 26(14), 1102–1104.
- Ho, K. M., C. T. Chan, and C. M. Soukoulis (1990, Dec). Existence of a photonic gap in periodic dielectric structures. *Phys. Rev. Lett.* 65, 3152–3155.
- Hosseini, A., X. Xu, D. N. Kwong, H. Subbaraman, W. Jiang, and R. T. Chen (2011). On the role of evanescent modes and group index tapering in slow light photonic crystal waveguide coupling efficiency. *Applied Physics Letters* 98(031107).
- Jackson, J. D. (1998, 8). *Classical Electrodynamics* (3 ed.). Wiley.
- John, S. (1987, Jun). Strong localization of photons in certain disordered dielectric superlattices. *Phys. Rev. Lett.* 58, 2486–2489.
- Johnson, S. G., P. Bienstman, M. A. Skorobogatiy, M. Ibanescu, E. Lidorikis, and J. D. Joannopoulos (2002, Dec). Adiabatic theorem and continuous coupled-mode theory for efficient taper transitions in photonic crystals. *Phys. Rev. E* 66, 066608.
- K. (EDT)/ Ohtaka, K. E. I. (1980). *Photonic Crystals*. NY.
- Lin, C.-Y., A. X. Wang, W.-C. Lai, J. L. Covey, S. Chakravarty, and R. T. Chen (2012, Jan). Coupling loss minimization of slow light slotted photonic crystal waveguides using mode matching with continuous group index perturbation. *Opt. Lett.* 37(2), 232–234.
- Lin, C.-Y., X. Wang, S. Chakravarty, B. S. Lee, W.-C. Lai, and R. T. Chen (2010). Wide-band group velocity independent coupling into slow light silicon photonic crystal

- waveguide. *Applied Physics Letters* 97, 183302.
- Mekis, A. and J. D. Joannopoulos (2001, Jun). Tapered couplers for efficient interfacing between dielectric and photonic crystal waveguides. *J. Lightwave Technol.* 19(6), 861.
- Momeni, B. and A. Adibi (2005). Adiabatic matching stage for coupling of light to extended Bloch modes of photonic crystals. *Applied Physics Letters* 87, 171104.
- Oskooi, A. F., D. Roundy, M. Ibanescu, P. Bermel, J. D. Joannopoulos, and S. G. Johnson (2010, January). MEEP: A flexible free-software package for electromagnetic simulations by the FDTD method. *Computer Physics Communications* 181, 687–702.
- Palamaru, M. and P. Lalanne (2001). Photonic crystal waveguides: Out-of-plane losses and adiabatic modal conversion. *Applied Physics Letters* 78.
- Säynätjoki, A., K. Vynck, M. Mulot, D. Cassagne, J. Ahopelto, and H. Lipsanen (2008). Efficient light coupling into a photonic crystal waveguide with flatband slow mode. *Photonics and Nanostructures - Fundamentals and Applications* 6(2), 127 – 133.
- Sözüer, H. S. (2008). Lecture notes on photonic structures.
- Taflove, A. and S. C. Hagness (2005, 6). *Computational Electrodynamics: The Finite-Difference Time-Domain Method* (3 ed.). Artech House.
- Wang, Z., N. Zhu, Y. Tang, L. Wosinski, D. Dai, and S. He (2009, May). Ultracompact low-loss coupler between strip and slot waveguides. *Opt. Lett.* 34(10), 1498–1500.
- Witzens, J., M. Hochberg, T. Baehr-Jones, and A. Scherer (2004, Apr). Mode matching interface for efficient coupling of light into planar photonic crystals. *Phys. Rev. E* 69, 046609.
- Xu, Y., R. K. Lee, and A. Yariv (2000, May). Adiabatic coupling between conventional dielectric waveguides and waveguides with discrete translational symmetry. *Opt. Lett.* 25(10), 755–757.
- Yablonovitch, E. (1987, May). Inhibited spontaneous emission in solid-state physics and electronics. *Phys. Rev. Lett.* 58, 2059–2062.
- Yee, K. (1966). Numerical solution of initial boundary value problems involving Maxwell's equations in isotropic media. *Antennas and Propagation, IEEE Transactions on* 14(3), 302–307.